TECHNISCHE UNIVERSITÄT MÜNCHEN

TUM School of Computation, Information and Technology

Collision Models for Gyrokinetic Simulations of Edge Turbulence in Fusion Plasmas

Philipp Ulbl

Vollständiger Abdruck der von der TUM School of Computation, Information and Technology der Technischen Universität München zur Erlangung der akademischen Grades eines

Doktors der Naturwissenschaften
(Dr. rer. nat.)

genehmigten Dissertation.

Vorsitz:	Prof. Dr. Martin Schulz
Prüfer*innen der Dissertation:	1. Hon.-Prof. Dr. Frank Jenko
	2. Prof. Dr. Eric Sonnendrücker
	3. Prof. Laurent Villard

Die Dissertation wurde am 30.06.2023 bei der Technischen Universität München eingereicht und durch die TUM School of Computation, Information and Technology am 27.11.2023 angenommen.

Abstract

The performance of future magnetic confinement fusion power plants depends heavily on the turbulence-influenced quality of plasma confinement and heat exhaust. The main tools to study turbulence in fusion devices are high-fidelity gyrokinetic simulations implemented in massively parallelized, high-performance computer codes. As the geometry in realistic, diverted tokamak plasmas is complex and challenging to simulate, turbulence in the relevant edge and scrape-off layer (SOL) regions remains to be understood. The `GENE-X` code fills this gap by providing a unique computational tool that can perform global gyrokinetic simulations in realistic device geometries.

This work presents a physics extension of the `GENE-X` code, adding collisional effects to the gyrokinetic model and improving the fidelity of the code. Including collisions is essential in the edge and SOL due to low temperatures and high collisionality. The implementations feature a basic Bhatnagar-Gross-Krook (BGK) operator and an improved Fokker-Planck-like Lenard-Bernstein/Dougherty (LBD) operator. The development of the numerical tools required to perform collisional gyrokinetic simulations is presented, along with constructing an efficient, conservative discretization of the collision operator. Further, the numerical developments are verified in physics-motivated test cases, analyzing collisional conservation and relaxation properties. The high-performance implementation of the computations shows excellent scaling in an intra- and inter-node performance benchmark.

The code validation against an experimental scenario in the TCV tokamak (TCV-X21) applies the newly developed collision models to a suitable test case. Simulations using the collisionless and the BGK and LBD models assess the possible realism achievable by the current model. The turbulence observed in this validation case is further analyzed using newly developed Fourier and trapped particle analysis tools. The obtained results allow the comparison of the effect of the three different collision models on the underlying physics of turbulence. As a result, the simulation with the advanced LBD operator shows remarkable agreement with the experiment in the confined region. In contrast, the other simulations cannot achieve the same level of agreement. The collisionless simulation predicts too high electron temperatures, while the BGK simulation suppresses turbulence significantly. The results show that the presented collisional extension considerably improves the realism of edge turbulence simulations, with the LBD collision operator posing a minimum requirement.

Zusammenfassung

Die Leistungsfähigkeit zukünftiger, auf dem Magneteinschlussverfahren basierender, Fusionskraftwerke hängt in hohem Maße von der turbulenzbestimmten Qualität des Plasmaeinschlusses und Wärmeabflusses ab. Computercodes, die in der Modellierung der Turbulenz hauptsächlich zur Anwendung kommen, basieren auf der höchst akkuraten gyrokinetischen Plasmatheorie, welche auf massiv parallelisierten Hochleistungsrechnern betrieben werden müssen. Da die Geometrie der für Fusion relevanten Tokamak Anlagen komplex ist, sind Turbulenz-Simulationen am Rand und in der sogenannten Abschürfschicht ("scrape-off layer" - SOL) des Plasmas besonders herausfordernd. Der `GENE-X` Code wurde speziell für diese Anwendungszwecke entwickelt und ermöglicht globale gyrokinetische Simulationen von Plasmaturbulenz in realistischer Geometrie.

Diese Arbeit präsentiert eine Erweiterung des `GENE-X` Codes, mit dem Ziel die Genauigkeit des gyrokinetischen Modells durch Berücksichtigung von Stoßprozessen zu erhöhen. Die Abkühlung des Plasmas am Rand und im SOL erhöht die Stoßrate erheblich womit der Einbezug von Stoßeffekten notwendig wird. Die Modellierung der Stoßprozesse erfolgt in mehreren Abstufungen, wobei zuerst ein einfaches Modell von Bhatnagar-Gross-Krook (BGK) und folgend ein fortgeschrittenes Lenard-Bernstein/Dougherty (LBD) Modell implementiert wird. Dies erfordert die Entwicklung von numerischen Methoden, um die stoßerweiterten gyrokinetischen Simulationen zu ermöglichen. Dazu wird ein Finite-Volumen Schema konstruiert, welches durch spezielle Korrekturterme die Erhaltung von Einzelspeziesdichten sowie Gesamtimpuls und -energie sicherstellt. Die Implementierung wird auf die geforderten Erhaltungseigenschaften sowie auf die Reproduktion von prognostizierten Relaxationsraten verifiziert. Die hocheffiziente Einbettung der Algorithmen in den `GENE-X` Code wird auf die Skalierungseigenschaften der Parallelisierung untersucht.

Zur Validierung wird der stoßerweiterte `GENE-X` Code auf ein Experiment des TCV Tokamaks (TCV-X21) angewandt. Simulationen mit dem stoßfreien, dem BGK und dem LBD Modell werden hierbei auf die Fähigkeit untersucht, die physikalische Realität in der Simulation nachzubilden. Die beobachtete Turbulenz wird mit eigens entwickelten Fourierdiagnostiken sowie Verfahren zur separaten Betrachtung der Beiträge von gefangenen Teilchen untersucht. Die Berücksichtigung aller Ergebnisse erlaubt eine allumfassende Analyse der Effekte verschiedener Stoßmodelle auf die Plasmaturbulenz. Das bemerkenswerte Ergebnis ist, dass das fortgeschrittene LBD Stoßmodell das Experiment in ausgezeichneter Näherung nachbilden kann. Im Gegensatz dazu, können das stoßfreie und das BGK Modell keine überzeugenden Resultate liefern. Ersteres enthält um Größenordnungen zu heiße Elektronen, zweiteres unterdrückt die Turbulenz zu stark. Der physikalische Realismusgrad in Simulationen von Rand und SOL Turbulenz kann mit der hier präsentierten Stoßerweiterung durch das LBD Modell signifikant gesteigert werden.

Publications

Part of this work has been published in the following first-author publications:

[1] **P. Ulbl**, D. Michels, F. Jenko, Contrib. Plasma Phys. 62, e202100180, DOI: https:doi.org/10.1002/ctpp.202100180 (2021).
[2] **P. Ulbl** et al., Phys. Plasmas 30, 052507, DOI: https:doi.org/10.1063/5.0144688 (2023).

The following co-author publications have been published during this thesis:

[3] D. Michels, A. Stegmeir, **P. Ulbl**, D. Jarema, F. Jenko, Comput. Phys. Commun. 264, 107986, DOI: https:doi.org/10.1016/j.cpc.2021.107986 (2021).
[4] D. Michels, **P. Ulbl** et al., Phys. Plasmas 29, 032307, DOI: https:doi.org/10.1063/5.0082413 (2022).
[5] W. Zholobenko, J. Pfennig, A. Stegmeir, T. Body, **P. Ulbl** et al., Nucl. Mater. Energy 34, 101351, DOI: https:doi.org/10.1016/j.nme.2022.101351 (2023).

Acknowledgements

I would like to thank all people who have supported this doctoral thesis's endeavor. Foremost, I would like to express my biggest gratitude to my supervisor Frank Jenko, who made this thesis possible and supported me throughout this journey. I am also thankful to my mentor Daniel Told and further to Andreas Stegmeir, who, despite not being a mentor on paper, performed this role with continuous commitment. Special thanks to Dominik Michels, who helped me a lot during the beginning of my thesis and motivated me to study, back then, new to me mathematical and numerical topics, as well as sparking the joy in professional code development. I would like to thank Wladimir Zholobenko for countless discussions on various topics. Further thanks to Tom Body for pioneering the work on validation that ultimately has led to our most important publication during this thesis.

I would like to thank everyone involved in the `GRILLIX`/`GENE-X` group in our department. Working in this group was always associated with a lot of joy, and our discussions at lunchtime or during off-work group activities were very engaging. I had the pleasure of working with Jordy Trilaksono, Marion Smedberg, Carl-Martin Pfeiler, Christoph Pitzal, Kayiu Zhang, Sergei Makarov, Konrad Eder, Jan Pfennig, Sabine Ogier-Collin, and Baptiste Frei.

Many thanks to Eric Sonnendrücker for advice and discussions on numerical methods. Thanks to Andreas Bergmann for discussions on collision operators, Tobias Görler for discussions on turbulence simulations, Thomas Hayward-Schneider for discussions on Fourier transforms, and Tilman Dannert for discussions and help with performance benchmarks. Further, it was a great pleasure to explore gyrokinetic theory with Brando Rettino. Thanks to Felix Wilms, Leonhard Leppin, Michael Bergmann, and Alexandr Mustonen for engaging discussions.

Finally, most importantly, I would like to thank my family and friends for always supporting me, especially during this time. I want to express my deepest gratitude to Esther, who joined me on the adventure to Garching and helped me overcome tough, work-intense times but also helped me enjoy successful, good times.

Table of Contents

1 Introduction **15**
- 1.1 Fusion Energy . . . 15
- 1.2 Open Problems in Edge Plasma Physics . . . 20
- 1.3 Scope of this Thesis . . . 21
- 1.4 Content Overview . . . 22

2 Gyrokinetic Theory and Simulation **25**
- 2.1 The Kinetic Equation . . . 25
- 2.2 Guiding-Center Dynamics . . . 26
  - 2.2.1 Guiding-Center Equations . . . 27
- 2.3 Gyrokinetic Equations . . . 30
- 2.4 Gyrokinetic Codes . . . 35
- 2.5 The `GENE-X` Code . . . 36

3 Theory of Coulomb Collisions in Plasmas **37**
- 3.1 Fokker-Planck Collision Operator . . . 38
  - 3.1.1 Rosenbluth Form . . . 39
  - 3.1.2 Landau Form . . . 40
  - 3.1.3 General Properties of Collision Operators . . . 41
  - 3.1.4 Coulomb Logarithm . . . 41
  - 3.1.5 Model Operators . . . 42
- 3.2 Lenard-Bernstein/Dougherty (LBD) Collision Operator . . . 43
  - 3.2.1 Ad-Hoc Derivation . . . 43
  - 3.2.2 Derivation from the Rosenbluth Form . . . 44
  - 3.2.3 Properties of the LBD Operator . . . 46
  - 3.2.4 Gyrokinetic Version . . . 51
  - 3.2.5 Properties of the Gyrokinetic Version . . . 55
  - 3.2.6 Normalized Gyrokinetic Version . . . 61
- 3.3 Bhatnagar-Gross-Krook (BGK) Collision Operator . . . 63

3.4 Chapter Summary . . . 65
3.4.1 Relation to Other Work . . . 65

4 Numerical Methods for Collision Operators 67
4.1 Discretized Velocity Space Moments . . . 68
4.1.1 Midpoint Quadrature . . . 70
4.1.2 Normalized Discrete Velocity Space Moments . . . 71
4.2 LBD - Finite Difference Discretization . . . 71
4.2.1 Construction of the Finite Difference Scheme . . . 73
4.2.2 Finite Difference Stencils for the LBD Operator . . . 73
4.2.3 Normalized Discrete Finite Difference Version . . . 76
4.3 LBD - Finite Volume Discretization . . . 76
4.3.1 Construction of the Finite Volume Scheme . . . 76
4.3.2 Conservation Properties of the Finite Volume Discretization . . . 81
4.3.3 Normalized Discrete Finite Volume Version . . . 90
4.4 Verification . . . 94
4.4.1 Verification of Numerical Conservation Properties . . . 94
4.4.2 Verification of Relaxation Rates . . . 97
4.4.3 Additional Verifications . . . 101
4.5 Time Stepping Schemes and Stability . . . 101
4.5.1 Simple Time-Step Criteria . . . 102
4.5.2 Eigenvalue Analysis . . . 103
4.5.3 Advanced Stability Analysis . . . 109
4.5.4 Advanced Time-Stepping Schemes . . . 119
4.6 Performance Analysis . . . 122
4.6.1 Node-Level Performance . . . 123
4.6.2 Parallel Efficiency . . . 124
4.7 Chapter Summary . . . 130

5 Collisional Gyrokinetic Simulations of the TCV Tokamak 131
5.1 Validation against TCV-X21 . . . 131
5.1.1 Simulation Setup . . . 132
5.1.2 Profile Validation . . . 134
5.1.3 Power Balance and Heat Exhaust Validation . . . 138
5.2 Turbulence Characterization of TCV-X21 . . . 142
5.2.1 Theory of Flux Surface Fourier Diagnostics . . . 146
5.2.2 Flux Surface Fourier Analysis . . . 156
5.3 Effect of Perpendicular Velocity Space Resolution . . . 161
5.4 Chapter Summary . . . 164

6 Summary and Outlook **165**
6.1 Summary . . . 166
6.2 Outlook . . . 167

Appendices **168**

A Quadrature Schemes **169**
A.1 Simpson Quadrature . . . 169
A.2 Gauss-Laguerre Quadrature . . . 171

B Finite Difference Stencils **173**

C Perpendicular Velocity Formulation of the LBD Operator **175**
C.1 Velocity Space Moments . . . 176
C.2 Finite Volume Discretization . . . 177
C.3 Conservation Properties . . . 179
C.3.1 Momentum Conservation . . . 180
C.3.2 Energy Conservation . . . 181
C.3.3 Conservative Corrections . . . 184
C.4 Normalized Version . . . 186
C.4.1 Normalized Velocity Space Moments . . . 187
C.4.2 Normalized Finite Volume Discretization . . . 188

D Turbulence Characterization Figures **193**
D.1 Temporal Fourier Spectra . . . 193
D.2 Spectral Fluxes . . . 195
D.3 Phase Shifts . . . 197
D.4 Trapped Particle Fluxes . . . 200
D.5 Trapped Particle Phase Shifts . . . 202
D.6 Trapped Particle Characterization . . . 205

Bibliography **207**

Chapter 1

Introduction

Fusion energy is a promising, yet to-be-realized, energy source that may provide a clean and safe way to humankind's long-term energy needs[1]. However, the road towards a viable fusion power plant is long, and as of today, a European electricity-producing demonstration power plant is years away from realization[2]. The heat loss by turbulence is among the main physics issues yet to be solved[3]. This research aims to advance the understanding of turbulence in fusion devices by developing computational tools and performing first-principles turbulence simulations.

This chapter presents the physics basics of fusion energy using magnetic confinement. The dependence of the performance of a future power plant on confinement quality and transport is highlighted, and the role of turbulence in that context is given. At the end of this introduction, the leading open research problems towards a fusion power plant from the perspective of turbulence and theory are addressed, and the relevance of this thesis in that context is discussed.

1.1 Fusion Energy

Nuclear fusion is a process that combines light atomic nuclei into heavier ones, releasing energy due to the difference in mass of the reaction's initial and resulting products. One example is the sun, which primary energy source is the fusion of protons into helium[4]. Proton-proton fusion happens in a multi-step fusion process. It is highly inefficient, as a single proton takes more than a billion years to get involved in such a reaction[5]. This reaction can sustain the "operation" of the sun because the sun's enormous size creates substantial gravitational forces. This gravitational confinement leads to high proton densities that counter for some

part of the low reactivity because the fusion power per volume scales directly with the overall reaction rate[6]. The large volume where fusion happens in the sun leads to a generated power of around[7*] 3.84×10^{26} W. This is almost a million times more energy per second than Earth's total energy consumption of 6.17×10^{20} J in 2019[8]. Unfortunately, this energy cannot be used directly on Earth, as only a fraction of it arrives through sunlight, and extracting all sunlight with solar panels is impractical. Thus it is desirable to bring fusion energy to Earth.

On Earth, proton-proton fusion is unfeasible since replicating the sun's large reaction volumes and gravitational confinement is impossible. Fortunately, there are other fusion processes available. The most promising one is deuterium-tritium (DT) fusion[6]. The reactivity of the fusion reaction is around 24 to 25 orders of magnitude higher for DT fusion compared to the sun's proton-proton fusion[9]. The reaction is given by

$$\mathrm{D}^2 + \mathrm{T}^3 \rightarrow \mathrm{He}^4(3.5\,\mathrm{MeV}) + \mathrm{n}^1(14.1\,\mathrm{MeV}), \tag{1.1}$$

creating a helium and a neutron. The brackets on the right indicate the kinetic energy of the reaction products. The total released energy of 17.6 MeV is a million times the order of the energy released in chemical reactions, such as the combustion of methane (around 9.2 eV)[10]. The DT reaction is promising because it has the highest reactivities at low energies, peaking between 100 million and 1 billion Kelvin (≈10-100 keV)[6]. The DT gas must be externally heated to achieve such temperatures, becoming an ionized gas or, in other words, a plasma.

How to Confine a Plasma and Generate Electricity with Fusion

Since charged particles in a plasma respond to electromagnetic fields, building devices that confine plasmas using magnetic cages is possible. This concept is called magnetic confinement fusion, and one of the most promising devices to build a reactor from is the tokamak[6] (Fig. 1.1). The tokamak has the topology of a torus where the major radial direction is called toroidal, and the minor radial direction is called poloidal. The tokamak combines a toroidal magnetic field generated by external coils with a poloidal magnetic field generated by a toroidal current induced by a central solenoid[11]. The combination of toroidal and poloidal fields creates a helical magnetic field, where field lines twist around toroidally shaped closed nested flux surfaces[12]. This approach provides a certain amount of confinement of the plasma within the magnetic field[†].

The configuration of interest in this work is the diverted tokamak, where using additional poloidal field coils, magnetic field lines at the edge are diverted towards target plates (di-

*Precisely this is the luminosity or power radiated by the sun, used as a lower estimate for the power generated by fusion.

[†]To be usable for a fusion reactor, the confined plasma must have a stable equilibrium state. The stability is typically analyzed with magnetohydrodynamic (MHD) theory and thus often referred to as MHD-stability of the equilibrium[11,12]. In this work, all considerations are built on top of an existing and reached MHD-stable equilibrium state.

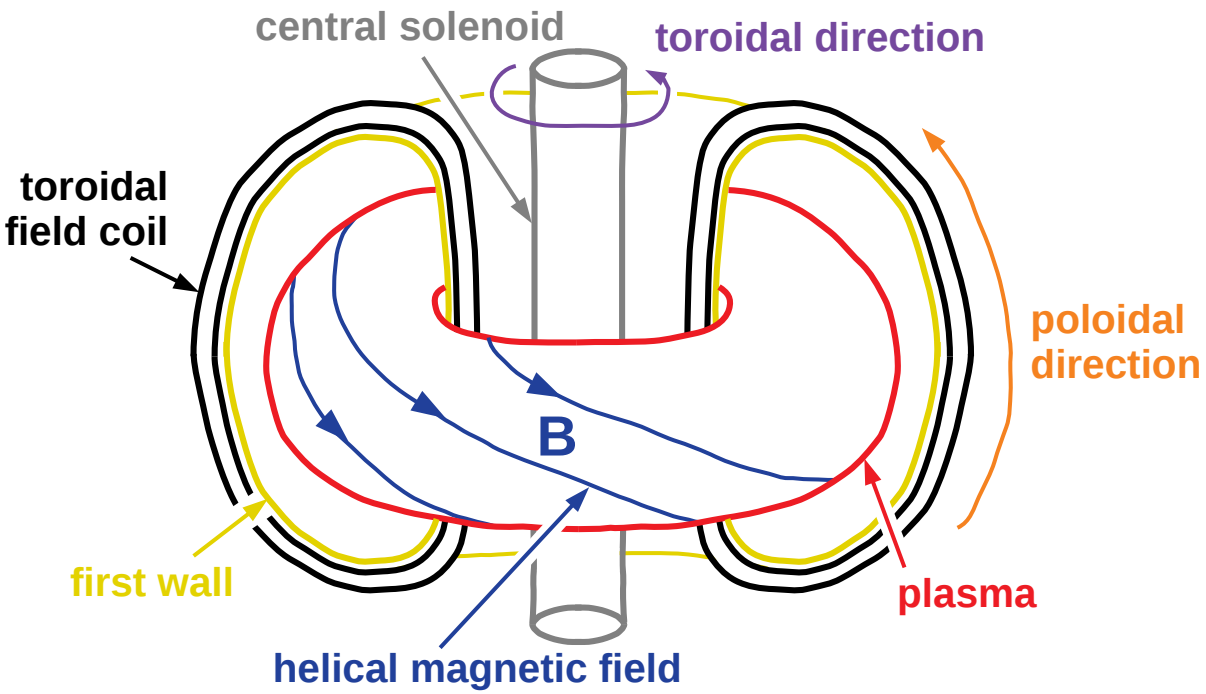

Figure 1.1. Schematic representation of a tokamak and its major (not all) components.

vertor)[12]. Figure 1.2 shows a cross-section of a diverted tokamak. The divertor creates a poloidal field null point, called the X-point, and the closed nested flux surfaces are separated to open field lines originating at the divertor plates by the last closed flux surface (separatrix)[11]. The open field line region is called the scrape-off layer (SOL) or the private flux region, dependent on the location (Fig. 1.2). The divertor reduces impurity build-up[12] and protects the vessel wall by focusing the heat exhaust on a specially designed and durable target plate[13]. Preventing the accumulation of impurities in the plasma is essential to reduce heat loss by radiation and to improve the performance of a fusion device[6]. The following section discusses the fusion performance in more detail.

Introducing the concept of magnetic confinement allows the discussion of the role of the two resulting fusion products of the DT fusion. The helium produced is ionized (alpha particle) and thus confined by the magnetic field. It contributes to the self-heating of the plasma. The neutrons are unaffected by the magnetic field and escape the plasma, depositing their energy to the outer walls, which heat up. The cooling of the walls can be used in a conventional thermic power plant cycle to generate electricity[13].

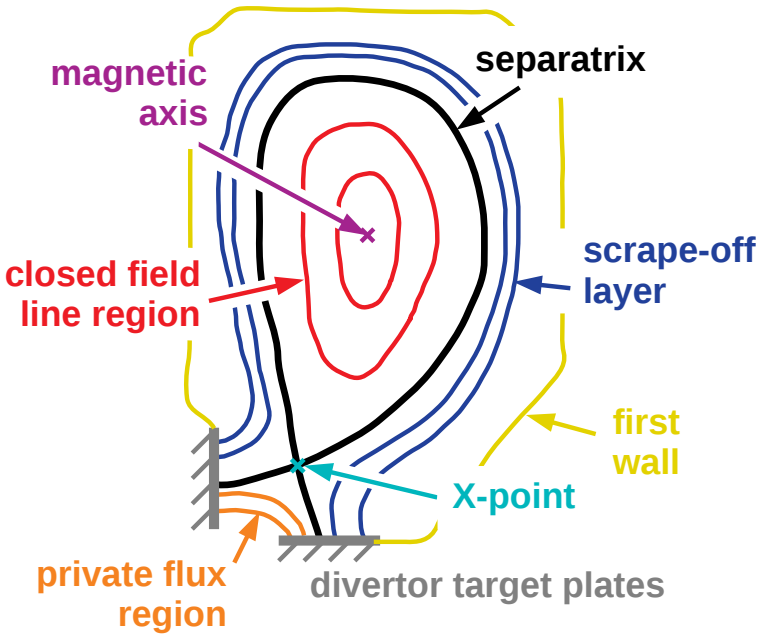

Figure 1.2. Schematic representation of a cross-section (poloidal plane) of a diverted tokamak.

How to Make Fusion Viable and Efficient

To achieve a sustainable fusion reaction, it is not necessarily required to operate at the conditions of the highest plasma temperature. Due to the non-ideal confinement properties of a fusion device, transport leads to losing parts of the energy provided by external heating. The time characterizing these losses is the energy confinement time τ_E. External heating is required to achieve the temperatures needed initially. Re-using parts of the fusion energy released in the alpha particles provides additional heating during the fusion process[13]. Considering the three mechanisms of external heating, energy loss, and alpha particle self-heating, the question arises if a condition exists where the fusion reaction provides enough self-heating to balance out the heat losses. This operating point is called ignition. The condition for achieving ignition is if the triple product of density n, temperature T, and energy confinement time τ_E exceeds a threshold[6]

$$nT\tau_E > 3 \times 10^{21}\,\mathrm{m}^{-3}\mathrm{keVs}. \tag{1.2}$$

This condition is called the Lawson criterion[14*]. For analyzing this criterion, the optimum temperature can be found within 100 and 300 million Kelvin (≈10-30 keV)[6]. The plasma density cannot be arbitrarily high in tokamaks due to operational limits[15]. Thus the energy confinement time τ_E is the central quantity that needs increasing to achieve a sustainable fusion reaction[13].

*The original criterion by Lawson in Ref. [14] considered a purely externally heated plasma and losses by Bremsstrahlung and is thus slightly different than the one shown here based on Ref. [6].

The Role of Turbulence in Fusion Devices

Transport is of interest for developing fusion energy since it leads to a degradation of the energy confinement. In early tokamak research, experimentally observed confinement times could not be explained by the standard paradigm of collision-induced, so-called neoclassical[16] transport. These findings gave rise to the terminology of anomalous transport, later connected to turbulence[17]. Turbulence, as a ubiquitous phenomenon, is also present in fusion devices. However, its exact nature differs from standard fluid turbulence[18]. In a plasma, instabilities occurring on the ion or electron gyroradius scale (micro-instabilities) can become unstable and grow, eventually leading to fine-scale turbulence[19]. The turbulence-induced transport across the confining magnetic field is the widely accepted explanation for anomalous transport[13].

Anomalous transport will dominate the energy confinement time in future fusion devices[3]. Thus the primary approach to reach sufficiently high confinement times is to build gigantic devices, culminating in the currently being built ITER tokamak[20]. Complementary to big machines is a less cost-intensive approach, reducing turbulent transport by optimizing the operational conditions. Achieving this goal requires a comprehensive understanding of the nature of plasma micro-turbulence.

A broad range of physical models exists to describe turbulence in a plasma, varying in the fidelity employed. The hierarchy reaches from simple fluid models commonly known as Hasegawa-Mima[21], Hasegawa-Wakatani[22] or drift-reduced Braginskii[23], to more advanced gyro-fluid[24] or gyro-moments[25] models, up to high fidelity gyrokinetic models (discussed in detail in section 2). Fluid models can capture essential properties of plasma turbulence, especially in the edge where the plasma is highly collisional and the theory is most valid. The details of turbulence cannot be fully described as kinetic effects are important[26,27]. Thus, gyrokinetic theory is considered the fundamental tool to simulate and describe micro-turbulence in a plasma[28].

Predicting turbulent transport requires nonlinear gyrokinetic simulations, running until the growth of the micro-instabilities saturates and the turbulence achieves a quasi-stationary state. The simulation of turbulence using gyrokinetic codes is costly in terms of computational time, requiring the massive parallelization of calculations on the world's leading supercomputers. These constraints led to the development of many computational tools, using different numerical techniques to reduce the required computational cost as much as possible (see section 2.4 for an overview). The last decades have brought enormous progress in understanding core turbulence (see Ref. [29] for a review). Contrary, the nature of the plasma edge is yet to be unraveled[30], despite critically determining the energy confinement time. Part of this issue is the inapplicability of the tools used in the plasma core, which rely on magnetic field-aligned coordinate systems, a choice that does not work with magnetic

X-points (see Fig. 1.2). The development of new tools to simulate turbulence in the complex magnetic geometry of diverted tokamaks was required[31–34]. The `GENE-X` code is among these tools, and its physics extension for the applicability in the plasma edge is the subject of this thesis.

1.2 Open Problems in Edge Plasma Physics

Improved Confinement Regimes and the LH-Transition

As fusion approaches more and more reactor-relevant conditions with high-temperature gradients, turbulence becomes a significant issue because it deteriorates the confinement of the system[1]. Plasma confinement is essential, as it determines the performance of a future reactor. Consequently, the cost of a future power plant is most sensitive to the quality of confinement[35]. For this reason, the Eurofusion roadmap for the realization of fusion energy[2] states that suitable plasma regimes of operations must minimize the energy losses due to turbulence. One possible operation regime is the so-called high confinement mode (H-mode) discovered more than 40 years ago[36]. The H-mode improves the confinement of the plasma by a factor of two, decreasing the cost of a potential fusion reactor by 60%[37].

The H-mode and the physics of the transition to advanced confinement regimes have yet to be fully understood. While recent years have shown substantial experimental progress to advance aspects of the understanding of the LH-transition[38–42], a comprehensive theory is still missing. Current modeling efforts focus on using fluid codes[43] or reduced turbulence models[44]. Recently, a fluid-like drift-Alfvén model achieved progress in explaining operational boundaries in the transition from L- to H-mode[45]. However, for a more profound understanding, first-principles high-fidelity simulations of the LH-transition are required. The complex geometry and significant changes in the background plasma make traditional gyrokinetic codes unusable. Only one high-fidelity gyrokinetic study could observe an LH-transition-like event so far[46]. Since that work was published more than five years ago, the lack of appropriate numerical tools has hindered achieving substantial progress. Independent verification by other gyrokinetic codes is necessary.

The Power Exhaust Problem

The dynamics in the closed and open field line regions differ significantly in a fusion device. The magnetic field lines can be considered an excellent thermal insulator. Little heat can penetrate across field lines compared to along field lines. This results in a situation where the heat crossing the last closed flux surface enters the open field line region and is quickly transported toward the divertor plates, resulting in a narrow region of power deposition. This so-called power exhaust problem is among the major obstacles for future reactors, as the estimated power densities exceed the currently supported engineering limits[47]. While

parallel transport dominates in the scrape-off layer (SOL), the width of the deposited heat flux depends on the exact ratio between parallel and cross-field transport. A projection, based on data from today's available machines to the currently being-built ITER tokamak, predicts extremely narrow widths of power deposition, posing a concern for the plasma-facing components of ITER[48]. Due to its importance, the Eurofusion roadmap for the realization of fusion energy[2] highlights the power (or heat) exhaust problem as one of the primary obstacles to realizing a fusion reactor.

To which extent this extrapolation holds is still subject to further studies, as the result of a gyrokinetic simulation predicts values larger by more than a factor of five[46]. Similar results were achieved by simulations with fluid models[49], although some studies indicate that kinetic effects could be relevant in the SOL[50]. Based on these more favorable results for ITER, a new scaling has been developed[51]. The verification of these results by other gyrokinetic codes remains an open task. The goal is to establish a confident prediction for the width of power deposition, allowing to design divertors accordingly[52].

The challenge for modeling is the involvement of multiple disparate regions in the plasma that, up to now, were mostly considered independent in gyrokinetic simulations. The dynamics in the SOL mainly govern the heat flux to the divertor plates, while the plasma edge determines the radial heat transport from the core to the SOL[30]. This complex situation requires simulations that capture the interplay of core, edge, and SOL turbulence[53].

1.3 Scope of this Thesis

The lack of a comprehensive theory of the LH-transition, the power exhaust problem, as well as the limited understanding of edge and scrape-off layer turbulence have led to the development of the `GENE-X` code[34]. The high-fidelity gyrokinetic model employed in the code is sufficient to develop turbulence. However, it cannot solely provide the necessary physics to model the plasma edge accurately. One of the most critical extensions is the inclusion of collisions because the temperature decreases toward the outside of the plasma, increasing the collisionality. Zonal flows, turbulence-generated mesoscale shear flows, provide a saturation mechanism for a large class of micro-instabilities[54] and are damped by collisions[55]. Micro-instabilities, driven by particles trapped in the low field side of the tokamak, are very sensitive to collisions[56]. In the vicinity of considerable density and temperature gradients, such as in the steep gradient region, which evolves during the LH transition, collisional effects could be important[57].

This work aims at extending the physics capabilities of the `GENE-X` code to include the effect of collisions in gyrokinetic simulations. The main research question is if collisions significantly

affect edge turbulence and what degree of fidelity a collision model must provide. Developing efficient numerical techniques is a crucial element in enabling collisional simulations. Facing future simulations of large-scale devices such as ITER, a high-performance code implementation is a primary objective. Since gyrokinetic codes are costly, finding a balance between computational complexity and model accuracy may be worthwhile. Quantifying the degree of trustworthiness of the implemented collision models requires performing a validation study against a real experiment. This work should provide a stepping stone toward future applications in exploring LH-transition physics, modeling divertor heat exhaust, and ultimately realizing fusion energy.

1.4 Content Overview

The content of this thesis is structured as follows. The second chapter chapter briefly introduces gyrokinetic theory, the model used to study turbulence in this work. The basic concepts of kinetic theory and charged particle dynamics are discussed to motivate the development of guiding-center theory. Subsequently, gyrokinetic theory is introduced, and an overview of existing gyrokinetic codes is given. At the end of that chapter, the `GENE-X` code is presented.

The third chapter reviews the basic theory of plasma collisions and discusses the general properties of collision operators. The Lenard-Bernstein/Dougherty (LBD) collision operator used in `GENE-X` is derived from the Fokker-Planck equation. The model parameters are selected such that collisions conserve the individual particle density, the total momentum, and the system's total energy on the continuous level. The relaxation rates reproduce either the Boltzmann collision operator's momentum or temperature relaxation rate, depending on the version chosen.

The fourth chapter contains the numerical developments required in order to make collisional simulations with `GENE-X` possible. The numerics include a modification of the quadrature schemes and the development of the discretized LBD collision operator. A finite difference version and an advanced, conservative finite volume version are presented. The latter is developed to achieve the exact numerical conservation of particle density, total momentum, and total energy up to machine precision. These corrections are necessary to enable simulations on a long time scale, which are required for gyrokinetic turbulence simulations. Additionally, details on verifying the discretizations (published in Ref. [58]) are presented. Further, the stability of the time-stepping scheme, combined with the discretized collision operator, is analyzed. It is shown that the implementation of advanced time-stepping schemes is required to use the collision operator in a gyrokinetic code. Finally, the LBD operator is implemented in the high-performance code `GENE-X`, and an intra- and inter-node performance benchmark is presented.

In the fifth chapter, applications of the newly developed collision models are shown. The code is validated in a realistic experimental scenario of the TCV tokamak, the first-of-its-kind validation of a global gyrokinetic code. Simulations without collisions, with basic Bhatnagar-Gross-Krook (BGK) and advanced LBD collisions, are compared, and the underlying turbulence is analyzed using newly developed tools, such as temporal and flux-surface Fourier diagnostics as well as trapped-particle diagnostics. The validation and turbulence characterization sections provide details of published results in Ref. [59]. Finally, the effect of the perpendicular velocity space resolution is analyzed by comparing the reference simulation to a simulation with reduced resolution, for which an improved numerical discretization of the LBD operator has been developed.

The final chapter contains the summary and conclusion of this thesis, as well as an outlook on open problems and the next steps required toward developing a comprehensive tool for the simulation of gyrokinetic turbulence in future fusion reactors.

Chapter 2

Gyrokinetic Theory and Simulation

Gyrokinetic theory is a physical model suited to simulate plasma turbulence[28]. The first nonlinear gyrokinetic equations were derived in the early 1980s in Ref. [60]. A summary of the theory can be found in the review article in Ref. [61]. The equations implemented in the gyrokinetic turbulence code `GENE-X` are given in Ref. [62].

This chapter aims to introduce gyrokinetic theory using a two-step approach. The first step introduces guiding-center theory, constructing equations with fast gyromotion removed from the dynamics. The second step introduces the gyrocenter as a perturbed guiding center, allowing for the inclusion of fluctuating electromagnetic fields in the resulting equations. The end of the chapter presents an overview of existing gyrokinetic codes, highlighting the `GENE-X` code relevant to this thesis.

2.1 The Kinetic Equation

The kinetic theory of plasmas describes the behavior of a distribution of particles f_α of species α in 6D phase space $(\mathbf{x}, \mathbf{v})$. Here, $\mathbf{x}$ denotes the particle position in real space, while $\mathbf{v}$ denotes the particle's velocity, or in the kinetic view, its position in velocity space. The temporal evolution of the distribution function is given by the kinetic equation[63,64]

$$\frac{\mathrm{d}f_\alpha}{\mathrm{d}t} = \frac{\partial f_\alpha}{\partial t} + \mathbf{v} \cdot \frac{\partial f_\alpha}{\partial \mathbf{x}} + \frac{\mathbf{F}_\alpha}{m_\alpha} \cdot \frac{\partial f_\alpha}{\partial \mathbf{v}} = \left.\frac{\mathrm{d}f_\alpha}{\mathrm{d}t}\right|_{\mathrm{coll}}, \tag{2.1}$$

where $\mathbf{F}_\alpha$ denotes forces on the particle, and the right-hand side describes the change due to collisions. In section 3, collisions will be treated in detail. Here a collisionless plasma

is assumed temporarily. The relevant force $\mathbf{F}_\alpha$ is the Lorentz force, which results in the collisionless kinetic or Vlasov equation[65],

$$\frac{\partial f_\alpha}{\partial t} + \mathbf{v} \cdot \frac{\partial f_\alpha}{\partial \mathbf{x}} + \frac{q_\alpha}{m_\alpha} \left(\mathbf{E} + \frac{1}{c} \mathbf{v} \times \mathbf{B} \right) \cdot \frac{\partial f_\alpha}{\partial \mathbf{v}} = 0. \tag{2.2}$$

Here q_α and m_α denote charge and mass, and c is the speed of light. In this work, Gaussian cgs units[66] are used. The macroscopic* electric and magnetic fields $\mathbf{E} = \mathbf{E}(\mathbf{x}, t)$ and $\mathbf{B} = \mathbf{B}(\mathbf{x}, t)$ are determined by Maxwell's equations[67],

$$\nabla \cdot \mathbf{E} = 4\pi\rho, \qquad \nabla \cdot \mathbf{B} = 0, \tag{2.3}$$

$$\nabla \times \mathbf{B} - \frac{1}{c}\frac{\partial \mathbf{E}}{\partial t} = \frac{4\pi}{c}\mathbf{J} \qquad \nabla \times \mathbf{E} + \frac{1}{c}\frac{\partial \mathbf{B}}{\partial t} = 0. \tag{2.4}$$

The Vlasov-Maxwell system is closed by expressions for the charge density ρ and current density $\mathbf{J}$, which are given by velocity space moments of the distribution function

$$\rho = \sum_\alpha q_\alpha \int f_\alpha \mathrm{d}\mathbf{v}, \tag{2.5}$$

$$\mathbf{J} = \sum_\alpha q_\alpha \int \mathbf{v} f_\alpha \mathrm{d}\mathbf{v}. \tag{2.6}$$

2.2 Guiding-Center Dynamics

Charged particles in magnetic fields will perform a circular periodic gyromotion with the gyro- (or cyclotron-) frequency $\Omega_{c,\alpha} = |q_\alpha| B/(m_\alpha c)$, where $B = |\mathbf{B}|$ is the magnitude of the magnetic field. The circle of gyration has the size of the Larmor radius $\rho_{L,\alpha} = v_{\perp,\alpha}/\Omega_{c,\alpha}$, where $v_{\perp,\alpha}$ is the velocity of the particle perpendicular to the field. A velocity component parallel to the magnetic field $v_{||,\alpha}$ results in a superposition of parallel motion and gyration. The moving charge represents a current $I_\alpha = |q_\alpha|\Omega_{c,\alpha}/(2\pi)$ that encloses the area $A_\alpha = \pi\rho_{L,\alpha}^2$ and creates a magnetic moment $\mu_\alpha = I_\alpha A_\alpha/c = m_\alpha v_{\perp,\alpha}^2/(2B)$[68]. For a magnetic field that is almost constant within the period of a single gyration, the magnetic moment is a conserved quantity $\mu_\alpha = \text{const.}$ (adiabatic invariant), along the orbit of the particle[65].

Due to the periodic nature of the gyromotion, gyrating particles will be sensitive to forces perpendicular to the magnetic field, i.e., within the plane of gyration. This results in cross-field drifts[64],

$$\mathbf{v}_{d,\alpha} = c\frac{\mathbf{E} \times \mathbf{B}}{B^2} + \frac{v_{\perp,\alpha}^2}{2\Omega_{c,\alpha}} \mathbf{b} \times \nabla \ln B + \frac{v_{||,\alpha}^2}{\Omega_{c,\alpha}} \mathbf{b} \times \boldsymbol{\kappa}, \tag{2.7}$$

*These are not the microscopic electromagnetic fields created by individual charges.

where $\mathbf{b}$ denotes the magnetic field unit vector. The three individual terms are called $\mathbf{E}\times\mathbf{B}$ drift, grad-B (∇B) drift, and curvature drift. This expression only holds for weak electric fields, such that the $\mathbf{E}\times\mathbf{B}$ drift is smaller than a Larmor radius per gyroperiod[64*]. An estimate for the typical time τ_d it takes a particle to pass a distance of the order or R_0 for all three drifts is $\tau_d^{-1} \sim v_{d,\alpha}/R_0 \sim v_{\mathrm{th},\alpha}^2/(\Omega_{c,\alpha}R_0^2) \sim \Omega_{c,\alpha}(\rho_{L,\alpha}/R_0)^2$. Thus, the drift motion happens on a much slower time scale than the gyration,

$$\tau_d^{-1} \ll \Omega_{c,\alpha}. \tag{2.8}$$

2.2.1 Guiding-Center Equations

The kinetic theory presented in section 2.1 includes the effect of all single particle dynamics. Resolving the fast electron gyromotion while considering the whole six-dimensional phase space is tremendously expensive for a computational code. Fortunately, the ordering (2.8) and the adiabatic invariance of the magnetic moment can be exploited. Consequently, it is not necessary to construct a kinetic theory for individual particles. Instead, a reduced kinetic theory of the particle guiding centers adequately describes processes on time scales slower than the gyration. Guiding-center theory aims to derive equations for the motion of the guiding center instead of the particle itself. As a result, these equations remove the fast dynamics of the gyromotion and conserve the magnetic moment. The procedure reduces the potential cost of numerical simulation enormously since, first, the time step does not need to be as small as the gyroperiod, and second, the equations become independent of the gyroangle, reducing the system to five dimensions.

The guiding center position is given as $\mathbf{x}_{\mathrm{gc}} \approx \mathbf{x} + \boldsymbol{\rho}_{L,\alpha}$ in lowest order approximation[†]. Here $\boldsymbol{\rho}_{L,\alpha}$ denotes the gyroradius vector, which contains the information about the displacement of the particle from its guiding center. Further, the velocity of a particle is written in cylindrical coordinates as $\mathbf{v} = (v_{||}, \mu, \theta)$, where the magnetic moment is a measure for the magnitude of the perpendicular velocity $\mu \sim v_\perp^2$ and θ is the gyroangle.

The guiding-center equations of motion are typically derived from a guiding-center Lagrangian, which is obtained by transforming the particle Lagrangian (either by Lie-transformation[71] or by gyroaveraging the particle Lagrangian and using a variational principle[72]). Moreover, a Vlasov equation for the distribution of guiding centers can be derived using a guiding-center Poisson bracket with the guiding-center Hamiltonian. The guiding-center

*For an estimation, the equilibrium electric field[69] $E_r = (\partial p_\alpha/\partial r)/(q_\alpha n_\alpha)$ can be considered, where $p_\alpha = n_\alpha T_\alpha$ denotes the pressure and all other terms in the momentum equation were neglected. It follows that $E_r \sim m_\alpha v_{\mathrm{th},\alpha}^2/(2q_\alpha R_0)$ which fulfills the above restriction on weak electric fields.

†This is exact for a uniform magnetic field[70].

Poisson bracket can be constructed from the guiding-center Lagrangian. See section 4 of Ref. [72] for more details.

The following summarizes the first-order guiding-center theory from Ref. [72]. The ordering concerns a small parameter $\epsilon_B = \rho_L/L_B$, specifying the ratio between the Larmor radius and the magnetic field non-uniformity scale length. The guiding center coordinates are $(\bar{\mathbf{x}}, \bar{v}_{||}, \bar{\mu}, \bar{\theta})$ which denote the position, parallel velocity, magnetic moment and gyroangle. The guiding center Lagrangian and Hamiltonian are,

$$\mathcal{L}_{\rm gc} = \left(\frac{q_\alpha}{c}\mathbf{A} + m_\alpha \bar{v}_{||}\mathbf{b}\right)\cdot\dot{\bar{\mathbf{x}}} + \frac{m_\alpha c}{q_\alpha}\bar{\mu}\dot{\bar{\theta}} - \mathcal{H}_{\rm gc}, \tag{2.9}$$

$$\mathcal{H}_{\rm gc} = \frac{1}{2}m_\alpha \bar{v}_{||}^2 + \bar{\mu}B + q_\alpha\phi, \tag{2.10}$$

where $\mathbf{A}$ denotes the vector potential and ϕ the electrostatic scalar potential. While the vector potential can be large, since the leading order term generates the background magnetic field, the electrostatic potential is assumed to be small. In the formulation of Ref. [73], the modified potential and fields are used

$$\mathbf{A}^* = \mathbf{A} + \frac{m_\alpha c}{q_\alpha}\bar{v}_{||}\mathbf{b}, \tag{2.11}$$

$$\mathbf{B}^* = \nabla\times\mathbf{A}^* = \mathbf{B} + \frac{m_\alpha c}{q_\alpha}\bar{v}_{||}\nabla\times\mathbf{b}, \tag{2.12}$$

and magnetic and electric fields constant in time[†] are assumed such that $\mathbf{E}^* = \mathbf{E} = -\nabla\phi$. The guiding-center equations of motion are

$$\dot{\bar{\mathbf{x}}} = \frac{1}{B_{||}^*}\left(\bar{v}_{||}\mathbf{B}^* + \frac{c}{q_\alpha}\mathbf{b}\times(\bar{\mu}\nabla B + q_\alpha\nabla\phi)\right), \tag{2.13}$$

$$\dot{\bar{v}}_{||} = -\frac{1}{m_\alpha}\frac{\mathbf{B}^*}{B_{||}^*}\cdot(\bar{\mu}\nabla B + q_\alpha\nabla\phi), \tag{2.14}$$

$$\dot{\bar{\mu}} = 0, \tag{2.15}$$

$$\dot{\bar{\theta}} = \Omega_{c,\alpha}. \tag{2.16}$$

First, taking the dot product $\mathbf{b}\cdot\dot{\bar{\mathbf{x}}} = \bar{v}_{||}$ shows that the latter coordinate is the guiding-center parallel velocity. Second, the perpendicular components of the first equation contain all three drifts discussed in eq. (2.7), the $\mathbf{E}\times\mathbf{B}$, the grad-B, and the curvature drift (the latter is contained within the modified magnetic field). Third, the parallel velocity change contains the mirror force and acceleration from the electric field. Fourth, the guiding center magnetic

[†]In the original reference [72], fields are allowed to vary slowly on a drift time scale. The only modification required is in the modified field $\mathbf{E}^*$. Here, for explanatory purposes, only the simpler case of static fields is considered.

moment is a conserved quantity. Fifth, the temporal change of the gyroangle is proportional to the gyrofrequency. The Jacobian of the guiding-center transformation $\mathcal{J}_{\mathrm{gc}}$ is given, up to a factor of mass, by the parallel component of the modified magnetic field,

$$B_{||}^{*} = B + \frac{m_\alpha c}{q_\alpha} \bar{v}_{||} \mathbf{b} \cdot (\nabla \times \mathbf{b}). \tag{2.17}$$

The guiding center Poisson bracket is constructed as mentioned in section 4 of Ref. [72]. Applied on two functions F, G, it reads

$$\{F, G\}_{\mathrm{gc}} = \left(\frac{\partial F}{\partial \bar{\theta}} \frac{\partial G}{\partial \bar{\mu}} - \frac{\partial G}{\partial \bar{\theta}} \frac{\partial F}{\partial \bar{\mu}} \right) + \frac{\mathbf{B}^*}{B_{||}^*} \cdot \left(\nabla F \frac{\partial G}{\partial \bar{v}_{||}} - \nabla G \frac{\partial F}{\partial \bar{v}_{||}} \right) + \frac{\mathbf{b}}{B_{||}^*} \cdot (\nabla F \times \nabla G) \,. \tag{2.18}$$

It can be easily verified that this reproduces the equations of motion (2.13)-(2.16) by evaluating Hamilton's equations $\dot{\bar{z}} = \{\bar{z}, \mathcal{H}_{\mathrm{gc}}\}_{\mathrm{gc}}$ for $\bar{z}$ denoting any of the guiding-center coordinates.

The guiding-center Vlasov equation is now straightforward to derive. The gyroangle independent distribution function $\bar{f}_\alpha = \left\langle \bar{f}_\alpha \right\rangle$ is introduced, where the brackets denote a gyroaverage. Since the fast dynamics on the scale of the gyromotion are not of interest, this is the quantity that is considered. The time derivative of this distribution is then given by $\dot{\bar{f}}_\alpha = \{\bar{f}_\alpha, \mathcal{H}_{\mathrm{gc}}\}_{\mathrm{gc}}$. Since the Hamiltonian (2.10) is gyroangle independent, the first contribution in the Poisson bracket is zero. Thus, evaluating the remaining terms results in

$$\frac{\partial \bar{f}_\alpha}{\partial t} + \frac{1}{B_{||}^*} \left(\mathbf{B}^* \bar{v}_{||} + \frac{c}{q_\alpha} \mathbf{b} \times \left(\bar{\mu} \nabla B + q_\alpha \nabla \phi \right) \right) \cdot \nabla \bar{f}_\alpha - \frac{\mathbf{B}^*}{m_\alpha B_{||}^*} \cdot \left(\bar{\mu} \nabla B + q_\alpha \nabla \phi \right) \frac{\partial \bar{f}_\alpha}{\partial t} = 0. \tag{2.19}$$

This equation is often called the drift-kinetic equation (with collisions included, otherwise drift-kinetic Vlasov equation). It describes the temporal evolution of the guiding-center distribution in 4D phase space. The gyroangle dependence has been eliminated, and the magnetic moment is only a parameter in this equation. The prefactors to the derivatives of $\bar{f}_\alpha$ are the characteristics (2.13) and (2.14). The given formulation is valid up to first-order in magnetic field non-uniformity ϵ_B.

While the above equations describe the dynamics of the guiding centers in electromagnetic fields, the equations for these fields are yet to be given. In the simplest case, one may use Maxwell's equations as is. However, the guiding-center charge and current densities

$$\bar{\rho} = 2\pi \sum_\alpha q_\alpha \int \mathcal{J}_{\mathrm{gc}} \bar{f}_\alpha \mathrm{d}\bar{v}_{||} \mathrm{d}\bar{\mu}, \tag{2.20}$$

$$\bar{\mathbf{J}} = 2\pi \sum_\alpha q_\alpha \int \mathcal{J}_{\mathrm{gc}} \bar{v}_{||} \bar{f}_\alpha \mathrm{d}\bar{v}_{||} \mathrm{d}\bar{\mu}, \tag{2.21}$$

are not necessarily the same as their particle counterparts (2.5) and (2.6). The difference between charge and current densities of the guiding centers and particles can be written in terms of polarization charges and magnetization currents[74]. It is possible to derive expressions for guiding-center polarization and magnetization using push-forward or variational approaches[75]. Alternatively, guiding-center field theory can be used to derive a consistent set of Vlasov-Maxwell equations[76].

This section has shown that equations for the guiding center of a particle and the corresponding evolution of the guiding-center distribution function can be derived. These equations are beneficial analytically and computationally, as the fast gyromotion has been removed, making the equation five-dimensional. However, this version assumed that the electromagnetic fields are either static or change slowly in time[72]. The question arises if it is possible to derive similar equations which allow the electromagnetic fields to fluctuate in time, suitable for the simulation of turbulence. A naive approach setting $\phi = \phi(t)$ in eq. (2.10) immediately introduces a gyroangle dependence to the Vlasov equation since the electrostatic potential would depend on the gyroangle, and $\partial\mathcal{H}/\partial\bar{\theta}$ would not be zero. Further, the magnetic moment would not be conserved, making the theory six-dimensional again. Using this naive approach would lose all benefits of guiding-center theory, leading to the development of the gyrokinetic equations.

2.3 Gyrokinetic Equations

In the last paragraph of section 2.2.1, it was sketched that the guiding-center equations are not suited to include fluctuating electromagnetic fields. Thus, constructing a kinetic theory for perturbed guiding centers, called gyrocenters, is necessary. The dependence on the fast gyromotion can be removed in a transformation very similar to the guiding-center transformation itself[61]. In the process, new gyrocenter coordinates $(\bar{\bar{\mathbf{x}}}, \bar{\bar{v}}_{||}, \bar{\bar{\mu}}, \bar{\bar{\theta}})$ are constructed, with dynamics similar to their guiding-center counterparts, i.e., conservation of gyrocenter magnetic moment $\bar{\bar{\mu}}$.

The first derivation of gyrokinetic equations was performed in Ref. [60], which used an asymptotic expansion regarding the magnitude of the fluctuating fields. While these equations were valid at second-order, the lack of conservation properties[61] and the missing of a systematic approach led to the development of alternative methods using Lie transformation theory (see, e.g., Refs [77, 78] for an introduction). Gyrokinetic equations derived using the Lie transformation approach can be found in Ref. [79] and [80]. As mentioned in section 2.2.1, the corresponding field equations were initially derived using push-forward methods until later in the early 2000s gyrokinetic field theory was formulated[81–83]. The variational methods allow deriving consistent Vlasov-Maxwell equations following exact conservation laws[61].

The typical approach in Lie transformation theory is applying the guiding-center and the gyrocenter transformation successively[61]. Other approaches exist where the guiding-center transformation can be replaced by using an appropriate translation in velocity, leaving only the gyrocenter transformation to be performed[84].

The following presents a specific version of the gyrokinetic equations that will be used in this work. This version is based on the parallel-symplectic model in Ref. [61] and generally formulated in Ref. [62]. Here, perpendicular vector potential fluctuations will be neglected, i.e., $\mathbf{A}_{1,\perp} = 0$, while keeping contributions from gyro-averaging the fluctuating potentials. The notation will be simplified by denoting (extended) gyrocenter coordinates as $(\mathbf{x}, v_{||}, \mu, \theta, t, w)$. The motion is described on a 7D hypersphere of constant energy w, embedded in 8D extended phase space. The fields are $\phi_1 = \phi_1(\mathbf{x} + \boldsymbol{\rho}_{\mathrm{gy},\alpha})$ and $A_{1,||} = A_{1,||}(\mathbf{x} + \boldsymbol{\rho}_{\mathrm{gy},\alpha})$. The displacement from the gyrocenter position is given in lowest order by $\boldsymbol{\rho}_{\mathrm{gy},\alpha} = \sqrt{2\mu B/(m_\alpha \Omega_{c,\alpha}^2)}\boldsymbol{\rho} + \mathcal{O}(\epsilon_B, \epsilon_\delta)$ where $\boldsymbol{\rho}$ denotes the gyroradius unit vector (see Ref. [61] for more details and higher-order expressions). Since the gyroradius unit vector essentially follows a particle through its gyration, the fluctuating potentials acquire a dependence on the gyroangle. Averaging through a single period of gyration is denoted by $\langle \phi_1 \rangle$ and called gyroaverage. The fluctuating part is then simply $\widetilde{\phi}_1 = \phi_1 - \langle \phi_1 \rangle$.

The gyrokinetic theory used assumes the following ordering[62]. First, magnetic field non-uniformity is assumed small $\epsilon_B \sim \rho_{\mathrm{th,i}}/L_B \ll 1$, where $L_B^{-1} = \nabla \ln B$ and $\rho_{\mathrm{th,i}}$ is the thermal Larmor radius of an ion. Second, fluctuation amplitudes $\epsilon_\delta \sim k_\perp \rho_{\mathrm{th,i}} q_\mathrm{i} \phi_1 / T_\mathrm{i} \sim (v_{\mathrm{th,i}}/c) q_\mathrm{i} A_{1,||}/T_\mathrm{i} \ll 1$ are small, where $k_\perp$ denotes the wavelength of the perturbations perpendicular to the magnetic field. Third, parallel dynamics are assumed to be much faster than perpendicular dynamics. Thus their scale must be larger $\epsilon_{||} \sim k_{||}/k_\perp \ll 1$. Fourth, the time scale of the fluctuations is assumed to be larger than the gyroperiod, $\epsilon_\omega \sim \omega/\Omega_{L,\mathrm{i}} \ll 1$. Further, $\epsilon_B \sim \epsilon_\delta^2$ and $\epsilon_\delta \sim \epsilon_{||} \sim \epsilon_\omega$.

The gyrocenter extended Hamiltonian is given as[61],

$$\begin{aligned}\mathcal{H}_{\mathrm{gy}} = {} & \frac{1}{2} m_\alpha v_{||} + \mu B + q_\alpha \langle \phi_1 \rangle \\ & + \frac{q_\alpha^2}{2B} \frac{\partial}{\partial \mu} \left\langle \widetilde{\phi}_1^2 \right\rangle - \frac{m_\alpha c^2}{2B_{||}^*} \mathbf{b} \cdot \left\langle \nabla \widetilde{\Phi}_1 \times \nabla \widetilde{\phi}_1 \right\rangle + \frac{q_\alpha^2}{2 m_\alpha c^2} \left(\left\langle A_{1,||}^2 \right\rangle - \left\langle A_{1,||} \right\rangle^2 \right) - w, \end{aligned} \tag{2.22}$$

where the first two terms are of order zero, the third term is of order one, and the second row is the second-order contribution (except the last term). Here $\partial \widetilde{\Phi}_1 / \partial \theta = \widetilde{\phi}_1$. The gyrokinetic

Poisson bracket is[61]*,

$$\{F,G\}_{\mathrm{gy}} = \frac{q_\alpha}{m_\alpha c}\left(\frac{\partial F}{\partial\theta}\frac{\partial G}{\partial\mu} - \frac{\partial G}{\partial\theta}\frac{\partial F}{\partial\mu}\right) + \frac{\mathbf{B}^*}{m_\alpha B_{||}^*}\cdot\left(\nabla^* F\frac{\partial G}{\partial v_{||}} - \nabla^* G\frac{\partial F}{\partial v_{||}}\right) + \frac{c\mathbf{b}}{q_\alpha B_{||}^*}\cdot(\nabla F\times\nabla G) + \left(\frac{\partial F}{\partial w}\frac{\partial G}{\partial t} - \frac{\partial F}{\partial t}\frac{\partial G}{\partial w}\right), \tag{2.23}$$

$$\nabla^* F = \nabla F + \frac{q_\alpha^2}{m_\alpha c^2}\left(\frac{\partial\left\langle A_{1,||}\right\rangle}{\partial\mu}\frac{\partial F}{\partial\theta} - \frac{\partial\left\langle A_{1,||}\right\rangle}{\partial t}\frac{\partial F}{\partial w}\right), \tag{2.24}$$

with the modified magnetic field

$$\mathbf{B}^* = \mathbf{B} + v_{||}\nabla\times\mathbf{b} + \nabla\times\left\langle A_{1,||}\right\rangle\mathbf{b}. \tag{2.25}$$

The parallel component $\mathcal{J} = B_{||}^* m_\alpha^2$ constitutes the gyrocenter Jacobian. The gyrokinetic equations of motions are[61],

$$\dot{\mathbf{x}} = \frac{1}{B_{||}^*}\left(\frac{\mathbf{B}^*}{m_\alpha}\frac{\partial\mathcal{H}_{\mathrm{gy}}}{\partial v_{||}} + \frac{c}{q_\alpha}\mathbf{b}\times\nabla\mathcal{H}_{\mathrm{gy}}\right), \tag{2.26}$$

$$\dot{v}_{||} = -\frac{\mathbf{B}^*}{m_\alpha B_{||}^*}\cdot\nabla\mathcal{H}_{\mathrm{gy}} - \frac{q_\alpha}{m_\alpha c}\frac{\partial\left\langle A_{1,||}\right\rangle}{\partial t}, \tag{2.27}$$

$$\dot{\mu} = 0, \tag{2.28}$$

$$\dot{\theta} = \Omega_{c,\alpha}, \tag{2.29}$$

and the gyrokinetic equation is[61]

$$\frac{\partial f_\alpha}{\partial t} + \dot{\mathbf{x}}\cdot\nabla f_\alpha + \dot{v}_{||}\frac{\partial f_\alpha}{\partial v_{||}} = 0, \tag{2.30}$$

where $f_\alpha = \langle f_\alpha\rangle$ denotes the gyroaveraged distribution of gyrocenters. This equation achieves the goal of deriving an equation similar to the drift-kinetic equation (2.19) but is valid in the presence of fluctuating electromagnetic fields. The derivation removed the fast gyromotion from the dynamics, and the magnetic moment is a conserved quantity. It is interesting to compare the equations from this section to their guiding-center counterparts. In the limit $A_{1,||} = 0$ and $\widetilde{\phi}_1 = 0$, both versions are the same†. While these equations can readily be used in gyrokinetic turbulence simulations, further simplifications can still be applied.

*Here the gyrogauge vector field[71] has been neglected.

†This is not the same as the drift-kinetic limit (long wavelength limit) of the gyrokinetic equation.

Long Wavelength Approximation

The fluctuating fields are typically approximated by an expansion[61],

$$\phi_1(\mathbf{x}+\boldsymbol{\rho}_{\mathrm{gy},\alpha}) \approx \mathrm{e}^{\boldsymbol{\rho}_{\mathrm{gy},\alpha}\cdot\nabla}\phi_1(\mathbf{x}) = \left(1+\boldsymbol{\rho}_{\mathrm{gy},\alpha}\cdot\nabla+\frac{1}{2}\boldsymbol{\rho}_{\mathrm{gy},\alpha}\boldsymbol{\rho}_{\mathrm{gy},\alpha}:\nabla\nabla+\mathcal{O}(\boldsymbol{\rho}_{\mathrm{gy},\alpha}^3)\right)\phi_1(\mathbf{x}). \tag{2.31}$$

The long wavelength approximation (LWA) only keeps the leading order terms. Using $\boldsymbol{\rho}_{L,\alpha}$ to denote the leading order term in the gyrocenter displacement, the assumption $\boldsymbol{\rho}_{L,\alpha}\cdot\nabla \sim \rho_{L,\alpha}k_\perp < 1$ leads to[85]

$$\phi_1^{\mathrm{LWA}}(\mathbf{x}+\boldsymbol{\rho}_{\mathrm{gy},\alpha}) \approx (1+\boldsymbol{\rho}_{L,\alpha}\cdot\nabla)\,\phi_1(\mathbf{x}), \tag{2.32}$$

$$\left\langle\phi_1^{\mathrm{LWA}}(\mathbf{x}+\boldsymbol{\rho}_{\mathrm{gy},\alpha})\right\rangle = \phi_1(\mathbf{x}), \tag{2.33}$$

$$\left\langle\left(\phi_1^{\mathrm{LWA}}(\mathbf{x}+\boldsymbol{\rho}_{\mathrm{gy},\alpha})\right)^2\right\rangle = \phi_1(\mathbf{x})^2+\frac{|\boldsymbol{\rho}_{L,\alpha}|^2}{2}|\nabla_\perp\phi_1(\mathbf{x})|^2. \tag{2.34}$$

In the last identity, the second-order term provides the factor one-half through gyroaveraging the squared gyroradius unit vector. Since the gyroradius unit vector is perpendicular to the magnetic field, the gradient is projected to the perpendicular plane by $(\mathbf{I}-\mathbf{bb})\cdot\nabla \equiv \nabla_\perp$. This can be inserted into the gyrokinetic Hamiltonian (2.22) to give[62],

$$\mathcal{H}_{\mathrm{gy}}^{\mathrm{LWA}} = \frac{1}{2}m_\alpha v_{||}+\mu B+q_\alpha\langle\phi_1\rangle+\frac{m_\alpha c^2}{2B^2}|\nabla_\perp\phi_1|^2-w. \tag{2.35}$$

The second-order Hamiltonian was approximated by the potential squared term only[85]. The Poisson bracket is given by replacing $\left\langle A_{1,||}\right\rangle \to A_{1,||}$ and dropping the contribution $\partial A_{1,||}/\partial\mu = 0$ in ∇^*.

The LWA of the equations of motions reads[62],

$$\dot{\mathbf{x}}^{\mathrm{LWA}} = \frac{1}{B_{||}^*}\left(\mathbf{B}^* v_{||}+\frac{c}{q_\alpha}\mathbf{b}\times(\mu\nabla B+q_\alpha\nabla\phi_1+\nabla H_2)\right), \tag{2.36}$$

$$\dot{v}_{||}^{\mathrm{LWA}} = -\frac{\mathbf{B}^*}{m_\alpha B_{||}^*}\cdot\left(\mu\nabla B+q_\alpha\nabla\phi_1+\nabla H_2\right)-\frac{q_\alpha}{m_\alpha c}\frac{\partial A_{1,||}}{\partial t}, \tag{2.37}$$

where the second-order Hamiltonian is

$$H_2 = \frac{m_\alpha c^2}{2B^2}|\nabla_\perp\phi_1|^2. \tag{2.38}$$

This term describes ponderomotive effects, i.e., effects on low-frequency dynamics due to averaged high-frequency dynamics[61]. The second term in eq. (2.22) involving the electrostatic potential fluctuations would also provide such effects in a non-simplified Hamiltonian.

Field Equations

The equations governing the electromagnetic field fluctuations ϕ_1 and $A_{1,||}$ can be derived using either push-forward methods to obtain gyrocenter polarization and magnetization[75] or variational methods in gyrokinetic field theory[81–83]. A detailed derivation is given in Ref. [62]. In the LWA, the resulting quasi-neutrality equation for ϕ_1 and Ampère's law for $A_{1,||}$ read

$$-\nabla\cdot\left(\sum_\alpha \frac{m_\alpha c^2 n_\alpha}{B^2}\nabla_\perp\phi_1\right) = \sum_\alpha q_\alpha \int f_\alpha \,\mathrm{d}V, \tag{2.39}$$

$$-\Delta_\perp A_{1,||} = 4\pi\sum_\alpha \frac{q_\alpha}{c}\int v_{||} f_\alpha \,\mathrm{d}V, \tag{2.40}$$

where the velocity space element is $\mathrm{d}V = 2\pi B^*_{||}/m_\alpha \,\mathrm{d}v_{||}\,\mathrm{d}\mu$ and $\Delta_\perp = \nabla\cdot\nabla_\perp$ is the perpendicular Laplacian. In the quasi-neutrality equation, the left-hand side describes the gyrocenter polarization, while the right-hand side is the gyrocenter charge. This equation results in a balance in terms of particle charges. The Laplacian term $\Delta\phi_1$ known from the Poisson equation[67] is typically ordered much smaller than the polarization term and thus removed by construction[86,87].

Linearized Quasi-Neutrality Equation

The long wavelength approximation can be further simplified by replacing the density in the gyrocenter polarization with an equilibrium density $n_\alpha \to n_{0,\alpha}$,

$$-\nabla\cdot\left(\sum_\alpha \frac{m_\alpha c^2 n_{0,\alpha}}{B^2}\nabla_\perp\phi_1\right) = \sum_\alpha q_\alpha \int f_\alpha \,\mathrm{d}V, \tag{2.41}$$

$$-\Delta_\perp A_{1,||} = 4\pi\sum_\alpha \frac{q_\alpha}{c}\int v_{||} f_\alpha \,\mathrm{d}V. \tag{2.42}$$

The theory is constructed such that the overall dynamics are energy consistent[88]. The corresponding equations of motion read[62],

$$\dot{\mathbf{x}}^{\mathrm{lqn}} = \frac{1}{B^*_{||}}\left(\mathbf{B}^* v_{||} + \frac{c}{q_\alpha}\mathbf{b}\times\left(\mu\nabla B + q_\alpha\nabla\phi_1\right)\right), \tag{2.43}$$

$$\dot{v}^{\mathrm{lqn}}_{||} = -\frac{\mathbf{B}^*}{m_\alpha B^*_{||}}\cdot\left(\mu\nabla B + q_\alpha\nabla\phi_1\right) - \frac{q_\alpha}{m_\alpha c}\frac{\partial A_{1,||}}{\partial t}, \tag{2.44}$$

where "lqn" labels the version that needs to be used with the linearized quasi-neutrality equation.

Decoupled Field Equations

The volume element containing $B_{||}^*$ implicitly couples the field equations since it depends on $A_{1,||}$ via eq. (2.25). The assumption $\nabla \times A_{1,||}\mathbf{b} \approx \nabla A_{1,||} \times \mathbf{b}$ decouples the field equations by removing this term from the Jacobian*. The simplified modified magnetic field reads[62],

$$\mathbf{B}^* \approx \mathbf{B} + \frac{m_\alpha c}{q_\alpha} v_{||} \nabla \times \mathbf{b} + \nabla A_{1,||} \times \mathbf{b}. \tag{2.45}$$

2.4 Gyrokinetic Codes

The development of gyrokinetic codes can be traced back to the 1980s[89] after the first derivation of the nonlinear gyrokinetic equation[60]. Since then, a lot of different codes have been developed, based on either the particle in cell (PIC)[90], semi-Lagrangian[91] or Eulerian (continuum)[92] approaches. While these three methods use different approaches† to solve the Vlasov equation, the fluctuating electromagnetic fields need to be represented and solved on a grid in all approaches. Another differentiation can be done between full-f and delta-f codes, the latter employing a splitting into equilibrium and fluctuating part $f = f_0 + \delta f$ of the distribution function and only evolving the fluctuating part[29].

There are a variety of gyrokinetic codes present. A selection without the claim of completeness is presented in the following. In the confined region of the plasma, codes are field-aligned to save upon the computational resources and better resolve the flute-like structure of turbulence. The PIC approach is followed by `GTC-P`[93], `ORB5`[94], `GTS`[95] or `GEM`[96]. Grid-based codes are `GENE`[97,98], `GS2`[92,99,100], (`C`)`GYRO`[101,102], `GKW`[103], `GKV`[104] and `GT5D`[105]. The semi-Lagrangian approach is used by `GYSELA`[106]. Field-alignment can also be used solely in the SOL, which is simulated by the PIC code `PICLS`[107] or the continuum code `GKEYLL`[108,109]. Only a few codes can simulate a tokamak's full, complicated magnetic geometry, including the magnetic X-point. Here, the PIC code `XGC`[31,32] and the continuum codes `COGENT`[33] and `GENE-X`[34] exist. The extension of the latter is the subject of this thesis.

*A simplification which cannot be done on the Lagrangian level alone[62], which may result in deviations from the energetic consistency of the model derived[88].

†Differences are discussed in Refs. [29, 87]

2.5 The GENE-X Code

The GENE-X code was developed[62] to combine high-fidelity gyrokinetic simulations with the capabilities of simulating in highly complex magnetic geometries, including the magnetic X-point. The code employs an Eulerian approach similar to the GENE code by solving the gyrokinetic Vlasov equation on a grid. Simulations in X-point geometry are possible with the so-called flux-coordinate independent (FCI)[110] approach pioneered by the drift-reduced Braginskii turbulence code GRILLIX[111]. The code features a full-f, nonlinear, global, electromagnetic[112] gyrokinetic model and is extended to include the physics of collisions during this thesis[58,59].

The equations solved by GENE-X were presented in this section: the electromagnetic gyrokinetic equation (2.30) in the long wavelength approximation with a linearized quasi-neutrality equation (2.41), (2.43), (2.44) and the approximation on the modified magnetic field (2.45) are used. Further, the Ampère equation (2.42) is solved, but for the term containing $\partial A_{||}/\partial t$ in (2.44), the same scheme as in Ref. [113] is used. An Ohm's law is derived for the independently treated variable $E_{||} \equiv -\partial A_{||}/\partial t$ and solved as a third field equation (see Ref. [62] for details). The collision models were developed in Refs. [58, 59] and will be presented in section 3.

Within the FCI approach, coordinates are locally field-aligned, i.e., Cartesian grids are used within poloidal planes, which are connected by a field-line map[34]. The Vlasov equation is discretized using fourth-order centered finite differences as well as an Arakawa[114] scheme for terms that can be represented by Poisson brackets ($\mathbf{E}\times\mathbf{B}$ and ∇B drifts)[34,112]. The elliptic field equations are solved within the poloidal planes $\nabla_\perp \approx (\partial/\partial R)\,\mathbf{e}_R + (\partial/\partial Z)\,\mathbf{e}_Z$, using a geometric multi-grid algorithm[115,116] to precondition a GMRES[117] solver. Dirichlet boundary conditions are used for the distribution functions, which are set to Maxwellians, and the potentials are pinned to zero at the real space domain boundaries. Dirichlet boundary conditions can be used by applying diffusion next to the domain boundaries and in front of the divertor plates[34]. Additionally, the option to add fourth-order hyperdiffusion[118] in real space and parallel velocity space is available[62]. The time-integrator is RK4, and for the quadrature schemes, Simpson in $v_{||}$ and Gauss-Laguerre in μ are used for collisionless simulations[62]. Chapter 4 details the different schemes used with collisions.

This chapter briefly introduced gyrokinetic theory. The long wavelength approximation and linearization of the quasi-neutrality equation were presented. Gyrokinetic codes were discussed, focusing on the GENE-X code.

Chapter 3

Theory of Coulomb Collisions in Plasmas

This chapter contains the theoretical part of developing collision models for the GENE-X code. The first part briefly reviews the theory of Coulomb collisions, and the Lenard-Bernstein/Dougherty (LBD) collision model is derived. The properties of this model are discussed, and the gyrokinetic formulation is presented. Based on this, model parameters ("mixing quantities") are derived so that the operator conserves species density, total momentum, and total energy. Two versions of collision rates are presented such that the model reproduces the Boltzmann collision operator's momentum or the temperature relaxation rates. In the end, a Bhatnagar-Gross-Krook (BGK) model is presented as a reference. The expressions for mixing quantities and relaxation rates for the LBD operator have been published in Ref. [58].

A fully ionized plasma does not contain neutral particles, and the Coulomb force governs the interaction between charged particles. Since the Coulomb force describes a long-range interaction, a particle will experience the forces of many other particles at any time. To obtain a kinetic theory of the plasma, one may start from the Boltzmann equation that describes the time evolution of a distribution $f_\alpha \equiv f_\alpha(\mathbf{x}, \mathbf{v}, t)$ of particles with species α due to transport, external fields and collisions[63],

$$\frac{\partial f_\alpha}{\partial t} + \mathbf{v} \cdot \frac{\partial f_\alpha}{\partial \mathbf{x}} + \frac{\mathbf{F}_\alpha}{m_\alpha} \cdot \frac{\partial f_\alpha}{\partial \mathbf{v}} = C_\alpha f_\alpha. \tag{3.1}$$

Here, $(\mathbf{x}, \mathbf{v})$ denotes the six dimensional phase space, t is the time and $\mathbf{F}_\alpha$ includes the external forces on species α with mass m_α. The right-hand side denotes the temporal change

due to collisions. For binary collision events, the collision operator is bi-linear[63],

$$C_\alpha f_\alpha = \sum_\beta C_{\alpha\beta}(f_\alpha, f_\beta). \tag{3.2}$$

The total change to the distribution of species α due to collisions is given by all individual changes due to collisions with species β, including self-collisions. Boltzmann assumed the number of collisions per second in an infinitesimal volume $\mathrm{d}\mathbf{v}_\alpha \mathrm{d}\mathbf{v}_\beta \mathrm{d}\Omega$ to be proportional to the distributions f_α and f_β as well as to the relative velocity $u = |v_\alpha - v_\beta|$ and the differential cross section $\mathrm{d}\sigma/\mathrm{d}\Omega$ ("Stoßzahlansatz")[119]. The solid angle is denoted as $\mathrm{d}\Omega$ (see Ref. [120] for more information on scattering theory). With this assumption, the Boltzmann collision integral is given by[121],

$$C_\alpha = \int \mathrm{d}\mathbf{v}_\beta u \int \mathrm{d}\Omega \frac{\mathrm{d}\sigma_{\alpha\beta}}{\mathrm{d}\Omega} \left(f'_\alpha f'_\beta - f_\alpha f_\beta \right), \tag{3.3}$$

where the prime denotes quantities after the scattering event. This expression is generally valid for binary collisions, independent of the interaction forces. For Coulomb interactions, the collision integral is evaluated for the Rutherford cross-section[120]

$$\frac{\mathrm{d}\sigma_{\alpha\beta}}{\mathrm{d}\Omega} = \frac{q_\alpha^2 q_\beta^2}{4u^4 m_{\alpha\beta}^2 \sin^4(\theta/2)}, \tag{3.4}$$

where θ is the scattering angle, q denotes the charge and $m_{\alpha\beta} = m_\alpha m_\beta/(m_\alpha + m_\beta)$ is the reduced mass. This integral has been evaluated in Ref. [122] and [123], resulting in the collision operator being Fokker-Planck-type.

3.1 Fokker-Planck Collision Operator

The evaluation of the Boltzmann collision integral for Coulomb interaction results in a collision operator of Fokker-Planck form[124]

$$C_{\alpha\beta} f_\alpha = -\frac{\partial}{\partial \mathbf{v}} \cdot \left(\mathbf{K}_{\alpha\beta} f_\alpha \right) + \frac{1}{2} \frac{\partial^2}{\partial \mathbf{v} \partial \mathbf{v}} : \left(\mathbf{D}_{\alpha\beta} f_\alpha \right), \tag{3.5}$$

where $\mathbf{K}_{\alpha\beta}$ is the friction coefficient (vector) and $\mathbf{D}_{\alpha\beta}$ the diffusion coefficient (tensor). The Fokker-Planck form is because Coulomb collisions lead to small angle scattering, effectively changing the distribution of particles by a large number of small changes. This fact is well known from the theory of Brownian motion[124]. The following sections present the two different versions of the Fokker-Planck equation for Coulomb collisions and the general properties of collision operators.

3.1.1 Rosenbluth Form

In this formulation, the friction and diffusion coefficients are given by[123,125],

$$\mathbf{K}_{\alpha\beta} = \Gamma_{\alpha\beta}\frac{\partial H_{\alpha\beta}}{\partial \mathbf{v}}, \tag{3.6}$$

$$\mathbf{D}_{\alpha\beta} = \Gamma_{\alpha\beta}\frac{\partial^2 G_{\alpha\beta}}{\partial \mathbf{v}\partial \mathbf{v}}, \tag{3.7}$$

with Rosenbluth potentials

$$H_{\alpha\beta} = \frac{m_\alpha + m_\beta}{m_\beta}\int \mathrm{d}\mathbf{v}' f_\beta(\mathbf{v}')|\mathbf{u}|^{-1}, \tag{3.8}$$

$$G_{\alpha\beta} = \int \mathrm{d}\mathbf{v}' f_\beta(\mathbf{v}')|\mathbf{u}|, \tag{3.9}$$

and factors

$$\Gamma_{\alpha\beta} = \frac{4\pi q_\alpha^2 q_\beta^2}{m_\alpha^2}\ln\Lambda_{\alpha\beta}, \tag{3.10}$$

where $\mathbf{u} = \mathbf{v} - \mathbf{v}'$. The quantity $\ln\Lambda_{\alpha\beta}$ denotes the Coulomb logarithm discussed in section 3.1.4. It is important to note that in the Boltzmann equation (3.3), the contribution after the collision event is present and denoted by a prime, whereas here, this explicit contribution was removed by evaluating the collision integral. For the remainder of this work, the standard notation from Ref. [123] is adopted, where $\mathbf{v}'$ denotes the velocity space of f_β.

The term "potentials" comes from the fact that there is an analogy to electrostatics, leading to additional relations

$$\left(\frac{\partial}{\partial \mathbf{v}}\right)^2 H_{\alpha\beta} = -4\pi\frac{m_\alpha + m_\beta}{m_\beta}f_\beta(\mathbf{v}), \tag{3.11}$$

$$\left(\frac{\partial}{\partial \mathbf{v}}\right)^4 G_{\alpha\beta} = -8\pi f_\beta(\mathbf{v}), \tag{3.12}$$

$$H_{\alpha\beta} = \frac{m_\alpha + m_\beta}{2m_\beta}\left(\frac{\partial}{\partial \mathbf{v}}\right)^2 G_{\alpha\beta}, \tag{3.13}$$

where the operator $(\partial/\partial\mathbf{v})^2$ denotes the Laplacian.

3.1.2 Landau Form

The Landau formulation of the Fokker-Planck equation is given by[122],

$$C_{\alpha\beta}\left(f_\alpha, f_\beta\right) = -\Gamma^L_{\alpha\beta}\frac{\partial}{\partial \mathbf{v}} \cdot \left[\int \mathrm{d}\mathbf{v}' \, \mathbf{U} \cdot \left(\frac{f_\alpha}{m_\beta}\frac{\partial f'_\beta}{\partial \mathbf{v}'} - \frac{f'_\beta}{m_\alpha}\frac{\partial f_\alpha}{\partial \mathbf{v}}\right)\right], \tag{3.14}$$

$$\mathbf{U} = \frac{u^2\mathbf{I} - \mathbf{u}\mathbf{u}}{u^3}, \tag{3.15}$$

$$\Gamma^L_{\alpha\beta} = \frac{2\pi q_\alpha^2 q_\beta^2}{m_\alpha}\ln\Lambda_{\alpha\beta}. \tag{3.16}$$

The velocity tensor $\mathbf{U}$ can be interpreted as a projection operator onto the plane in velocity space perpendicular to the relative velocity direction $\mathbf{u}$. The prefactor is related to (3.10) by $\Gamma^L_{\alpha\beta} = \Gamma_{\alpha\beta} m_\alpha/2$.

From the Landau form, it is immediately clear that the collision operator can alternatively be written as the divergence of a collisional current,

$$C_{\alpha\beta}\left(f_\alpha, f_\beta\right) = -\frac{\partial}{\partial \mathbf{v}} \cdot \mathbf{J}_{\alpha\beta}, \tag{3.17}$$

$$\mathbf{J}_{\alpha\beta} = \mathbf{K}_{\alpha\beta} f_\alpha + \mathbf{D}_{\alpha\beta} \cdot \frac{\partial}{\partial \mathbf{v}} f_\alpha, \tag{3.18}$$

where the friction and diffusion coefficients take the form,

$$\mathbf{K}_{\alpha\beta} = +\frac{\Gamma_{\alpha\beta}}{m_\beta}\int \mathrm{d}\mathbf{v}' \, \mathbf{U} \cdot \frac{\partial}{\partial \mathbf{v}'} f'_\beta, \tag{3.19}$$

$$\mathbf{D}_{\alpha\beta} = -\frac{\Gamma_{\alpha\beta}}{m_\alpha}\int \mathrm{d}\mathbf{v}' \, \mathbf{U} \, f'_\beta. \tag{3.20}$$

The Landau formulation is equivalent to the Rosenbluth formulation[125]. Typically the Landau form is used to prove the basic properties (see next section) of the collision operator[126] since the symmetric form in f_α and f'_β is convenient in that case. Otherwise, the Rosenbluth form is often more convenient[16], as it avoids handling the velocity tensor, and for certain assumptions (e.g., isotropic velocity distributions), the operator can be simplified considerably.

3.1.3 General Properties of Collision Operators

A physically relevant collision operator must satisfy several fundamental properties[63]. Here, some of the most important ones will be listed. First, there are local conservation properties, such as the conservation of single species density, total momentum, and total energy in the laboratory frame

$$\int \mathrm{d}\mathbf{v}\, C_{\alpha\beta} = 0, \tag{3.21}$$

$$\int \mathrm{d}\mathbf{v}\, m_\alpha \mathbf{v} C_{\alpha\beta} + \int \mathrm{d}\mathbf{v}\, m_\beta \mathbf{v} C_{\beta\alpha} = 0, \tag{3.22}$$

$$\int \mathrm{d}\mathbf{v}\, \frac{1}{2} m_\alpha v^2 C_{\alpha\beta} + \int \mathrm{d}\mathbf{v}\, \frac{1}{2} m_\beta v^2 C_{\beta\alpha} = 0. \tag{3.23}$$

Further, the collision operator should fulfill the H-theorem,

$$\frac{\partial \mathcal{H}}{\partial t} \leq 0, \tag{3.24}$$

where the Boltzmann H-function $\mathcal{H} = -S$ is the negative entropy,

$$\mathcal{H} = \int \mathrm{d}\mathbf{v}\, f_\alpha \ln(f_\alpha). \tag{3.25}$$

In other words, the H-theorem states that collisions always increase entropy. The temporal change of $\mathcal{H}$ can only be zero if the collision operator is zero. Further, there must be an equilibrium distribution f_0 for which the collision operator is zero. Finally, if the collision operator is repeatedly applied to any distribution, then $f \to f_0$ as $t \to \infty$.

For the Fokker-Planck collision operator, the three conservation properties (3.21)-(3.23) as well as the H-theorem (3.24) can be proven easily using the Landau form[126].

3.1.4 Coulomb Logarithm

The Coulomb logarithm $\ln \Lambda_{\alpha\beta}$ was introduced in Eqs. (3.10) and (3.16). Its origin connects to the nature of Coulomb collisions that lead to small angle deflections. Ref. [122] provides a detailed discussion. Essentially, it stems from the fact that in the derivation from the Boltzmann collision integral, an integration over all possible impact parameters* in the scattering process must be performed. Small impact parameters would lead to head-on collisions of particles in which the small angle assumption for the Coulomb scattering is invalid. The collision integral diverges logarithmically for large impact parameters due to the infinite

*The impact parameter is a measure to describe the distance of two particles in a scattering process. In a moving frame where one particle is static, the impact parameter is the distance perpendicular to the relative velocity vector. Details can be found in Ref. [120].

extent of the Coulomb force without shielding. Thus, two cut-offs must be introduced in the Boltzmann collision integral, which leads to the definition of the Coulomb logarithm

$$\ln\left(\frac{b_{\max}}{b_{\min}}\right) := \ln\Lambda. \tag{3.26}$$

The impact parameter is denoted by b, and the species indices are suppressed for simplicity. Typical expressions are given in, e.g., Refs. [127], [69] and [128]. A natural choice for the upper cut-off is the Debye length $\lambda_{\mathrm{D}} = \sqrt{T/(4\pi n e^2)}$ since above this distance, the plasma is quasi-neutral, and the Coulomb force is screened. Here, T and n denote temperature and density, and e is the elementary charge. For the lower cut-off, either the Landau length (classical distance of closest approach)[65] $\lambda_{\mathrm{L}} = e^2/T$ or, in the case quantum effects may become important, the de Broglie wavelength $\lambda_{\mathrm{dB}} = \hbar/\sqrt{mT}$, or a combination of both, is used. In Ref. [129], different versions were developed. In this work, version No. 4 of that reference is chosen,

$$\ln\Lambda = \frac{1}{2}\ln\left(1 + \frac{\lambda_{\mathrm{D}}^2}{\lambda_{\mathrm{dB}}^2 + \lambda_{\mathrm{L}}^2}\right). \tag{3.27}$$

Due to the weak dependence of the logarithm on the exact form of the argument, the later-on calculations in this work will not distinguish the Coulomb logarithm for different species and $\ln\Lambda \equiv \ln\Lambda_{\alpha\beta}$ will be used interchangeably.

3.1.5 Model Operators

The full Fokker-Planck collision operator (3.5),(3.14) is a complicated integrodifferential operator, and as such it is not straightforward to solve. Thus, various simplifications have been developed (see, e.g., Refs. [16], [130] and [64] and references therein) typically called "model operators", since they model particular aspects of the full operator.

A standard procedure[130] is to linearize the collision operator for small deviations f_1 around an equilibrium distribution f_0,

$$C_{\alpha\beta}\left(f_\alpha, f_\beta\right) \approx C_{\alpha\beta}\left(f_{0,\alpha}, f_{0,\beta}\right) + C_{\alpha\beta}\left(f_{1,\alpha}, f_{0,\beta}\right) + C_{\alpha\beta}\left(f_{0,\alpha}, f_{1,\beta}\right), \tag{3.28}$$

where the higher order term $C_{\alpha\beta}\left(f_{1,\alpha}, f_{1,\beta}\right)$ has been dropped. The first term is called the "equilibrium operator", the second is the "test particle operator", and the third is the "field particle operator". Different model operators will approximate these three terms differently.

3.2 Lenard-Bernstein/Dougherty (LBD) Collision Operator

In this section, a simplified model collision operator is derived and discussed. The model was first introduced by Lenard and Bernstein[131] and later, in a more general way, by Dougherty[132]. Thus, this operator will be called the Lenard-Bernstein/Dougherty (LBD) collision operator.

3.2.1 Ad-Hoc Derivation

The simplest derivation[132] of the LBD collision operator makes assumptions on the form of the friction and diffusion coefficients. The approximation on the friction assumes a linear dependence on the difference between the local velocity $\mathbf{v}$ and the flow velocity $\mathbf{u}_{\alpha\beta}$, weighted with a parameter $\nu_{\alpha\beta}$ called "collision frequency",

$$\mathbf{K}_{\alpha\beta} \approx -\nu_{\alpha\beta} \left(\mathbf{v} - \mathbf{u}_{\alpha\beta}\right). \tag{3.29}$$

The diffusion is assumed to be isotropic in velocity space and depends on the mean thermal energy

$$\mathbf{D}_{\alpha\beta} \approx \nu_{\alpha\beta} v_{\mathrm{th},\alpha\beta}^2 \mathbf{I}. \tag{3.30}$$

In these assumptions, the collision frequency is velocity-independent and the same for friction and diffusion. The other two free parameters are the flow velocity $\mathbf{u}_{\alpha\beta}$ and the temperature $T_{\alpha\beta}$ defined through the thermal energy

$$v_{\mathrm{th},\alpha\beta} = \sqrt{\frac{2T_{\alpha\beta}}{m_\alpha}}. \tag{3.31}$$

The exact choice of these parameters is given in section 3.2.5. The index $\alpha\beta$ indicates that these quantities may depend on both particle species. Using (3.29) and (3.30), Eq. (3.5) can be rewritten as

$$C_{\alpha\beta} f_\alpha = \nu_{\alpha\beta} \frac{\partial}{\partial \mathbf{v}} \cdot \left(\left(\mathbf{v} - \mathbf{u}_{\alpha\beta}\right) f_\alpha + \frac{1}{2} v_{\mathrm{th},\alpha\beta}^2 \frac{\partial f_\alpha}{\partial \mathbf{v}} \right). \tag{3.32}$$

This is the three-dimensional Lenard-Bernstein[131] or Dougherty[132] (LBD) collision operator. There are two main deficiencies of this model collision operator. First, the velocity-independent collision frequency does not fall off with increasing velocity, thus incorrectly describing the collision rate of high energy particles that live in the tail of the distribution function[132]. Second, the isotropic diffusion coefficient leads to the same collision rates

for pitch-angle scattering and energy diffusion, a distinction which would be important for neoclassical physics[130].

3.2.2 Derivation from the Rosenbluth Form

The LBD model can be derived by considering the first two terms of (3.28). In that sense, it is a model operator for the equilibrium and test particle operators combined,

$$C_{\alpha\beta}\left(f_\alpha, f_\beta\right) \approx C_{\alpha\beta}\left(f_{0,\alpha}, f_{0,\beta}\right) + C_{\alpha\beta}\left(f_{1,\alpha}, f_{0,\beta}\right) = C_{\alpha\beta}\left(f_\alpha, f_{0,\beta}\right). \tag{3.33}$$

In other words, the Fokker-Planck collision operator needs to be evaluated for a Maxwellian distribution of background particles. Simplifications are made at the final step of the derivation, making the categorization based on test/field particle operators only partially applicable. The following derivation is based on a brief description in Ref. [133].

The equilibrium distribution used in the following is

$$f_\beta = f_{0,\beta} = \frac{n_\beta}{\left(\sqrt{\pi} v_{\mathrm{th},\beta}\right)^3} \exp\left(-\frac{\mathbf{v}^2}{v_{\mathrm{th},\beta}^2}\right), \tag{3.34}$$

where n_β and $v_{\mathrm{th},\beta}$ are density and thermal velocity of the background distribution. A mean flow $\mathbf{u}_\beta$ is not considered for simplicity. Given this background distribution, the test particle operator is available in the literature (see eq. (3) in Ref. [130]). The derivation here is different, as further simplifications will be applied first.

First, one can evaluate the $G_{\alpha\beta}$ potential for distribution (3.34). It is convenient to choose the relative velocity frame $\mathbf{u} = \mathbf{v} - \mathbf{v}'$ and switch to spherical coordinates (u, θ, ϕ), where $u = |\mathbf{u}|$ is the velocity magnitude, θ the polar angle and ϕ the azimuthal angle. Using the volume element $\mathrm{d}\mathbf{v}' = \mathrm{d}\mathbf{u} = u^2 \mathrm{d}u \mathrm{d}(\cos\theta)\mathrm{d}\phi$, the potential is

$$\begin{aligned} G_{\alpha\beta} &= \int_0^\infty \mathrm{d}u \int_{-1}^1 \mathrm{d}(\cos\theta) \int_0^{2\pi} \mathrm{d}\phi\, u^3 \frac{n_\beta}{\left(\sqrt{\pi} v_{\mathrm{th},\beta}\right)^3} \exp\left(-\frac{(\mathbf{u}+\mathbf{v})^2}{v_{\mathrm{th},\beta}^2}\right), \\ &= n_\beta v_{\mathrm{th},\beta} \left[\frac{2}{\sqrt{\pi}} \exp\left(-\frac{v^2}{v_{\mathrm{th},\beta}^2}\right) + \left(\frac{v_{\mathrm{th},\beta}}{v} + \frac{2v}{v_{\mathrm{th},\beta}}\right) \mathrm{erf}\left(\frac{v}{v_{\mathrm{th},\beta}}\right)\right]. \end{aligned} \tag{3.35}$$

Using $(\mathbf{u}+\mathbf{v})^2 = u^2 + v^2 + 2uv\cos\theta$, the integration over the angle variables is trivial, and the remaining integration over u can be performed with any computer algebra tool. Here the error function was used,

$$\mathrm{erf}(x) = \frac{2}{\sqrt{\pi}} \int_0^x \exp\left(-t^2\right) \mathrm{d}t. \tag{3.36}$$

The spherical coordinate system is now changed to (v, θ, ϕ). The relevant differential operators are obtained using formulas from Ref. [66]. For a function $g(v)$ they are given by

$$\frac{\partial}{\partial \mathbf{v}} g(v) = \frac{\mathbf{v}}{v} \frac{\partial}{\partial v} g(v), \tag{3.37}$$

$$\left(\frac{\partial}{\partial \mathbf{v}}\right)^2 g(v) = \frac{\partial}{\partial v}\left(v^2 \frac{\partial}{\partial v} g(v)\right), \tag{3.38}$$

$$\frac{\partial^2}{\partial \mathbf{v} \partial \mathbf{v}} g(v) = \frac{1}{v}\frac{\partial}{\partial v} g(v)\mathbf{I} + \frac{1}{v}\frac{\partial}{\partial v}\left(\frac{1}{v}\frac{\partial}{\partial v} g(v)\right)\mathbf{v}\mathbf{v}. \tag{3.39}$$

Then, the second Rosenbluth potential is calculated using (3.13),

$$H_{\alpha\beta} = \frac{2n_\beta(m_\alpha + m_\beta)}{m_\beta v} \mathrm{erf}\left(\frac{v}{v_{\mathrm{th},\beta}}\right). \tag{3.40}$$

The Fokker-Planck coefficients (3.6) and (3.7) are given by derivatives of the two potentials, obtained via straightforward computations

$$\mathbf{K}_{\alpha\beta} = \frac{2n_\beta(m_\alpha + m_\beta)\Gamma_{\alpha\beta}}{m_\beta}\left[\frac{2}{v_{\mathrm{th},\beta}\sqrt{\pi}}\frac{1}{v^2}\exp\left(-\frac{v^2}{v_{\mathrm{th},\beta}^2}\right) - \frac{1}{v^3}\mathrm{erf}\left(\frac{v}{v_{\mathrm{th},\beta}}\right)\right]\mathbf{v}, \tag{3.41}$$

$$\begin{aligned}\mathbf{D}_{\alpha\beta} = \Gamma_{\alpha\beta} n_\beta v_{\mathrm{th},\beta}\Bigg\{ &\left[\frac{2}{\sqrt{\pi}v^2}\exp\left(-\frac{v^2}{v_{\mathrm{th},\beta}^2}\right) + \left(-\frac{v_{\mathrm{th},\beta}}{v^3} + \frac{2}{v_{\mathrm{th},\beta} v}\right)\mathrm{erf}\left(\frac{v}{v_{\mathrm{th},\beta}}\right)\right]\mathbf{I} \\ &+ \left[-\frac{6}{\sqrt{\pi}v^4}\exp\left(-\frac{v^2}{v_{\mathrm{th},\beta}^2}\right) + \left(\frac{3v_{\mathrm{th},\beta}}{v^5} - \frac{2}{v_{\mathrm{th},\beta} v^3}\right)\mathrm{erf}\left(\frac{v}{v_{\mathrm{th},\beta}}\right)\right]\mathbf{v}\mathbf{v}\Bigg\}.\end{aligned} \tag{3.42}$$

Next, an expansion in small velocities $x \equiv v/v_{\mathrm{th},\beta} \ll 1$ is applied

$$\mathrm{erf}(x) \approx \frac{2}{\sqrt{\pi}}x - \frac{2}{3\sqrt{\pi}}x^3 + \mathcal{O}\left(x^5\right), \tag{3.43}$$

$$\exp\left(-x^2\right) \approx 1 - x^2 + \mathcal{O}\left(x^4\right), \tag{3.44}$$

resulting in

$$\mathbf{K}_{\alpha\beta} \approx -\frac{8n_\beta(m_\alpha + m_\beta)\Gamma_{\alpha\beta}}{3\sqrt{\pi}m_\beta v_{\mathrm{th},\beta}^3}\mathbf{v}, \tag{3.45}$$

$$\mathbf{D}_{\alpha\beta} \approx \frac{2\Gamma_{\alpha\beta}n_\beta}{\sqrt{\pi}}\left[\frac{4}{3v_{\mathrm{th},\beta}}\mathbf{I} - \frac{2}{3v_{\mathrm{th},\beta}^3}\left(v^2\mathbf{I} - \mathbf{v}\mathbf{v}\right)\right]. \tag{3.46}$$

Before insertion into the Fokker-Planck equation (3.5), it can be rewritten as

$$\begin{aligned} C_{\alpha\beta} f_\alpha &= \frac{\partial}{\partial \mathbf{v}} \cdot \left[-\mathbf{K}_{\alpha\beta} f_\alpha + \frac{1}{2} \left(\mathbf{D}_{\alpha\beta} \cdot \frac{\partial f_\alpha}{\partial \mathbf{v}} + f_\alpha \frac{\partial}{\partial \mathbf{v}} \cdot \mathbf{D}_{\alpha\beta} \right) \right], \\ &= \frac{\partial}{\partial \mathbf{v}} \cdot \left[-\frac{m_\alpha}{m_\alpha + m_\beta} \mathbf{K}_{\alpha\beta} f_\alpha + \frac{1}{2} \mathbf{D}_{\alpha\beta} \cdot \frac{\partial f_\alpha}{\partial \mathbf{v}} \right], \end{aligned} \tag{3.47}$$

where the second equality used (3.13) for the third term in the first line. Now, (3.45) and (3.46) can be inserted into (3.47) to get

$$C_{\alpha\beta} f_\alpha = \nu'_{\alpha\beta} \frac{\partial}{\partial \mathbf{v}} \cdot \left[\mathbf{v} f_\alpha + \frac{1}{2} \left(v_{\mathrm{th},\beta}^2 \mathbf{I} - \frac{1}{2} \left(v^2 \mathbf{I} - \mathbf{v}\mathbf{v} \right) \right) \cdot \frac{\partial f_\alpha}{\partial \mathbf{v}} \right], \tag{3.48}$$

$$\nu'_{\alpha\beta} = \frac{8 \Gamma_{\alpha\beta} n_\beta}{3\sqrt{\pi} v_{\mathrm{th},\beta}^3} = \frac{64\sqrt{\pi} q_\alpha^2 q_\beta^2 n_\beta}{3 m_\alpha^2 v_{\mathrm{th},\beta}^3} \ln \Lambda_{\alpha\beta}. \tag{3.49}$$

To arrive at the LBD operator, the anisotropic part $(v^2 \mathbf{I} - \mathbf{v}\mathbf{v})$ is dropped, the mean flow of the background is introduced $\mathbf{v} \to \mathbf{v} - \mathbf{u}_\beta$ and $\mathbf{u}_\beta$, $v_{\mathrm{th},\beta}^2$ and $\nu'_{\alpha\beta}$ are replaced by new, free parameters,

$$C_{\alpha\beta} f_\alpha = \nu_{\alpha\beta} \frac{\partial}{\partial \mathbf{v}} \cdot \left[(\mathbf{v} - \mathbf{u}_{\alpha\beta}) f_\alpha + \frac{1}{2} v_{\mathrm{th},\alpha\beta}^2 \frac{\partial f_\alpha}{\partial \mathbf{v}} \right]. \tag{3.50}$$

This is the same expression as in eq. (3.32). The parameters introduced give some freedom to account for the simplifications made in the derivation. Naturally, one can choose them to maintain the basic properties expected from a collision operator, density, momentum, and energy conservation. The exact choice will be given in section 3.2.5. It should be noted that they will depend on moments n_β, $\mathbf{u}_\beta$ and T_β of the full distribution f_β, re-introducing a nonlinearity to the operator. This dependence is why categorizing as combined equilibrium and test particle operator does not apply.

3.2.3 Properties of the LBD Operator

This section discusses the essential properties of the LBD collision operator, such as equilibrium distribution, conservation properties, entropy production, and steady-state solution, as well as the relation to the pitch-angle operator and the formulation in cylindrical velocity space coordinates.

Equilibrium Distribution

It can be trivially shown that a Maxwellian distribution,

$$f_{0,\alpha} = \frac{n_\alpha}{(\sqrt{\pi} v_{\mathrm{th},\alpha\beta})^3} \exp\left(-\frac{(\mathbf{v}-\mathbf{u}_{\alpha\beta})^2}{v_{\mathrm{th},\alpha\beta}^2}\right), \tag{3.51}$$

is an equilibrium distribution of the LBD operator. Insertion of the derivative

$$\frac{\partial f_{0,\alpha}}{\partial \mathbf{v}} = -\frac{2}{v_{\mathrm{th},\alpha\beta}^2}(\mathbf{v}-\mathbf{u}_{\alpha\beta}) f_{0,\alpha}, \tag{3.52}$$

into (3.50) cancels the friction term, making the operator zero.

Conservation Properties

Conservation of density (3.21) is automatically fulfilled since the operator can be written similarly to (3.17), using a collisional flux

$$\int_V \mathrm{d}\mathbf{v}\, C_{\alpha\beta} f_\alpha = -\int_V \mathrm{d}\mathbf{v} \frac{\partial}{\partial \mathbf{v}} \cdot \mathbf{J}_{\alpha\beta} = -\int_{\partial V} \mathrm{d}\mathbf{n}_v \cdot \mathbf{J}_{\alpha\beta}, \tag{3.53}$$

where the integration was applied on a spherical volume V with radius $v \to \infty$ so that Gauss' theorem could be applied. Here ∂V denotes the boundary of the sphere, and $\mathbf{n}_v$ is the normal vector to its surface. The distribution function is assumed to vanish sufficiently fast at the velocity space domain boundaries. Thus, the collisional flux and the integral are zero, and density is conserved. The flux introduced in eq. (3.53) is given by,

$$\mathbf{J}_{\alpha\beta} = (\mathbf{v}-\mathbf{u}_{\alpha\beta}) f_\alpha + \frac{1}{2} v_{\mathrm{th},\alpha\beta}^2 \frac{\partial f_\alpha}{\partial \mathbf{v}}. \tag{3.54}$$

For momentum conservation (3.22), the following term needs to be considered

$$\begin{aligned} m_\alpha \int_V \mathrm{d}\mathbf{v}\, \mathbf{v} C_{\alpha\beta} f_\alpha &= -m_\alpha \int_V \mathrm{d}\mathbf{v} \left[\frac{\partial}{\partial \mathbf{v}}\left(\mathbf{v}\mathbf{J}_{\alpha\beta}\right) - \mathbf{J}_{\alpha\beta}\right], \\ &= m_\alpha \nu_{\alpha\beta} \int_V \mathrm{d}\mathbf{v} \left[(\mathbf{v}-\mathbf{u}_{\alpha\beta}) f_\alpha + \frac{1}{2} v_{\mathrm{th},\alpha\beta}^2 \frac{\partial f_\alpha}{\partial \mathbf{v}}\right]. \end{aligned} \tag{3.55}$$

The first term on the right-hand side of the first line again vanished due to Gauss' law. In contrast to density conservation, this is not trivially fulfilled and will depend on the choice of the parameters in the operator. The same holds for energy conservation. Since the required computation is tedious, only the gyrokinetic version will be used to choose the parameters in section 3.2.5.

H Theorem

The temporal change of the H-function can be written as[63]

$$\frac{\partial \mathcal{H}_\alpha}{\partial t} = \int \mathrm{d}\mathbf{v}\, C_\alpha \left(1 + \ln f_\alpha\right), \tag{3.56}$$

where $\partial f_\alpha / \partial t$ has been replaced by C_α since only entropy production is considered. In principle, the total temporal change given by the kinetic equation should be included, but advection does not contribute to entropy production by definition[134].

The first term in (3.56) vanishes due to the conservation of density (3.21). In the following, it is sufficient to analyze the contribution to entropy production by $C_{\alpha\beta}$ only,

$$\frac{\partial \mathcal{H}_\alpha}{\partial t} = \int \mathrm{d}\mathbf{v} \left[\frac{\partial}{\partial \mathbf{v}} \cdot \left(\mathbf{J}_{\alpha\beta} \ln f_\alpha\right) - \mathbf{J}_{\alpha\beta} \cdot \frac{\partial}{\partial \mathbf{v}} \ln f_\alpha\right]. \tag{3.57}$$

Due to Gauss' theorem, the first term vanishes. An explicit expression for the velocity space derivative of f_α can be obtained[109]

$$\frac{\partial f_\alpha}{\partial \mathbf{v}} = \frac{2}{v_{\mathrm{th},\alpha\beta}^2} \left(\frac{1}{\nu_{\alpha\beta}} \mathbf{J}_{\alpha\beta} - (\mathbf{v} - \mathbf{u}_{\alpha\beta}) f_\alpha\right). \tag{3.58}$$

Inserting into (3.57) and expanding the terms leads to

$$\frac{\partial \mathcal{H}_\alpha}{\partial t} = -\frac{2}{v_{\mathrm{th},\alpha\beta}^2} \int \mathrm{d}\mathbf{v} \left(\frac{1}{f_\alpha} \mathbf{J}_{\alpha\beta}^2 - (\mathbf{v} - \mathbf{u}_{\alpha\beta})^2 f_\alpha - \frac{1}{2} v_{\mathrm{th},\alpha\beta}^2 (\mathbf{v} - \mathbf{u}_{\alpha\beta}) \cdot \frac{\partial f_\alpha}{\partial \mathbf{v}}\right). \tag{3.59}$$

The last term vanishes upon integration by parts, assuming the distribution function falls off sufficiently fast at the velocity space domain boundaries. If the operator fulfills the conservation of energy (3.23), the second term vanishes. Thus, the remaining term is

$$\frac{\partial \mathcal{H}_\alpha}{\partial t} = -\frac{2}{v_{\mathrm{th},\alpha\beta}^2} \int \mathrm{d}\mathbf{v}\, \frac{1}{f_\alpha} \mathbf{J}_{\alpha\beta}^2 \leq 0, \tag{3.60}$$

since the distribution function is always positive $f_\alpha > 0$. Because no assumptions on the species were used, interchanging the indices $\alpha \leftrightarrow \beta$ leads to the same relation for the second contribution of the entropy production of C_α. Consequently, this means that if the free parameters of the LBD operator are chosen to conserve the total energy, the H-theorem is fulfilled.

Steady State Solution

Given the H-theorem (3.60), the remaining question is, which distribution function satisfies the condition $\mathcal{H} = 0$. The entropy production will be zero for a steady state distribution, given by vanishing collisional flux (3.54),

$$(\mathbf{v} - \mathbf{u}_{\alpha\beta}) f_\alpha + \frac{1}{2} v_{\text{th},\alpha\beta}^2 \frac{\partial f_\alpha}{\partial \mathbf{v}} = 0. \tag{3.61}$$

Taking the dot product with $\mathbf{v}$ and dividing by f_α, using $(1/f_\alpha)\partial f_\alpha/\partial \mathbf{v} = \partial \ln(f_\alpha)/\partial \mathbf{v} = (\mathbf{v}/v)\partial \ln(f_\alpha)/\partial v$, this can be integrated over v to write

$$\ln f_\alpha = -\frac{2}{v_{\text{th},\alpha\beta}^2}\left(\frac{1}{2}v^2 - \left(\frac{\mathbf{v}}{v}\cdot \mathbf{u}_{\alpha\beta}\right) v\right) + C, \tag{3.62}$$

where C is a constant of integration. The constant may be rewritten as $C = C_1 - u_{\alpha\beta}^2/v_{\text{th},\alpha\beta}^2$ to complete the square. Using the abbreviation $1/Z \equiv \exp(C_1)$ the result for f_α is

$$f_\alpha = \frac{1}{Z}\exp\left(-\frac{(\mathbf{v} - \mathbf{u}_{\alpha\beta})^2}{v_{\text{th},\alpha\beta}^2}\right). \tag{3.63}$$

Here Z plays the role of a normalization, which is obtained by requiring the result of the velocity space integration to be the density n_α. The resulting normalization is $Z = n_\alpha/(\sqrt{\pi} v_{\text{th},\alpha\beta})^3$, making (3.63) the same as (3.51). Consequently, this shows that the Maxwellian distribution is the distribution for which the collision operator produces zero entropy. To fully show that this is the steady-state solution, it must be proven that this is the maximum entropy solution. Such a proof can is given in Ref. [109].

Relation to Pitch-Angle Scattering Operator

Using the Laplacian in spherical velocity space[66] (v, θ, ϕ) introduced in section 3.2.2,

$$\frac{\partial^2 f}{\partial \mathbf{v}^2} = \frac{1}{v^2}\frac{\partial}{\partial v}\left(v^2 \frac{\partial f}{\partial v}\right) + \frac{1}{v^2 \sin\theta}\frac{\partial}{\partial \theta}\left(\sin\theta \frac{\partial f}{\partial \theta}\right) + \frac{1}{v^2 \sin^2\theta}\frac{\partial^2 f}{\partial \phi^2}, \tag{3.64}$$

the diffusion part in eq. (3.50) can be written as

$$C_{\alpha\beta} f_\alpha = \frac{1}{2}\nu_{\alpha\beta} v_{\text{th},\alpha\beta}^2 \left[\frac{1}{v^2}\frac{\partial}{\partial v}\left(v^2 \frac{\partial f_\alpha}{\partial v}\right) + \frac{1}{v^2 \sin\theta}\frac{\partial}{\partial \theta}\left(\sin\theta \frac{\partial f_\alpha}{\partial \theta}\right) + \frac{1}{v^2 \sin^2\theta}\frac{\partial^2 f_\alpha}{\partial \phi^2}\right]. \tag{3.65}$$

The operator now contains two distinct terms: energy diffusion and pitch-angle scattering. The pitch-angle part is related to the standard pitch-angle or so-called Lorentz collision

operator[64]

$$\mathcal{L} = \frac{1}{2}\left[\frac{1}{\sin\theta}\frac{\partial}{\partial\theta}\left(\sin\theta\frac{\partial f}{\partial\theta}\right) + \frac{1}{\sin^2\theta}\frac{\partial^2 f}{\partial\phi^2}\right]. \tag{3.66}$$

The prefactors in the Lorentz and LBD operators are not the same due to the various assumptions in the LBD model. The anisotropic diffusion that was dropped in (3.48), is

$$C^{\mathrm{A}}_{\alpha\beta} f_\alpha = -\frac{1}{4}\nu_{\alpha\beta} v^2_{\mathrm{th},\alpha\beta}\frac{\partial}{\partial\mathbf{v}}\cdot\left[\left(v^2\frac{\partial f_\alpha}{\partial\mathbf{v}} - \mathbf{v}\mathbf{v}\cdot\frac{\partial f_\alpha}{\partial\mathbf{v}}\right)\right]. \tag{3.67}$$

The second term cancels the v component of the gradient in the first term, leaving only angular parts. Using the divergence in spherical coordinates[66],

$$\frac{\partial}{\partial\mathbf{v}}\cdot\mathbf{A} = \frac{1}{v^2}\frac{\partial}{\partial v}\left(v^2 A_v\right) + \frac{1}{v\sin\theta}\frac{\partial}{\partial\theta}\left(\sin\theta A_\theta\right) + \frac{1}{v\sin\theta}\frac{\partial A_\phi}{\partial\phi}, \tag{3.68}$$

where $\mathbf{A}\sim\partial f/\partial\mathbf{v}$, this results in

$$C^{\mathrm{A}}_{\alpha\beta} f_\alpha = -\frac{1}{4}\nu_{\alpha\beta} v^2_{\mathrm{th},\alpha\beta}\left[\frac{1}{v^2\sin\theta}\frac{\partial}{\partial\theta}\left(\sin\theta\frac{\partial f_\alpha}{\partial\theta}\right) + \frac{1}{v^2\sin^2\theta}\frac{\partial f^2_\alpha}{\partial\phi^2}\right]. \tag{3.69}$$

From the above considerations, the approximations of the LBD model can be analyzed. First, the energy diffusion and pitch-angle scattering in (3.65) have the same collision frequencies. Second, the velocity dependence of the pitch-angle part is different than in the standard case (3.66). Third, within the approximation of a Maxwellian field particle distribution and the small velocity expansion, the pitch-angle part is overestimated by a factor of two, as the term (3.69) was neglected.

Formulation in Cylindrical Velocity Space

Here, the LBD operator is formulated in the cylindrical velocity space aligned to an external magnetic field $\mathbf{B} = B\,\mathbf{b}$, where B denotes the magnitude of the field. The coordinates are given by $(v_\perp, \theta, v_{||})$, where $v_{||}$ and $v_\perp$ are the velocity components parallel and perpendicular to the magnetic field and θ is the gyroangle. The coordinate transformation is standard (see Ref. [135] §1.5). The components of the collisional current in cylindrical velocity space are given by,

$$J_\perp = v_\perp f_\alpha + \frac{1}{2}v^2_{\mathrm{th},\alpha\beta}\frac{\partial f_\alpha}{\partial v_\perp}. \tag{3.70}$$

$$J_\theta = 0. \tag{3.71}$$

$$J_{||} = \left(v_{||} - u_{\alpha\beta}\right) f_\alpha + \frac{1}{2}v^2_{\mathrm{th},\alpha\beta}\frac{\partial f_\alpha}{\partial v_{||}}, \tag{3.72}$$

where $u_{\alpha\beta}$ is the magnitude of the mean flow $\mathbf{u}_{\alpha\beta} = u_{\alpha\beta}\mathbf{b}$. Using the divergence in cylindrical coordinates (r, ϕ, z)[66],

$$\nabla \cdot \mathbf{A} = \frac{1}{r}\frac{\partial}{\partial r}\left(rA_r\right) + \frac{1}{r}\frac{\partial A_\phi}{\partial \phi} + \frac{\partial A_z}{\partial z}, \tag{3.73}$$

the LBD operator in cylindrical velocity space is given by

$$C_{\alpha\beta}f_\alpha = \nu_{\alpha\beta}\left[\frac{\partial}{\partial v_{||}}\left(\left(v_{||} - u_{\alpha\beta}\right)f_\alpha + \frac{1}{2}v_{\mathrm{th},\alpha\beta}^2\frac{\partial f_\alpha}{\partial v_{||}}\right) + \frac{1}{v_\perp}\frac{\partial}{\partial v_\perp}\left(v_\perp^2 f_\alpha + \frac{1}{2}v_\perp v_{\mathrm{th},\alpha\beta}^2\frac{\partial f_\alpha}{\partial v_\perp}\right)\right]. \tag{3.74}$$

Alternatively it can be written using the magnetic moment μ, which is related to the perpendicular kinetic energy by $v_\perp^2 m_\alpha/2 = \mu B$,

$$C_{\alpha\beta}f_\alpha = \nu_{\alpha\beta}\left[\frac{\partial}{\partial v_{||}}\left(\left(v_{||} - u_{\alpha\beta}\right)f_\alpha + \frac{1}{2}v_{\mathrm{th},\alpha\beta}^2\frac{\partial f_\alpha}{\partial v_{||}}\right) + \frac{\partial}{\partial \mu}\left(2\mu f_\alpha + \frac{m_\alpha v_{\mathrm{th},\alpha\beta}^2}{B}\mu\frac{\partial f_\alpha}{\partial \mu}\right)\right]. \tag{3.75}$$

The following Maxwellian gives the corresponding equilibrium distribution,

$$\mathcal{M}_{\alpha\beta} = n_\alpha\left(\frac{m_\alpha}{2\pi T_{\alpha\beta}}\right)^{3/2}\exp\left(-\frac{\frac{1}{2}m_\alpha(v_{||} - u_{\alpha\beta})^2 + \mu B}{T_{\alpha\beta}}\right), \tag{3.76}$$

which can be obtained using $\mathbf{v} = v_{||}\mathbf{b} + v_\perp\mathbf{e}_\perp$ and (3.31), and verified by insertion into (3.75).

3.2.4 Gyrokinetic Version

The general objective is to use the LBD collision operator (3.50) in a gyrokinetic code. Thus a complete, self-consistent collisional gyrokinetic system needs to be developed. In gyrokinetic field theory[81], the general approach is to formulate the system based on a Lagrangian. One can derive the desired equations from the transformed Lagrangian in gyrocenter coordinates. For a collisional, electromagnetic gyrokinetic system, such a formulation has not been found yet[136]. Thus, an approximate transformation is used instead. For a brief introduction to gyrokinetic theory, see section 2.

The collision operator will consider only the leading order terms for simplicity. Investigating the guiding-center transformation instead of the gyrocenter in this work will suffice. In both the guiding-center[137] and in the gyrocenter formulation (see, e.g., Refs. [138], [139]), the transformed collision operator is given by a gyroaverage in lowest order. The following section summarizes the essential aspects developed in Ref. [137] that are required to formulate a gyrokinetic (guiding-center) version of the LBD operator.

The basic ordering assumption in the guiding-center transformation of the kinetic equation (with collisions) is that the ordering parameter $\epsilon_\nu = \nu/\Omega \ll 1$, i.e., the collision frequency is small compared to the gyrofrequency. Denoting guiding center variables with "gc", the transformed kinetic equation for the gyroaveraged distribution $\langle f_{\rm gc}(\mathbf{z}_{\rm gc}, t)\rangle$ is given by

$$\frac{\mathrm{d}_{\rm gc}}{\mathrm{d}t}\langle f_{\rm gc}\rangle = \left\langle C_{\rm gc}(\langle f_{\rm gc}\rangle + \widetilde{f}_{\rm gc})\right\rangle, \tag{3.77}$$

where species indices are suppressed for simplicity. The collision operator can have a non-zero gyroangle-independent contribution if applied on the gyroangle-dependent part of the distribution $\widetilde{f}_{\rm gc}$. Thus this couples to the kinetic equation for $\widetilde{f}_{\rm gc}$,

$$\frac{\mathrm{d}_{\rm gc}}{\mathrm{d}t}\widetilde{f}_{\rm gc} = C_{\rm gc}(f_{\rm gc}) - \langle C_{\rm gc}(f_{\rm gc})\rangle\,. \tag{3.78}$$

The kinetic equation for $\widetilde{f}_{\rm gc}$ is formally solved by a Fourier expansion in the gyroangle θ. The leading order term up to first order in ϵ_ν can then be inserted into the kinetic equation for $\langle f_{\rm gc}\rangle$ to get

$$\frac{\mathrm{d}_{\rm gc}}{\mathrm{d}t}\langle f_{\rm gc}\rangle = \langle C_{\rm gc}\rangle - \mathrm{i}\epsilon_\nu \sum_{l\neq 0}\left\langle C_{\rm gc}\left(\frac{\mathrm{e}^{\mathrm{i}l\theta}}{l\Omega}\left\langle \mathrm{e}^{-\mathrm{i}l\theta}C_{\rm gc}\Big(\langle f_{\rm gc}\rangle\Big)\right\rangle\right)\right\rangle + \mathcal{O}(\epsilon_B\epsilon_\nu, \epsilon_\nu^2). \tag{3.79}$$

As suggested by Ref. [137], the leading order term is considered sufficient in the following. The remaining task is to find an explicit expression for $C_{\rm gc}$ and apply the gyroaverage operation.

The procedure is given in Ref. [137], the collision operator can be formulated using a Poisson bracket

$$\{f, g\} = \frac{1}{m}\frac{\partial f}{\partial \mathbf{x}}\cdot\frac{\partial g}{\partial \mathbf{v}} - \frac{1}{m}\frac{\partial g}{\partial \mathbf{x}}\cdot\frac{\partial f}{\partial \mathbf{v}} + \frac{e\mathbf{B}}{cm^2}\cdot\frac{\partial f}{\partial \mathbf{v}}\times\frac{\partial g}{\partial \mathbf{v}}. \tag{3.80}$$

It follows that $\{\mathbf{x}, f\} = -\partial f/\partial \mathbf{x}$ and the collision operator (3.50) is

$$C_{\alpha\beta}f_\alpha = -\nu_{\alpha\beta}\left\{\mathbf{x}, (\mathbf{v}-\mathbf{u}_{\alpha\beta})f_\alpha - \frac{1}{2}v_{{\rm th},\alpha\beta}^2\{\mathbf{x}, f_\alpha\}\right\},, \tag{3.81}$$

where in this notation $\{\mathbf{x}, \mathbf{v}f\} = \mathbf{I}\cdot\partial(\mathbf{v}f)/\partial\mathbf{v} = \partial/\partial\mathbf{v}\cdot(\mathbf{v}f)$.

The general transformation of a Poisson bracket is known (see, e.g., Refs. [61], [74] or [137]), and the resulting collision operator is

$$C_{\rm gc} = -\frac{1}{\mathcal{J}_{\rm gc}}\frac{\partial}{\partial z_{\rm gc}^\gamma}\cdot\left[\mathcal{J}_{\rm gc}\left(K_{\rm gc}^\gamma\langle f_{\rm gc}\rangle - D_{\rm gc}^{\gamma\delta}\frac{\partial\langle f_{\rm gc}\rangle}{\partial z_{\rm gc}^\delta}\right)\right], \tag{3.82}$$

with indices γ, δ denoting the summation over phase space variables. The coefficients are given by projecting the LBD Fokker-Planck coefficients $\mathbf{K}^{\mathrm{LBD}} = \nu_{\alpha\beta}(\mathbf{v} - \mathbf{u}_{\alpha\beta})$ and $\mathbf{D}^{\mathrm{LBD}} = \frac{1}{2}\nu_{\alpha\beta}v_{\mathrm{th},\alpha\beta}^2\mathbf{I}$ into six dimensional guiding center phase space and applying the gyroaverage[140]. The projection involves the guiding-center Poisson bracket[74,137]. The guiding-center phase space of relevance is $z^\gamma = (\mathbf{x}_{\mathrm{gc}}, v_{||,\mathrm{gc}}, \mu_{\mathrm{gc}})$. Projected coefficients for this phase space are given in Ref. [140]. However, the addition of parallel flow $\mathbf{u}_{\alpha\beta} = u_{\alpha\beta}\mathbf{b}$ and modification for the isotropic diffusion is performed in this work. The result for the components of the friction coefficient is,

$$K_{\mathrm{gc}}^{\mathbf{x}} = -\nu\frac{\left(\mathbf{V}_{\mathrm{gc}} - \left\langle \mathbf{u}(\mathbf{x}_{\mathrm{gc}} + \boldsymbol{\rho}_{\mathrm{gc}})\right\rangle\right) \times \mathbf{b}}{\Omega_{||}^*}, \tag{3.83}$$

$$K_{\mathrm{gc}}^{||} = -\nu\left(v_{||} - u(\mathbf{x}_{\mathrm{gc}}) + \epsilon_B\frac{v_{||}}{\Omega_{||}^*}\mathbf{b}\cdot\nabla\times\mathbf{b}\frac{\mu B}{m v_{||}}\right), \tag{3.84}$$

$$K_{\mathrm{gc}}^{\mu} = -\nu\left(2 - \epsilon_B\frac{v_{||}}{\Omega_{||}^*}\mathbf{b}\cdot\nabla\times\mathbf{b}\right)\mu, \tag{3.85}$$

suppressing the species indices and using the modified gyrofrequency $\Omega_{||}^* = eB_{||}^*/m$. Here the guiding-center velocity[61,137] was used,

$$\mathbf{V}_{\mathrm{gc}} = v_{||}\mathbf{b} + \epsilon_B\frac{\mathbf{b}}{m\Omega_{||}^*}\times\Big(\mu\nabla B + m v_{||}^2\mathbf{b}\cdot\nabla\mathbf{b}\Big), \tag{3.86}$$

and $\boldsymbol{\rho}_{\mathrm{gc}} = \boldsymbol{\rho}_0 + \mathcal{O}(\epsilon_B^2)$ denotes the guiding-center displacement. It is given by the gyroradius vector in leading order, and an explicit expression for the first-order contribution can be found in the appendix of Ref. [137].

The flow term in the first component of the friction coefficient can be evaluated similarly to the leading order guiding center polarization[75]. Using the expansion $\mathbf{u}(\mathbf{x}_{\mathrm{gc}} + \boldsymbol{\rho}_{\mathrm{gc}}) = \mathbf{u}(\mathbf{x}_{\mathrm{gc}}) + \boldsymbol{\rho}_{\mathrm{gc}}\cdot\nabla\mathbf{u} + \mathcal{O}(\epsilon_B^2)$, $\langle\boldsymbol{\rho}_0\rangle = 0$ and the gyroangle independence of $\nabla\mathbf{u}$, the gyroaveraged flow term is

$$\left\langle \mathbf{u}(\mathbf{x}_{\mathrm{gc}} + \boldsymbol{\rho}_{\mathrm{gc}})\right\rangle \approx \mathbf{u}(\mathbf{x}_{\mathrm{gc}}) + \langle\boldsymbol{\rho}_{\mathrm{gc}}\rangle\cdot\nabla\mathbf{u} \equiv \mathbf{u}(\mathbf{x}_{\mathrm{gc}}) + \mathcal{O}(\epsilon_B^2). \tag{3.87}$$

Only second-order terms from the guiding-center displacement would survive the gyroaverage*. The flow $\mathbf{u}(\mathbf{x})$ is treated as a general space-dependent variable so far.

The components of the diffusion coefficient are given in Ref. [140]. For isotropic diffusion,

*Compare to eqs. (36) and (37) in Ref. [75].

they take the form

$$D_{\mathrm{gc}}^{\mathbf{x},\mathbf{x}} = \frac{\nu}{2} v_{\mathrm{th}}^2 \frac{\mathbf{I} - \mathbf{bb}}{(m\Omega_{||}^*)^2}, \tag{3.88}$$

$$D_{\mathrm{gc}}^{\mathbf{x},||} = \epsilon_B \frac{\nu}{2} v_{\mathrm{th}}^2 \frac{v_{||}}{(m\Omega_{||}^*)^2} \mathbf{b} \cdot \nabla \mathbf{b}, \tag{3.89}$$

$$D_{\mathrm{gc}}^{\mathbf{x},\mu} = 0, \tag{3.90}$$

$$D_{\mathrm{gc}}^{||,||} = \frac{\nu}{2m^2} v_{\mathrm{th}}^2, \tag{3.91}$$

$$D_{\mathrm{gc}}^{||,\mu} = \epsilon_B \frac{\nu}{2} v_{\mathrm{th}}^2 \frac{v_{||}}{\Omega_{||}^*} \mathbf{b} \cdot \nabla \times \mathbf{b} \frac{\mu}{v_{||} m^2}, \tag{3.92}$$

$$D_{\mathrm{gc}}^{\mu,\mu} = \nu\, v_{\mathrm{th}}^2 \left(1 - \epsilon_B \frac{v_{||}}{\Omega_{||}^*} \mathbf{b} \cdot \nabla \times \mathbf{b}\right) \frac{\mu}{mB}. \tag{3.93}$$

From these expressions, it is possible to derive a collision operator in guiding-center space up to first order in magnetic field non-uniformity. For simplicity, the operator in this work will only consider the leading order terms in ϵ_B. The spatial contribution $D_{\mathrm{gc}}^{\mathbf{x},\mathbf{x}}$ results in second-order spatial derivatives of order $(\rho_L k_\perp)^2$ which are neglected within the long wavelength approximation (see section 2.3). Given these simplifications, the guiding-center collision operator is

$$C_{\mathrm{gc}} = \frac{\nu}{B_{||}^*} \left\{ \frac{\partial}{\partial v_{||}} \left[B_{||}^* \left(\left(v_{||} - u\right) \langle f_{\mathrm{gc}} \rangle + \frac{1}{2} v_{\mathrm{th}}^2 \frac{\partial \langle f_{\mathrm{gc}} \rangle}{\partial v_{||}} \right) \right] + \frac{\partial}{\partial \mu} \left[B_{||}^* \left(2\mu \langle f_{\mathrm{gc}} \rangle + \frac{m v_{\mathrm{th}}^2}{B} \mu \frac{\partial \langle f_{\mathrm{gc}} \rangle}{\partial \mu} \right) \right] \right\}, \tag{3.94}$$

where the Jacobian $\mathcal{J} = mB_{||}^*$ was used. The following term

$$\frac{1}{2} v_{\mathrm{th}}^2 \frac{\partial B_{||}^*}{\partial v_{||}} = \frac{mcv_{\mathrm{th}}^2}{2q} \mathbf{b} \cdot \nabla \times \mathbf{b} = \mathcal{O}(\epsilon_B), \tag{3.95}$$

is a first-order correction. Neglecting this correction, the Jacobian $B_{||}^*$ can be pulled into the $v_{||}$ derivative of $\langle f_{\mathrm{gc}} \rangle$. Writing $f \equiv \langle f_{\mathrm{gc}} \rangle$ and re-introducing all species indices results in the final form of the guiding-center LBD operator[58,133]

$$C_{\alpha\beta} f_\alpha = \frac{\nu_{\alpha\beta}}{B_{||}^*} \left[\frac{\partial}{\partial v_{||}} \left(\left(v_{||} - u_{\alpha\beta}\right) B_{||}^* f_\alpha + \frac{1}{2} v_{\mathrm{th},\alpha\beta}^2 \frac{\partial B_{||}^* f_\alpha}{\partial v_{||}} \right) + \frac{\partial}{\partial \mu} \left(2\mu B_{||}^* f_\alpha + \frac{m_\alpha v_{\mathrm{th},\alpha\beta}^2}{B} \mu \frac{\partial B_{||}^* f_\alpha}{\partial \mu} \right) \right]. \tag{3.96}$$

The combination of $B_{||}^* f_\alpha$ is very convenient when considering the conservation properties of the collision operator later. This form of the "gyroaveraged" collision operator (3.96) is the same as the version in cylindrical velocity space (3.75) up to the factor $B_{||}^*$ inserted at suitable positions.

3.2.5 Properties of the Gyrokinetic Version

In this section the free parameters $u_{\alpha\beta}$, $T_{\alpha\beta} = m_\alpha v_{\mathrm{th},\alpha\beta}^2/2$ and $\nu_{\alpha\beta}$ will be determined. Density conservation was shown in section 3.2.3. Momentum and energy conservation were indicated not to be trivially fulfilled. The free parameters will be determined such that the conservation laws are fulfilled. Such a procedure was done in Ref. [141] for a Bhatnagar-Gross-Krook (BGK)[142] collision operator. This work applies it to the LBD operator, with results published in Ref. [58].

The collision operator written in divergence form is,

$$C_{\alpha\beta} f_\alpha = \frac{\nu_{\alpha\beta}}{B_{||}^*} \left[\frac{\partial J_{||}}{\partial v_{||}} + \frac{\partial J_\mu}{\partial \mu} \right], \tag{3.97}$$

with collisional fluxes

$$J_{||} = \left(v_{||} - u_{\alpha\beta} \right) B_{||}^* f_\alpha + \frac{T_{\alpha\beta}}{m_\alpha} \frac{\partial B_{||}^* f_\alpha}{\partial v_{||}}, \tag{3.98}$$

$$J_\mu = 2\mu B_{||}^* f_\alpha + \frac{2T_{\alpha\beta}}{B} \mu \frac{\partial B_{||}^* f_\alpha}{\partial \mu}. \tag{3.99}$$

The following moments of the distribution function are defined,

$$n_\alpha = 2\pi \int \frac{B_{||}^*}{m_\alpha} f_\alpha \mathrm{d}v_{||} \mathrm{d}\mu, \tag{3.100}$$

$$u_\alpha = \frac{2\pi}{n_\alpha} \int \frac{B_{||}^*}{m_\alpha} f_\alpha v_{||} \mathrm{d}v_{||} \mathrm{d}\mu, \tag{3.101}$$

$$W_{||,\alpha} = \pi \int B_{||}^* f_\alpha v_{||}^2 \mathrm{d}v_{||} \mathrm{d}\mu, \tag{3.102}$$

$$W_{\perp,\alpha} = 2\pi \int \frac{B_{||}^*}{m_\alpha} f_\alpha \mu B \mathrm{d}v_{||} \mathrm{d}\mu, \tag{3.103}$$

$$T_\alpha^L = \frac{2}{3n_\alpha} \left(W_{||,\alpha} + W_{\perp,\alpha} \right). \tag{3.104}$$

$$T_\alpha = T_\alpha^L - \frac{1}{3} m_\alpha u_\alpha^2, \tag{3.105}$$

which are the density, parallel flow, parallel and perpendicular energy, and laboratory and moving frame temperature, respectively.

Momentum Conservation

The conservation of momentum is achieved if the following condition is satisfied,

$$\int B_{||}^{*} \left(C_{\alpha\beta} f_\alpha + C_{\beta\alpha} f_\beta\right) v_{||} \mathrm{d}v_{||} \mathrm{d}\mu \stackrel{!}{=} 0.|| \tag{3.106}$$

Considering the first integral and switching indices in the result is sufficient to account for both contributions. Using (3.97),

$$\int B_{||}^{*} C_{\alpha\beta} f_\alpha v_{||} \mathrm{d}v_{||} \mathrm{d}\mu = \nu_{\alpha\beta} \int \left(\frac{\partial J_{||}}{\partial v_{||}} + \frac{\partial J_\mu}{\partial \mu}\right) v_{||} \mathrm{d}v_{||} \mathrm{d}\mu \equiv \nu_{\alpha\beta} \left(\mathcal{I}_1 + \mathcal{I}_2\right). \tag{3.107}$$

The first part is evaluated using integration by parts,

$$\mathcal{I}_1 = -\int J_{||} \mathrm{d}v_{||} \mathrm{d}\mu = -\int \left(\left(v_{||} - u_{\alpha\beta}\right) B_{||}^{*} f_\alpha + \frac{T_{\alpha\beta}}{m_\alpha} \frac{\partial B_{||}^{*} f_\alpha}{\partial v_{||}}\right) \mathrm{d}v_{||} \mathrm{d}\mu, \tag{3.108}$$

where the boundary term vanishes due to the assumption that the distribution function (and thus the fluxes) fall off sufficiently fast at the velocity space domain boundaries. The first two terms are trivially integrated using (3.100) and (3.101), and the third term vanishes. The result is

$$\mathcal{I}_1 = \frac{n_\alpha m_\alpha}{2\pi} \left(u_{\alpha\beta} - u_\alpha\right). \tag{3.109}$$

The second integral is $\mathcal{I}_2 = 0$ which leads to

$$\nu_{\alpha\beta} \left(\frac{n_\alpha m_\alpha}{2\pi} \left(u_{\alpha\beta} - u_\alpha\right)\right) + \nu_{\beta\alpha} \left(\frac{n_\beta m_\beta}{2\pi} \left(u_{\beta\alpha} - u_\beta\right)\right) \stackrel{!}{=} 0. \tag{3.110}$$

Demanding the symmetry relation[141],

$$u_{\alpha\beta} = u_{\beta\alpha}, \tag{3.111}$$

results in an expression for the mixing flow[58]

$$u_{\alpha\beta} = \frac{u_\alpha \nu_{\alpha\beta} n_\alpha m_\alpha + u_\beta \nu_{\beta\alpha} n_\beta m_\beta}{\nu_{\alpha\beta} n_\alpha m_\alpha + \nu_{\beta\alpha} n_\beta m_\beta}. \tag{3.112}$$

Energy Conservation

The conservation of energy is achieved if the following condition is met

$$\int \left[\frac{B_{||}^*}{m_\alpha} C_{\alpha\beta} f_\alpha \left(\frac{m_\alpha}{2} v_{||}^2 + \mu B \right) + \frac{B_{||}^*}{m_\beta} C_{\beta\alpha} f_\beta \left(\frac{m_\beta}{2} v_{||}^2 + \mu B \right) \right] \mathrm{d}v_{||} \mathrm{d}\mu \stackrel{!}{=} 0. \tag{3.113}$$

The first integral is

$$\begin{aligned} \int \frac{B_{||}^*}{m_\alpha} C_{\alpha\beta} f_\alpha \left(\frac{m_\alpha}{2} v_{||}^2 + \mu B \right) \mathrm{d}v_{||} \mathrm{d}\mu &= \nu_{\alpha\beta} \int \left(\frac{\partial J_{||}}{\partial v_{||}} + \frac{\partial J_\mu}{\partial \mu} \right) \left(\frac{1}{2} v_{||}^2 + \frac{1}{m_\alpha} \mu B \right) \mathrm{d}v_{||} \mathrm{d}\mu, \\ &\equiv \nu_{\alpha\beta} \left(\mathcal{J}_1 + \mathcal{J}_2 + \mathcal{J}_3 + \mathcal{J}_4 \right). \end{aligned} \tag{3.114}$$

The same procedure used in evaluating moment conservation can be applied. The individual integrals are given by

$$\mathcal{J}_1 = \frac{1}{\pi} \left(\frac{1}{2} T_{\alpha\beta} n_\alpha + \frac{m_\alpha}{2} u_{\alpha\beta} u_\alpha n_\alpha - W_{||,\alpha} \right), \tag{3.115}$$

$$\mathcal{J}_2 = 0, \tag{3.116}$$

$$\mathcal{J}_3 = 0, \tag{3.117}$$

$$\mathcal{J}_4 = \frac{1}{\pi} \left(T_{\alpha\beta} n_\alpha - W_{\perp,\alpha} \right). \tag{3.118}$$

Thus, energy conservation requires

$$\begin{aligned} &\nu_{\alpha\beta} \frac{1}{\pi} \left[\frac{3}{2} n_\alpha \left(T_{\alpha\beta} - T_\alpha \right) + \frac{1}{2} n_\alpha m_\alpha u_\alpha \left(u_{\alpha\beta} - u_\alpha \right) \right] \\ &+ \nu_{\beta\alpha} \frac{1}{\pi} \left[\frac{3}{2} n_\beta \left(T_{\beta\alpha} - T_\beta \right) + \frac{1}{2} n_\beta m_\beta u_\beta \left(u_{\beta\alpha} - u_\beta \right) \right] \stackrel{!}{=} 0. \end{aligned} \tag{3.119}$$

Demanding the symmetry relation[141],

$$T_{\alpha\beta} = T_{\beta\alpha}, \tag{3.120}$$

leads after some algebra to[58]

$$T_{\alpha\beta} = \frac{T_\alpha \nu_{\alpha\beta} n_\alpha + T_\beta \nu_{\beta\alpha} n_\beta}{\nu_{\alpha\beta} n_\alpha + \nu_{\beta\alpha} n_\beta} + \frac{1}{3} \frac{\nu_{\alpha\beta} n_\alpha m_\alpha \left(u_\alpha^2 - u_{\alpha\beta}^2 \right) + \nu_{\beta\alpha} n_\beta m_\beta \left(u_\beta^2 - u_{\alpha\beta}^2 \right)}{\nu_{\alpha\beta} n_\alpha + \nu_{\beta\alpha} n_\beta}. \tag{3.121}$$

Given Eqs. (3.112) and (3.121), the LBD collision operator fulfills momentum and energy conservation by construction. Since these quantities are given by combinations of the individual flow and temperature moments, these are referred to as "mixing quantities" in the following.

Relaxation Rates

The free parameter left to determine is the collision frequency $\nu_{\alpha\beta}$. In the case of a model collision operator with velocity-independent collision frequency, it is possible to adjust this parameter to achieve physically reasonable behavior. One possibility is to choose collision frequencies such that the relaxation rates of the collision operator approximate the relaxation rate of the Boltzmann collision operator. Relaxation rates for the Boltzmann collision operator have been calculated in Ref. [143]. It is not trivial to satisfy both the momentum and energy relaxation rates simultaneously[141]. Ref. [144] treated this case by introducing a free parameter. In contrast, Ref. [141] introduces two different, entropic (E) versions*, one to match the momentum relaxation rate exactly (EM) and one to match the temperature relaxation rate approximately (ET). In each case, the corresponding other relaxation rate is not matched. These two models have been implemented for the LBD operator in Ref. [58], and the following section provides details. Ref. [145] compares versions from Refs. [144], [141] and [58] for the LBD operator.

The change in momentum due to collisions is given by a calculation similar to (3.109),

$$\frac{\partial}{\partial t}(u_\alpha n_\alpha) = 2\pi \int \frac{B_{||}^*}{m_\alpha} v_{||} C_{\alpha\beta} f_\alpha \mathrm{d}v_{||}\mathrm{d}\mu = \nu_{\alpha\beta} n_\alpha (u_{\alpha\beta} - u_\alpha). \tag{3.122}$$

Thus, the momentum relaxation rate is,

$$\left.\frac{\partial}{\partial t}(u_\beta - u_\alpha)\right|_{\mathrm{LBD}} = \nu_{\beta\alpha} n_\beta (u_{\beta\alpha} - u_\beta) - \nu_{\alpha\beta} n_\alpha (u_{\alpha\beta} - u_\alpha). \tag{3.123}$$

The change in energy due to collisions can be calculated similarly,

$$\begin{aligned}\frac{\partial}{\partial t}\left(\frac{3}{2} n_\alpha T_\alpha\right) &= 2\pi \int \frac{B_{||}^*}{m_\alpha} \frac{1}{2} m_\alpha \left((v_{||} - u_{\alpha\beta})^2 + \frac{2\mu B}{m_\alpha}\right) C_{\alpha\beta} f_\alpha \mathrm{d}v_{||}\mathrm{d}\mu, \\ &= \nu_{\alpha\beta}\left(3n_\alpha (T_{\alpha\beta} - T_\alpha) - m_\alpha n_\alpha (u_{\alpha\beta} - u_\alpha)^2\right).\end{aligned} \tag{3.124}$$

The energy relaxation rate is

$$\begin{aligned}\left.\frac{\partial}{\partial t}(T_\beta - T_\alpha)\right|_{\mathrm{LBD}} = 2\Bigg\{&\nu_{\beta\alpha}\left[(T_{\beta\alpha} - T_\beta) - \frac{m_\beta}{3}(u_{\beta\alpha} - u_\beta)^2\right] \\ &- \nu_{\alpha\beta}\left[(T_{\alpha\beta} - T_\alpha) - \frac{m_\alpha}{3}(u_{\alpha\beta} - u_\alpha)^2\right]\Bigg\}.\end{aligned} \tag{3.125}$$

*For both versions, the BGK collision operator satisfies the H-theorem and is thus called entropic.

The relaxation rates for the Boltzmann collision operator are given in Refs. [143] and [141] and adapted for a scalar flow parameter,

$$\frac{\partial}{\partial t}\left(u_\beta - u_\alpha\right)\bigg|_{\text{Boltz}} = -A_{\alpha\beta}\frac{m_\alpha n_\alpha + m_\beta n_\beta}{m_\alpha n_\alpha m_\beta n_\beta}\frac{m_\alpha + m_\beta}{2}\left(u_\beta - u_\alpha\right), \tag{3.126}$$

$$\frac{\partial}{\partial t}\left(T_\beta - T_\alpha\right)\bigg|_{\text{Boltz}} = -A_{\alpha\beta}\left[\frac{n_\alpha + n_\beta}{n_\alpha n_\beta}(T_\beta - T_\alpha) + \frac{1}{3}\frac{m_\beta n_\beta - m_\alpha n_\alpha}{n_\alpha n_\beta}(u_\beta - u_\beta)^2\right], \tag{3.127}$$

with

$$A_{\alpha\beta} = \frac{8\sqrt{2\pi}n_\alpha n_\beta\sqrt{m_\alpha m_\beta}(Z_\alpha Z_\beta e^2)^2\ln\Lambda_{\alpha\beta}}{3(m_\alpha T_\beta + m_\beta T_\alpha)^{3/2}}, \tag{3.128}$$

for Coulomb collisions. Here Z denotes the signed charge number, with $Z = -1$ for electrons and $Z > 0$ for ions.

In the first case, the momentum relaxation rates can be matched

$$\frac{\partial}{\partial t}\left(u_\beta - u_\alpha\right)\bigg|_{\text{LBD}} \stackrel{!}{=} \frac{\partial}{\partial t}\left(u_\beta - u_\alpha\right)\bigg|_{\text{Boltz}}, \tag{3.129}$$

which yields the condition

$$A_{\alpha\beta}\frac{m_\alpha + m_\beta}{2} = \frac{m_\alpha n_\alpha m_\beta n_\beta \nu_{\beta\alpha}\nu_{\alpha\beta}}{m_\alpha n_\alpha \nu_{\alpha\beta} + m_\beta n_\beta \nu_{\beta\alpha}}. \tag{3.130}$$

In the second case, matching the temperature relaxation rates

$$\frac{\partial}{\partial t}\left(T_\beta - T_\alpha\right)\bigg|_{\text{LBD}} \stackrel{!}{=} \frac{\partial}{\partial t}\left(T_\beta - T_\alpha\right)\bigg|_{\text{Boltz}}, \tag{3.131}$$

yields,

$$\begin{aligned}
&-\frac{A_{\alpha\beta}}{2}\left[\frac{n_\alpha + n_\beta}{n_\alpha n_\beta}(T_\beta - T_\alpha) + \frac{1}{3}\frac{m_\beta n_\beta - m_\alpha n_\alpha}{n_\alpha n_\beta}(u_\beta - u_\alpha)^2\right] \\
&\quad = -\frac{(n_\alpha + n_\beta)\nu_{\alpha\beta}\nu_{\beta\alpha}}{n_\alpha\nu_{\alpha\beta} + n_\beta\nu_{\beta\alpha}}(T_\beta - T_\alpha) \\
&\qquad - \frac{(n_\alpha + n_\beta)m_\alpha m_\beta \nu_{\alpha\beta}\nu_{\beta\alpha}(m_\alpha n_\alpha^2\nu_{\alpha\beta}^2 - m_\beta n_\beta^2\nu_{\beta\alpha}^2)}{3(n_\alpha\nu_{\alpha\beta} + n_\beta\nu_{\beta\alpha})(m_\alpha n_\alpha\nu_{\alpha\beta} + m_\beta n_\beta\nu_{\beta\alpha})^2}(u_\beta - u_\alpha)^2.
\end{aligned} \tag{3.132}$$

Expressions (3.130) and (3.132) correspond to the ones in Ref. [141] except for the factor of

1/2 in (3.132) which arises from a different temperature relaxation rate of the LBD operator compared to the BGK.

Momentum Relaxation (EM)
In this version, Eq. (3.130) and the following version of the temperature relaxation are chosen to be satisfied[141]

$$-A_{\alpha\beta}\frac{n_\alpha + n_\beta}{n_\alpha n_\beta}(T_\beta - T_\alpha) = -\frac{(n_\alpha + n_\beta)\nu_{\alpha\beta}\nu_{\beta\alpha}}{n_\alpha\nu_{\alpha\beta} + n_\beta\nu_{\beta\alpha}}(T_\beta - T_\alpha). \tag{3.133}$$

From this, the following relation is obtained,

$$\nu_{\alpha\beta} = -\frac{A_{\alpha\beta}n_\beta\nu_{\beta\alpha}}{n_\alpha A_{\alpha\beta} - \nu_{\beta\alpha}n_\alpha n_\beta}. \tag{3.134}$$

Insertion into (3.130) yields,

$$\nu_{\beta\alpha} = A_{\alpha\beta}\frac{m_\alpha + m_\beta}{m_\beta n_\beta}, \qquad \nu_{\alpha\beta} = A_{\alpha\beta}\frac{m_\alpha + m_\beta}{m_\alpha n_\alpha}. \tag{3.135}$$

Additionally, the relation $\nu_{\alpha\beta}m_\alpha n_\alpha = \nu_{\beta\alpha}m_\beta n_\beta$ is fulfilled and[58]

$$\nu_{\alpha\beta}^{\mathrm{EM,LBD}} = \frac{8\sqrt{2\pi}n_\beta\sqrt{m_\alpha m_\beta}(Z_\alpha Z_\beta e^2)^2\ln\Lambda_{\alpha\beta}}{3(m_\alpha T_\beta + m_\beta T_\alpha)^{3/2}}\frac{m_\alpha + m_\beta}{m_\alpha}. \tag{3.136}$$

In (3.133), the factor of 1/2 was neglected. Otherwise, collision frequencies would be negative. Given these simplifications, one has to expect an error twice as high in the temperature relaxation rate compared to the BGK version[141]. The collision frequency for the EM version of the LBD operator (3.136) can additionally be found in Ref. [58].

In the EM version, the expressions for the mixing quantities (3.112) and (3.121) simplify to[141]

$$u_{\alpha\beta}^{\mathrm{EM}} = \frac{1}{2}(u_\alpha + u_\beta), \tag{3.137}$$

$$T_{\alpha\beta}^{\mathrm{EM}} = \frac{T_\alpha m_\beta + T_\beta m_\alpha}{m_\alpha + m_\beta} + \frac{1}{6}\frac{m_\alpha m_\beta}{m_\alpha + m_\beta}(u_\alpha - u_\beta)^2. \tag{3.138}$$

Temperature Relaxation (ET)

Constructing this version is not straightforward. In Ref. [141] the approach is to require $n_\alpha \nu_{\alpha\beta} = n_\beta \nu_{\beta\alpha}$, which simplifies (3.132) to

$$-\frac{A_{\alpha\beta}}{2}\left[\frac{n_\alpha + n_\beta}{n_\alpha n_\beta}(T_\beta - T_\alpha) + \frac{1}{3}\frac{m_\beta n_\beta - m_\alpha n_\alpha}{n_\alpha n_\beta}(u_\beta - u_\alpha)^2\right]$$
$$= -\frac{1}{2}\nu_{\alpha\beta}\frac{n_\alpha + n_\beta}{n_\beta}(T_\beta - T_\alpha) - \frac{1}{6}\nu_{\alpha\beta}\frac{n_\alpha + n_\beta}{n_\beta}\frac{m_\alpha m_\beta (m_\alpha - m_\beta)}{(m_\alpha + m_\beta)^2}(u_\beta - u_\alpha)^2. \tag{3.139}$$

Matching the temperature terms yields

$$\nu_{\alpha\beta} = \frac{A_{\alpha\beta}}{n_\alpha} \qquad\qquad \nu_{\beta\alpha} = \frac{A_{\alpha\beta}}{n_\beta}, \tag{3.140}$$

and for the collision frequency[58]

$$\nu_{\alpha\beta}^{\mathrm{ET,LBD}} = \frac{8\sqrt{2\pi} n_\beta \sqrt{m_\alpha m_\beta}(Z_\alpha Z_\beta e^2)^2 \ln \Lambda_{\alpha\beta}}{3(m_\alpha T_\beta + m_\beta T_\alpha)^{3/2}}. \tag{3.141}$$

This expression can be found in Ref. [58]. This version only approximates the temperature relaxation rate and will not achieve a perfect match in temperature and momentum relaxation rates.

The simplified expressions for the mixing quantities in the ET version are given by[141]

$$u_{\alpha\beta}^{\mathrm{ET}} = \frac{u_\alpha m_\alpha + u_\beta m_\beta}{m_\alpha + m_\beta}, \tag{3.142}$$

$$T_{\alpha\beta}^{\mathrm{ET}} = \frac{T_\alpha + T_\beta}{2} + \frac{1}{6}\frac{m_\alpha m_\beta}{m_\alpha + m_\beta}\left(u_\alpha - u_\beta\right)^2. \tag{3.143}$$

3.2.6 Normalized Gyrokinetic Version

The version of the LBD operator used in a code such as `GENE-X` must be normalized. As such, all quantities have to be written as $T_\alpha = \hat{T}_\alpha T_{\mathrm{ref}}$, where the hat indicates the normalized version and the subscript "ref" the reference. These reference quantities are given in Refs. [34] and [112] and the detailed procedure on how to normalize can be found in Ref. [62].

The basic reference quantities are the reference density n_{ref}, temperature T_{ref}, length L_{ref}, magnetic field B_{ref} and mass m_{ref}. Derived reference quantities used in the following normalization are $\mu_{\mathrm{ref}} = T_{\mathrm{ref}}/B_{\mathrm{ref}}$, $t_{\mathrm{ref}} = L_{\mathrm{ref}}/c_{\mathrm{ref}}$, $c_{\mathrm{ref}} = \sqrt{T_{\mathrm{ref}}/m_{\mathrm{ref}}}$, $\rho_{\mathrm{ref}} = c_{\mathrm{ref}}/\Omega_{\mathrm{ref}}$ and $\Omega_{\mathrm{ref}} = eB_{\mathrm{ref}}/(m_{\mathrm{ref}}c)$. These are the reference magnetic moment, time, speed, gyroradius, and gyrofrequency. For the parallel velocity, a species-dependent normalization $v_{\mathrm{ref},\alpha} = \sqrt{2/\hat{m}_\alpha}c_{\mathrm{ref}}$ is used, which leads to $f_{\mathrm{ref},\alpha} = n_{\mathrm{ref}}/v_{\mathrm{th},\alpha}^3$.

The normalized moments of the distribution function are given by,

$$\hat{n}_\alpha = \pi \int \hat{B}^*_{||} \hat{f}_\alpha \mathrm{d}\hat{v}_{||} \mathrm{d}\hat{\mu}, \tag{3.144}$$

$$\hat{u}_\alpha = \frac{\pi}{\hat{n}_\alpha} \int \hat{B}^*_{||} \hat{f}_\alpha \hat{v}_{||} \mathrm{d}\hat{v}_{||} \mathrm{d}\mu, \tag{3.145}$$

$$\hat{T}_\alpha = \frac{2\pi}{3\hat{n}_\alpha} \int \hat{B}^*_{||} \hat{f}_\alpha \left(\hat{v}^2_{||} + \hat{\mu}\hat{B} \right) \mathrm{d}\hat{v}_{||} \mathrm{d}\hat{\mu} - \frac{2}{3}\hat{u}^2_\alpha, \tag{3.146}$$

with

$$\hat{B}^*_{||} = \hat{B} + \frac{\sqrt{2\hat{m}_\alpha}\rho_{\mathrm{ref}}}{\hat{q}_\alpha L_{\mathrm{ref}}} \hat{v}_{||} \mathbf{b} \cdot (\nabla \times \mathbf{b}). \tag{3.147}$$

The normalized Maxwellian is,

$$\hat{\mathcal{M}}_{\alpha\beta} = \frac{\hat{n}_\alpha}{\left(\pi \hat{T}_{\alpha\beta}\right)^{3/2}} \exp\left(- \frac{\left(\hat{v}_{||} - \hat{u}_{\alpha\beta}\right)^2 + \hat{\mu}\hat{B}}{\hat{T}_{\alpha\beta}} \right). \tag{3.148}$$

The collision frequency is normalized to $\nu_{\mathrm{ref}} = c_{\mathrm{ref}}/L_{\mathrm{ref}}$,

$$\hat{\nu}^{\mathrm{LBD}}_{\alpha\beta} = p_\nu \frac{n_{\mathrm{ref}} L_{\mathrm{ref}}}{T^2_{\mathrm{ref}}} \frac{8\hat{n}_\beta \sqrt{2\pi \hat{m}_\alpha \hat{m}_\beta} \left(Z_\alpha Z_\beta e^2\right)^2}{3\left(\hat{m}_\alpha \hat{T}_\beta + \hat{m}_\beta \hat{T}_\alpha\right)^{3/2}} \ln \Lambda_{\alpha\beta}, \tag{3.149}$$

where the prefactor depends on the version

$$p_\nu = \begin{cases} 1, & \mathrm{ET}, \\ \frac{\hat{m}_\alpha + \hat{m}_\beta}{\hat{m}_\alpha}, & \mathrm{EM}, \end{cases} \tag{3.150}$$

The constants in this expression are combined into a parameter*

$$\texttt{coll\_ref} = \frac{n_{\mathrm{ref}} L_{\mathrm{ref}}}{T^2_{\mathrm{ref}}} \frac{16\sqrt{2\pi} e^4}{3}. \tag{3.151}$$

There is a relative factor of 2 between eqs. (3.149) and (3.151), since the latter was first defined withe respect to the collision frequency of the BGK operator[58,141].

The normalized mixing quantities (3.137)-(3.138) and (3.142)-(3.143) are given by,

$$\hat{u}_{\alpha\beta} = p_{u,\alpha}\hat{u}_\alpha + p_{u,\beta}\hat{u}_\beta, \tag{3.152}$$

$$\hat{T}_{\alpha\beta} = p_{T,\alpha}\hat{T}_\alpha + p_{T,\beta}\hat{T}_\beta + \frac{m_\alpha m_\beta}{3(m_\alpha + m_\beta)} \left(\frac{\hat{u}_\beta}{\sqrt{m_\beta}} - \frac{\hat{u}_\alpha}{\sqrt{m_\alpha}} \right)^2, \tag{3.153}$$

*This is not the same parameter as in the GENE code[146,147].

with

$$p_{u,\alpha} = \begin{cases} \frac{\hat{m}_\alpha}{\hat{m}_\alpha+\hat{m}_\beta}, & \text{ET}, \\ \frac{1}{2}, & \text{EM}, \end{cases} \qquad p_{u,\beta} = \begin{cases} \frac{\sqrt{\hat{m}_\alpha \hat{m}_\beta}}{\hat{m}_\alpha+\hat{m}_\beta}, & \text{ET}, \\ \frac{1}{2}\sqrt{\frac{\hat{m}_\alpha}{\hat{m}_\beta}}, & \text{EM}. \end{cases} \tag{3.154}$$

$$p_{T,\alpha} = \begin{cases} \frac{1}{2}, & \text{ET}, \\ \frac{\hat{m}_\beta}{\hat{m}_\alpha+\hat{m}_\beta}, & \text{EM}, \end{cases} \qquad p_{T,\beta} = \begin{cases} \frac{1}{2}, & \text{ET}, \\ \frac{\hat{m}_\alpha}{\hat{m}_\alpha+\hat{m}_\beta}, & \text{EM}. \end{cases} \tag{3.155}$$

Using $C_{\text{ref}} = \nu_{\text{ref}}$, the normalized LBD operator (3.96) is given by

$$\hat{C}_{\alpha\beta}\hat{f}_\alpha = \frac{\hat{\nu}_{\alpha\beta}}{\hat{B}^*_{||}} \left\{ \frac{\partial}{\partial \hat{v}_{||}} \left(\left(\hat{v}_{||} - \hat{u}_{\alpha\beta} \right) \hat{B}^*_{||} \hat{f}_\alpha + \frac{1}{2} \hat{T}_{\alpha\beta} \frac{\partial \hat{B}^*_{||} \hat{f}_\alpha}{\partial \hat{v}_{||}} \right) + \frac{\partial}{\partial \hat{\mu}} \left(2\hat{\mu} \hat{B}^*_{||} \hat{f}_\alpha + \frac{2\hat{T}_{\alpha\beta}}{\hat{B}} \hat{\mu} \frac{\partial \hat{B}^*_{||} \hat{f}_\alpha}{\partial \hat{\mu}} \right) \right\}. \tag{3.156}$$

3.3 Bhatnagar-Gross-Krook (BGK) Collision Operator

The collision operator introduced by Bhatnagar-Gross-Krook (BGK)[142] is an ad-hoc collision operator describing relaxation processes. It is given by

$$C_{\alpha\beta} = \nu_{\alpha\beta} \left(\mathcal{M}_{\alpha\beta} - f_\alpha \right). \tag{3.157}$$

This expression can be used in cylindrical velocity space with Maxwellians in Eq. (3.76). This collision operator models the relaxation of the distribution f_α to the Maxwellian $\mathcal{M}_{\alpha\beta}$. It completely neglects the velocity space structure of the distribution function (no derivatives), and thus the physics will be different from the Fokker-Planck type LBD operator. Nevertheless, it is simple in terms of complexity and thus of good use as a reference case. The exact physical implications are not entirely evident, and in a later section, this collision operator is compared to the LBD operator in a physics simulation.

The mixing quantities $\nu_{\alpha\beta}$, $u_{\alpha\beta}$, and $T_{\alpha\beta}$ are yet to be determined and do not necessarily have to be the same as for the LBD operator. The original reference did not contain mixing quantities but the moments of the single species distributions instead, which generally leads to violations in the conservation of density, momentum, and energy[142]. A version that conserves density was given in the same reference and later in, e.g., Refs. [144] and [141] improved versions have been constructed.

The "gyrokinetic" form that is used in this work is given by an ad-hoc approach

$$C_{\alpha\beta} = \nu_{\alpha\beta}\left(\frac{B}{B^*_{||}}\mathcal{M}_{\alpha\beta} - f_\alpha\right). \tag{3.158}$$

Since the BGK operator is introduced in an ad-hoc way and the gyrokinetic form of the Maxwellian is not trivially obtained, an ad-hoc version is used for the gyrokinetic version. This version makes sense in two ways. First, for $B^*_{||} = B$, it reduces to the standard version. Second, for example, the calculation of the momentum change can be considered,

$$\begin{aligned}\int B^*_{||} C_{\alpha\beta} f_\alpha v_{||} \mathrm{d}v_{||}\mathrm{d}\mu &= \nu_{\alpha\beta}\left(\int B\mathcal{M}_{\alpha\beta} v_{||}\mathrm{d}v_{||}\mathrm{d}\mu - \int B^*_{||} f_\alpha v_{||}\mathrm{d}v_{||}\mathrm{d}\mu\right), \\ &= \nu_{\alpha\beta}\left(m_\alpha n_\alpha u_{\alpha\beta} - m_\alpha n_\alpha u_\alpha\right).\end{aligned} \tag{3.159}$$

The factor $B/B^*_{||}$ cancels the Jacobian $B^*_{||}$ in the integration, which allows for the explicit evaluation of the integrals of the Maxwellian distribution.

The evaluation of the conservation properties is analogous to the LBD operator. Expressions for the mixing quantities were obtained in Ref. [141]. The mixing flow and temperature are the same as for the LBD operator,

$$u^{\mathrm{ET,BGK}}_{\alpha\beta} = u^{\mathrm{ET,LBD}}_{\alpha\beta}, \qquad T^{\mathrm{ET,BGK}}_{\alpha\beta} = T^{\mathrm{ET,LBD}}_{\alpha\beta}, \tag{3.160}$$

$$u^{\mathrm{EM,BGK}}_{\alpha\beta} = u^{\mathrm{EM,LBD}}_{\alpha\beta}, \qquad T^{\mathrm{EM,BGK}}_{\alpha\beta} = T^{\mathrm{EM,LBD}}_{\alpha\beta}. \tag{3.161}$$

The collision frequencies are almost the same, up to a factor of 2 in the ET version[58],

$$\nu^{\mathrm{ET,BGK}}_{\alpha\beta} = 2\nu^{\mathrm{ET,LBD}}_{\alpha\beta}, \qquad \nu^{\mathrm{EM,BGK}}_{\alpha\beta} = \nu^{\mathrm{EM,LBD}}_{\alpha\beta}. \tag{3.162}$$

The normalized BGK operator is,

$$\hat{C}_{\alpha\beta}\hat{f}_\alpha = \hat{\nu}_{\alpha\beta}\left(\frac{\hat{B}}{\hat{B}^*_{||}}\hat{\mathcal{M}}_{\alpha\beta} - \hat{f}_\alpha\right), \tag{3.163}$$

with normalized Maxwellian given by eq. (3.148), moments by eqs. (3.144)-(3.146). The normalization of the LBD collision rate given in (3.149) can be used in (3.162) to obtain normalized BGK collision rates.

3.4 Chapter Summary

This chapter provided the theoretical foundation for the kinetic treatment of Coulomb collision in a plasma. A literature review of the derivation of the Fokker-Planck collision operator and general properties was given. Further, the Lenard-Bernstein/Dougherty (LBD) collision operator was introduced, and a derivation from the Fokker-Planck Rosenbluth form has been presented. The LBD operator has been transformed to gyrocenter coordinates for use in the gyrokinetic code `GENE-X`. Particular choices for the model's parameters to account for the exact conservation of momentum and energy have been given. Relaxation rates to reproduce the momentum relaxation rate or approximate the temperature relaxation rate of the Boltzmann collision operator has been developed. Finally, a Bhatnagar-Gross-Krook (BGK) operator has been presented to be used as a reference to the LBD operator.

The choice of LBD parameters (mixing flow and temperature) and the relaxation rates was published in Ref. [58].

3.4.1 Relation to Other Work

The LBD collision operator is commonly used in gyrokinetic codes[58,104,133,148–150] as it provides an estimation of collisional effects with low complexity and computational costs. The full Fokker-Planck collision operator, either based on Rosenbluth potentials or the Landau formulation, is expensive, and thus only a few gyrokinetic codes implemented the full-f nonlinear version[151,152]. Due to the deficiencies of the LBD models that ultimately lead to a non-appropriate description of neoclassical transport, advanced model collision operators[139,153–156] are commonly considered. The influence of such models on plasma turbulence strongly depends on the case that is analysed[154–159]. The commonality of these advanced models is that they use a linearized collision operator, which neglects interactions between the perturbed parts of the distribution function. While the LBD model presented in this chapter initially only contains the equilibrium and test particle part, due to the introduction of a nonlinearity with the mixing flow and temperature, it can be considered advanced in that respect.

Chapter 4

Numerical Methods for Collision Operators

This chapter considers the numerical algorithms developed to include collisions into the gyrokinetic code `GENE-X`. First, the quadrature schemes used to evaluate velocity space moments of the distribution function are summarized. Second, the LBD collision operator is discretized with two different discretizations (finite difference and finite volume), which are compared within a verification study. Further, the time-stepping schemes and stability are analyzed. Finally, the high-performance implementation's intra- and inter-node performance benchmark is given. The finite volume discretization and the verification study have been published in Ref. [58].

Before considering the detailed numerics of collisions, the way of adding collisions to the existing algorithm to solve the gyrokinetic Vlasov equation must be examined. The (gyro-) kinetic equation written in general form is,

$$\frac{\mathrm{d}f}{\mathrm{d}t} = \left(\frac{\mathrm{d}f}{\mathrm{d}t}\right)_{\mathrm{Vlasov}} + \left(\frac{\mathrm{d}f}{\mathrm{d}t}\right)_{\mathrm{coll}}, \tag{4.1}$$

where the temporal change due to collisions is given by the collision operator introduced in the previous chapter. The equation is solved with the method of lines[160], which means first discretizing the time dimension and applying a time integrator of choice, e.g., Runge-Kutta 4 (RK4)[161]. Then, the right-hand side is discretized in (phase-) space to evaluate the stages in the time integrator required to advance the equation in time. The Vlasov part of the gyrokinetic equation is discretized using a finite difference method[34,62]. This chapter presents two different discretizations for the LBD collision operator. First, a finite difference method

using the same grid as the velocity space discretization of the Vlasov part. Second, a finite volume method using volume cells with cell centers at these grid points. As an introductory text into finite difference and finite volume methods, Ref. [162] can be considered.

4.1 Discretized Velocity Space Moments

The evaluation of the BGK and LBD collision operators requires the evaluation of velocity space moments (3.100)-(3.104) of the distribution function. These require integrating the distribution function over the two velocity space dimensions. These expressions are discretized on a regular grid (not necessarily uniform) of dimension $(N \times M)$ in $(v_{||}, \mu)$, where (i, j) denotes a grid point. Quantities defined on a grid are denoted by $f \to f(i, j)$. The discretized formulas for the integrals (also called quadrature[163]) is then given by,

$$M_{0,\alpha} = \sum_{i=1}^{N}\sum_{j=1}^{M} \Delta W(i,j) f_\alpha(i,j) B^*_{||}(i), \tag{4.2}$$

$$M_{1,\alpha} = \sum_{i=1}^{N}\sum_{j=1}^{M} \Delta W(i,j) v_{||}(i) f_\alpha(i,j) B^*_{||}(i), \tag{4.3}$$

$$M_{2,\perp,\alpha} = \sum_{i=1}^{N}\sum_{j=1}^{M} \Delta W(i,j) \mu(j) B f_\alpha(i,j) B^*_{||}(i), \tag{4.4}$$

$$M_{2,||,\alpha} = \sum_{i=1}^{N}\sum_{j=1}^{M} \Delta W(i,j) v^2_{||}(i) f_\alpha(i,j) B^*_{||}(i), \tag{4.5}$$

$$M_{2,\alpha} = \frac{1}{m_\alpha} M_{2,\perp,\alpha} + \frac{1}{2} M_{2,||,\alpha}. \tag{4.6}$$

Here, $\Delta W(i, j)$ are integration weights that depend on the quadrature method chosen. In `GENE-X`, open (midpoint) and closed (trapezoidal, Simpson) quadrature schemes are used (see Fig. 4.1) as well as Gauss (-Laguerre) quadrature[62]. The BGK operator has no restriction on the quadrature scheme and only requires a discretized representation of the moments at a grid point. Thus, Simpson Quadrature in $v_{||}$ and Gauss-Laguerre quadrature in μ are used. The LBD collision operator requires derivatives in μ, which makes Gauss-Laguerre quadrature unfavorable in that case. The finite difference version of the LBD operator (see section 4.2) uses a quadratic spacing in μ with trapezoidal weights and non-uniform spacing as well as Simpson quadrature in $v_{||}$. The finite volume version of the LBD operator (see section 4.3) requires a quadrature scheme that is the same as used in the construction of the discretization (midpoint). The Simpson and Gauss-Laguerre quadrature schemes are given in appendix A.

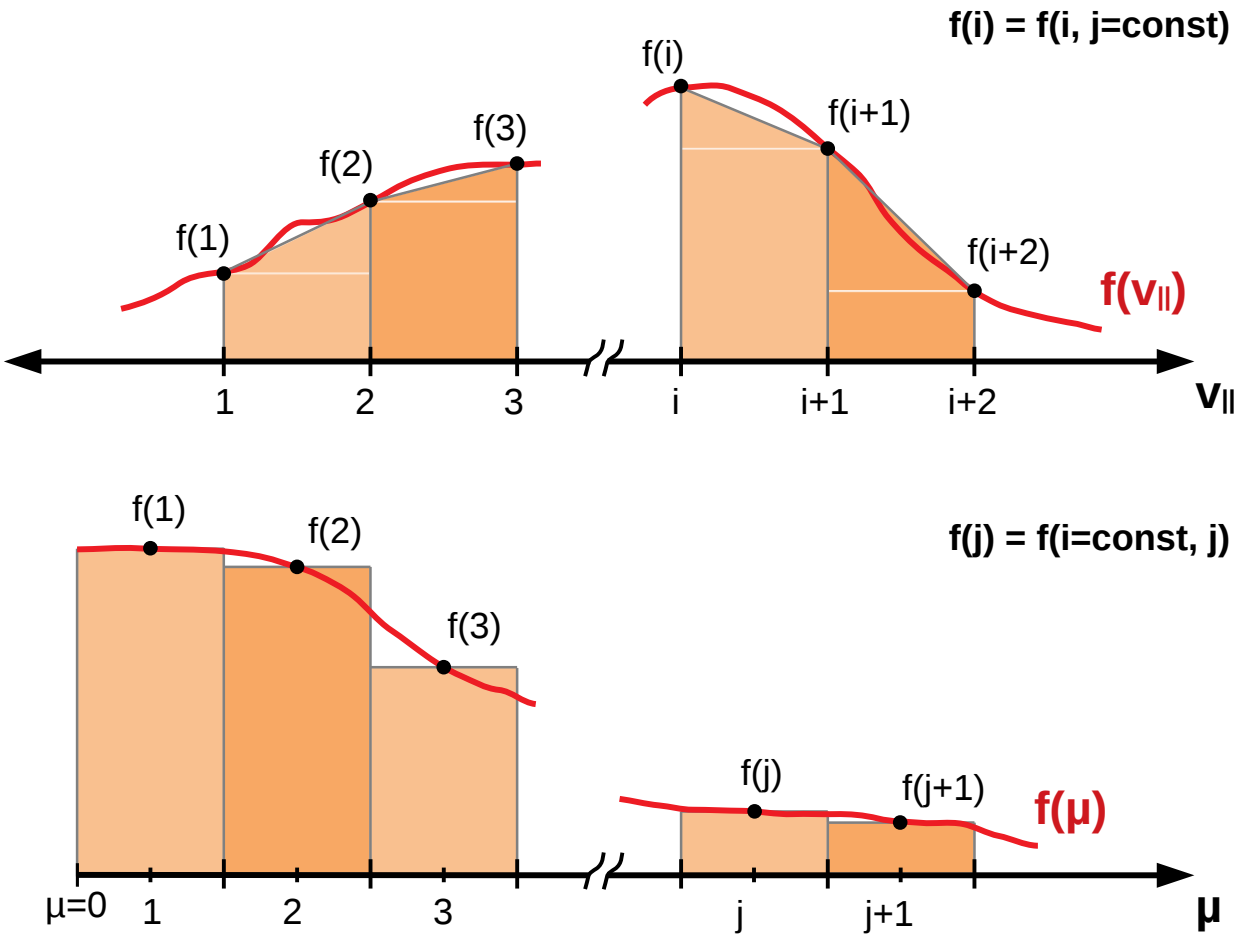

Figure 4.1. Schematic view of quadrature schemes. The top figure shows a closed (trapezoidal) scheme applied on a symmetric two-sided interval. The bottom figure shows an open (midpoint) scheme applied on a one-sided interval, additionally highlighting the need to shift the definition of the grid by half a grid spacing due to the $\mu = 0$ boundary. The wave-like symbol ≀ represents a cut in the axis. The choice of closed scheme for $v_{||}$ and open for μ is only exemplary.

4.1.1 Midpoint Quadrature

The midpoint quadrature method approximates the integral with boxes of width Δx and height of the function value in the center of the box[164],

$$\int_{x(i)-\Delta x/2}^{x(i)+\Delta x/2} f \mathrm{d}x \approx \Delta x f(i). \tag{4.7}$$

Figure 4.1 (lower part) shows the midpoint quadrature for integrating in μ. Due to the restriction of the lower domain boundary $\mu = 0$ in this dimension, the grid points have to be chosen to offset $\Delta\mu/2$ with respect to the lower domain boundary. There is no restriction on the grid points for the $v_{||}$ dimension.

Extended or composite midpoint formulas are given by applying the method on each grid point[164]. For the construction of the finite volume discretization of the LBD operator (section 4.3), the following discretizations of the velocity space moments (4.2)-(4.5) are used

$$M_{0,\alpha}^{\mathrm{midp}} = \Delta W \sum_{i=1}^{N}\sum_{j=1}^{M} f_\alpha(i,j) B_{||}^*(i), \tag{4.8}$$

$$M_{1,\alpha}^{\mathrm{midp}} = \Delta W \sum_{i=1}^{N}\sum_{j=1}^{M} v_{||}(i) f_\alpha(i,j) B_{||}^*(i), \tag{4.9}$$

$$M_{2,\perp,\alpha}^{\mathrm{midp}} = \Delta W \sum_{i=1}^{N}\sum_{j=1}^{M} \mu(j) B f_\alpha(i,j) B_{||}^*(i), \tag{4.10}$$

$$M_{2,||,\alpha}^{\mathrm{midp}} = \Delta W \sum_{i=1}^{N}\sum_{j=1}^{M} v_{||}^2(i) f_\alpha(i,j) B_{||}^*(i), . \tag{4.11}$$

4.1.2 Normalized Discrete Velocity Space Moments

The velocity space moments given in (4.2)-(4.6) are normalized as (see section 3.2.6 for details),

$$\begin{aligned} M_{0,\alpha} &= 2\pi v_{\text{th},\alpha}\frac{T_{\text{ref}}}{B_{\text{ref}}}\sum_{i=1}^{N}\sum_{j=1}^{M}\Delta\hat{v}_{||}(i)\Delta\hat{\mu}(j)\frac{n_{\text{ref}}B_{\text{ref}}}{v_{\text{th},\alpha}^3}\hat{f}_\alpha(i,j)\hat{B}_{||}^*(i), \\ &= n_{\text{ref}}m_\alpha\sum_{i=1}^{N}\sum_{j=1}^{M}\Delta\hat{W}(i,j)\hat{f}_\alpha(i,j)\hat{B}_{||}^*(i), \end{aligned} \tag{4.12}$$

$$\begin{aligned} M_{1,\alpha} &= 2\pi v_{\text{th},\alpha}\frac{T_{\text{ref}}}{B_{\text{ref}}}\sum_{i=1}^{N}\sum_{j=1}^{M}\Delta\hat{v}_{||}(i)\Delta\hat{\mu}(j)\frac{n_{\text{ref}}B_{\text{ref}}}{v_{\text{th},\alpha}^3}v_{\text{th},\alpha}\hat{f}_\alpha(i,j)\hat{B}_{||}^*(i)\hat{v}_{||}, \\ &= n_{\text{ref}}\sqrt{2T_{\text{ref}}m_\alpha}\sum_{i=1}^{N}\sum_{j=1}^{M}\Delta\hat{W}(i,j)\hat{f}_\alpha(i,j)\hat{B}_{||}^*(i), \end{aligned} \tag{4.13}$$

$$\begin{aligned} M_{2,\alpha} &= 2\pi v_{\text{th},\alpha}\frac{T_{\text{ref}}}{B_{\text{ref}}}\sum_{i=1}^{N}\sum_{j=1}^{M}\Delta\hat{v}_{||}(i)\Delta\hat{\mu}(j)\frac{n_{\text{ref}}B_{\text{ref}}}{v_{\text{th},\alpha}^3}\hat{f}_\alpha(i,j)\hat{B}_{||}^*(i)\left[\frac{1}{m_\alpha}B_{\text{ref}}\mu_{\text{ref}}\hat{\mu}(j)\hat{B}+\frac{1}{2}v_{\text{th},\alpha}^2\hat{v}_{||}^2(i)\right], \\ &= n_{\text{ref}}T_{\text{ref}}\sum_{i=1}^{N}\sum_{j=1}^{M}\Delta\hat{W}(i,j)\hat{f}_\alpha(i,j)\hat{B}_{||}^*(i)\left(\hat{\mu}(j)\hat{B}+\hat{v}_{||}^2(i)\right), \end{aligned} \tag{4.14}$$

where $\Delta\hat{W}(i,j) = \pi\Delta\hat{v}_{||}(i)\Delta\hat{\mu}(j)$. This normalization is independent of the quadrature scheme used. Summarizing,

$$M_{0,\alpha} = n_{\text{ref}}m_\alpha\hat{M}_{0,\alpha}, \tag{4.15}$$

$$M_{1,\alpha} = 2n_{\text{ref}}T_{\text{ref}}v_{\text{th},\alpha}^{-1}\hat{M}_{1,\alpha}, \tag{4.16}$$

$$M_{2\perp,\alpha} = n_{\text{ref}}T_{\text{ref}}m_\alpha\hat{M}_{2\perp,\alpha}, \tag{4.17}$$

$$M_{2||,\alpha} = 2n_{\text{ref}}T_{\text{ref}}\hat{M}_{2||,\alpha}, \tag{4.18}$$

$$M_{2,\alpha} = n_{\text{ref}}T_{\text{ref}}\hat{M}_{2,\alpha}. \tag{4.19}$$

4.2 LBD - Finite Difference Discretization

The finite difference method provides the simplest discretization for the LBD collision operator (3.96). A grid first discretizes the computational domain, and discrete approximations replace derivatives in the operator. However, it is not entirely trivial because the magnetic moment is only defined on the positive half-axis $\mu \in [0, \infty)$. This implication will be discussed later in this section.

First, rewrite the LBD collision operator (3.96) by applying the product rule on the inner

derivatives,

$$C_{\alpha\beta}f_\alpha = \nu_{\alpha\beta}\Bigg\{\frac{1}{B^*_{||}}\frac{\partial}{\partial v_{||}}\left(\left(v_{||}-u_{\alpha\beta}\right)f_\alpha B^*_{||}+\frac{1}{2}v^2_{\mathrm{th},\alpha\beta}B^*_{||}\frac{\partial f_\alpha}{\partial v_{||}}+\frac{1}{2}v^2_{\mathrm{th},\alpha\beta}f_{\alpha\beta}(B^*_{||})'\right) + \frac{\partial}{\partial\mu}\left(2\mu f_\alpha+\frac{m_\alpha v^2_{\mathrm{th},\alpha\beta}}{B}\mu\frac{\partial f_\alpha}{\partial\mu}\right)\Bigg\}, \tag{4.20}$$

where

$$(B^*_{||})' \equiv \frac{\partial B^*_{||}}{\partial v_{||}} = \frac{m_\alpha c}{q_\alpha}\mathbf{b}\cdot(\nabla\times\mathbf{b}). \tag{4.21}$$

Further expanding the parallel terms,

$$C_{||} \equiv f_\alpha + \left(v_{||}-u_{\alpha\beta}\right)\frac{\partial f_\alpha}{\partial v_{||}}+\frac{1}{2}v^2_{\mathrm{th},\alpha\beta}\frac{\partial^2 f_\alpha}{\partial v^2_{||}}+\left(\left(v_{||}-u_{\alpha\beta}\right)f_\alpha+v^2_{\mathrm{th},\alpha\beta}\frac{\partial f_\alpha}{\partial v_{||}}\right)\frac{(B^*_{||})'}{B^*_{||}}, \tag{4.22}$$

and the perpendicular terms,

$$C_\mu \equiv 2f_\alpha+\left(2\mu+\frac{m_\alpha v^2_{\mathrm{th},\alpha\beta}}{B}\right)\frac{\partial f_\alpha}{\partial\mu}+\frac{m_\alpha v^2_{\mathrm{th},\alpha\beta}}{B}\mu\frac{\partial^2 f_\alpha}{\partial\mu^2}. \tag{4.23}$$

Collecting both results in

$$C_{\alpha\beta}f_\alpha = \nu_{\alpha\beta}\Bigg\{3f_\alpha+\left(v_{||}-u_{\alpha\beta}\right)\frac{\partial f_\alpha}{\partial v_{||}}+\frac{1}{2}v^2_{\mathrm{th},\alpha\beta}\frac{\partial^2 f_\alpha}{\partial v^2_{||}}+\left(\left(v_{||}-u_{\alpha\beta}\right)f_\alpha+v^2_{\mathrm{th},\alpha\beta}\frac{\partial f_\alpha}{\partial v_{||}}\right)\frac{(B^*_{||})'}{B^*_{||}} + 2\left(\mu+\frac{m_\alpha v^2_{\mathrm{th},\alpha\beta}}{B}\right)\frac{\partial f_\alpha}{\partial\mu}+\frac{m_\alpha v^2_{\mathrm{th},\alpha\beta}}{B}\mu\frac{\partial^2 f_\alpha}{\partial\mu^2}\Bigg\}. \tag{4.24}$$

This version can now be discretized by replacing the continuous distribution function and its derivative with discrete approximations.

4.2.1 Construction of the Finite Difference Scheme

Now the velocity space can be discretized, introducing a regular two-dimensional grid of size $N_{||} \times N_\mu$. The spacing is given by

$$\Delta v_{||} = \frac{v_{||,\max} - v_{||,\min}}{N_{||}} = \frac{2v_{||,\max}}{N_{||}}, \tag{4.25}$$

$$\Delta \mu = \frac{\mu_{\max} - \mu_{\min}}{N_\mu} = \frac{\mu_{\max}}{N_\mu}, \tag{4.26}$$

where the grid boundaries are defined symmetric in parallel velocity, i.e., $v_{||,\min} = -v_{||,\max}$ and asymmetric in magnetic moment with $\mu_{\min} = 0$. Outside the so-called inner grid, a ghost grid is defined to avoid modifying the stencil of the finite difference scheme on the boundaries. The ghost grid has $N_{\text{ghost},||}$ points on both boundaries of the $v_{||}$ dimension, and $N_{\text{ghost},\mu}$ only on the positive μ dimension. It does not make sense to define negative ghosts in μ since $\mu \sim v_\perp^2$ is not defined there. Thus, the stencil will be adjusted close to the $\mu = 0$ boundary. Dirichlet boundary conditions with $f_\alpha = 0$ are employed on all ghost points since the distribution function is supposed to fall off to zero at infinity. One has to be careful when using the collision operator. The box must be chosen large enough to not introduce too much error due to large values of f_α at the boundaries. A visual representation of the velocity space grid used in the finite difference implementation is given in Fig. 4.2.

4.2.2 Finite Difference Stencils for the LBD Operator

This section contains two different finite difference stencils, one for a second-order method and one for a fourth-order method.

Second-Order Scheme

This scheme is based on ordinary second-order central difference stencils for the $v_{||}$ and μ derivatives. At the $\mu = 0$ ($j = 1$) plane, no ghost point exists on the lower μ boundary. Thus a second-order forward difference stencil is used. This choice in the stencil reflects the physics that no negative magnetic moment exists since it is the square of the perpendicular velocity magnitude $\mu \sim v_\perp^2$. The second-order finite difference discretization is given by the parallel parts

$$\left.\frac{\partial f_\alpha}{\partial v_{||}}\right|_{i,j} = \frac{1}{\Delta v_{||}} \left(-\frac{1}{2} f_\alpha(i-1,j) + \frac{1}{2} f_\alpha(i+1,j) \right), \tag{4.27}$$

$$\left.\frac{\partial^2 f_\alpha}{\partial v_{||}^2}\right|_{i,j} = \frac{1}{(\Delta v_{||})^2} \left(f_\alpha(i-1,j) - 2f_\alpha(i,j) + f_\alpha(i+1,j) \right), \tag{4.28}$$

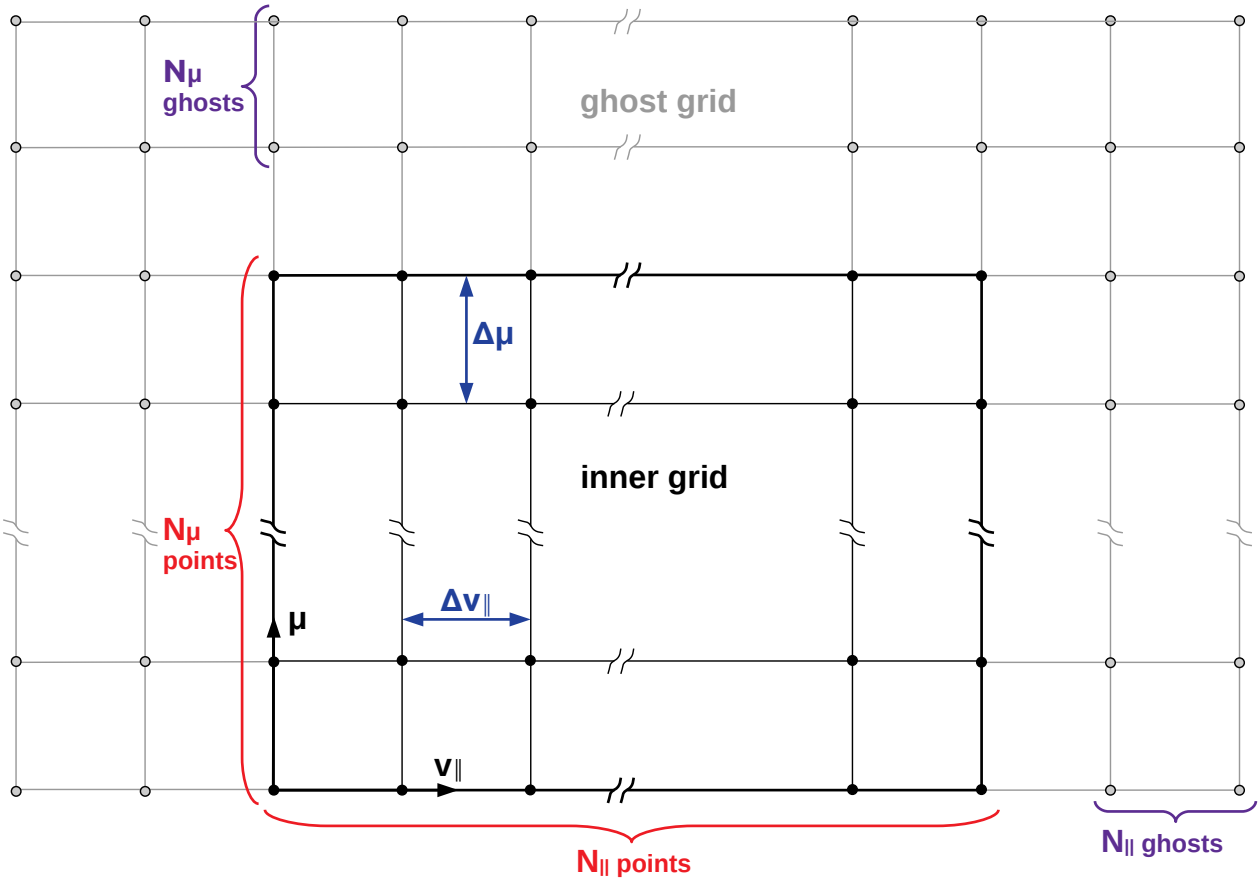

Figure 4.2. Representation of the velocity space grid used for the finite difference implementation. Only the outer parts of the grid are shown. The inner continuation is indicated by the wave-like symbol ∾.

and the perpendicular parts

$$\left.\frac{\partial f_\alpha}{\partial \mu}\right|_{i,j} = \frac{1}{\Delta\mu}\begin{cases} -\frac{3}{2}f_\alpha(i,j) + 2f_\alpha(i,j+1) - \frac{1}{2}f_\alpha(i,j+2), & j=1, \\ -\frac{1}{2}f_\alpha(i,j-1) + \frac{1}{2}f_\alpha(i,j+1), & j>1, \end{cases} \tag{4.29}$$

$$\left.\frac{\partial^2 f_\alpha}{\partial \mu^2}\right|_{i,j} = \frac{1}{(\Delta\mu)^2}\begin{cases} 2f_\alpha(i,j) - 5f_\alpha(i,j+1) + 4f_\alpha(i,j+2) - f_\alpha(i,j+3), & j=1, \\ f_\alpha(i,j-1) - 2f_\alpha(i,j) + f_\alpha(i,j+1), & j>1. \end{cases} \tag{4.30}$$

Fourth-Order Scheme

This scheme is based on a central difference stencil as well. Here, the first and second μ planes ($j = 1, 2$) need special treatment due to the absence of ghost points. A fourth-order forward difference scheme is used for the first plane, and a mixed stencil with one previous and three next points for the second plane. The coefficients are constructed with the method summarized in appendix B. It is given by,

$$\left.\frac{\partial f_\alpha}{\partial v_{||}}\right|_{i,j} = \frac{1}{\Delta v_{||}}\left(\frac{1}{12}f_\alpha(i-2,j) - \frac{2}{3}f_\alpha(i-1,j) + \frac{2}{3}f_\alpha(i+1,j) - \frac{1}{12}f_\alpha(i+2,j)\right), \tag{4.31}$$

$$\left.\frac{\partial^2 f_\alpha}{\partial v_{||}^2}\right|_{i,j} = \frac{1}{(\Delta v_{||})^2}\Bigg(-\frac{1}{12}f_\alpha(i-2,j) + \frac{4}{3}f_\alpha(i-1,j) - \frac{5}{2}f_\alpha(i,j) + \frac{4}{3}f_\alpha(i+1,j) - \frac{1}{12}f_\alpha(i+2,j)\Bigg), \tag{4.32}$$

$$\left.\frac{\partial f_\alpha}{\partial \mu}\right|_{i,j} = \frac{1}{\Delta\mu}\begin{cases} -\frac{25}{12}f_\alpha(i,j) + 4f_\alpha(i,j+1) - 3f_\alpha(i,j+2) \\ \qquad +\frac{4}{3}f_\alpha(i,j+3) - \frac{1}{4}f_\alpha(i,j+4), & j=1, \\ -\frac{1}{4}f_\alpha(i,j-1) - \frac{5}{6}f_\alpha(i,j) + \frac{3}{2}f_\alpha(i,j+1) \\ \qquad -\frac{1}{2}f_\alpha(i,j+2) + \frac{1}{12}f_\alpha(i,j+3), & j=2, \\ \frac{1}{12}f_\alpha(i,j-2) - \frac{2}{3}f_\alpha(i,j-1) + \frac{2}{3}f_\alpha(i,j+1) \\ \qquad -\frac{1}{12}f_\alpha(i,j+2), & j>2, \end{cases} \tag{4.33}$$

$$\left.\frac{\partial^2 f_\alpha}{\partial \mu^2}\right|_{i,j} = \frac{1}{(\Delta\mu)^2}\begin{cases} +\frac{15}{4}f_\alpha(i,j) - \frac{77}{6}f_\alpha(i,j+1) + \frac{107}{6}f_\alpha(i,j+2) - 13f_\alpha(i,j+3) \\ \qquad +\frac{61}{12}f_\alpha(i,j+4) - \frac{5}{6}f_\alpha(i,j+5), & j=1, \\ +\frac{5}{6}f_\alpha(i,j-1) - \frac{5}{4}f_\alpha(i,j) - \frac{1}{3}f_\alpha(i,j+1) + \frac{7}{6}f_\alpha(i,j+2) \\ \qquad -\frac{1}{2}f_\alpha(i,j+3) + \frac{1}{12}f_\alpha(i,j+4), & j=2, \\ -\frac{1}{12}f_\alpha(i,j-2) + \frac{4}{3}f_\alpha(i,j-1) - \frac{5}{2}f_\alpha(i,j) + \frac{4}{3}f_\alpha(i,j+1) \\ \qquad -\frac{1}{12}f_\alpha(i,j+2), & j>2. \end{cases} \tag{4.34}$$

4.2.3 Normalized Discrete Finite Difference Version

The normalized version of the expanded LBD operator is given by,

$$\hat{C}_{\alpha\beta}\hat{f}_\alpha = \hat{\nu}_{\alpha\beta}\Bigg\{3\hat{f}_\alpha + (\hat{v}_{||}-\hat{u}_{\alpha\beta})\frac{\partial\hat{f}_\alpha}{\partial\hat{v}_{||}} + \frac{1}{2}\hat{T}_{\alpha\beta}\frac{\partial^2\hat{f}_\alpha}{\partial\hat{v}_{||}^2} + \left((\hat{v}_{||}-\hat{u}_{\alpha\beta})\hat{f}_\alpha + \hat{T}_{\alpha\beta}\frac{\partial\hat{f}_\alpha}{\partial\hat{v}_{||}}\right)\frac{(\hat{B}^*_{||})'}{\hat{B}^*_{||}} + 2\left(\hat{\mu}+\frac{\hat{T}_{\alpha\beta}}{\hat{B}}\right)\frac{\partial\hat{f}_\alpha}{\partial\hat{\mu}} + 2\frac{\hat{T}_{\alpha\beta}}{\hat{B}}\hat{\mu}\frac{\partial^2\hat{f}_\alpha}{\partial\hat{\mu}^2}\Bigg\}. \tag{4.35}$$

with normalized Jacobian given in eq. (3.147) and

$$(\hat{B}^*_{||})' = \frac{\sqrt{2\hat{m}_\alpha}\rho_{\text{ref}}}{\hat{q}_\alpha L_{\text{ref}}}\mathbf{b}\cdot(\nabla\times\mathbf{b}). \tag{4.36}$$

Expressions of the finite difference coefficients (4.27)-(4.30) or (4.31)-(4.34) can be readily used with the normalized distribution function $\hat{f}_\alpha$.

4.3 LBD - Finite Volume Discretization

The idea to create a finite volume version of the LBD operator originated from initial numerical experiments on the conservation properties of the finite difference version. The finite difference version, while correctly showing a second/fourth order convergence on the conservation of density, momentum, and energy, led to significant absolute errors on grid sizes $(N_{||}\times N_\mu)\sim(64\times 64)$[58]. In applying the collision operators over several thousands of time steps, the simulations experienced a significant loss in density, momentum, and energy, followed by numerical instabilities. To not use a higher resolved velocity space (which would also slow down the Vlasov part in the simulation), the approach was to create a conservative discretization that can be run with limited velocity space resolution. In this section, the basic finite volume scheme is constructed. Conservative corrections are developed so that single species density, total momentum, and energy are conserved up to machine precision. This section presents a more detailed derivation of the discretization published in Ref. [58].

4.3.1 Construction of the Finite Volume Scheme

Constructing the finite volume scheme is based on considering the integral of the collision operator over a test volume W in velocity space

$$\int_W B^*_{||}\left(\frac{\mathrm{d}f_\alpha}{\mathrm{d}t}\right)_{\text{coll}}\mathrm{d}W = \int_W B^*_{||}\sum_\beta C_{\alpha\beta}f_\alpha\mathrm{d}W = \sum_\beta\int_W B^*_{||}\frac{1}{B^*_{||}}\nabla\cdot\mathbf{J}_{\alpha\beta}\,\mathrm{d}W = \sum_\beta\oint_{\partial W}\mathbf{J}_{\alpha\beta}\cdot\mathbf{n}\,\mathrm{d}\partial W, \tag{4.37}$$

where ∂W is the boundary of W and $B^*_{||}$ is the Jacobian. Gauss' theorem was used to rewrite the volume integral in terms of a surface integral in the last step, where $\mathbf{n}$ is the surface normal of the volume cell enclosing boundary, and the divergence formulation of the collision operator is given in eq. (3.17).

In restricting the volume W to a rectangular shape, the closed surface integral can be split into four parts ∂W_k with $k = 1...4$,

$$\oint_{\partial W} \mathbf{J} \cdot \mathbf{n} \, \mathrm{d}\partial W = \sum_{k=1}^{4} \int_{\partial W_k} \mathbf{J} \cdot \mathbf{n}_k \, \mathrm{d}\partial W_k, \tag{4.38}$$

$$\begin{aligned} &= 2\pi \Bigg[\int_{\min_W(v_{||})}^{\max_W(v_{||})} \mathrm{d}v_{||}(-J_\mu)\Big|_{\min_W(\mu)} + \int_{\min_W(\mu)}^{\max_W(\mu)} \mathrm{d}\mu J_{||}\Big|_{\max_W(v_{||})} \\ &\quad + \int_{\max_W(v_{||})}^{\min_W(v_{||})} \mathrm{d}v_{||} J_\mu \Big|_{\max_W(\mu)} + \int_{\max_W(\mu)}^{\min_W(\mu)} \mathrm{d}\mu(-J_{||})\Big|_{\min_W(v_{||})} \Bigg]. \end{aligned} \tag{4.39}$$

Here J_μ and $J_{||}$ are the parallel and perpendicular velocity components of $\mathbf{J}$ and the functions $\min_W$ and $\max_W$ yield the minima and maxima of $v_{||}$ and μ in W, defining the boundaries of the rectangular test volume. The species indices are suppressed for simplicity. So far, no discretization has been applied. This expression is exact and relates the volume integral of the collision operator with the surface integral of its collisional fluxes. The factor 2π originates from the volume element $\mathrm{d}W = 2\pi \mathrm{d}v_{||}\mathrm{d}\mu$. The volume integral can be considered a three-dimensional integral in velocity space, where the gyroangle integration (third coordinate) is trivial.

In the next step, a discretization in velocity space is introduced. It covers the whole domain with rectangular cells of finite volume centered around the grid points given by the spatial discretization of the Vlasov part. The grid is chosen to cover the whole velocity space without holes, and boundary conditions at the domain boundaries will be given. The points of the finite difference grid are denoted by (i, j) where $i = 1...N$ is the index of the parallel coordinate $v_{||}$ and $j = 1...M$ is the index of the perpendicular coordinate μ. Since the velocity space cells are centered around these grid points, the cells can also be labeled with the indices (i, j). The boundaries of the cells lie at $(i, j \pm \frac{1}{2})$ and $(i \pm \frac{1}{2}, j)$ with $(i \pm \frac{1}{2}, j \pm \frac{1}{2})$ denoting the 4 corners. The volume element of each cell is denoted as $\Delta W = 2\pi \Delta v_{||} \Delta\mu$, which is constant for a uniform grid. Fig. 4.3 visually represents the discretization.

Since a relation between the volume-integrated collision operator and the surface integrals of its' collisional fluxes has been established on a rectangular grid, this can be directly applied in the discretized space just introduced. The discretization is constructed by discretizing the

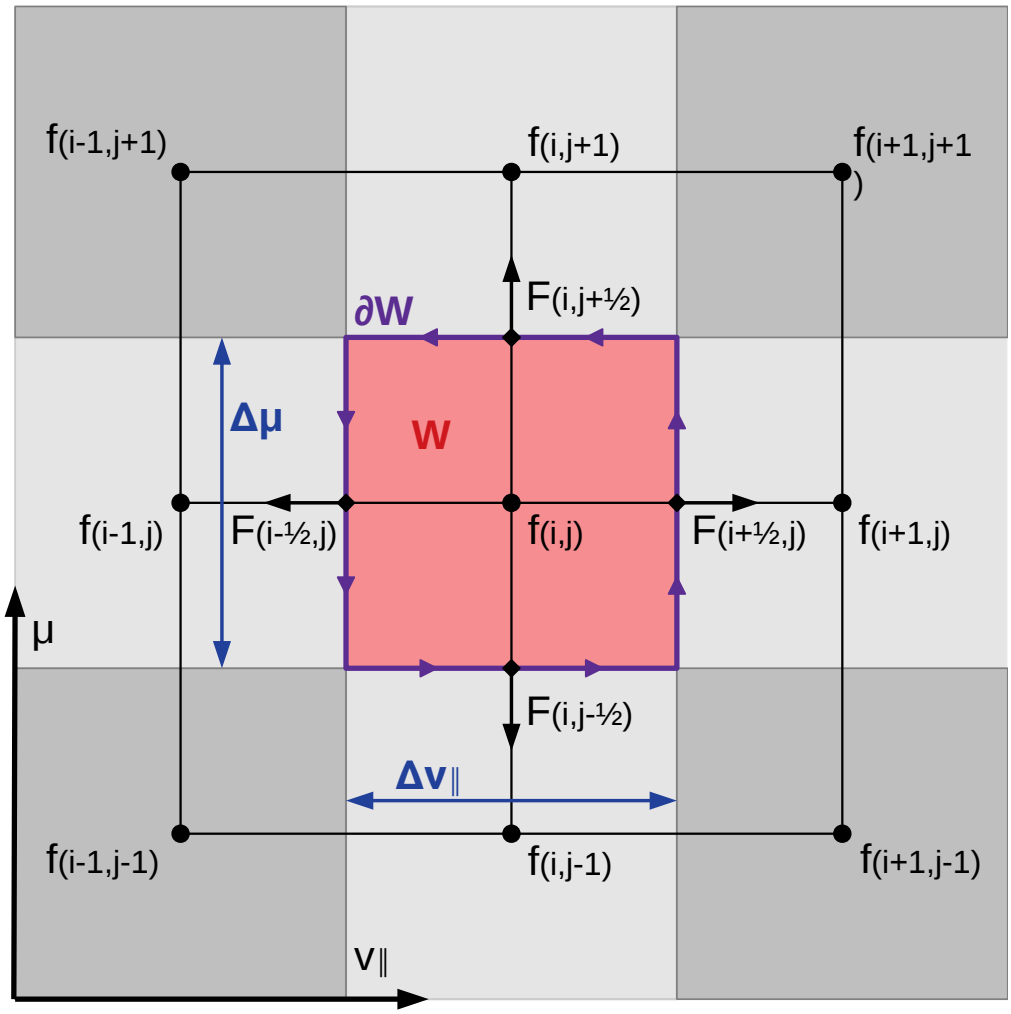

Figure 4.3. Velocity space grid and the definition of fluxes and volumes for the finite volume discretization of the LBD collision operator. In the center, a particular cell is shown, which is used to construct the finite volume discretization. Taken from Ref. [58].

volume and surface integrals of the collision operator above. In second-order the midpoint rule (see section 4.1.1) can be used,

$$\int_{W(i,j)} Q\mathrm{d}W \approx Q(i,j)\Delta W, \tag{4.40}$$

$$\int_{\min_W(v_{||})}^{\max_W(v_{||})} Q\mathrm{d}v_{||} \approx Q(i,j\pm\frac{1}{2})\Delta v_{||}, \tag{4.41}$$

$$\int_{\min_W(\mu)}^{\max_W(\mu)} Q\mathrm{d}\mu \approx Q(i\pm\frac{1}{2},j)\Delta \mu, \tag{4.42}$$

where Q is a function, and the sign $\pm$ depends on which surface is integrated. The boundary integrals involve knowledge of the function Q at the volume cell boundaries. These points form a grid themselves, often called the staggered grid. Values of the function Q are generally known on the actual grid $Q(i,j)$. Thus the values on the staggered grid can be obtained via interpolation. Since the discretization of the integrals is second-order, it is sufficient to consider a second-order interpolation given by

$$Q(i\pm\frac{1}{2},j) \approx \frac{1}{2}\Big(Q(i,j)+Q(i\pm1,j)\Big), \tag{4.43}$$

$$Q(i,j\pm\frac{1}{2}) \approx \frac{1}{2}\Big(Q(i,j)+Q(i,j\pm1)\Big), \tag{4.44}$$

$$\left.\frac{\partial Q}{\partial v_{||}}\right|_{i,j\pm\frac{1}{2}} \approx \frac{1}{\Delta v_{||}}\Big(\pm Q(i,j\pm1)\mp Q(i,j)\Big), \tag{4.45}$$

$$\left.\frac{\partial Q}{\partial \mu}\right|_{i,j\pm\frac{1}{2}} \approx \frac{1}{\Delta \mu}\Big(\pm Q(i,j\pm1)\mp Q(i,j)\Big). \tag{4.46}$$

Applying the second-order midpoint rule (4.40) to the left-hand side of the collision operator (4.37),

$$\int_{W(i,j)} B^*_{||}C_{\alpha\beta}f_\alpha \mathrm{d}W \approx B^*_{||}(i)\Big(C_{\alpha\beta}f_\alpha\Big)(i,j)\Delta W, \tag{4.47}$$

yields an explicit expression of the discretized collision operator evaluated at the cell center (i.e., the finite difference grid of the spatial discretization of the Vlasov part),

$$\Big(C_{\alpha\beta}f_\alpha\Big)(i,j) \approx \frac{1}{\Delta W B^*_{||}(i)}\oint_{\partial W(i,j)} \mathbf{J}_{\alpha\beta}\cdot\mathbf{n}\,\mathrm{d}\partial W. \tag{4.48}$$

On the right-hand side of this expression, the surface integral (4.39) can now be approximated

using the second-order midpoint rule (4.41)-(4.42),

$$\oint_{\partial W(i,j)} \mathbf{J}_{\alpha\beta}\cdot\mathbf{n}\,\mathrm{d}\partial W \approx 2\pi\Bigg[-\Delta v_{||}J_{\mu,\alpha\beta}(i,j-\frac{1}{2})+\Delta\mu J_{||,\alpha\beta}(i+\frac{1}{2},j) + \Delta v_{||}J_{\mu,\alpha\beta}(i,j+\frac{1}{2})-\Delta\mu J_{||,\alpha\beta}(i-\frac{1}{2},j)\Bigg]. \tag{4.49}$$

Inserting this into (4.48) yields,

$$(C_{\alpha\beta}f_\alpha)(i,j) = \frac{1}{B^*_{||}(i)}\Bigg[\frac{1}{\Delta v_{||}}\Big(J_{||,\alpha\beta}(i+\frac{1}{2},j)-J_{||,\alpha\beta}(i-\frac{1}{2},j)\Big) + \frac{1}{\Delta\mu}\Big(J_{\mu,\alpha\beta}(i,j+\frac{1}{2})-J_{\mu,\alpha\beta}(i,j-\frac{1}{2})\Big)\Bigg]. \tag{4.50}$$

The square bracket can be viewed as a direct discretization of the divergence operator, as obtained in Ref. [152].

The fluxes need to be evaluated at the staggered grid points $v_{||}(i\pm\frac{1}{2})$ and $\mu(j\pm\frac{1}{2})$. Given by eqs. (3.98) and (3.99)*,

$$J_{||,\alpha\beta}(i\pm\frac{1}{2},j) = \nu_{\alpha\beta}\left\{\Big(v_{||}(i\pm\frac{1}{2})-u_{\alpha\beta}\Big)\,f_\alpha(i\pm\frac{1}{2},j)\,B^*_{||}(i\pm\frac{1}{2})+\frac{T_{\alpha\beta}}{m_\alpha}\frac{\partial f_\alpha B^*_{||}}{\partial v_{||}}\bigg|_{i\pm\frac{1}{2},j}\right\}, \tag{4.51}$$

$$J_{\mu,\alpha\beta}(i,j\pm\frac{1}{2}) = \nu_{\alpha\beta}\left\{2\mu(j\pm\frac{1}{2})f_\alpha(i,j\pm\frac{1}{2})\,B^*_{||}(i)+\frac{2T_{\alpha\beta}}{B}\mu(j\pm\frac{1}{2})\frac{\partial f_\alpha B^*_{||}}{\partial\mu}\bigg|_{i,j\pm\frac{1}{2}}\right\}. \tag{4.52}$$

Eqs. (4.43)-(4.46) give the interpolated distribution function and its derivative,

$$f_\alpha(i\pm\frac{1}{2},j) = \frac{1}{2}\Big(f_\alpha(i,j)+f_\alpha(i\pm1,j)\Big), \tag{4.53}$$

$$f_\alpha(i,j\pm\frac{1}{2}) = \frac{1}{2}\Big(f_\alpha(i,j)+f_\alpha(i,j\pm1)\Big), \tag{4.54}$$

$$\frac{\partial f_\alpha B^*_{||}}{\partial v_{||}}\bigg|_{i\pm\frac{1}{2},j} = \frac{1}{\Delta v_{||}}\Big(\pm f_\alpha(i\pm1,j)B^*_{||}(i\pm1)\mp f_\alpha(i,j)B^*_{||}(i)\Big), \tag{4.55}$$

$$\frac{\partial f_\alpha}{\partial\mu}\bigg|_{i,j\pm\frac{1}{2}} = \frac{1}{\Delta\mu}\Big(\pm f_\alpha(i,j\pm1)\mp f_\alpha(i,j)\Big). \tag{4.56}$$

*The collision frequencies $\nu_{\alpha\beta}$ have been shifted into $J_{\alpha\beta}$ in this section.

To complete the discretization, boundary conditions must be imposed at the velocity space domain boundaries. A natural choice is zero flux boundary conditions,

$$J_{||,\alpha\beta}(\frac{1}{2},j) = J_{||,\alpha\beta}(N+\frac{1}{2},j) = J_{\mu,\alpha\beta}(i,\frac{1}{2}) = J_{\mu,\alpha\beta}(i,M+\frac{1}{2}) = 0, \tag{4.57}$$

since these will automatically ensure the density conservation of the system (see next section).

4.3.2 Conservation Properties of the Finite Volume Discretization

This section analyzes the conservation properties of the previously developed finite volume discretization. The discretization errors are analyzed and quantified. The development of correction terms based on re-formulating the mixing quantities $u_{\alpha\beta}$ and $T_{\alpha\beta}$ ensures the exact conservation of density, momentum, and energy.

Ref. [152] gives an elegant way to consider the discretized collision operator's conservation properties. A summary of the following derivation can be found in Appendix A of Ref. [58]. The discretized volume integral of a test function ϕ times the collision operator is

$$\sum_{i=1}^{N}\sum_{j=1}^{M}\Delta W\phi(i,j)(\nabla\cdot\mathbf{J}_{\alpha\beta})(i,j) = \sum_{i=1}^{N}\sum_{j=1}^{M}\Delta W\phi(i,j)\left[\frac{1}{\Delta\mu}\left(J_{\mu,\alpha\beta}(i,j+\frac{1}{2}) - J_{\mu,\alpha\beta}(i,j-\frac{1}{2})\right)\right.$$
$$\left. + \frac{1}{\Delta v_{||}}\left(J_{||,\alpha\beta}(i+\frac{1}{2},j) - J_{||,\alpha\beta}(i-\frac{1}{2},j)\right)\right]. \tag{4.58}$$

Applying the boundary conditions (4.57) splits the right-hand side of the expression into four different sums,

$$\Delta W\left\{\frac{1}{\Delta\mu}\sum_{i=1}^{N}\sum_{j=1}^{M-1}\phi(i,j)J_{\mu,\alpha\beta}(i,j+\frac{1}{2}) + \frac{1}{\Delta v_{||}}\sum_{i=1}^{N-1}\sum_{j=1}^{M}\phi(i,j)J_{||,\alpha\beta}(i+\frac{1}{2},j)\right.$$
$$\left. - \frac{1}{\Delta\mu}\sum_{i=1}^{N}\sum_{j=2}^{M}\phi(i,j)J_{\mu,\alpha\beta}(i,j-\frac{1}{2}) - \frac{1}{\Delta v_{||}}\sum_{i=2}^{N}\sum_{j=1}^{M}\phi(i,j)J_{||,\alpha\beta}(i-\frac{1}{2},j)\right\}. \tag{4.59}$$

A re-indexing of the last two sums can be performed, i.e., $j\to j+1$ and $i\to i+1$, respectively

$$\sum_{i=1}^{N}\sum_{j=2}^{M}\phi(i,j)J_{\mu,\alpha\beta}(i,j-\frac{1}{2}) = \sum_{i=1}^{N}\sum_{j=1}^{M-1}\phi(i,j+1)J_{\mu,\alpha\beta}(i,j+\frac{1}{2}), \tag{4.60}$$

$$\sum_{i=2}^{N}\sum_{j=1}^{M}\phi(i,j)J_{||,\alpha\beta}(i-\frac{1}{2},j) = \sum_{i=1}^{N-1}\sum_{j=1}^{M}\phi(i+1,j)J_{||,\alpha\beta}(i+\frac{1}{2},j). \tag{4.61}$$

Applying the re-indexing and consolidating the sums over the same ranges yields

$$\Delta W\left\{\sum_{i=1}^{N}\sum_{j=1}^{M-1} J_{\mu,\alpha\beta}(i,j+\frac{1}{2})\frac{\phi(i,j)-\phi(i,j+1)}{\Delta\mu}+\sum_{i=1}^{N-1}\sum_{j=1}^{M} J_{||,\alpha\beta}(i+\frac{1}{2},j)\frac{\phi(i,j)-\phi(i+1,j)}{\Delta v_{||}}\right\}. \tag{4.62}$$

Using eqs. (4.45)-(4.46) the final result is

$$\sum_{i=1}^{N}\sum_{j=1}^{M}\Delta W\phi(i,j)(\nabla\cdot\mathbf{J}_{\alpha\beta})(i,j)=-\Delta W\left\{\sum_{i=1}^{N}\sum_{j=1}^{M-1} J_{\mu,\alpha\beta}(i,j+\frac{1}{2})\frac{\partial\phi}{\partial\mu}\bigg|_{i,j+\frac{1}{2}}+\sum_{i=1}^{N-1}\sum_{j=1}^{M} J_{||,\alpha\beta}(i+\frac{1}{2},j)\frac{\partial\phi}{\partial v_{||}}\bigg|_{i+\frac{1}{2},j}\right\}. \tag{4.63}$$

In other words, the discretization conserves the properties of integration by parts. This property is very convenient since calculating the density, momentum, and energy change of applying the collision operator requires operations given by eq. (4.58), where the test function is replaced by $\phi_\alpha = 1$, $\phi_\alpha = m_\alpha v_{||}$ or $\phi_\alpha = \frac{1}{2}m_\alpha v_{||}^2 + \mu B$.

Density Conservation

The conservation of single particle density is trivial for the discretization constructed. Given eq. (4.63), one has to use $\phi_\alpha = 1$ which derivatives with respect to $v_{||}$ and μ are both zero. Thus, the collision operator conserves single-particle density on the discrete level

$$\sum_{i=1}^{N}\sum_{j=1}^{M}\Delta W(\nabla\cdot\mathbf{J}_{\alpha\beta})(i,j)=0. \tag{4.64}$$

Momentum Change

To calculate the single species momentum change, $\phi_\alpha = m_\alpha v_{||}$ is used, which results in

$$P_{\alpha\beta}\equiv\sum_{i=1}^{N}\sum_{j=1}^{M}\Delta W m_\alpha v_{||}(i)(\nabla\cdot\mathbf{J}_{\alpha\beta})(i,j)=-\Delta W m_\alpha\sum_{i=1}^{N-1}\sum_{j=1}^{M} J_{||,\alpha\beta}(i+\frac{1}{2},j). \tag{4.65}$$

Inserting the discretized parallel flux (4.51), yields

$$\tilde{P}_{\alpha\beta}\equiv\frac{P_{\alpha\beta}}{m_\alpha\nu_{\alpha\beta}}=-\Delta W\sum_{i=1}^{N-1}\sum_{j=1}^{M}\left[\left(v_{||}(i+\frac{1}{2})-u_{\alpha\beta}\right)f_\alpha(i+\frac{1}{2},j)B_{||}^*(i+\frac{1}{2})+\frac{T_{\alpha\beta}}{m_\alpha}\frac{\partial f_\alpha B_{||}^*}{\partial v_{||}}\bigg|_{i+\frac{1}{2},j}\right]. \tag{4.66}$$

Using eqs. (4.43)-(4.45) and $v_{||}(i+1/2) = v_{||}(i) + \Delta v_{||}/2$, results upon re-ordering of the terms in

$$\tilde{P}_{\alpha\beta} = -\Delta W \sum_{i=1}^{N-1}\sum_{j=1}^{M}\left[\frac{1}{2}\left(v_{||}(i) + \frac{\Delta v_{||}}{2} - u_{\alpha\beta} - \frac{2T_{\alpha\beta}}{m_\alpha \Delta v_{||}}\right) f_\alpha(i,j) B^*_{||}(i) \right. \\ \left. + \frac{1}{2}\left(v_{||}(i) + \frac{\Delta v_{||}}{2} - u_{\alpha\beta} + \frac{2T_{\alpha\beta}}{m_\alpha \Delta v_{||}}\right) f_\alpha(i+1,j) B^*_{||}(i+1)\right]. \tag{4.67}$$

The sum in the second term can be re-indexed by $i+1 \to i$,

$$\sum_{i=1}^{N-1}\sum_{j=1}^{M}\frac{1}{2}\left(v_{||}(i) + \frac{\Delta v_{||}}{2} - u_{\alpha\beta} + \frac{2T_{\alpha\beta}}{m_\alpha \Delta v_{||}}\right) f_\alpha(i+1,j) B^*_{||}(i+1) \\ = \sum_{i=2}^{N}\sum_{j=1}^{M}\frac{1}{2}\left(v_{||}(i-1) + \frac{\Delta v_{||}}{2} - u_{\alpha\beta} + \frac{2T_{\alpha\beta}}{m_\alpha \Delta v_{||}}\right) f_\alpha(i,j) B^*_{||}(i) \tag{4.68}$$

Using $v_{||}(i-1) + \Delta v_{||}/2 = v_{||}(i) - \Delta v_{||}/2$ and shifting the lower bound of the sum to $i = 1$ by adding 1,

$$\sum_{i=2}^{N}\sum_{j=1}^{M}\frac{1}{2}\left(v_{||}(i-1) + \frac{\Delta v_{||}}{2} - u_{\alpha\beta} + \frac{2T_{\alpha\beta}}{m_\alpha \Delta v_{||}}\right) f_\alpha(i,j) B^*_{||}(i) = \\ \sum_{i=1}^{N}\sum_{j=1}^{M}\frac{1}{2}\left(v_{||}(i) - \frac{\Delta v_{||}}{2} - u_{\alpha\beta} + \frac{2T_{\alpha\beta}}{m_\alpha \Delta v_{||}}\right) f_\alpha(i,j) B^*_{||}(i) \\ - \sum_{j=1}^{M}\frac{1}{2}\left(v_{||}(1) - \frac{\Delta v_{||}}{2} - u_{\alpha\beta} + \frac{2T_{\alpha\beta}}{m_\alpha \Delta v_{||}}\right) f_\alpha(1,j) B^*_{||}(1). \tag{4.69}$$

The same is applied to the first term in eq. (4.67), where the missing N term in the sum is added

$$\sum_{i=1}^{N-1}\sum_{j=1}^{M}\frac{1}{2}\left(v_{||}(i) + \frac{\Delta v_{||}}{2} - u_{\alpha\beta} - \frac{2T_{\alpha\beta}}{m_\alpha \Delta v_{||}}\right) f_\alpha(i,j) B^*_{||}(i) = \\ \sum_{i=1}^{N}\sum_{j=1}^{M}\frac{1}{2}\left(v_{||}(i) + \frac{\Delta v_{||}}{2} - u_{\alpha\beta} - \frac{2T_{\alpha\beta}}{m_\alpha \Delta v_{||}}\right) f_\alpha(i,j) B^*_{||}(i) \\ - \sum_{j=1}^{M}\frac{1}{2}\left(v_{||}(N) + \frac{\Delta v_{||}}{2} - u_{\alpha\beta} - \frac{2T_{\alpha\beta}}{m_\alpha \Delta v_{||}}\right) f_\alpha(N,j) B^*_{||}(N). \tag{4.70}$$

Re-assembling (4.67) using the eqs. (4.69)-(4.70), cancels all terms involving $\Delta v_{||}$ in the double sum

$$\begin{aligned}\tilde{P}_{\alpha\beta} = -\Delta W \Bigg\{ & \sum_{i=1}^{N}\sum_{j=1}^{M} \left(v_{||}(i) - u_{\alpha\beta}\right) f_\alpha(i,j) B^*_{||}(i) \\ & -\frac{1}{2}\sum_{j=1}^{M} \Bigg[\left(v_{||}(1) - \frac{\Delta v_{||}}{2} - u_{\alpha\beta} + \frac{2T_{\alpha\beta}}{m_\alpha \Delta v_{||}} \right) f_\alpha(1,j) B^*_{||}(1) \\ & + \left(v_{||}(N) + \frac{\Delta v_{||}}{2} - u_{\alpha\beta} - \frac{2T_{\alpha\beta}}{m_\alpha \Delta v_{||}} \right) f_\alpha(N,j) B^*_{||}(N) \Bigg] \Bigg\}. \end{aligned} \tag{4.71}$$

The double sum can be evaluated using the definition of the discretized velocity space moments (4.8) and (4.9),

$$\tilde{P}_{\alpha\beta} = -\left(M_{1,\alpha} - u_{\alpha\beta} M_{0,\alpha} - P_{\mathrm{BC},\alpha\beta}\right), \tag{4.72}$$

where the last term is called the *boundary correction* term

$$\begin{aligned} P_{\mathrm{BC},\alpha\beta} = \frac{\Delta W}{2} \sum_{j=1}^{M} \Bigg[& \left(v_{||}(1) - \frac{\Delta v_{||}}{2} - u_{\alpha\beta} + \frac{2T_{\alpha\beta}}{m_\alpha \Delta v_{||}} \right) f_\alpha(1,j) B^*_{||}(1) \\ & + \left(v_{||}(N) + \frac{\Delta v_{||}}{2} - u_{\alpha\beta} - \frac{2T_{\alpha\beta}}{m_\alpha \Delta v_{||}} \right) f_\alpha(N,j) B^*_{||}(N) \Bigg], \end{aligned} \tag{4.73}$$

since it involves sums over the parallel velocity space domain boundaries and is added to the standard momentum change expression given by the first two terms. The boundary correction terms represent discretization errors that arise because the velocity space is truncated at finite values of the distribution function.

Energy Change

The energy change due to collisions is calculated analogously to the momentum change, but using $\phi_\alpha = m_\alpha v_{||}^2/2 + \mu B$

$$\begin{aligned} E_{\alpha\beta} &\equiv \sum_{i=1}^{N}\sum_{j=1}^{M} \Delta W \left(\frac{1}{2} m_\alpha v_{||}^2(i) + \mu(j) B \right) (\nabla \cdot \mathbf{J}_{\alpha\beta})(i,j) \\ &= \underbrace{-\Delta W \sum_{i=1}^{N}\sum_{j=1}^{M-1} J_{\mu,\alpha\beta}(i, j+\frac{1}{2}) B}_{E_\perp} \underbrace{-\Delta W \sum_{i=1}^{N-1}\sum_{j=1}^{M} J_{||,\alpha\beta}(i+\frac{1}{2}, j) m_\alpha v_{||}(i)}_{E_{||}}. \end{aligned} \tag{4.74}$$

The perpendicular and parallel contributions are

$$\tilde{E}_{\perp} \equiv \frac{E_{\perp}}{\nu_{\alpha\beta}} = -B\Delta W \sum_{i=1}^{N}\sum_{j=1}^{M-1}\left[2\mu(j+\frac{1}{2})f_{\alpha}(i,j+\frac{1}{2})B^{*}_{||}(i) + \frac{2T_{\alpha\beta}}{B}\mu(j+\frac{1}{2})\frac{\partial f_{\alpha}B^{*}_{||}}{\partial\mu}\bigg|_{i,j+\frac{1}{2}}\right], \tag{4.75}$$

$$\tilde{E}_{||} \equiv \frac{E_{||}}{\nu_{\alpha\beta}} = -m_{\alpha}\Delta W \sum_{i=1}^{N-1}\sum_{j=1}^{M}\left[\left(v_{||}(i+\frac{1}{2}) - u_{\alpha\beta}\right)f_{\alpha}(i+\frac{1}{2},j)B^{*}_{||}(i+\frac{1}{2}) + \frac{T_{\alpha\beta}}{m_{\alpha}}\frac{\partial f_{\alpha}B^{*}_{||}}{\partial v_{||}}\bigg|_{i+\frac{1}{2},j}\right]v_{||}(i+\frac{1}{2}). \tag{4.76}$$

By applying the same procedure as shown in the last section, the perpendicular contribution becomes,

$$\begin{aligned}\tilde{E}_{\perp} = -B\Delta W\Bigg\{ &\sum_{i=1}^{N}\sum_{j=1}^{M} B^{*}_{||}(i)\left(\mu(j) + \frac{\Delta\mu}{2} - \frac{2T_{\alpha\beta}}{B\Delta\mu}\left(\mu(j)+\frac{\Delta\mu}{2}\right)\right)f_{\alpha}(i,j)\\ &+\sum_{i=1}^{N}\sum_{j=1}^{M} B^{*}_{||}(i)\left(\mu(j) - \frac{\Delta\mu}{2} + \frac{2T_{\alpha\beta}}{B\Delta\mu}\left(\mu(j)-\frac{\Delta\mu}{2}\right)\right)f_{\alpha}(i,j)\\ &-\sum_{i=1}^{N} B^{*}_{||}(i)\left[\left(\mu(M)+\frac{\Delta\mu}{2}\right)f_{\alpha}(i,M) - \frac{2T_{\alpha\beta}}{B\Delta\mu}\left(\mu(M)+\frac{\Delta\mu}{2}\right)f_{\alpha}(i,M)\right]\\ &-\sum_{i=1}^{N} B^{*}_{||}(i)\left[\left(\mu(1)-\frac{\Delta\mu}{2}\right)f_{\alpha}(i,1) + \frac{2T_{\alpha\beta}}{B\Delta\mu}\left(\mu(1)-\frac{\Delta\mu}{2}\right)f_{\alpha}(i,1)\right]\Bigg\},\end{aligned} \tag{4.77}$$

where terms with $\Delta\mu$ cancel in the double sum. The parallel contribution is similar, but uses

the property $v_{||}^2(i-1) + v_{||}(i-1)\Delta v_{||} = v_{||}^2(i) - v_{||}(i)\Delta v_{||}$ in the calculation,

$$\begin{aligned}\tilde{E}_{||} = -m_\alpha \Delta W \Bigg\{ & \sum_{i=1}^{N}\sum_{j=1}^{M} \frac{1}{2}\Bigg[v_{||}^2(i) + v_{||}(i)\Delta v_{||} + \frac{(\Delta v_{||})^2}{4} \\ & \qquad - \left(u_{\alpha\beta} + \frac{2T_{\alpha\beta}}{m_\alpha \Delta v_{||}}\right)\left(v_{||}(i) + \frac{\Delta v_{||}}{2}\right)\Bigg] f_\alpha(i,j) B_{||}^*(i) \\ & + \sum_{i=1}^{N}\sum_{j=1}^{M} \frac{1}{2}\Bigg[v_{||}^2(i) - v_{||}(i)\Delta v_{||} + \frac{(\Delta v_{||})^2}{4} \\ & \qquad - \left(u_{\alpha\beta} - \frac{2T_{\alpha\beta}}{m_\alpha \Delta v_{||}}\right)\left(v_{||}(i) - \frac{\Delta v_{||}}{2}\right)\Bigg] f_\alpha(i,j) B_{||}^*(i) \\ & - \sum_{j=1}^{M} \frac{1}{2}\left[\left(v_{||}(N) + \frac{\Delta v_{||}}{2}\right)^2 - \left(u_{\alpha\beta} + \frac{2T_{\alpha\beta}}{m_\alpha \Delta v_{||}}\right)\left(v_{||}(N) + \frac{\Delta v_{||}}{2}\right)\right] f_\alpha(N,j) B_{||}^*(N) \\ & - \sum_{j=1}^{M} \frac{1}{2}\left[\left(v_{||}(1) - \frac{\Delta v_{||}}{2}\right)^2 - \left(u_{\alpha\beta} - \frac{2T_{\alpha\beta}}{m_\alpha \Delta v_{||}}\right)\left(v_{||}(1) - \frac{\Delta v_{||}}{2}\right)\right] f_\alpha(1,j) B_{||}^*(1)\Bigg\}. \end{aligned} \tag{4.78}$$

The terms linear in $\Delta v_{||}$ will cancel in the double sum, but there are also terms in the boundary sums that cancel. This point can be seen by expanding,

$$\left(u_{\alpha\beta} + \frac{2T_{\alpha\beta}}{m_\alpha \Delta v_{||}}\right)\left(v_{||}(i) + \frac{\Delta v_{||}}{2}\right) = u_{\alpha\beta} v_{||}(i) + \frac{\Delta v_{||}}{2} u_{\alpha\beta} + \frac{2T_{\alpha\beta}}{m_\alpha \Delta v_{||}} v_{||}(i) + \frac{T_{\alpha\beta}}{m_\alpha}, \tag{4.79}$$

$$\left(u_{\alpha\beta} - \frac{2T_{\alpha\beta}}{m_\alpha \Delta v_{||}}\right)\left(v_{||}(i) - \frac{\Delta v_{||}}{2}\right) = u_{\alpha\beta} v_{||}(i) - \frac{\Delta v_{||}}{2} u_{\alpha\beta} - \frac{2T_{\alpha\beta}}{m_\alpha \Delta v_{||}} v_{||}(i) + \frac{T_{\alpha\beta}}{m_\alpha}. \tag{4.80}$$

The final result is obtained by collecting eqs. (4.77) and (4.78) as well as using the definitions of the discretized moments (4.8)-(4.11),

$$\bar{E}_{\alpha\beta} \equiv \frac{\tilde{E}_\perp + \tilde{E}_{||}}{m_\alpha} = M_{2,\alpha} - \frac{u_{\alpha\beta}}{2} M_{1,\alpha} - \frac{3T_{\alpha\beta}}{2m_\alpha} M_{0,\alpha} + \frac{(\Delta v_{||})^2}{8} M_0 - E_{\mathrm{BC},\alpha\beta}. \tag{4.81}$$

The boundary correction terms are

$$E_{\mathrm{BC},\alpha\beta} = E_{\mathrm{BC},\perp,\alpha\beta} + E_{\mathrm{BC},||,\alpha\beta}, \tag{4.82}$$

$$E_{\mathrm{BC},\perp,\alpha\beta} = \frac{\Delta W}{2m_\alpha}\sum_{i=1}^{N} B^*_{||}(i)\left[\left(B + \frac{2T_{\alpha\beta}}{\Delta\mu}\right)\left(\mu(1) - \frac{\Delta\mu}{2}\right) f_\alpha(i,1) + \left(B - \frac{2T_{\alpha\beta}}{\Delta\mu}\right)\left(\mu(M) + \frac{\Delta\mu}{2}\right) f_\alpha(i,M)\right]. \tag{4.83}$$

$$E_{\mathrm{BC},||,\alpha\beta} = \frac{\Delta W}{2}\left\{\sum_{j=1}^{M}\frac{1}{2}\left[\left(v_{||}(1) - \frac{\Delta v_{||}}{2}\right)^2 - \left(u_{\alpha\beta} - \frac{2T_{\alpha\beta}}{m_\alpha\Delta v_{||}}\right)\left(v_{||}(1) - \frac{\Delta v_{||}}{2}\right)\right] f_\alpha(1,j)B^*_{||}(1) + \sum_{j=1}^{M}\frac{1}{2}\left[\left(v_{||}(N) + \frac{\Delta v_{||}}{2}\right)^2 - \left(u_{\alpha\beta} + \frac{2T_{\alpha\beta}}{m_\alpha\Delta v_{||}}\right)\left(v_{||}(N) + \frac{\Delta v_{||}}{2}\right)\right] f_\alpha(N,j)B^*_{||}(N)\right\}. \tag{4.84}$$

Like the single species momentum change, the energy change in (4.81) contains standard contributions in the first three terms and the boundary correction terms. The energy change contains an additional discretization error that depends on $(\Delta v_{||})^2$.

The remainder of this section presents the algorithm for correcting the boundary and $(\Delta v_{||})^2$ discretization errors. Modifying the definition of $u_{\alpha\beta}$ and $T_{\alpha\beta}$ will apply a correction such that the error terms cancel.

Boundary Correction Terms

The boundary correction terms (4.73), (4.83) and (4.84) can be rewritten into a slightly handier form,

$$P_{\mathrm{BC},\alpha\beta} = S_{1,\alpha}\left(v_{||}^- - u_{\alpha\beta} + \frac{2T_{\alpha\beta}}{m_\alpha\Delta v_{||}}\right) + S_{2,\alpha}\left(v_{||}^+ - u_{\alpha\beta} - \frac{2T_{\alpha\beta}}{m_\alpha\Delta v_{||}}\right), \tag{4.85}$$

$$E_{\mathrm{BC},\alpha\beta} = S_{3,\alpha}\left(\frac{B}{m_\alpha}\mu^- + \frac{2T_{\alpha\beta}}{m\Delta\mu}\mu^-\right) + S_{4,\alpha}\left(\frac{B}{m_\alpha}\mu^+ - \frac{2T_{\alpha\beta}}{m_\alpha\Delta\mu}\mu^+\right) + S_{1,\alpha}\left(\frac{1}{2}(v_{||}^-)^2 - \left(u_{\alpha\beta} - \frac{2T_{\alpha\beta}}{m_\alpha\Delta v_{||}}\right)\frac{v_{||}^-}{2}\right) + S_{2,\alpha}\left(\frac{1}{2}(v_{||}^+)^2 - \left(u_{\alpha\beta} + \frac{2T_{\alpha\beta}}{m_\alpha\Delta v_{||}}\right)\frac{v_{||}^+}{2}\right). \tag{4.86}$$

using staggered velocities

$$v_{||}^{-} \equiv v_{||}(1) - \frac{\Delta v_{||}}{2}, \qquad v_{||}^{+} \equiv v_{||}(N) + \frac{\Delta v_{||}}{2}, \tag{4.87}$$

$$\mu^{-} \equiv \mu(1) - \frac{\Delta \mu}{2}, \qquad \mu^{+} \equiv \mu(M) + \frac{\Delta \mu}{2}, \tag{4.88}$$

and velocity space boundary sums

$$S_{1,\alpha} \equiv \frac{\Delta W}{2} \sum_{j=1}^{M} f_\alpha(1,j) B_{||}^*(1), \qquad S_{2,\alpha} \equiv \frac{\Delta W}{2} \sum_{j=1}^{M} f_\alpha(N,j) B_{||}^*(N), \tag{4.89}$$

$$S_{3,\alpha} \equiv \frac{\Delta W}{2} \sum_{i=1}^{N} f_\alpha(i,1) B_{||}^*(i), \qquad S_{4,\alpha} \equiv \frac{\Delta W}{2} \sum_{i=1}^{N} f_\alpha(i,M) B_{||}^*(i). \tag{4.90}$$

It is useful to collect factors of $u_{\alpha\beta}$ and $T_{\alpha\beta}$,

$$P_{\mathrm{BC},\alpha\beta} = u_{\alpha\beta}\, p_{1,\alpha} + T_{\alpha\beta}\, p_{2,\alpha} + p_{3,\alpha}, \tag{4.91}$$

$$E_{\mathrm{BC},\alpha\beta} = u_{\alpha\beta}\, p_{4,\alpha} + T_{\alpha\beta}\, p_{5,\alpha} + p_{6,\alpha}, \tag{4.92}$$

with

$$p_{1,\alpha} \equiv -\left(S_{1,\alpha} + S_{2,\alpha}\right), \tag{4.93}$$

$$p_{2,\alpha} \equiv \frac{2}{m_\alpha \Delta v_{||}} \left(S_{1,\alpha} - S_{2,\alpha}\right), \tag{4.94}$$

$$p_{3,\alpha} \equiv v_{||}^{-} S_{1,\alpha} + v_{||}^{+} S_{2,\alpha}, \tag{4.95}$$

$$p_{4,\alpha} \equiv -\frac{1}{2}\left(v_{||}^{-} S_{1,\alpha} + v_{||}^{+} S_{2,\alpha}\right) = -\frac{1}{2} p_{3,\alpha}, \tag{4.96}$$

$$p_{5,\alpha} \equiv \frac{1}{m_\alpha \Delta v_{||}}\left(v_{||}^{-} S_{1,\alpha} - v_{||}^{+} S_{2,\alpha}\right) + \frac{2}{m_\alpha \Delta \mu}\left(\mu^{-} S_{3,\alpha} - \mu^{+} S_{4,\alpha}\right), \tag{4.97}$$

$$p_{6,\alpha} \equiv \frac{1}{2}\left((v_{||}^{-})^2 S_{1,\alpha} + (v_{||}^{+})^2 S_{2,\alpha}\right) + \frac{B}{m_\alpha}\left(\mu^{-} S_{3,\alpha} + \mu^{+} S_{4,\alpha}\right). \tag{4.98}$$

Momentum and Energy Conservation

The first of the conditions imposed on the discretized collision operator is that the total momentum should be conserved. This condition means that the single species contributions of (4.72) should add to zero,

$$m_\alpha \nu_{\alpha\beta}\left(M_{1,\alpha} - u_{\alpha\beta} M_{0,\alpha} - P_{\mathrm{BC},\alpha}\right) + m_\beta \nu_{\beta\alpha}\left(M_{1,\beta} - u_{\beta\alpha} M_{0,\beta} - P_{\mathrm{BC},\beta}\right) \stackrel{!}{=} 0. \tag{4.99}$$

The second condition is that the total energy should be conserved, i.e

$$m_\alpha \nu_{\alpha\beta} \left(M_{2,\alpha} - \frac{1}{2} u_{\alpha\beta} M_{1,\alpha} - \frac{3}{2m_\alpha} T_{\alpha\beta} M_{0,\alpha} + \frac{(\Delta v_{||})^2}{8} M_{0,\alpha} - E_{\mathrm{BC},\alpha} \right) + m_\beta \nu_{\beta\alpha} \left(M_{2,\beta} - \frac{1}{2} u_{\beta\alpha} M_{1,\beta} - \frac{3}{2m_\beta} T_{\beta\alpha} M_{0,\beta} + \frac{(\Delta v_{||})^2}{8} M_{0,\beta} - E_{\mathrm{BC},\beta} \right) \stackrel{!}{=} 0. \tag{4.100}$$

To account for the ET and EM versions of the LBD at once, eqs. (3.135) and (3.140) are written as

$$\nu_{\alpha\beta} = \nu_{\beta\alpha} \frac{M_{0,\alpha}}{M_{0,\beta}} \kappa_{\alpha\beta}, \tag{4.101}$$

$$\kappa_{\alpha\beta} \equiv \begin{cases} 1, & \text{ET}, \\ m_\alpha / m_\beta, & \text{EM}. \end{cases} \tag{4.102}$$

Further, the equations will be normalized for use in a computational code. Since the velocity normalization will depend on the particle species, the symmetry condition $u_{\alpha\beta} = u_{\beta\alpha}$ does not hold in normalized units. To avoid re-deriving the equations again in that case, one can insert a placeholder variable

$$u_{\beta\alpha} = u_{\alpha\beta} \eta, \tag{4.103}$$

$$\eta \equiv \begin{cases} 1, & \text{physical units}, \\ \eta_{\mathrm{ref}}, & \text{normalized units}. \end{cases} \tag{4.104}$$

Using these definitions in the conditions for momentum and energy conservation and re-grouping factors of $u_{\alpha\beta}$ and $T_{\alpha\beta}$ yields

$$u_{\alpha\beta} s_{1,\alpha} + T_{\alpha\beta} s_{2,\alpha} = s_{3,\alpha}, \tag{4.105}$$

$$u_{\alpha\beta} s_{4,\alpha} + T_{\alpha\beta} s_{5,\alpha} = s_{6,\alpha}, \tag{4.106}$$

where

$$s_{1,\alpha\beta} = m_\alpha \left(1 + \frac{p_{1,\alpha}}{M_{0,\alpha}}\right) + m_\beta \kappa_{\alpha\beta}\eta \left(1 + \frac{p_{1,\beta}}{M_{0,\beta}}\right), \tag{4.107}$$

$$s_{2,\alpha\beta} = m_\alpha \frac{p_{2,\alpha}}{M_{0,\alpha}} + m_\beta \kappa_{\alpha\beta} \frac{p_{2,\beta}}{M_{0,\beta}}, \tag{4.108}$$

$$s_{3,\alpha\beta} = \frac{m_\alpha}{M_{0,\alpha}}\Big(M_{1,\alpha} - p_{3,\alpha}\Big) + \frac{m_\beta \kappa_{\alpha\beta}}{M_{0,\beta}}\Big(M_{1,\beta} - p_{3,\beta}\Big), \tag{4.109}$$

$$s_{4,\alpha\beta} = \frac{m_\alpha}{M_{0,\alpha}}\left(\frac{1}{2}M_{1,\alpha} + p_{4,\alpha}\right) + \frac{m_\beta \kappa_{\alpha\beta}\eta}{M_{0,\beta}}\left(\frac{1}{2}M_{1,\beta} + p_{4,\beta}\right), \tag{4.110}$$

$$s_{5,\alpha\beta} = \frac{3}{2}\Big(1 + \kappa_{\alpha\beta}\Big) + m_\alpha \frac{p_{5,\alpha}}{M_{0,\alpha}} + m_\beta \kappa_{\alpha\beta} \frac{p_{5,\beta}}{M_{0,\beta}}, \tag{4.111}$$

$$s_{6,\alpha\beta} = \frac{m_\alpha}{M_{0,\alpha}}\Big(M_{2,\alpha} - p_{6,\alpha}\Big) + \frac{m_\beta \kappa_{\alpha\beta}}{M_{0,\beta}}\Big(M_{2,\beta} - p_{6,\beta}\Big) + \frac{(\Delta v_{||})^2}{8}\Big(m_\alpha + m_\beta \kappa_{\alpha\beta}\Big). \tag{4.112}$$

The system of equations (4.105)-(4.106) is easily solved by,

$$u_{\alpha\beta} = \frac{1}{s_{1,\alpha\beta}}\Big(s_{3,\alpha\beta} - T_{\alpha\beta} s_{2,\alpha\beta}\Big), \tag{4.113}$$

$$T_{\alpha\beta} = \frac{s_{1,\alpha\beta} s_{6,\alpha\beta} - s_{4,\alpha\beta} s_{3,\alpha\beta}}{s_{1,\alpha\beta} s_{5,\alpha\beta} - s_{4,\alpha\beta} s_{2,\alpha\beta}}. \tag{4.114}$$

If the mixing quantities are chosen according to these two equations, the resulting finite volume scheme will conserve total momentum and energy on the discrete level. The algorithm to calculate these quantities is lengthy but simple. First calculate the discretized moments (4.8)-(4.11), second the "p-factors" (4.93)-(4.98), third the "s-factors" (4.107)-(4.112) and finally the mixing quantities (4.113) and (4.114). The algorithm for applying conservative corrections to the finite volume discretization has been presented in Ref. [58] (see Appendix B therein).

4.3.3 Normalized Discrete Finite Volume Version

The collision operator in finite volume discretization (4.50) is given in normalized form as

$$\begin{aligned}(\hat{C}_{\alpha\beta}\hat{f}_\alpha)(i,j) = \frac{1}{\hat{B}^*_{||}(i)}\Bigg[&\frac{1}{\Delta\hat{v}_{||}}\left(\hat{J}_{||,\alpha\beta}(i+\frac{1}{2},j) - \hat{J}_{||,\alpha\beta}(i-\frac{1}{2},j)\right)\\ &+ \frac{1}{\Delta\hat{\mu}}\left(\hat{J}_{\mu,\alpha\beta}(i,j+\frac{1}{2}) - \hat{J}_{\mu,\alpha\beta}(i,j-\frac{1}{2})\right)\Bigg],\end{aligned} \tag{4.115}$$

where $C_{\text{ref}} = \nu_{\text{ref}}$ and the fluxes must be normalized with respect to $J_{||,\text{ref},\alpha} = \nu_{\text{ref}} f_{\text{ref},\alpha} B_{\text{ref}} v_{\text{th},\alpha}$ and $J_{\mu,\text{ref},\alpha} = \nu_{\text{ref}} f_{\text{ref},\alpha} T_{\text{ref}}$. Normalizing the fluxes (4.51)-(4.52) with these reference values

yields,

$$\hat{J}_{||,\alpha\beta}(i\pm\frac{1}{2},j)=\hat{\nu}_{\alpha\beta}\left\{\left(\hat{v}_{||}(i\pm\frac{1}{2})-\hat{u}_{||,\alpha\beta}\right)\hat{f}_{\alpha}(i\pm\frac{1}{2},j)\,\hat{B}^{*}_{||}(i\pm\frac{1}{2})+\frac{\hat{T}_{\alpha\beta}}{2}\frac{\partial\hat{f}_{\alpha}\hat{B}^{*}_{||}}{\partial\hat{v}_{||}}\bigg|_{i\pm\frac{1}{2},j}\right\}, \tag{4.116}$$

$$\hat{J}_{\mu,\alpha\beta}(i,j\pm\frac{1}{2})=\hat{\nu}_{\alpha\beta}\left\{2\hat{\mu}(j\pm\frac{1}{2})\hat{f}_{\alpha}(i,j\pm\frac{1}{2})\,\hat{B}^{*}_{||}(i)+\frac{2\hat{T}_{\alpha\beta}}{\hat{B}}\hat{\mu}(j\pm\frac{1}{2})\frac{\partial\hat{f}_{\alpha}\hat{B}^{*}_{||}}{\partial\hat{\mu}}\bigg|_{i,j\pm\frac{1}{2}}\right\}, \tag{4.117}$$

where the interpolations and derivatives of the normalized quantities are obtained from eqs. (4.53)-(4.56). The mixing quantities are normalized according to

$$u_{\alpha\beta}=v_{\mathrm{th},\alpha}\hat{u}_{\alpha\beta}, \tag{4.118}$$

$$T_{\alpha\beta}=T_{\mathrm{ref}}\hat{T}_{\alpha\beta}, \tag{4.119}$$

$$\hat{u}_{\beta\alpha}=v^{-1}_{\mathrm{th},\beta}u_{\beta\alpha}=\frac{v_{\mathrm{th},\alpha}}{v_{\mathrm{th},\beta}}\hat{u}_{\alpha\beta}=\sqrt{\frac{m_{\beta}}{m_{\alpha}}}\hat{u}_{\alpha\beta}, \tag{4.120}$$

$$\hat{T}_{\beta\alpha}=T^{-1}_{\mathrm{ref}}T_{\alpha\beta}=\hat{T}_{\alpha\beta}. \tag{4.121}$$

Comparing with (4.104), it is apparent that $\eta_{\mathrm{ref}}=\sqrt{m_{\beta}/m_{\alpha}}$. Next, the boundary sums are normalized with $S_{i,\alpha}=n_{\mathrm{ref}}m_{\alpha}\hat{S}_{i,\alpha}$ with $i=1\ldots4$, where

$$\hat{S}_{1,\alpha}\equiv\frac{\Delta\hat{W}}{2}\sum_{j=1}^{M}\hat{f}_{\alpha}(1,j)\hat{B}^{*}_{||}(1),\qquad\hat{S}_{2,\alpha}\equiv\frac{\Delta\hat{W}}{2}\sum_{j=1}^{M}\hat{f}_{\alpha}(N,j)\hat{B}^{*}_{||}(N), \tag{4.122}$$

$$\hat{S}_{3,\alpha}\equiv\frac{\Delta\hat{W}}{2}\sum_{i=1}^{N}\hat{f}_{\alpha}(i,1)\hat{B}^{*}_{||}(i),\qquad\hat{S}_{4,\alpha}\equiv\frac{\Delta\hat{W}}{2}\sum_{i=1}^{N}\hat{f}_{\alpha}(i,M)\hat{B}^{*}_{||}(i). \tag{4.123}$$

The boundary correction terms are normalized by considering eqs. (4.99) and (4.100), realizing that the common dimensional prefactors are $m_{\alpha}n_{\mathrm{ref}}v_{\mathrm{th},\alpha}$ and $n_{\mathrm{ref}}T_{\mathrm{ref}}$ respectively. To achieve dimensionless equations, the reference values for the boundary correction terms have to be the same, i.e.

$$P_{\mathrm{BC},\alpha\beta}=m_{\alpha}n_{\mathrm{ref}}v_{\mathrm{th},\alpha}\hat{P}_{\mathrm{BC},\alpha\beta}, \tag{4.124}$$

$$E_{\mathrm{BC},\alpha\beta}=n_{\mathrm{ref}}T_{\mathrm{ref}}\hat{E}_{\mathrm{BC},\alpha\beta}, \tag{4.125}$$

resulting in

$$\hat{P}_{\mathrm{BC},\alpha\beta} = \hat{p}_{1,\alpha}\hat{u}_{\alpha\beta} + \hat{p}_{2,\alpha}\hat{T}_{\alpha\beta} + \hat{p}_{3,\alpha}, \tag{4.126}$$

$$\hat{P}_{\mathrm{BC},\beta\alpha} = \hat{p}_{1,\beta}\hat{u}_{\alpha\beta}\eta + \hat{p}_{2,\beta}\hat{T}_{\alpha\beta} + \hat{p}_{3,\beta}, \tag{4.127}$$

$$\hat{E}_{\mathrm{BC},\alpha\beta} = \hat{p}_{4,\alpha}\hat{u}_{\alpha\beta} + \hat{p}_{5,\alpha}\hat{T}_{\alpha\beta} + \hat{p}_{6,\alpha}, \tag{4.128}$$

$$\hat{E}_{\mathrm{BC},\beta\alpha} = \hat{p}_{4,\beta}\hat{u}_{\alpha\beta}\eta + \hat{p}_{5,\beta}\hat{T}_{\alpha\beta} + \hat{p}_{6,\beta}. \tag{4.129}$$

The normalized "p-factors" are calculated by considering $\hat{P}_{\mathrm{BC},\alpha\beta}P_{\mathrm{BC,ref}} = \hat{u}_{\alpha\beta}v_{\mathrm{th}}p_{1,\alpha}+\hat{T}_{\alpha\beta}T_{\mathrm{ref}}p_{2,\alpha}+p_{3,\alpha}$ and $\hat{E}_{\mathrm{BC},\alpha\beta}E_{\mathrm{BC,ref}} = \hat{u}_{\alpha\beta}v_{\mathrm{th}}p_{4,\alpha}+\hat{T}_{\alpha\beta}T_{\mathrm{ref}}p_{5,\alpha}+p_{6,\alpha}$, and choosing the normalization such that all terms are dimensionless,

$$\begin{aligned}
\hat{p}_{1,\alpha} &= \frac{v_{\mathrm{th}}p_{1,\alpha}}{P_{\mathrm{BC,ref}}} = -(\hat{S}_1+\hat{S}_2)\frac{v_{\mathrm{th}}n_{\mathrm{ref}}m_\alpha}{n_{\mathrm{ref}}}\sqrt{\frac{1}{2m_\alpha T_{\mathrm{ref}}}} = -(\hat{S}_1+\hat{S}_2),\\
\hat{p}_{2,\alpha} &= \frac{T_{\mathrm{ref}}p_{2,\alpha}}{P_{\mathrm{BC,ref}}} = \frac{2}{\Delta\hat{v}_{||}}(\hat{S}_1-\hat{S}_2)\frac{n_{\mathrm{ref}}}{v_{\mathrm{th}}}T_{\mathrm{ref}}\frac{1}{n_{\mathrm{ref}}}\sqrt{\frac{1}{2m_\alpha T_{\mathrm{ref}}}} = \frac{1}{\Delta\hat{v}_{||}}(\hat{S}_1-\hat{S}_2),\\
\hat{p}_{3,\alpha} &= \frac{p_{3,\alpha}}{P_{\mathrm{BC,ref}}} = v_{\mathrm{th}}n_{\mathrm{ref}}m_\alpha\left(\hat{v}_{||}^-\hat{S}_1+\hat{v}_{||}^+\hat{S}_2\right)\frac{1}{n_{\mathrm{ref}}}\sqrt{\frac{1}{2m_\alpha T_{\mathrm{ref}}}} = \left(\hat{v}_{||}^-\hat{S}_1+\hat{v}_{||}^+\hat{S}_2\right),\\
\hat{p}_{4,\alpha} &= \frac{v_{\mathrm{th}}p_{4,\alpha}}{E_{\mathrm{BC,ref}}} = -\frac{1}{2}\frac{2}{n_{\mathrm{ref}}T_{\mathrm{ref}}}v_{\mathrm{th}}\frac{1}{2}v_{\mathrm{th}}n_{\mathrm{ref}}m_\alpha\left(v_{||}^-\hat{S}_1+v_{||}^+\hat{S}_2\right) = -\left(v_{||}^-\hat{S}_1+v_{||}^+\hat{S}_2\right),\\
\hat{p}_{5,\alpha} &= \frac{T_{\mathrm{ref}}p_{5,\alpha}}{E_{\mathrm{BC,ref}}} = \frac{T_{\mathrm{ref}}}{n_{\mathrm{ref}}T_{\mathrm{ref}}}\left[\frac{n_{\mathrm{ref}}}{\Delta\hat{v}_{||}}\left(\hat{v}_{||}^-\hat{S}_1-\hat{v}_{||}^+\hat{S}_2\right)+\frac{2n_{\mathrm{ref}}}{\Delta\hat{\mu}}\left(\hat{\mu}^-\hat{S}_3-\hat{\mu}^+\hat{S}_4\right)\right],\\
&= \frac{1}{\Delta\hat{v}_{||}}\left(\hat{v}_{||}^-\hat{S}_1-\hat{v}_{||}^+\hat{S}_2\right)+\frac{2}{\Delta\hat{\mu}}\left(\hat{\mu}^-\hat{S}_3-\hat{\mu}^+\hat{S}_4\right),\\
\hat{p}_{6,\alpha} &= \frac{p_{6,\alpha}}{E_{\mathrm{BC,ref}}} = \frac{1}{n_{\mathrm{ref}}T_{\mathrm{ref}}}T_{\mathrm{ref}}n_{\mathrm{ref}}\left[\left((\hat{v}_{||}^-)^2\hat{S}_1+(\hat{v}_{||}^+)^2\hat{S}_2\right)+\hat{B}\left(\hat{\mu}^-\hat{S}_3+\hat{\mu}^+\hat{S}_4\right)\right],\\
&= \left((\hat{v}_{||}^-)^2\hat{S}_1+(\hat{v}_{||}^+)^2\hat{S}_2\right)+\hat{B}\left(\hat{\mu}^-\hat{S}_3+\hat{\mu}^+\hat{S}_4\right).
\end{aligned}$$

Summarizing,

$$\hat{p}_{1,\alpha} = -\left(\hat{S}_{1,\alpha}+\hat{S}_{2,\alpha}\right), \tag{4.130}$$

$$\hat{p}_{2,\alpha} = \frac{1}{\Delta\hat{v}_{||}}\left(\hat{S}_{1,\alpha}-\hat{S}_{2,\alpha}\right), \tag{4.131}$$

$$\hat{p}_{3,\alpha} = \hat{S}_{1,\alpha}\hat{v}_{||}^- + \hat{S}_{2,\alpha}\hat{v}_{||}^+, \tag{4.132}$$

$$\hat{p}_{4,\alpha} = -\left(\hat{S}_{1,\alpha}\hat{v}_{||}^- + \hat{S}_{2,\alpha}\hat{v}_{||}^+\right) = -\hat{p}_{3,\alpha}, \tag{4.133}$$

$$\hat{p}_{5,\alpha} = \frac{2}{\Delta\hat{\mu}}\left(\hat{S}_{3,\alpha}\hat{\mu}^- - \hat{S}_{4,\alpha}\hat{\mu}^+\right)+\frac{1}{\Delta\hat{v}_{||}}\left(\hat{S}_{1,\alpha}\hat{v}_{||}^- - \hat{S}_{2,\alpha}\hat{v}_{||}^+\right), \tag{4.134}$$

$$\hat{p}_{6,\alpha} = \hat{B}\left(\hat{S}_{3,\alpha}\hat{\mu}^- + \hat{S}_{4,\alpha}\hat{\mu}^+\right)+\left(\hat{S}_{1,\alpha}\left(\hat{v}_{||}^-\right)^2 + \hat{S}_{2,\alpha}\left(\hat{v}_{||}^+\right)^2\right). \tag{4.135}$$

The conservation of momentum is normalized as,

$$\begin{aligned}0 &= m_\alpha \left(\frac{\hat{M}_{1,\alpha}}{\hat{M}_{0,\alpha}} v_{\mathrm{th},\alpha} - \hat{u}_{\alpha\beta} v_{\mathrm{th},\alpha} - \frac{m_\alpha n_{\mathrm{ref}} v_{\mathrm{th},\alpha} \hat{P}_{\mathrm{BC},\alpha\beta}}{\hat{M}_{0,\alpha} n_{\mathrm{ref}} m_\alpha} \right) \\ &+ m_\beta \left(\frac{\hat{M}_{1,\beta}}{\hat{M}_{0,\beta}} v_{\mathrm{th},\beta} - \hat{u}_{\alpha\beta} \eta v_{\mathrm{th},\beta} - \frac{m_\beta n_{\mathrm{ref}} v_{\mathrm{th},\beta} \hat{P}_{\mathrm{BC},\beta\alpha}}{\hat{M}_{0,\beta} n_{\mathrm{ref}} m_\beta} \right), \\ &= \sqrt{\hat{m}_\alpha} \left(\frac{\hat{M}_{1,\alpha}}{\hat{M}_{0,\alpha}} - \hat{u}_{\alpha\beta} - \frac{\hat{P}_{\mathrm{BC},\alpha\beta}}{\hat{M}_{0,\alpha}} \right) + \sqrt{\hat{m}_\beta} \left(\frac{\hat{M}_{1,\beta}}{\hat{M}_{0,\beta}} - \hat{u}_{\alpha\beta} \eta - \frac{\hat{P}_{\mathrm{BC},\beta\alpha}}{\hat{M}_{0,\beta}} \right). \end{aligned} \tag{4.136}$$

Similar to the conservation of energy,

$$\begin{aligned}0 &= m_\alpha \left(\frac{\hat{M}_{2,\alpha}}{\hat{M}_{0,\alpha}} \frac{T_{\mathrm{ref}}}{m_\alpha} - \frac{1}{2} \hat{u}_{\alpha\beta} \frac{\hat{M}_{1,\alpha}}{\hat{M}_{0,\alpha}} v_{\mathrm{th},\alpha}^2 - \frac{3}{2m_\alpha} \hat{T}_{\alpha\beta} T_{\mathrm{ref}} + \frac{\left(\Delta \hat{v}_{||}\right)^2}{8} v_{\mathrm{th},\alpha}^2 - \frac{n_{\mathrm{ref}} T_{\mathrm{ref}} \hat{E}_{\mathrm{BC},\alpha\beta}}{\hat{M}_{0,\alpha} n_{\mathrm{ref}} m_\alpha} \right) \\ &+ m_\beta \left(\frac{\hat{M}_{2,\beta}}{\hat{M}_{0,\beta}} \frac{T_{\mathrm{ref}}}{m_\beta} - \frac{1}{2} \hat{u}_{\alpha\beta} \eta \frac{\hat{M}_{1,\beta}}{\hat{M}_{0,\beta}} v_{\mathrm{th},\beta}^2 - \frac{3}{2m_\beta} \hat{T}_{\alpha\beta} T_{\mathrm{ref}} + \frac{\left(\Delta \hat{v}_{||}\right)^2}{8} v_{\mathrm{th},\beta}^2 - \frac{n_{\mathrm{ref}} T_{\mathrm{ref}} \hat{E}_{\mathrm{BC},\beta\alpha}}{\hat{M}_{0,\beta} n_{\mathrm{ref}} m_\beta} \right), \\ &= \frac{\hat{M}_{2,\alpha}}{\hat{M}_{0,\alpha}} + \frac{\hat{M}_{2,\beta}}{\hat{M}_{0,\beta}} - \hat{u}_{\alpha\beta} \frac{\hat{M}_{1,\alpha}}{\hat{M}_{0,\alpha}} - \hat{u}_{\alpha\beta} \eta \frac{\hat{M}_{1,\beta}}{\hat{M}_{0,\beta}} - 3\hat{T}_{\alpha\beta} + \frac{1}{2} \left(\Delta \hat{v}_{||}\right)^2 - \frac{\hat{E}_{\mathrm{BC},\alpha\beta}}{\hat{M}_{0,\alpha}} - \frac{\hat{E}_{\mathrm{BC},\beta\alpha}}{\hat{M}_{0,\beta}}. \end{aligned} \tag{4.137}$$

These equations can be written as a linear system of equations,

$$\hat{u}_{\alpha\beta} \hat{s}_{1,\alpha} + \hat{T}_{\alpha\beta} \hat{s}_{2,\alpha} = \hat{s}_{3,\alpha}, \tag{4.138}$$

$$\hat{u}_{\alpha\beta} \hat{s}_{4,\alpha} + \hat{T}_{\alpha\beta} \hat{s}_{5,\alpha} = \hat{s}_{6,\alpha}. \tag{4.139}$$

The normalized "s-factors" can be easily extracted from eqs. (4.136) and (4.137)

$$\hat{s}_{1,\alpha\beta} = \hat{\gamma}_\alpha + \hat{\gamma}_\beta \hat{\delta}_{\alpha\beta} + \hat{\gamma}_\alpha \frac{\hat{p}_{1,\alpha}}{\hat{M}_{0,\alpha}} + \hat{\gamma}_\beta \hat{\delta}_{\alpha\beta} \frac{\hat{p}_{1,\beta}}{\hat{M}_{0,\beta}}, \tag{4.140}$$

$$\hat{s}_{2,\alpha\beta} = \hat{\gamma}_\alpha \frac{\hat{p}_{2,\alpha}}{\hat{M}_{0,\alpha}} + \hat{\gamma}_\beta \frac{\hat{p}_{2,\beta}}{\hat{M}_{0,\beta}}, \tag{4.141}$$

$$\hat{s}_{3,\alpha\beta} = \hat{\gamma}_\alpha \frac{\hat{M}_{1,\alpha}}{\hat{M}_{0,\alpha}} + \hat{\gamma}_\beta \frac{\hat{M}_{1,\beta}}{\hat{M}_{0,\beta}} - \hat{\gamma}_\alpha \frac{\hat{p}_{3,\alpha}}{\hat{M}_{0,\alpha}} - \hat{\gamma}_\beta \frac{\hat{p}_{3,\beta}}{\hat{M}_{0,\beta}}, \tag{4.142}$$

$$\hat{s}_{4,\alpha\beta} = \hat{\epsilon}_\alpha \frac{\hat{M}_{1,\alpha}}{\hat{M}_{0,\alpha}} + \hat{\epsilon}_\beta \hat{\delta}_{\alpha\beta} \frac{\hat{M}_{1,\beta}}{\hat{M}_{0,\beta}} - \hat{\epsilon}_\alpha \frac{\hat{p}_{4,\alpha}}{\hat{M}_{0,\alpha}} - \hat{\epsilon}_\beta \hat{\delta}_{\alpha\beta} \frac{\hat{p}_{4,\beta}}{\hat{M}_{0,\beta}}, \tag{4.143}$$

$$\hat{s}_{5,\alpha\beta} = \frac{3}{2}(\hat{\epsilon}_\alpha + \hat{\epsilon}_\beta) + \hat{\epsilon}_\alpha \frac{\hat{p}_{5,\alpha}}{\hat{M}_{0,\alpha}} + \hat{\epsilon}_\beta \frac{\hat{p}_{5,\beta}}{\hat{M}_{0,\beta}}, \tag{4.144}$$

$$\hat{s}_{6,\alpha\beta} = \hat{\epsilon}_\alpha \frac{\hat{M}_{2,\alpha}}{\hat{M}_{0,\alpha}} + \hat{\epsilon}_\beta \frac{\hat{M}_{2,\beta}}{\hat{M}_{0,\beta}} + \frac{1}{4} \left(\Delta \hat{v}_{||}\right)^2 (\hat{\epsilon}_\alpha + \hat{\epsilon}_\beta) - \hat{\epsilon}_\alpha \frac{\hat{p}_{6,\alpha}}{\hat{M}_{0,\alpha}} - \hat{\epsilon}_\beta \frac{\hat{p}_{6,\beta}}{\hat{M}_{0,\beta}}, \tag{4.145}$$

with

$$\hat{\gamma}_\alpha = \begin{cases} \frac{1}{\sqrt{\hat{m}_\alpha}}, & \text{EM}, \\ \sqrt{\hat{m}_\alpha}, & \text{ET}, \end{cases} \tag{4.146}$$

$$\hat{\epsilon}_\alpha = \begin{cases} \frac{1}{\hat{m}_\alpha}, & \text{EM}, \\ 1, & \text{ET}, \end{cases} \tag{4.147}$$

$$\hat{\delta}_{\alpha\beta} = \sqrt{\frac{\hat{m}_\beta}{\hat{m}_\alpha}} \equiv \eta. \tag{4.148}$$

The normalized eqs. (4.114) and (4.113) then determine the normalized mixing quantities. The overall formulation presented here is universal for the ET and EM versions of the LBD collision operator.

4.4 Verification

Two verifications of the implemented discretized collision operators have been performed. First, the conservation properties are analyzed in a single application of the collision operator. Second, relaxation rates over several thousands of time steps are measured. This section summarizes the results published in Ref. [58]. The derivation of the analytical relaxation rates used in section 4.4.2 is given additionally.

4.4.1 Verification of Numerical Conservation Properties

The conservation of density, momentum, and energy (3.21)-(3.23) belong to the central properties of a collision operator. Significant efforts have been made to retain these properties upon discretizing the LBD collision operator. The following verification considers the investigation of these properties.

Conservation properties are tested with collisions of electrons and ions, where both species are initialized with distribution functions

$$\hat{f}_\alpha = \frac{\hat{n}_\alpha}{2(\pi\hat{T}_\alpha)^{3/2}} \left[\exp\left(-\frac{(\hat{v}_{||} - \hat{u}_{1,\alpha})^2 + \hat{\mu}\hat{B}}{\hat{T}_\alpha} \right) + \exp\left(-\frac{(\hat{v}_{||} - \hat{u}_{2,\alpha})^2 + \hat{\mu}\hat{B}}{\hat{T}_\alpha} \right) \right], \tag{4.149}$$

describing the superposition of two Maxwellians ("double" Maxwellian). Here, the shifts $\hat{u}_{1,\alpha}$ and $\hat{u}_{2,\alpha}$ can be chosen individually for each species. This choice is well suited for the test under consideration, given at least one flow $\neq 0$ since this distribution will not be an equilibrium. Otherwise, the case $C_\alpha f_\alpha = 0$ would trivially fulfill the conservation properties if this relation holds for the discretized version.

The verification of the conservation properties considers the BGK operator (3.163), the fourth-order finite difference (FD) discretization of the LBD operator (4.31)-(4.34) and the second-order finite volume (FV) discretization of the LBD operator (4.58). The velocity space grid is chosen as $v_{||,\max} = 8$ and $\mu_{\max} = 64$ for the BGK case and the FD and FV LBD operators, $v_{||,\max} = 3$, $\mu_{\max} = 9$ and $v_{||,\max} = 4$, $\mu_{\max} = 16$ respectively. The parallel velocity space grids are symmetric around 0, and the μ grid has its lower domain bound at zero. The number of grid points is varied to study convergence. The shifts are $\hat{u}_{1,\alpha} = 0$ and $\hat{u}_{2,\alpha} = -0.87\text{sign}(q_\alpha)$ for the BGK case and $\hat{u}_{1,\alpha} = -0.27$ and $\hat{u}_{2,\alpha} = 0.54$ for both LBD cases. For the real space discretization, either a slab or toroidal geometry[34] is chosen (the latter is used together with the label "guiding center corrections"), with profiles in density and temperature detailed in the original reference [58].

Fig. 4.4 contains the results of this conservation study*, where the average over the real space is shown (with no outliers present). For the BGK operator, which is only a function evaluation, the conservation properties essentially depend on the precision to which the velocity space moments can be calculated numerically (Fig. 4.4 (a)). The quadrature schemes presented in section 4.1 determine the conservation and are confirmed to be second-order for the trapezoidal method, fourth-order for Simpson, and much faster for Gauss-Laguerre quadrature. The LBD FD operator shows a fourth-order convergence of the conservation properties, given that the multi-species (ms) corrections discussed in section 3.2.5 for the mean flow and temperature are used (Fig. 4.4 (c)). As a comparison, the conservation using a $v_{||,\max} = 3$, $\mu_{\max} = 9$ box is shown, which is improved for small grids due to the enhanced resolution, but starts to become worse at large grids due to the cutoff of the distribution function. For the BGK and LBD FD operator, the effect of the use of "guiding center corrections" ($B^*_{||} \neq B$) is shown in (Fig. 4.4 (b) and (d)). For these two cases, the toroidal geometry mentioned above is used since $\mathbf{b} \cdot (\nabla \times \mathbf{b}) \neq 0$ in eq. (3.147) in such a geometry. The conservation properties of the LBD FV operator are shown in Fig. 4.4 (e). Here, the second-order convergence of the $(\Delta\hat{v}_{||})^2$ term in the corrections (4.81) of an initial version of the operator can be seen (green). A second version, where only this term has been corrected, shows the remaining errors constant with grid-spacing (orange), which are the boundary correction terms in eqs. (4.72) and (4.81). Correcting these yields a fully conservative discretization, where density, momentum, and energy are conserved up to machine precision (purple). Fig. 4.4 (f) shows the difference between the FD and the FV version.

*Upon calculating the total momentum, one has to consider the species dependent normalization in the `GENE-X` code. The single species momenta are normalized with $p_{\text{ref}} = m_\alpha v_{\text{th},\alpha}$ and thus

$$\hat{p}_{\text{tot}} = \sum_\alpha \hat{p}_\alpha \sqrt{\hat{m}_\alpha},$$

by choosing the total momentum to be normalized to mass $\hat{m} = 1$.

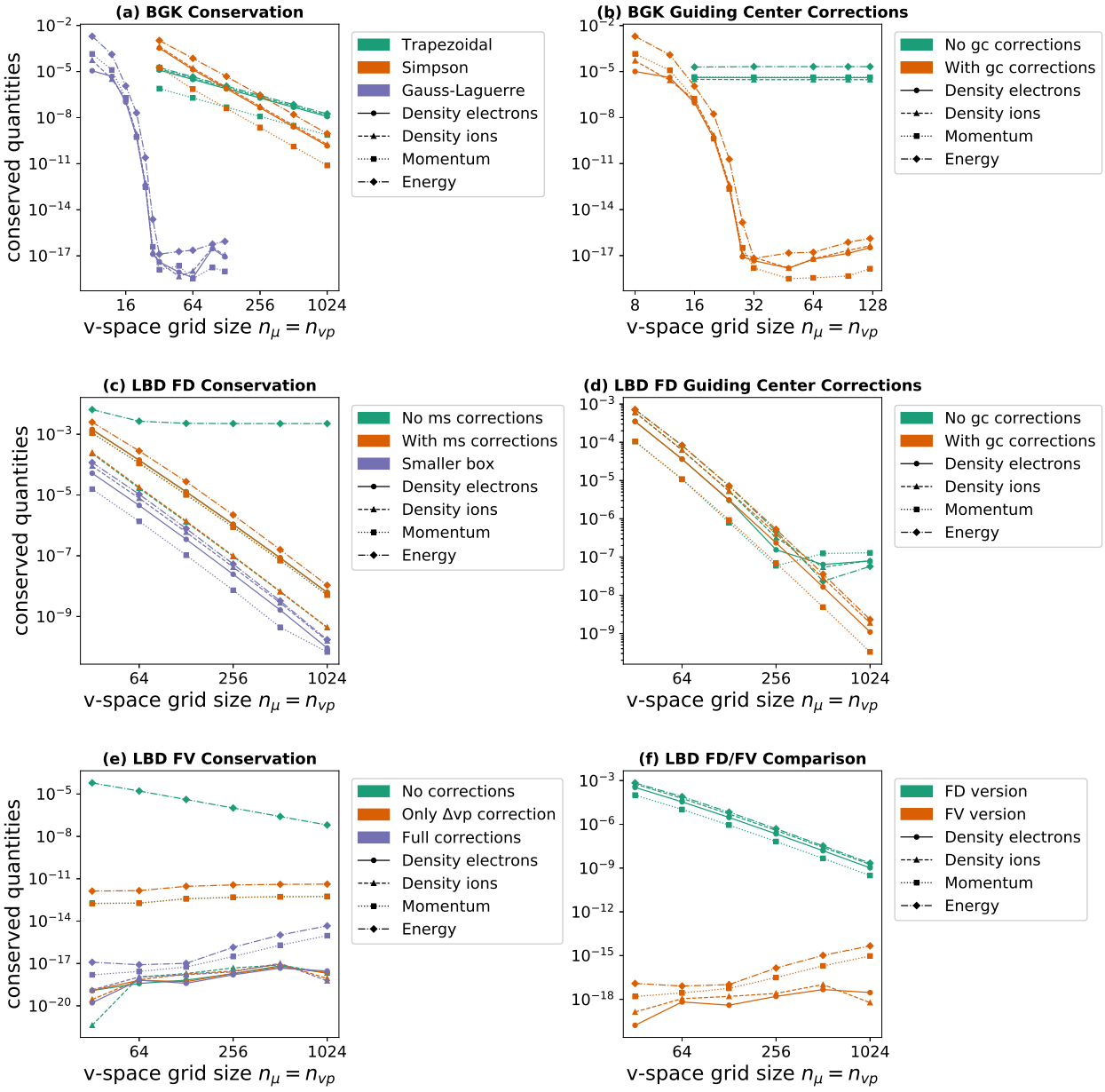

Figure 4.4. Verification of the conservation properties of the BGK, finite difference (FD), and finite volume (FV) LBD operators. The plots contain convergence curves of the conserved properties (different symbols and lines) against grid size. The abbreviation "gc" means guiding center, and "ms" means multi-species. Details on the sub-figures are described in the main text. Taken from Ref. [58].

4.4.2 Verification of Relaxation Rates

Another physical property of a collision operator is the relaxation towards an equilibrium state (section 3.2.3). This test has been initially performed by Hager in Ref. [152]. In the following, a summary of the analytical estimations of the relaxation curves is given*. The distributions of electrons and ions are initialized as shifted bi-Maxwellians,

$$\hat{f}_\alpha = \frac{\hat{n}_\alpha}{\pi^{3/2}\sqrt{\hat{T}_{||,\alpha}}\hat{T}_{\perp,\alpha}} \exp\left(-\frac{(\hat{v}_{||}-\hat{u}_\alpha)^2}{\hat{T}_{||,\alpha}} - \frac{\hat{\mu}\hat{B}}{\hat{T}_{\perp,\alpha}}\right). \tag{4.150}$$

This equation describes an anisotropic distribution function, which means that the temperatures along ($\hat{T}_{||,\alpha}$) and perpendicular ($\hat{T}_{\perp,\alpha}$) to the magnetic field are different. Further, these are chosen differently for electrons and ions. The effect of the collision operator on such a system is described by three different stages[125,127,128]. Since $\nu_{ee} \sim \sqrt{m_i/m_e}\nu_{ii} \sim (m_i/m_e)\nu_{ie}$[64], first electron-electron intra-species collisions will isotropize the electron distribution to a Maxwellian. Second, ion-ion intra-species collisions will isotropize the ions. Third, ion-electron inter-species collisions will thermalize the whole system. These processes can be modeled by coupled ordinary differential equations (ODEs)[66],

$$\frac{\mathrm{d}T_{\perp,\alpha}}{\mathrm{d}t} = -\frac{1}{2}\frac{\mathrm{d}T_{||,\alpha}}{\mathrm{d}t} = -\nu_{T,\alpha}(T_{\perp,\alpha} - T_{||,\alpha}), \tag{4.151}$$

$$\frac{\mathrm{d}T_\alpha}{\mathrm{d}t} = -\nu_{E,\alpha\beta}(T_\alpha - T_\beta), \tag{4.152}$$

$$T_\alpha = \frac{2}{3}T_{\perp,\alpha} + \frac{1}{3}T_{||,\alpha}, \tag{4.153}$$

where the index T labels temperature isotropization and E equilibration. For the equilibration process, it is easy to see that the temperature $T_E = (T_\mathrm{e} + T_\mathrm{i})/2$ describes the system equilibrium since the right-hand side in the time evolution equation vanishes for this value. The above equations can be solved by any computer algebra tool to obtain analytical relax-

*Thanks to R. Hager for pointing out the necessary steps to obtain analytical estimations for the relaxation curves.

ation curves

$$T_\alpha(t) = T_E + \Big(T_\alpha(0) - T_E\Big)\mathrm{e}^{-2\nu_{E,\mathrm{ei}}t}, \tag{4.154}$$

$$T_{||,\alpha}(t) = T_E + \Big(T_E - T_\alpha(0)\Big)\frac{3\nu_{T,\alpha}}{2\nu_{E,\mathrm{ei}} - 3\nu_{T,\alpha}}\mathrm{e}^{-2\nu_{E,\mathrm{ei}}t} + \left(T_{||,\alpha}(0) - \frac{2\nu_{E,\mathrm{ei}}T_E - 3\nu_{T,\alpha}T_\alpha(0)}{2\nu_{E,\mathrm{ei}} - 3\nu_{T,\alpha}}\right)\mathrm{e}^{-3\nu_{T,\alpha}t}, \tag{4.155}$$

$$T_{\perp,\alpha}(t) = T_E + \Big(T_E - T_\alpha(0)\Big)\frac{3\nu_{T,\alpha}}{2\nu_{E,\mathrm{ei}} - 3\nu_{T,\alpha}}\mathrm{e}^{-2\nu_{E,\mathrm{ei}}t} + \left(T_{\perp,\alpha}(0) - \frac{2\nu_{E,\mathrm{ei}}T_E - 3\nu_{T,\alpha}T_\alpha(0)}{2\nu_{E,\mathrm{ei}} - 3\nu_{T,\alpha}}\right)\mathrm{e}^{-3\nu_{T,\alpha}t}. \tag{4.156}$$

valid for $\alpha \in \{\mathrm{e}, \mathrm{i}\}$.

The relaxation rates that are used are given by approximates[66],

$$\nu_{T,\mathrm{i}} = 1.9187 \times 10^{-8}\sqrt{\frac{m_\mathrm{p}}{m_\mathrm{i}}}Z^2 n T^{-3/2}\ln\Lambda, \tag{4.157}$$

$$\nu_{T,\mathrm{e}} = 8.22163 \times 10^{-7} n T^{-3/2}\ln\Lambda, \tag{4.158}$$

$$\nu_{E,\mathrm{ei}} = 3.16621 \times 10^{-9}\frac{m_\mathrm{p}}{m_\mathrm{i}}Z^2 n T^{-3/2}\ln\Lambda, \tag{4.159}$$

where $T_{\perp,\alpha} \approx T_{||,\alpha}$, $T_\mathrm{i} \approx T_\mathrm{e}$ and $n_\mathrm{i} \approx n_\mathrm{e}$ is assumed. The density n must be given in cgs units, the temperature T in eV, Z is the ion charge state, $m_\mathrm{i}/m_\mathrm{p}$ the ion to proton mass ratio, and $\ln\Lambda$ the Coulomb logarithm evaluated with T and n.

Initializing different parallel flows for electrons and ions in eq. (4.150) will lead to flow relaxation. An approximation can be obtained by considering the flow relaxation due to the small mass ratio friction force (parallel component)[16]

$$\mathbf{R}_\mathrm{ei} = -\Gamma_\mathrm{ee} n_\mathrm{i} m_\mathrm{e}\int \mathrm{d}\mathbf{v} f_\mathrm{e}(\mathbf{v})\frac{\mathbf{v}}{v^3} + \frac{m_\mathrm{e} n_\mathrm{e}}{\tau_\mathrm{e}}\mathbf{u}_\mathrm{i}, \tag{4.160}$$

where Γ_ee is given by (3.10) and $\tau_\mathrm{e} = 3\sqrt{\pi}v_{\mathrm{th,e}}^3/(4n_\mathrm{i}\Gamma_\mathrm{ee}) \sim \nu_\mathrm{ee}^{-1}$ is the electron collision time. For this approximation, the electron distribution is assumed to be a shifted Maxwellian (like eq. (3.34) but with flow shift $\mathbf{u}_\mathrm{e}$). Using $(\mathbf{v} - \mathbf{u}_\mathrm{e})^2 = v^2 - 2u_\mathrm{e}v\cos\theta + u_\mathrm{e}^2$ and expanding in $u_\mathrm{e}/v_\mathrm{th,e} \ll 1$ yields

$$\begin{aligned} f_\mathrm{e} &= \frac{n_\mathrm{e}}{\pi^{3/2}v_\mathrm{th,e}^3}\exp\left(-\frac{v^2 - 2u_\mathrm{e}v\cos\theta + u_\mathrm{e}^2}{v_\mathrm{th,e}^2}\right), \\ &\approx \frac{n_\mathrm{e}}{\pi^{3/2}v_\mathrm{th,e}^3}\exp\left(-\frac{v^2}{v_\mathrm{th,e}^2}\right)\left(1 + \frac{2u_\mathrm{e}v\cos\theta}{v_\mathrm{th,e}^2} + \mathcal{O}\left(\frac{u_\mathrm{e}^2}{v_\mathrm{th,e}^2}\right)\right). \end{aligned} \tag{4.161}$$

Considering the parallel component $R_{||,\mathrm{ei}} = \mathbf{R}_{\mathrm{ei}} \cdot \mathbf{b}$, one can use spherical coordinates (v, θ, ϕ) in velocity space (as in section 3.2.2) with the toroidally symmetric volume element $\mathrm{d}\mathbf{v} = 2\pi v^2 \sin\theta \mathrm{d}v\mathrm{d}\theta$ and $v_{||} = v\cos\theta$ to write

$$R_{||,\mathrm{ei}} \approx -\frac{2\pi\Gamma_{\mathrm{ee}} n_{\mathrm{i}} m_{\mathrm{e}} n_{\mathrm{e}}}{\pi^{3/2} v_{\mathrm{th,e}}^3} \int_0^{\pi} \mathrm{d}\theta \sin\theta\cos\theta \int_0^{\infty} \mathrm{d}v \exp\left(-\frac{v^2}{v_{\mathrm{th,e}}^2}\right)\left(1 + \frac{2u_{\mathrm{e}} v\cos\theta}{v_{\mathrm{th,e}}^2}\right) + \frac{m_{\mathrm{e}} n_{\mathrm{e}}}{\tau_{\mathrm{e}}} u_{\mathrm{i}}. \tag{4.162}$$

The θ integral over the first term is an even integral over an odd function, thus zero. For the second term, the v integral yields $v_{\mathrm{th,e}}^2/2$ and the θ integral $2/3$. Thus,

$$R_{||,\mathrm{ei}} = -m_{\mathrm{e}} n_{\mathrm{e}} \nu_e (u_{\mathrm{e}} - u_{\mathrm{i}}). \tag{4.163}$$

Since also $R_{||,\mathrm{ei}} := -\mathrm{d}(m_{\mathrm{e}} n_{\mathrm{e}} u_{\mathrm{e}})/\mathrm{d}t$, the momentum relaxation rate is the same as the electron collision rate $\nu_{\mathrm{e}} = \tau_{\mathrm{e}}^{-1}$ in this case. Since the total momentum must be conserved, the equilibrium flow u_E can be determined via,

$$p_{\mathrm{tot}} = m_{\mathrm{e}} u_{\mathrm{e}} + m_{\mathrm{i}} u_{\mathrm{i}} = (m_{\mathrm{e}} + m_{\mathrm{i}}) u_E. \tag{4.164}$$

This relation allows solving the ODE analytically,

$$u_{\mathrm{e}}(t) = u_E + \Big(u_{\mathrm{e}}(0) - u_E\Big)\mathrm{e}^{-(1+m_{\mathrm{e}}/m_{\mathrm{i}})\nu_e t}, \tag{4.165}$$

$$u_{\mathrm{i}}(t) = u_E + \frac{m_{\mathrm{e}}}{m_{\mathrm{i}}}\Big(u_E - u_{\mathrm{e}}(0)\Big)\mathrm{e}^{-(1+m_{\mathrm{e}}/m_{\mathrm{i}})\nu_e t}. \tag{4.166}$$

The numerical tests[58] use the same plasma parameters as in Ref. [152]. Essentially, an electron-deuterium ($m_{\mathrm{D}} = 2m_{\mathrm{p}}$) system is simulated, where both species have different parallel and perpendicular temperatures as well as mean flows. The verification is performed with the EM (entropic momentum relaxation) and ET (entropic temperature relaxation) versions given by eqs. (3.135), (3.140) and (3.162). The grids are chosen as $\hat{v}_{||,\max} = 4$, $\hat{\mu}_{\max} = 8$ with $N = 513$ and $M = 64$ for the BGK operator, $\hat{v}_{||,\max} = 3$, $\hat{\mu}_{\max} = 9$ with $N = 126$ and $M = 128$ for the LBD FD with ET relaxation and $\hat{v}_{||,\max} = 4$, $\hat{\mu}_{\max} = 8$ with $N = 126$ and $M = 128$ for the LBD FD with EM relaxation. These values are chosen such that the simulations are stable over the long simulation period (the energy loss due to insufficient conservation properties would otherwise lead to an abrupt end). For the LBD FV operator, a grid with $\hat{v}_{||,\max} = 2$, $\hat{\mu}_{\max} = 4$ with $N = 63$ and $M = 64$ could be used without issues in the stability of the simulation.

Fig. 4.5 shows the result of the relaxation test against the analytical approximations (4.154)-(4.156) and (4.165)-(4.166). As expected, the overall temperature relaxation happens in three

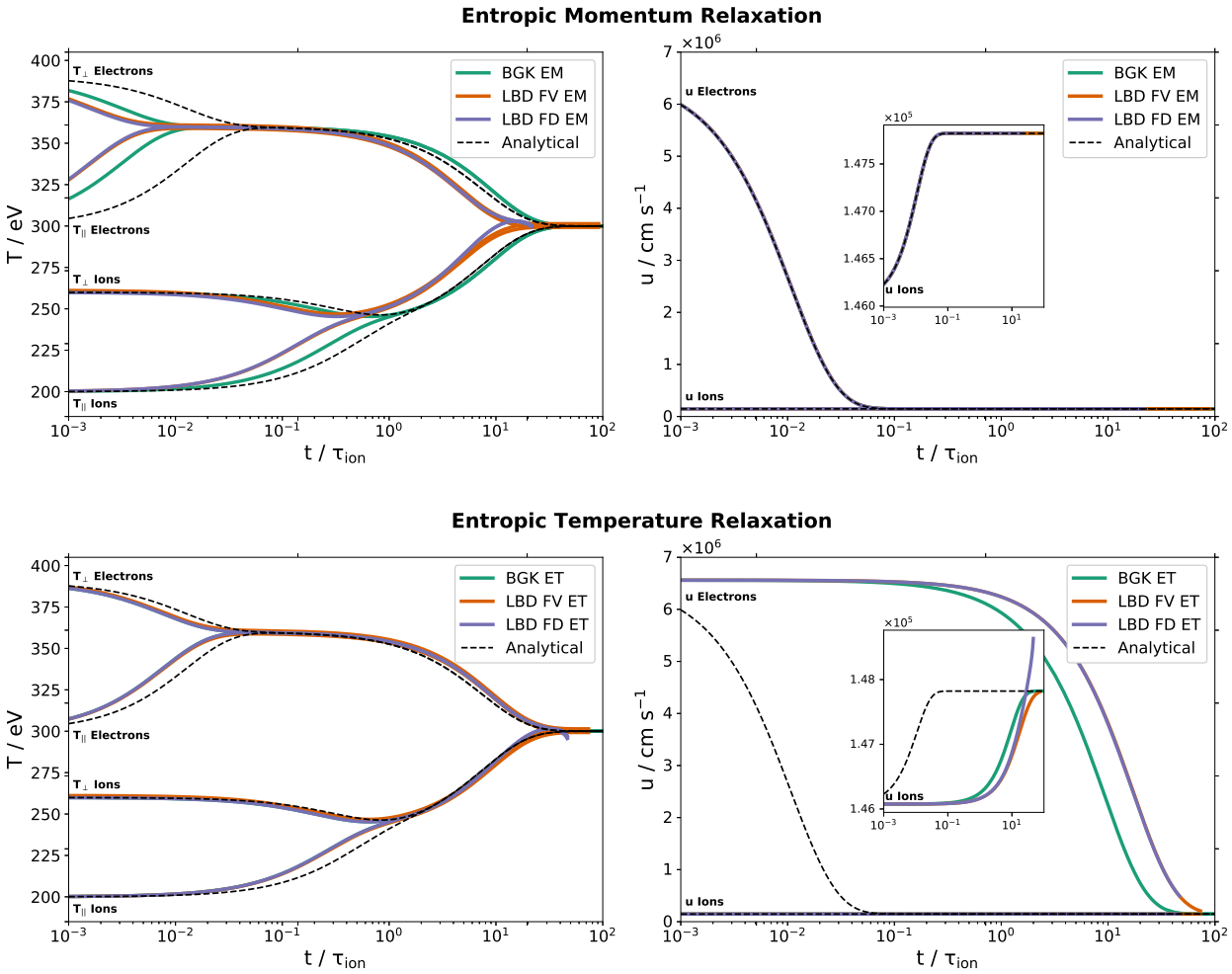

Figure 4.5. Relaxation of an anisotropic electron-deuterium system used to verify the implemented BGK and LBD collision operators. The top row shows the entropic momentum (EM) version, and the bottom row the entropic temperature (ET) version. Taken from Ref. [58].

stages over a temporal scale of five orders of magnitude in terms of the ion collision time[66]. The ratio between the equilibration processes is approximately $\sqrt{m_e/m_D} = 1/60$. Analyzing the numerical relaxation rates obtained by the discretized collision operators, one can observe the qualitative difference between the EM and ET versions. The EM versions reproduce the flow relaxation curves exactly while having an error in the temperature relaxation. The ET versions have an error in the flow relaxation while approximating the temperature relaxation much better. The relative factor of 2 between the LBD and BGK rates (3.162) can also be observed. Finally, the LBD FD version fails at the end of the simulation, as seen by a kink for both the EM and ET versions. This failure happens due to the energy loss caused by the discretized version's insufficient conservation properties. In fact, after the last point of the LBD FD curve, the simulation became unstable and ended abruptly.

4.4.3 Additional Verifications

Additional verifications have been performed by checking the H-theorem (3.24) for all cases considered. The H-function (3.25) is calculated as

$$\mathcal{H}_{\alpha\beta} = 2\pi \int \frac{B^*_{||}}{m_\alpha} \ln(f_\alpha) C_{\alpha\beta}(f_\alpha) \mathrm{d}v_{||} \mathrm{d}\mu. \tag{4.167}$$

In practice, the logarithm is modified $\ln(f_\alpha) \to \ln(|f_\alpha| + \epsilon)$, where ϵ is the machine-epsilon ($\sim 10^{-16}$) since the numerical scheme is not positivity preserving. In all cases considered, the H-theorem is fulfilled, and no violations have been found so far.

4.5 Time Stepping Schemes and Stability

In this section, the various discretizations of the LBD collision operator are analyzed concerning stability, and advanced time-stepping schemes are introduced. Using the normalized version of the equations is more appropriate since these are implemented in a code. Further, the approximation $B^*_{||} \approx B$ will be made for the stability analysis.

Including collisional physics into the gyrokinetic system poses a numerical challenge since, due to the disparate time scales, collisions are numerically stiff[165]. Explicit schemes are often not suited to treat such equations[166]. This section shows that the diffusive nature of electron-electron collisions poses the main limitation at high temperatures. Eventually, implicit schemes need to be considered since the time step reduces with increasing collisionality, also slowing down the Vlasov part of the code. With advanced splitting methods, explicit schemes can still be used in the cases considered here. For example, the time step of the LBD simulation in section 5.1 could be chosen a factor of two larger with the splitting scheme introduced in section 4.5.4.

The simplest way to achieve an optimal time step in a simulation is trial and error. As the time step depends on the grid spacing, this cannot be performed on a reduced problem, and the fully resolved problem needs to be chosen to check for numerical stability. This situation could be improved since many compute nodes on a supercomputer must be occupied for such tests. Thus, informed time step criteria are a valuable tool to reduce a simulation's resource usage and setup phase. In the following, three different time step criteria, differing in accuracy, are presented.

4.5.1 Simple Time-Step Criteria

The LBD collision operator (3.156) is essentially an advection-diffusion operator (for the definition, see Ref. [160]). For an advection operator, a fundamental constraint on the time step of a finite difference scheme is given by the Courant-Friedrichs-Lewy[167] (CFL) condition[160,168], $\Delta t \leq C_a \Delta x/a$. Here, C_a is called the Courant number* and $a > 0$ is a constant advection speed in an equation $\partial u/\partial t + a\,\partial u/\partial x = 0$. For a pure diffusion equation $\partial u/\partial t + d\,\partial^2 u/\partial x^2 = 0$, there is a similar condition[160,168], $\Delta t \leq C_d(\Delta x)^2/d$, where $d > 0$ is the diffusion coefficient, and C_d could be called "diffusive Courant number". The same considerations hold for the finite volume scheme constructed since the numerical fluxes are computed using finite differences[169]. The above criteria hold for constant advection and diffusion coefficients. Generally, for hyperbolic or parabolic problems, the coefficients are replaced by the maximum advection/diffusion coefficients in the system[169]. For the LBD collision operator (3.156), the CFL conditions can be written as,

$$v_{||}\text{ adv}: \quad \Delta\hat{t} \leq C_a \frac{\Delta\hat{v}_{||}}{\hat{\nu}_{\alpha\beta}\max(\hat{v}_{||})}, \qquad v_{||}\text{ diff}: \quad \Delta\hat{t} \leq C_d \frac{2(\Delta\hat{v}_{||})^2}{\hat{\nu}_{\alpha\beta}\hat{T}_{\alpha\beta}}, \tag{4.168}$$

$$\mu\text{ adv}: \quad \Delta\hat{t} \leq C_a \frac{\Delta\hat{\mu}}{2\hat{\nu}_{\alpha\beta}(\max(\hat{\mu}) + \hat{T}_{\alpha\beta}/\hat{B})}, \quad \mu\text{ diff}: \quad \Delta\hat{t} \leq C_d \frac{(\Delta\hat{\mu})^2}{2\hat{\nu}_{\alpha\beta}\max(\hat{\mu})\hat{T}_{\alpha\beta}/\hat{B}}. \tag{4.169}$$

It is important to note that first, these expressions are only necessary but not sufficient conditions, and second, these only consider advection and diffusion as well as parallel and perpendicular dynamics independently. The Courant numbers for second and fourth-order centered difference stencils in space, combined with an RK4 scheme in time, are given by[160]

$$C_a^{2,\mathrm{CD}} = 2.82, \qquad C_a^{4,\mathrm{CD}} = 2.05, \tag{4.170}$$

$$C_d^{2,\mathrm{CD}} = 0.69, \qquad C_d^{4,\mathrm{CD}} = 0.52. \tag{4.171}$$

The question of advection or diffusion dominating can be analyzed by considering the so-called Péclet number[160,162] $\mathrm{Pe} = aL/d$, where L is a typical length scale. Taking the grid spacing as the length scale, the local Péclet numbers for the LBD operator are

$$\mathrm{Pe}_{||}(\hat{v}_{||}) = \frac{2\hat{v}_{||}\Delta\hat{v}_{||}}{\hat{T}_{\alpha\beta}}, \qquad \mathrm{Pe}_{\mu}(\hat{\mu}) = \frac{(\hat{\mu}\hat{B} + \hat{T}_{\alpha\beta})\Delta\hat{\mu}}{\hat{T}_{\alpha\beta}\hat{\mu}} = \frac{\hat{B}\Delta\hat{\mu}}{\hat{T}_{\alpha\beta}} + \frac{\Delta\hat{\mu}}{\hat{\mu}}. \tag{4.172}$$

If $\mathrm{Pe} \ll 1$, diffusion dominates, whereas advection dominates for $\mathrm{Pe} \gg 1$. Given this information, one can choose the correct CFL criterion (4.168)-(4.169) to approximate the maximal possible time step. Further, taking the velocity space grid as fixed, it is apparent from (4.172)

*Typically the symbol ν is used, which is avoided here due to possible ambiguities with the collision frequency.

that the Péclet numbers will be dominantly affected by the plasma temperature (since magnetic field changes are typically much weaker compared to temperature changes). The varying temperature means that considering a simulation of a fusion device that spans a domain from the hot plasma core to the cold SOL, the LBD collision operator will change its behavior from diffusion dominated in the core to advection dominated in the SOL.

The case where $\mathrm{Pe} = 1$ is more complicated in practice since one cannot easily deduce if advection or diffusion will dominate the CFL restrictions on the time step. The same holds for the case if parallel or perpendicular dynamics are dominating. However, conditions (4.168)-(4.169) are still useful expressions to get an approximate idea about the maximum Δt. The following section presents improved criteria.

4.5.2 Eigenvalue Analysis

As already mentioned, the discretization of the gyrokinetic equation in `GENE-X` is based on the method of lines[160,168]. First, the (phase-) space dimensions are discretized, followed by applying a time integrator such as, e.g., RK4. For the case of collisions, the dimension of interest is the velocity space. In the following, the action of the collision operator on the distribution function $C_{\alpha\beta}(f_\alpha)$ is considered. Within a finite difference or finite volume discretization, this can be viewed as the action of a collision matrix $\mathbb{L}_C$ on the distribution function vector $\mathbf{f}$. For example in 1D, one can write $\mathbf{f} = (f(1), f(2), f(3), \dots f(N))^\mathsf{T}$ and the collision matrix,

$$\mathbb{L}_C = \begin{pmatrix} \alpha(1) & \gamma(1) & \iota(1) & 0 & 0 & 0 & 0 \\ \beta(2) & \alpha(2) & \gamma(2) & \iota(2) & 0 & 0 & 0 \\ \kappa(3) & \ddots & \ddots & \ddots & \ddots & 0 & 0 \\ 0 & \ddots & \ddots & \ddots & \ddots & \ddots & 0 \\ 0 & 0 & \ddots & \ddots & \ddots & \ddots & \iota(N-2) \\ 0 & 0 & 0 & \kappa(N-1) & \beta(N-1) & \alpha(N-1) & \gamma(N-1) \\ 0 & 0 & 0 & 0 & \kappa(N) & \beta(N) & \alpha(N) \end{pmatrix}, \tag{4.173}$$

where this form of $\mathbb{L}_C$ allows for up to fourth-order symmetric stencils. For a second-order scheme $\iota(i) = \kappa(i) = 0$. The change due to collisions is then $\mathrm{d}\mathbf{f}/\mathrm{d}t|_{\mathrm{coll}} = \mathbb{L}_C \cdot \mathbf{f}$.

One can call this a semi-discrete formulation[168]. The full discretized equation depends on the time-stepping scheme. For the simplest scheme, explicit Euler, it can be written as $\mathbf{f}(t+\Delta t) = \mathbf{f}(t) + \Delta t\, \mathbb{L}_C \cdot \mathbf{f}(t)$.

The standard criterion for the stability of the method of lines is given in Ref. [160]. Here a summary is given. Assuming the matrix $\mathbb{L}_C$ is normal, the method is based on the stability region of the explicit time stepping scheme $\mathcal{S} = \{z \in \mathbb{C} : |R(z)| \leq 1\}$, defined by all points enclosed by the contour where the stability function $R(z)$ equals one. The scheme is stable if the set of eigenvalues of the matrix scaled by the time-step lies within this stability region, $\Delta t \lambda_k \in \mathcal{S}$, $\forall k$, where λ_k are the eigenvalues of $\mathbb{L}_C$. The case of non-normal matrices is treated in section 4.5.3.

Construction of the Total Collision Matrix

The stability of the full LBD operator must be analyzed by combining the parallel and perpendicular parts. It is illustrative to consider, as an example, a grid with two points in each $v_{||}$ and μ. For each μ, the parallel operator would act on $\mathbf{f}_{2\times 2,||} = (f(1,j), f(2,j))^{\mathsf{T}}$ and for each $v_{||}$ the perpendicular operator on $\mathbf{f}_{2\times 2,\mu} = (f(i,1), f(i,2))^{\mathsf{T}}$. This results in the individual matrices (for the second-order finite difference discretization),

$$\mathbb{L}_{2,||}^{N=2} = \begin{pmatrix} 1 - d_{||} & \frac{d_{||}}{2} + a_{||}(1) \\ \frac{d_{||}}{2} - a_{||}(2) & 1 - d_{||} \end{pmatrix}, \quad \mathbb{L}_{2,\mu}^{M=2} = \begin{pmatrix} 2 - 2d_{\mu}(1) & d_{\mu}(1) + a_{\mu}(1) \\ d_{\mu}(2) - a_{\mu}(2) & 2 - 2d_{\mu}(2) \end{pmatrix}, \tag{4.174}$$

where a and d denote the operator's grid-dependent, parallel, and perpendicular advection and diffusion coefficients (details do not matter at this point). The distribution function vector can be written as $\mathbf{f}_{2\times 2} = (f(1,1), f(1,2), f(2,1), f(2,2))^{\mathsf{T}}$. Neighboring points in $v_{||}$ are now separated by points in μ, whereas neighboring points in μ are still neighbors. It can

be easily figured out that the parallel and perpendicular collision matrices change to

$$\mathbb{L}_{2,||}^{2\times2} = \begin{pmatrix} 1-d_{||} & 0 & \frac{d_{||}}{2}+a_{||}(1) & 0 \\ 0 & \frac{d_{||}}{2}-a_{||}(2) & 0 & 1-d_{||} \\ 1-d_{||} & 0 & \frac{d_{||}}{2}+a_{||}(1) & 0 \\ 0 & \frac{d_{||}}{2}-a_{||}(2) & 0 & 1-d_{||} \end{pmatrix}, \tag{4.175}$$

$$\mathbb{L}_{2,\mu}^{2\times2} = \begin{pmatrix} 2-2d_{\mu}(1) & d_{\mu}(1)+a_{\mu}(1) & 0 & 0 \\ d_{\mu}(2)-a_{\mu}(2) & 2-2d_{\mu}(2) & 0 & 0 \\ 0 & 0 & 2-2d_{\mu}(1) & d_{\mu}(1)+a_{\mu}(1) \\ 0 & 0 & d_{\mu}(2)-a_{\mu}(2) & 2-2d_{\mu}(2) \end{pmatrix}. \tag{4.176}$$

Further, it can be seen that the matrices are related to the original ones by $\mathbb{L}_{2,||}^{2\times2} = \mathbb{L}_{2,||}^{N=2} \otimes \mathbb{I}_{M=2}$ and $\mathbb{L}_{2,\mu}^{2\times2} = \mathbb{I}_{N=2} \otimes \mathbb{L}_{2,\mu}^{M=2}$, where $\otimes$ denotes the Kronecker product and $\mathbb{I}$ the unit matrix with dimensionality given by N, the number of $v_{||}$ points or M, the number of μ points. The sum of the two matrices gives the total action of the collision operator. In terms of the original matrices, this can be written as a Kronecker sum[170],

$$\mathbb{L}_C = \mathbb{L}_{||} \otimes \mathbb{I}_M + \mathbb{I}_N \otimes \mathbb{L}_{\mu}. \tag{4.177}$$

The above expression also holds for a more generalized grid since the assumption of a 2×2 grid is arbitrary and only used for visualization purposes. Equation (4.177) is very convenient since it allows individually constructing the parallel and perpendicular collision matrices, combining the result afterward.

LBD Collision Matrices

Next, the collision matrices for the different discretizations of the LBD collision operator are given as components of the general form of the collision matrix (4.173). For a simpler

presentation, the following abbreviations will be used

$$E(i) \equiv \frac{\hat{v}_{||}(i) - \hat{u}_{\alpha\beta}}{\Delta\hat{v}_{||}}, \qquad F \equiv \frac{\hat{T}_{\alpha\beta}}{(\Delta\hat{v}_{||})^2}, \tag{4.178}$$

$$G(j) \equiv \frac{\hat{\mu}(j) + \hat{T}_{\alpha\beta}/\hat{B}}{\Delta\hat{\mu}}, \qquad H(j) \equiv \frac{\hat{T}_{\alpha\beta}\hat{\mu}(j)}{\hat{B}(\Delta\hat{\mu})^2}. \tag{4.179}$$

The parallel part in second-order finite difference discretization is given by

$$\alpha_{2,||}(i) = \hat{\nu}_{\alpha\beta}\Big(1 - F\Big), \quad \beta_{2,||}(i) = \hat{\nu}_{\alpha\beta}\left(-\frac{E(i)}{2} + \frac{F}{2}\right), \quad \gamma_{2,||}(i) = \hat{\nu}_{\alpha\beta}\left(\frac{E(i)}{2} + \frac{F}{2}\right). \tag{4.180}$$

The corresponding perpendicular part is

$$\alpha_{2,\mu}(j) = \hat{\nu}_{\alpha\beta}\Big(2 - 4H(j)\Big), \qquad j > 1, \tag{4.181}$$

$$\beta_{2,\mu}(j) = \hat{\nu}_{\alpha\beta}\Big(-G(j) + 2H(j)\Big), \tag{4.182}$$

$$\gamma_{2,\mu}(j) = \hat{\nu}_{\alpha\beta}\Big(G(j) + 2H(j)\Big), \qquad j > 1. \tag{4.183}$$

The first row is different due to the change in the stencil. It reads,

$$\mathbb{L}_{2,\mu}(1,1) = \hat{\nu}_{\alpha\beta}\Big(2 - 3G(1) + 4H(1)\Big), \qquad \mathbb{L}_{2,\mu}(1,2) = \hat{\nu}_{\alpha\beta}\Big(4G(1) - 10H(1)\Big), \tag{4.184}$$

$$\mathbb{L}_{2,\mu}(1,3) = \hat{\nu}_{\alpha\beta}\Big(G(1) + 8H(1)\Big), \qquad \mathbb{L}_{2,\mu}(1,4) = -2\hat{\nu}_{\alpha\beta}H(1), \tag{4.185}$$

$$\mathbb{L}_{2,\mu}(1,j) = 0, \quad j > 4. \tag{4.186}$$

The parallel part of the fourth-order finite difference discretization is,

$$\alpha_{4,||}(i) = \hat{\nu}_{\alpha\beta}\left(1 - \frac{5}{4}F\right), \qquad \beta_{4,||}(i) = \hat{\nu}_{\alpha\beta}\left(-\frac{2}{3}E(i) + \frac{2}{3}F\right), \tag{4.187}$$

$$\gamma_{4,||}(i) = \hat{\nu}_{\alpha\beta}\left(\frac{2}{3}E(i) + \frac{2}{3}F\right), \qquad \kappa_{4,||}(i) = \hat{\nu}_{\alpha\beta}\left(-\frac{1}{12}E(i) - \frac{1}{24}F\right), \tag{4.188}$$

$$\iota_{4,||}(i) = \hat{\nu}_{\alpha\beta}\left(\frac{1}{12}E(i) - \frac{1}{24}F\right), \tag{4.189}$$

and the corresponding perpendicular part

$$\alpha_{4,\mu}(j) = \hat{\nu}_{\alpha\beta}\left(2 - 5H(j)\right), \qquad j > 2, \tag{4.190}$$

$$\beta_{4,\mu}(j) = \hat{\nu}_{\alpha\beta}\left(-\frac{4}{3}G(j) + \frac{8}{3}H(j)\right), \qquad j > 2, \tag{4.191}$$

$$\gamma_{4,\mu}(j) = \hat{\nu}_{\alpha\beta}\left(\frac{4}{3}G(j) + \frac{8}{3}H(j)\right), \qquad j > 2, \tag{4.192}$$

$$\kappa_{4,\mu}(j) = \hat{\nu}_{\alpha\beta}\left(-\frac{1}{6}G(j) - \frac{1}{6}H(j)\right), \tag{4.193}$$

$$\iota_{4,\mu}(j) = \hat{\nu}_{\alpha\beta}\left(\frac{1}{6}G(j) - \frac{1}{6}H(j)\right), \qquad j > 2. \tag{4.194}$$

The first row is modified due to the different stencils,

$$\mathbb{L}_{4,\mu}(1,1) = \hat{\nu}_{\alpha\beta}\left(2 - \frac{25}{6}G(1) + \frac{15}{2}H(1)\right), \quad \mathbb{L}_{4,\mu}(1,2) = \hat{\nu}_{\alpha\beta}\left(8G(1) - \frac{77}{3}H(1)\right), \tag{4.195}$$

$$\mathbb{L}_{4,\mu}(1,3) = \hat{\nu}_{\alpha\beta}\left(-6G(1) + \frac{107}{3}H(1)\right), \quad \mathbb{L}_{4,\mu}(1,4) = \hat{\nu}_{\alpha\beta}\left(\frac{8}{3}G(1) - 26H(1)\right), \tag{4.196}$$

$$\mathbb{L}_{4,\mu}(1,5) = \hat{\nu}_{\alpha\beta}\left(-\frac{1}{2}G(1) + \frac{61}{6}H(1)\right), \quad \mathbb{L}_{4,\mu}(1,6) = \hat{\nu}_{\alpha\beta}\left(-\frac{5}{3}H(1)\right), \tag{4.197}$$

$$\mathbb{L}_{4,\mu}(1,j) = 0, \quad j > 6, \tag{4.198}$$

as well as the second row,

$$\mathbb{L}_{4,\mu}(2,1) = \hat{\nu}_{\alpha\beta}\left(-\frac{1}{2}G(2) + \frac{5}{3}H(2)\right), \quad \mathbb{L}_{4,\mu}(2,2) = \hat{\nu}_{\alpha\beta}\left(2 - \frac{5}{3}G(2) - \frac{5}{2}H(2)\right), \tag{4.199}$$

$$\mathbb{L}_{4,\mu}(2,3) = \hat{\nu}_{\alpha\beta}\left(3G(2) - \frac{2}{3}H(2)\right), \quad \mathbb{L}_{4,\mu}(2,4) = \hat{\nu}_{\alpha\beta}\left(-G(2) - \frac{7}{3}H(2)\right), \tag{4.200}$$

$$\mathbb{L}_{4,\mu}(2,5) = \hat{\nu}_{\alpha\beta}\left(\frac{1}{6}G(2) - H(2)\right), \quad \mathbb{L}_{4,\mu}(2,6) = \hat{\nu}_{\alpha\beta}\left(-\frac{1}{6}H(2)\right), \tag{4.201}$$

$$\mathbb{L}_{4,\mu}(2,j) = 0, \quad j > 6. \tag{4.202}$$

For the finite volume discretization, the parallel part is

$$\alpha_{V,||}(i) = \hat{\nu}_{\alpha\beta}\left(\frac{1}{2} - F\right), \qquad 1 < i < N, \tag{4.203}$$

$$\beta_{V,||}(i) = \hat{\nu}_{\alpha\beta}\left(-\frac{E(i-\frac{1}{2})}{2} + \frac{F}{2}\right), \qquad i < (N-1), \tag{4.204}$$

$$\gamma_{V,||}(i) = \hat{\nu}_{\alpha\beta}\left(\frac{E(i+\frac{1}{2})}{2} + \frac{F}{2}\right), \qquad i > 1, \tag{4.205}$$

with boundary conditions realized as modifications to the first and last row,

$$\mathbb{L}_{V,||}(1,1) = \hat{\nu}_{\alpha\beta}\left(\frac{1}{2}E(\frac{1}{2}) - \frac{1}{2}F\right), \quad \mathbb{L}_{V,||}(N,N-1) = \hat{\nu}_{\alpha\beta}\left(-\frac{1}{2}E(N-\frac{1}{2}) + \frac{1}{2}F\right), \tag{4.206}$$

$$\mathbb{L}_{V,||}(1,2) = \hat{\nu}_{\alpha\beta}\left(\frac{1}{2}E(\frac{1}{2}) + \frac{1}{2}F\right), \qquad \mathbb{L}_{V,||}(N,N) = \hat{\nu}_{\alpha\beta}\left(-\frac{1}{2}E(N-\frac{1}{2}) - \frac{1}{2}F\right), \tag{4.207}$$

$$\mathbb{L}_{V,||}(1,i) = 0, \quad i > 2, \qquad \mathbb{L}_{V,||}(N,i) = 0, \quad i < (N-1), \tag{4.208}$$

and the perpendicular part,

$$\alpha_{V,\mu}(j) = \hat{\nu}_{\alpha\beta}\left(1 - 2\left(H(j+\frac{1}{2}) + H(j-\frac{1}{2})\right)\right), \qquad 1 < j < M, \tag{4.209}$$

$$\beta_{V,\mu}(j) = \hat{\nu}_{\alpha\beta}\left(-\widetilde{G}(i-\frac{1}{2}) + 2H(j-\frac{1}{2})\right), \qquad j < (M-1), \tag{4.210}$$

$$\gamma_{V,\mu}(j) = \hat{\nu}_{\alpha\beta}\left(\widetilde{G}(i+\frac{1}{2}) + 2H(j+\frac{1}{2})\right), \qquad j > 1, \tag{4.211}$$

with $\widetilde{G}(j) = \hat{\mu}(j)/\Delta\hat{\mu}$ and boundary conditions,

$$\mathbb{L}_{V,\mu}(1,1) = \hat{\nu}_{\alpha\beta}\left(\widetilde{G}(\frac{1}{2}) - 2H(\frac{1}{2})\right), \quad \mathbb{L}_{V,\mu}(M,M-1) = \hat{\nu}_{\alpha\beta}\left(-\widetilde{G}(M-\frac{1}{2}) + 2H(M-\frac{1}{2})\right), \tag{4.212}$$

$$\mathbb{L}_{V,\mu}(1,2) = \hat{\nu}_{\alpha\beta}\left(\widetilde{G}(\frac{1}{2}) + 2H(\frac{1}{2})\right), \qquad \mathbb{L}_{V,\mu}(M,M) = \hat{\nu}_{\alpha\beta}\left(-\widetilde{G}(M-\frac{1}{2}) - 2H(M-\frac{1}{2})\right), \tag{4.213}$$

$$\mathbb{L}_{V,\mu}(1,j) = 0, \quad j > 2, \qquad \mathbb{L}_{V,\mu}(M,j) = 0, \quad j < (M-1). \tag{4.214}$$

The eigenvalues of these matrices are exemplarily shown in Fig. 4.6 for a 40×20 grid with normalized parameters for density, temperature, and magnetic field set to one (see the caption for the full set of parameters)*. The Péclet numbers for a typical velocity of $\hat{v}_{||} = 3$ and $\hat{\mu} = 9$ are $\mathrm{Pe}_{||} \approx 2.46$ and $\mathrm{Pe}_{\mu} \approx 3.55$, indicating a mixed advective-diffusive character. This behavior is confirmed by comparing the magnitudes of the real and imaginary parts of the eigenvalues. Both second-order schemes have similar but not identical eigenvalues, whereas the fourth-order scheme shows larger eigenvalues, as expected. Comparing the parallel and perpendicular agianst the total eigenvalues, one can observe that the parallel and perpendicular eigenvalues "combine" in a peculiar way. One could obtain the total eigenvalues by repeating the structure of the parallel eigenvalues centered at each perpendicular eigenvalue. As a result, the total operator has larger maximal eigenvalues than the individual ones.

A diffusion-dominated case is shown in Fig. 4.7. Here, only the temperature has been increased to $\hat{T} = 30$. This result confirms that the temperature plays a key role in determining

*For simplicity, the mixing quantities have been replaced by constant temperatures $\hat{T}$ and zero flow $\hat{u} = 0$.

the advective or diffusive character of the collision operator. In this case the Péclet numbers are $\mathrm{Pe}_{||} \approx 0.08$ and $\mathrm{Pe}_{\mu} \approx 0.46$ (for $\hat{v}_{||} = 3$ and $\hat{\mu} = 9$).

Stability of the Discretized LBD Operator with RK4 Time-Integration
The standard time-integration scheme in the `GENE-X` code is the RK4 scheme[62]. The stability polynomial that defines the stability region is given by[166]

$$R_{\mathrm{RK4}}(z) = 1 + z + \frac{1}{2}z^2 + \frac{1}{6}z^3 + \frac{1}{24}z^4. \tag{4.215}$$

The $R(z) = 1$ contour of the RK4 stability region has a typical "bean" shape. In Figs. 4.8 and 4.9, the eigenvalues of the total collision matrices for the different discretizations of the LBD operator have been plotted against the stability region of the RK4 scheme. The time steps have been approximately maximized for the given parameters. The fourth-order scheme has a stricter requirement, with a ratio close to the ones given by the Courant numbers in the simple criterion (4.171). In the $\hat{T} = 30$ case, the strictest CFL criterion is the perpendicular diffusion, suggesting time steps of $\Delta\hat{t} \approx 4.24 \times 10^{-3}$ for the second-order schemes and $\Delta\hat{t} \approx 3.19 \times 10^{-3}$ fourth-order schemes to be stable. Such time steps would be unstable according to the eigenvalue analysis. For the $\hat{T} = 1$ case, the CFL criterion on the fourth-order scheme would be stable, whereas, for the second-order schemes, a single eigenvalue would cross the stability region.

This example shows that the eigenvalue analysis yields a more accurate analysis than the simple CFL criteria in section 4.5.1. However, one condition for the analysis to apply is a normal collision matrix. The following section will analyze the effect of non-normality.

4.5.3 Advanced Stability Analysis

In the last section, the eigenvalues of the LBD collision matrices have been analyzed. While this method is simple and intuitive, it is only a necessary condition for the stability of the scheme. For the eigenvalue criterion to be sufficient, the matrix under consideration must be normal, which is not the case, as will be shown in the following. For non-normal matrices, the pseudo-eigenvalues of the matrix should be analyzed instead[168]. In this section, such an advanced stability analysis is performed.

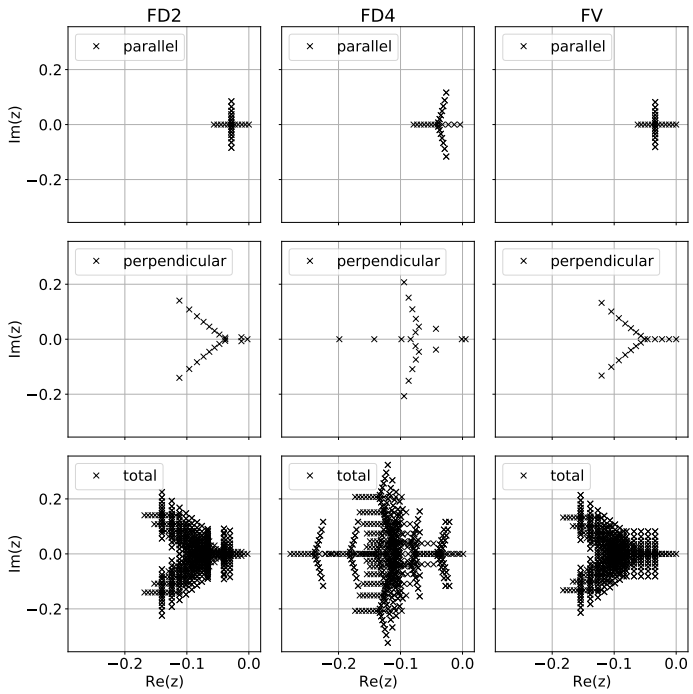

Figure 4.6. Eigenvalues of the parallel, perpendicular, and total collision matrix for the second and fourth-order finite difference (FD2 and FD4) and the second-order finite volume (FV) discretization. The grid chosen is 40×20 in $\hat{v}_{||} \times \hat{\mu}$ with extent $v_{||,\max} = 8$ and $\mu_{\max} = 64$ and parameters $\hat{n} = 1$, $\hat{B} = 1$, $\hat{T} = 1$ and $\hat{u} = 0$ for electron-electron collisions. The normalization used $n_{\text{ref}} = 10^{19}$ m^{-3}, $T_{\text{ref}} = 0.02$ keV, $B_{\text{ref}} = 0.929$ T and $L_{\text{ref}} = 0.906$ m with mass normalized to the mass of a proton. The eigenvalues are scaled by $\Delta\hat{t} = 10^{-4}$.

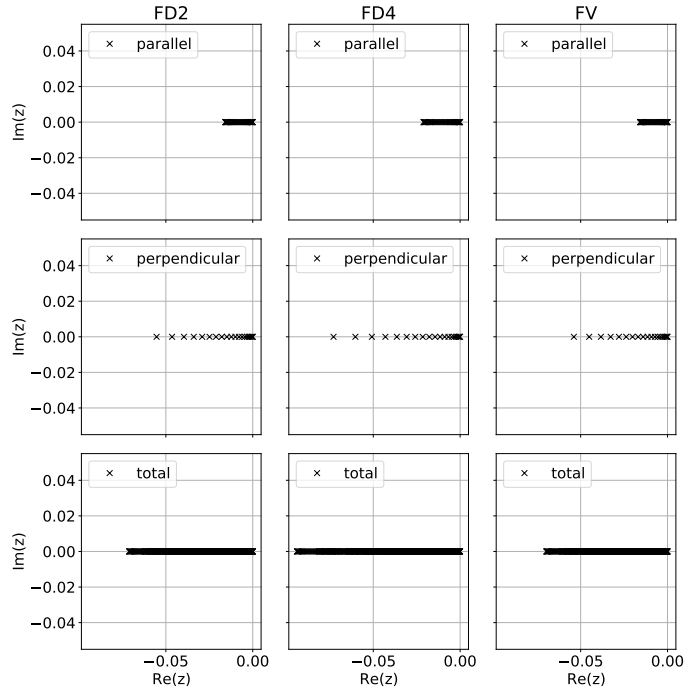

Figure 4.7. Same as Fig. 4.6 but for $\hat{T} = 30$.

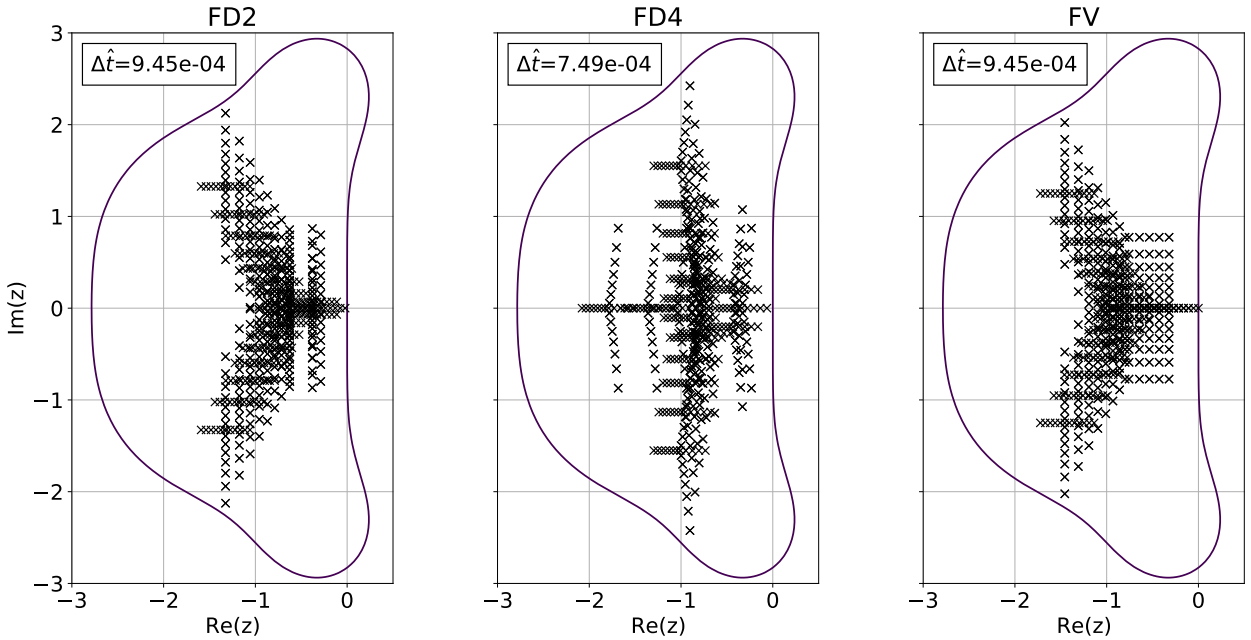

Figure 4.8. Eigenvalues of the total collision matrix for the second and fourth-order finite difference (FD2 and FD4) and the second-order finite volume (FV) discretization against the stability region of the RK4 scheme (enclosed by the purple line). Time-steps chosen are listed in the box. The other parameters are the same as in the case in Fig. 4.6, the normalized temperature is $\hat{T} = 1$.

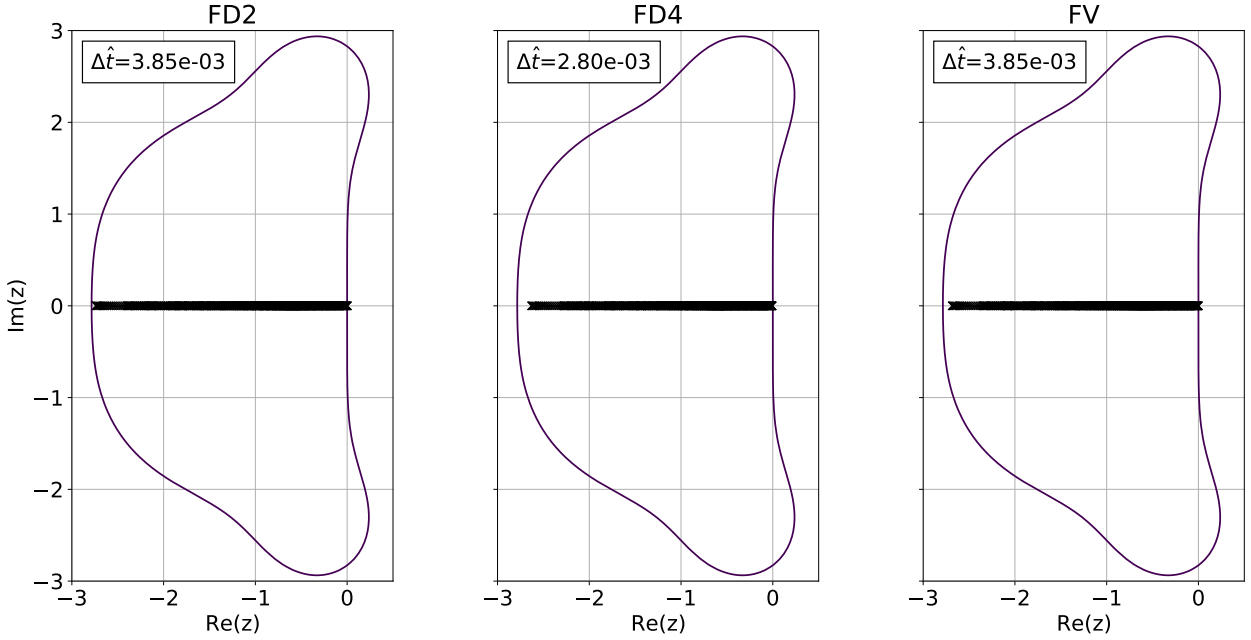

Figure 4.9. Same as Fig. 4.8 but for $\hat{T} = 30$.

Table 4.1. Degree of non-normality Q_n given by eq. (4.217) evaluated for the two cases given by Figs. 4.6 and 4.7.

Case $\hat{T} = 1$:

	parallel	perpendicular	total
FD2	0.07	0.17	0.43
FD4	0.09	0.23	0.58
FV	0.10	0.19	0.47

Case $\hat{T} = 30$:

	parallel	perpendicular	total
FD2	0.003	0.008	0.020
FD4	0.004	0.013	0.033
FV	0.003	0.008	0.020

Non-Normality of the Discretized LBD Operator

Considering the stability of the method of lines requires a normal matrix. To be normal, the defining condition on a real matrix $\mathbb{A}$ is[171] $\mathbb{A}\mathbb{A}^\mathsf{T} = \mathbb{A}^\mathsf{T}\mathbb{A}$. The continuous advection-diffusion operator is non-normal[172] due to boundary conditions or non-constant advection and or diffusion coefficients[173]. This property suggests analyzing the non-normality of the matrices approximating these operators. For example, the parallel part of the second-order finite difference discretization on a 2×2 grid is

$$\begin{aligned}
&\mathbb{L}_{2,||}^{2\times2}\left(\mathbb{L}_{2,||}^{2\times2}\right)^\mathsf{T} - \left(\mathbb{L}_{2,||}^{2\times2}\right)^\mathsf{T}\mathbb{L}_{2,||}^{2\times2} \\
&\qquad = \begin{pmatrix} \left(\frac{1}{2}B + A(0)\right)^2 - \left(\frac{1}{2}B - A(1)\right)^2 & 0 \\ 0 & -\left(\frac{1}{2}B + A(0)\right)^2 + \left(\frac{1}{2}B - A(1)\right)^2 \end{pmatrix}.
\end{aligned} \tag{4.216}$$

While under certain special parameter choices, the matrix $\mathbb{L}_{2,||}^{2\times2}$ can be normal, it is certainly not the case in general. There are several different quantifications of the non-normality of matrices[174]. One of the most basic ones measures the violation of the defining condition,

$$Q_n(\mathbb{A}) = ||\mathbb{A}\mathbb{A}^\mathsf{T} - \mathbb{A}^\mathsf{T}\mathbb{A}||_F^{1/2}, \tag{4.217}$$

where $||\mathbb{A}||_F = (\sum_{ij} |\mathbb{A}_{ij}|^2)^{1/2}$ is the Frobenius norm. For example, Table 4.1 shows these numbers for the two cases considered in Figs. 4.6 and 4.7. In these cases, the total collision matrices have a higher degree of non-normality than the individual parallel and perpendicular ones. Further, one can observe that the degree of non-normality is lower for the diffusion-dominated case, consistent with the behavior expected from the continuous advection-diffusion operator[173].

The dependence on the velocity space grid can be seen in Figs. 4.10 and 4.11. First, the expected growth of non-normality with the number of grid points can be observed, in agreement with the literature[172]. Second, in the range considered, the non-normality seems dominated mainly by the perpendicular contributions. The scaling for the total collision matrix flattens

for a small number of parallel grid points. Further, a kink in the parallel contributions for the finite difference schemes is observed at $N = 12$ due to the matrix coefficients having numbers such that approximately $\mathbb{L}_{\mathrm{FD},||} \approx \mathbb{D} + \mathbb{S}$, where $\mathbb{D}$ is diagonal and $\mathbb{S}$ is skew-symmetric. This outlier is an example of a "lucky shot" where the matrix became almost normal (however, only for the parallel part of the finite difference schemes for a single temperature value and grid spacing).

The measure of non-normality (4.217) used above is helpful to check *if* a matrix is non-normal (which is the case for the discretized LBD operator). Further, the dependence of non-normality with different parameters can be analyzed. However, a scalar measure of non-normality is not sufficient, and one must check separately for each matrix if there are consequences for the numerical stability[173].

Pseudospectra of the Discretized LBD Operator

The theory of using pseudospectra for the stability of the method of lines can be found in Ref. [175]. Here a summary is given. A number $z \in \mathbb{C}$ is called an ϵ-pseudo-eigenvalue of a matrix $\mathbb{A}$ if z is an eigenvalue of $\mathbb{A} + \mathbb{E}$, where $\mathbb{E}$ is a perturbation matrix with L2-norm $||\mathbb{E}||_2 \leq \epsilon$. For normal matrices, the pseudo-eigenvalues will form balls of radius ϵ around the eigenvalues, whereas, for non-normal matrices, the pseudo-eigenvalues can form much larger regions. Even if an eigenvalue lies inside the region of stability of the time integrator, the discretization may become unstable if the matrix is highly non-normal. Standard cases that experience this behavior are, e.g., the first order upwind scheme as well as spectral discretization methods[173,175*].

In the previous section, it has been shown that the discretized LBD operator is non-normal. In the following, the pseudo-eigenvalues will be analyzed. For brevity, only the finite volume collision matrix is considered. The small parameter ϵ can represent errors in calculating temperature and mean flow, as these determine the entries in the collision matrix. As such, it is of interest if the stability of the discretization is affected by these discretization errors.

The full-discretization is written as $\mathbf{f}^{n+1} = G(\Delta t\, \mathbb{L}(\Delta t))\mathbf{f}^n := \mathbb{A}(\Delta t)\mathbf{f}^n$, where n labels the discretized time, $\mathbb{L}$ is the collision matrix and $G(w)$ is a function that characterizes the time integration[175]. For example, for the RK4 scheme[173],

$$G^{\mathrm{RK4}}(\Delta t\, \mathbb{L}) = \mathbb{I}_L + \Delta t\, \mathbb{L} + \frac{1}{2}(\Delta t)^2\mathbb{L}^2 + \frac{1}{6}(\Delta t)^3\mathbb{L}^3 + \frac{1}{24}(\Delta t)^4\mathbb{L}^4, \tag{4.218}$$

where $\mathbb{I}_L$ is the unit matrix with the same size as $\mathbb{L}$. Since $\mathbb{A}(\Delta t)$ is applied repeatedly on the distribution function vector to advance it in time, the total time evolution can be seen

*In the standard cases the upwind scheme is typically combined with explicit Euler and the spectral methods with third order Adams-Bashforth time integrators.

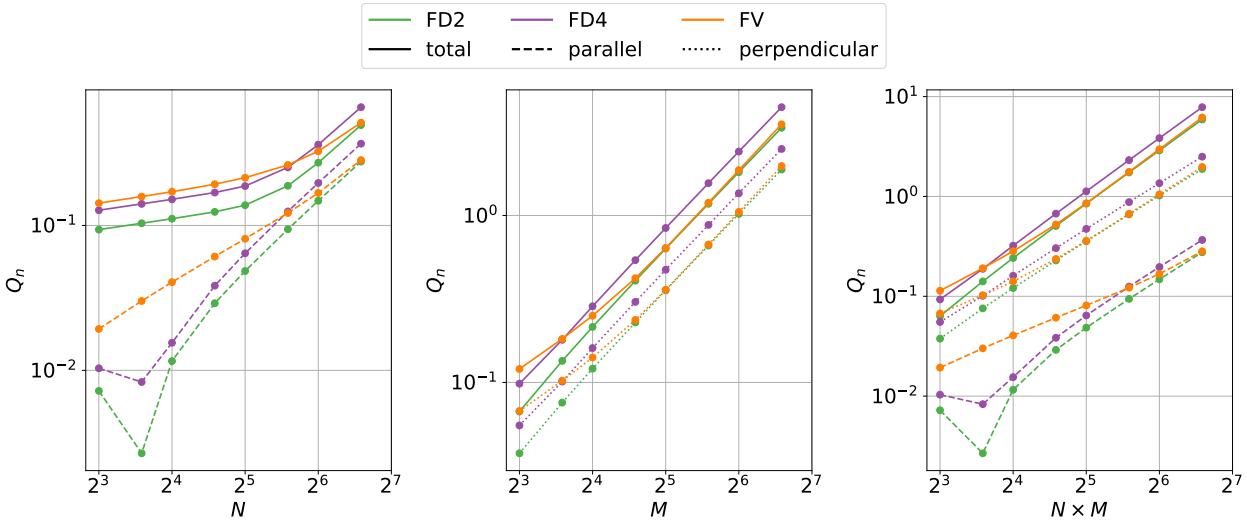

Figure 4.10. Dependence of the degree of non-normality Q_n on the number of grid points for the parallel, perpendicular, and total collision matrix for the second and fourth-order finite difference (FD2 and FD4) and the second-order finite volume (FV) discretization. The left plot shows a scaling in the parallel dimension (for fixed $M = 10$), the center one in the perpendicular dimension (for fixed $N = 10$), and the right scaling for both dimensions simultaneously. The parameters are the same as in the case in Fig. 4.6, the normalized temperature is $\hat{T} = 1$.

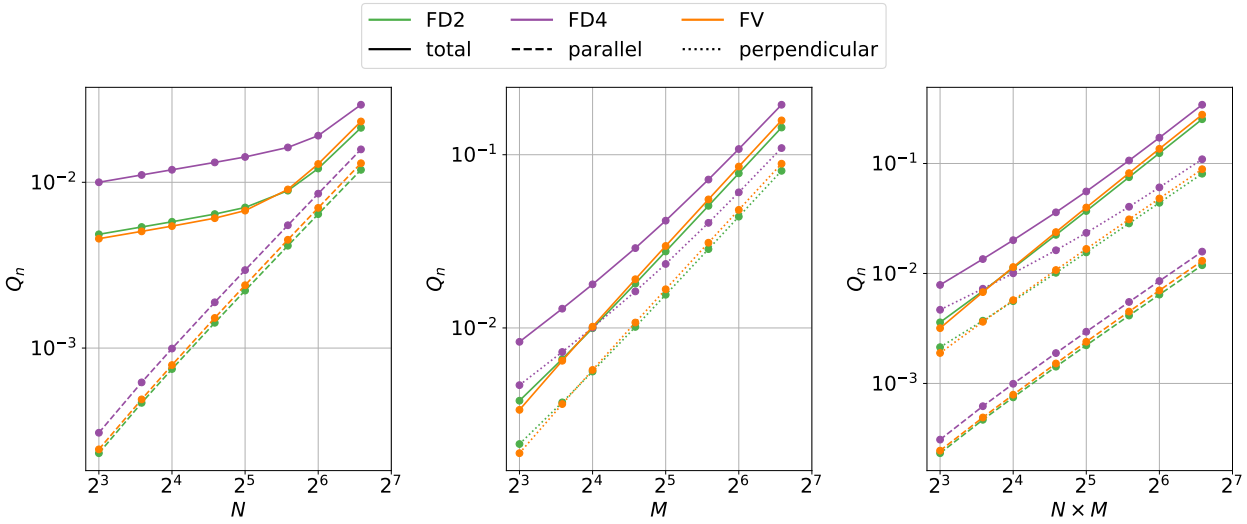

Figure 4.11. Same as Fig. 4.10 but for $\hat{T} = 30$.

as applying the N_t-th power of $\mathbb{A}(\Delta t)$ on $\mathbf{f}$, where N_t is the total amount of time steps. This fact is only the case if the coefficients are constant. Otherwise, $\mathbb{A}(\Delta t)$ must be re-evaluated at each time step. In the following, the former case is assumed. The discretization is defined as Lax-stable if the powers of this matrix are bounded $||\mathbb{A}(\Delta t)^n|| \leq C$ for all n and sufficiently small Δt, such that $0 \leq n\Delta t \leq T_{\max}$ for $t \in [0, T_{\max}]$ where C is a constant[176]. This criterion is necessary and sufficient for stability*.

The theorem that connects a discretization's Lax-stability with the discretized operators' pseudo-spectrum has been established and proven in Ref. [175]. The version applied on one-step time integrators is summarized in the following (Theorem 7.1 within Ref. [175]). If the matrix powers are bounded $||\mathbb{A}(\Delta t)^n|| \leq C_1$ for all $n \geq 0$, then the ϵ-pseudo-eigenvalues $\{z_\epsilon\}$ of $\Delta t\, \mathbb{L}(\Delta t)$ lie at most within a distance of order ϵ away from the region of stability of the time integration scheme. In other words $\text{dist}(z_\epsilon, S) \leq C_2\epsilon$ for all $\epsilon \geq 0$. Further, this implies that the power bound will depend on either the number of spatial grid points or on the number of time steps performed via $||\mathbb{A}(\Delta t)^n|| \leq C_3 \min(N_r, n)$, where $N_r = N_r(\Delta t)$ exemplarily denotes the space dimension chosen for a given time step. For the theorem to hold, S must be bounded, and $G'(w)$ must not be equal to zero at the boundary of S, which is fulfilled for the RK4 scheme. Further, the family of matrices $\{\Delta t\, \mathbb{L}(\Delta t)\}$ must be uniformly bounded, a condition which can be met for the LBD operator by choosing at least $\Delta\hat{\mu} \sim \Delta\hat{v}_{||} \sim \Delta\hat{t}$. The constants C_1, C_2, C_3 depend on the number of grid points or time steps. The above condition is formulated for an infinite maximum time. It can be relaxed to $0 \leq n\Delta t \leq T_{\max}$ by using $C_2\epsilon + C_4\Delta t$ as the upper bound for the distance of the pseudo-eigenvalues from the region of stability[173].

Fig. 4.12 shows an example of the pseudo-spectra for the perpendicular part of the finite volume version of the LBD operator with parameters $\hat{T} = 1$, $L_\mu = 64$, $M = 32$ and $\Delta\hat{t} = 4 \times 10^{-4}$ (other parameters are the same as in the cases before). The continuous lines show bounds of the pseudo-spectra computed with the `pseudopy`[177] package based on algorithms in Ref. [173]. The markers show a way to estimate the pseudo-spectra by evaluating the eigenvalues of the perturbed matrix $\mathbb{L}+\mathbb{E}$, where $\mathbb{E}$ is a random complex matrix with L2 norm $||\mathbb{E}||_2 \leq \epsilon$. It is constructed using normally distributed random numbers with zero mean and standard deviation of one. Real and imaginary parts of each matrix entry use independent random numbers, and the total matrix is scaled such that its L2 norm is equal to ϵ. This method does not create all possible matrices with norm ϵ. Thus not the whole region within the continuous lines is filled. The algorithm computing the bounds on the pseudo-spectra becomes very slow for matrices of dimension 100 or more. In contrast, the estimation via random matrices can still be used with larger matrices.

*And also for convergence as $\Delta t \to 0$, given that the discretization is consistent. This additional relation is called the Lax Equivalence Theorem[176].

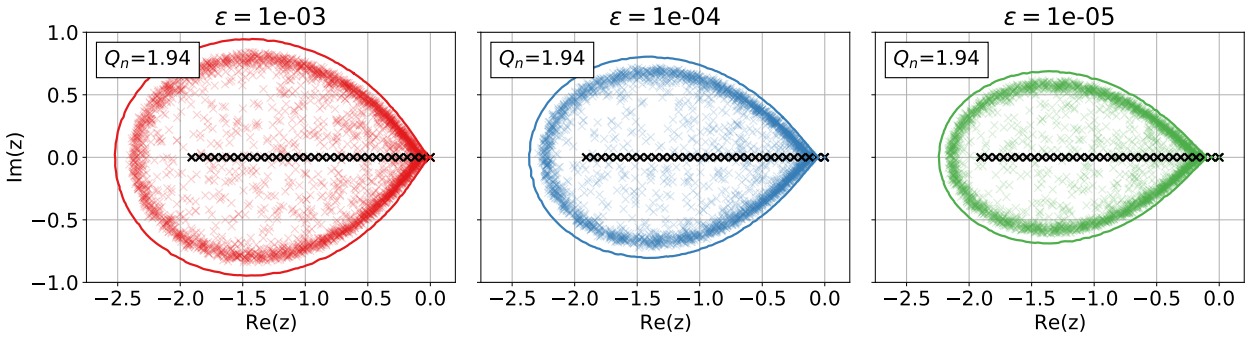

Figure 4.12. Eigenvalues (black crosses), some pseudo-eigenvalues (colored crosses), and bounds on the pseudo-spectra (continuous lines) for the perpendicular finite volume collision matrix. Parameters are $\hat{T} = 1$, $M = 32$ and $\Delta\hat{t} = 4 \times 10^{-4}$ with the other relevant ones being the same as in the case in Fig. 4.6. The three subplots show the different ϵ-pseudo-spectra, and the box indicates the degree of non-normality (4.217). The pseudo-eigenvalues (colored crosses) are calculated using 100 perturbed matrices.

Additionally, Fig. 4.12 shows a case where the non-normality of the matrix has a significant effect. While all the eigenvalues are real-valued, the pseudo-eigenvalues have substantial imaginary eigenvalues, and further, the extent on the real axis is increased. This discretization is time-stable with the RK4 scheme as a time integrator. For the explicit Euler scheme, on the other hand, the eigenvalues would be within the stability region, a unit circle centered at -1. In contrast, the pseudo-eigenvalues exceed that boundary even for small ϵ. One can see that the distance between the boundary of the stability region and the pseudo-spectra is not of $\mathcal{O}(\epsilon)$. Thus this discretization is unstable, providing a simple example of where the eigenvalue analysis fails. The instability can be remedied by choosing a smaller time step. However, it would not be clear from the eigenvalue analysis why the time step is restricted.

The previous (simplified) case showed how the eigenvalue analysis might fail in certain cases to predict stable time steps of a discretization. Next, the full collision matrix with an RK4 time integrator is considered. Fig. 4.13 shows the power norm of the matrix $\mathbb{A}(\Delta\hat{t})$ under consideration for the Lax-stability of the discretization. The time steps have been chosen to be approximately maximal while keeping all eigenvalues within the region of stability of the RK4 time integrator (Table 4.2). As the number of grid points increases, the power norm grows significantly, reaching a maximum at $N \times M = 32 \times 32$*. However, increasing the number of grid points further does not result in an unbounded growth of the power norm. This behavior can be explained by considering the (approximate) pseudo-spectra shown in Fig. 4.14. One can observe that for $N \times M = 32 \times 32$ grid points the $\epsilon = 10^{-7}$ and potentially the $\epsilon = 10^{-9}$ pseudo-eigenvalues exceed the stability region of the RK4 scheme. This results in a transient growth[173] in the order of up to 10^9, as observed in Fig. 4.13. Due to the high computational cost of computing the pseudo-spectra, only the approximate method is

*This has been tested against other grid sizes such as 31×31 or 33×33.

Table 4.2. Values of the time step used for different grid sizes in Fig. 4.13.

$N \times M$	16×16	28×28	32×32	36×36	48×48	64×64
$\Delta\hat{t}/10^{-4}$	16.432	8.9	7.06576	4.3	2.02	1.049

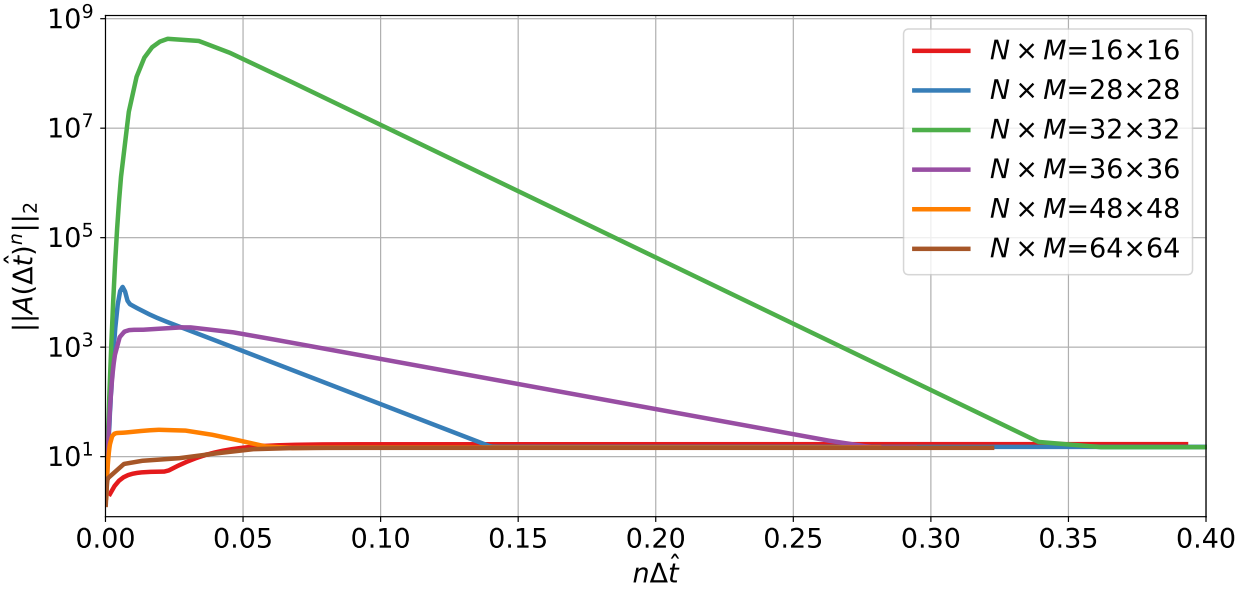

Figure 4.13. Power norm of the total finite volume LBD collision matrix $\mathbb{A}(\Delta\hat{t}) = G(\Delta\hat{t}\,\mathbb{L}_V(\Delta\hat{t}))$ for different grid sizes. The time steps are given in Table 4.2. All other parameters are the same as in the case in Fig. 4.6.

used. The exact pseudo-eigenvalues are larger, as can be seen by comparing the growth of the $N \times M = 28 \times 28$ curve in Fig. 4.13 with its approximate pseudo-eigenvalues in Fig. 4.14. However, observing pseudo-eigenvalues outside the stability region is sufficient to identify stability issues.

The stability issue is confirmed in a test where the collision matrix is applied on the anisotropic distribution function $f = a_1\pi^{-3/2}\exp\left(-(\hat{v}_{||}+0.3)^2/a_2 - \hat{\mu}\hat{B}/a_3)\right)$. The parameters are chosen such that the moments of this distribution are $\hat{n} \approx 1$ and $\hat{T} \approx 1$*. While for the $N \times M = 28 \times 28$ case, no stability issue is found within 500 time steps (which covers approximately the temporal range in Fig. 4.13), the $N \times M = 32 \times 32$ case experienced a numerical instability after 264 time steps, followed by an abrupt ending. Using only 90% of the maximal time step given by the eigenvalue analysis leads to a stable simulation.

The apparent reason for this peculiar behavior of the discretization is the fact that the character of the LBD collision matrix changes from advection to diffusion dominated (see

*The numbers are $a_1 = 9.16$, $a_2 = 0.7$ and $a_3 = 0.4$ for the $N \times M = 28 \times 28$ case and $a_1 = 3.16$, $a_2 = 0.9$ and $a_3 = 0.55$ for the $N \times M = 32 \times 32$ case. Further, a mean flow is used. The collision operator has been applied with conservative corrections and nonlinear coefficients, where the moments are calculated at each time step and RK4 stage.

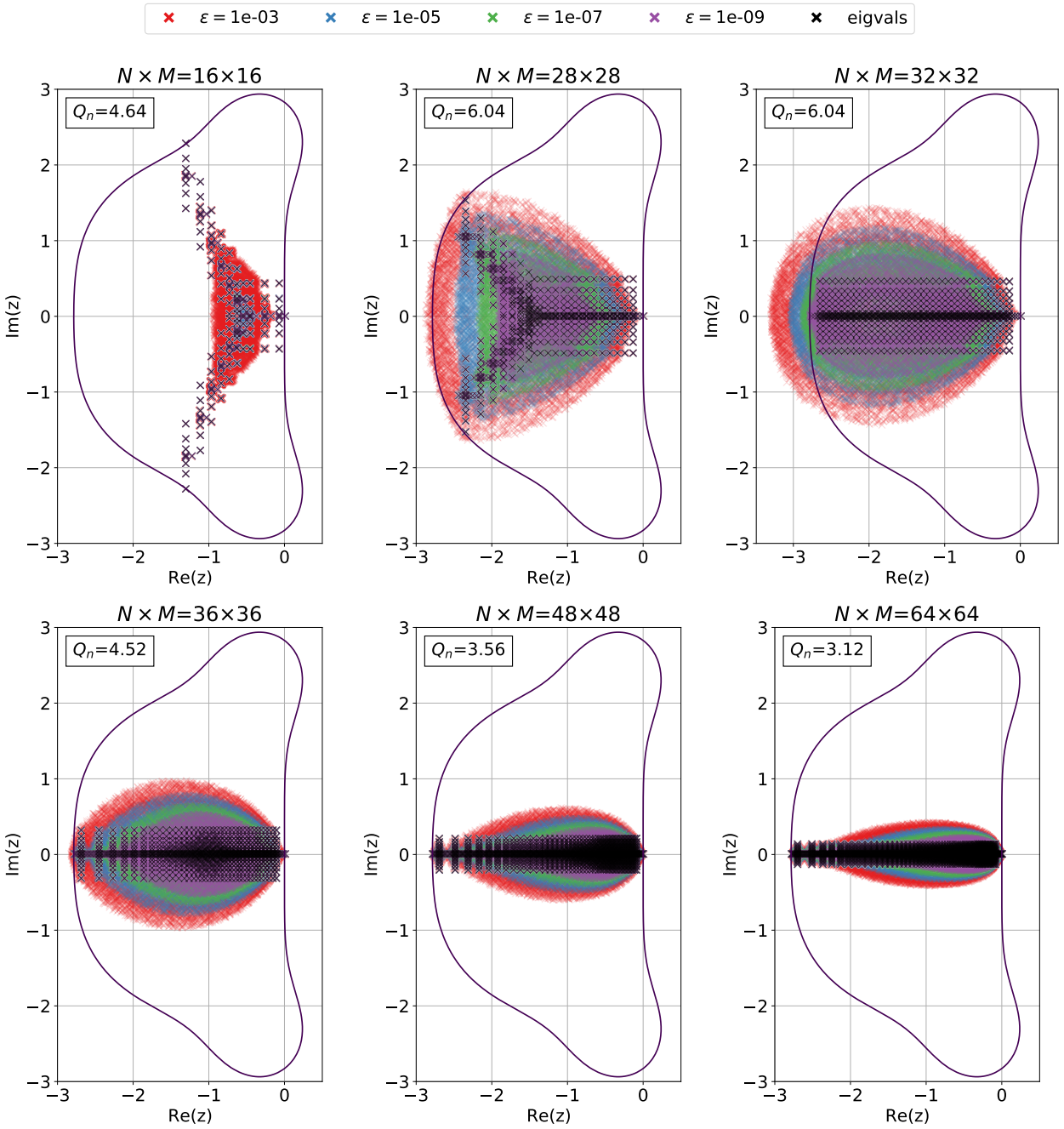

Figure 4.14. Eigenvalues and approximated pseudo-spectra of the total finite volume LBD collision matrix for different grid sizes. Parameters are explained in the caption of Fig. 4.13. The degree of non-normality (4.217) is shown in the box. The purple line shows the stability region of the RK4 time integrator. The pseudo-spectra are approximated with the method shown in Fig. 4.12, using 100, 10, 10, 10, 5, and 5 perturbed matrices, respectively.

eigenvalues in Fig. 4.14). The shape of the pseudo-spectra seems to be relatively bounded on the real axis, except for the case $N \times M = 32 \times 32$, for which $\Delta\hat{\mu} = 2$ given $M = 32$ and $\mu_{\max} = 64$. In that case, the advective and diffusive terms are balanced in the perpendicular part of eq. (4.211). This is the case with the highest non-normality*. An interesting fact is the concentration of eigenvalues at large negative real values in this case, distinguishing it from the $N \times M = 36 \times 36$ case, where the spectrum looks very similar. However, the eigenvalues are more concentrated at smaller real values.

The final point is that Fig. 4.13 suggests that the discretization is Lax-stable for the given parameters within the range of grid sizes considered. Since the maximum of the power norm does not seem to grow with larger grids, it can be bound by a constant independent of the number of grid points or time steps. However, in the choice of the time step, care must be taken not to excite instabilities, especially in conditions where the operator has a mixed advective-diffusive character. A pragmatic approach is to estimate the possible time step with the eigenvalue method, take some "safety factor" like 90% (especially when the spectrum indicates a mixed advective-diffusive character), and try for some hundreds of steps. For realistic simulation cases, where several hundreds of thousands of real-space points with different parameters (density, temperature, magnetic field) are present, analyzing each parameter set individually is not practical. In such a situation, carefully chosen cases with extremal parameters may be investigated instead.

4.5.4 Advanced Time-Stepping Schemes

So far, this section has covered the stability of the discretized collision operator only. The target application cases consider the gyrokinetic Vlasov equation and the collisional part. Thus, the stability of the complete discretized equation needs to be considered. In practice, the stability analysis of the discretized Vlasov part is non-trivial due to the complexity of the operator (see Ref. [62] for the full discretized Vlasov operator). Further, compared to collisions-only, the dimensionality of the full problem increases rapidly due to the necessary inclusion of real-space dynamics. The scaling of the problem leads quickly to matrices with dimensions of 10^9, making a detailed stability analysis impractical.

On the other hand, performing a detailed stability analysis for each case is often unnecessary. Given a time-stable collisionless simulation (found using estimations with the CFL criterion for that problem[62]), collisions will most likely restrict the maximum time step possible. The consideration from section 4.5.2 can explain this. Supposing the discretized Vlasov part has eigenvalues close to the stability boundary, adding collisions will shift these outside the

*Although the $N \times M = 28 \times 28$ case has the same non-normality, the impact on the stability is less severe due to the shape of the pseudo-spectrum. In this case, the single measure of non-normality is insufficient to provide a detailed prediction of the behavior of the matrix.

stability region, requiring a decrease in the time step to keep the simulation stable*. Such a global decrease in the time step makes collisional simulations very expensive, despite using a relatively simple and computationally cheap collision operator. This potential decrease in time step motivates a splitting between the time evolution of the collisionless and the collisional processes in the simulation. Ref. [160] provides an overview of different splitting methods.

Strang Splitting

The method of Strang splitting[178] is an accurate second-order technique to split the time evolution of an operator into two parts[59],

$$\mathcal{T}(\Delta t) f_\alpha = \left(\mathcal{T}_\mathrm{C}\left(\frac{\Delta t}{2}\right) \circ \mathcal{T}_\mathrm{V}\left(\Delta t\right) \circ \mathcal{T}_\mathrm{C}\left(\frac{\Delta t}{2}\right) \right) f_\alpha, \tag{4.219}$$

where $\mathcal{T}$ denotes the total time evolution operator and $\mathcal{T}_\mathrm{C}$ and $\mathcal{T}_\mathrm{V}$ the time evolution due to the collisional and Vlasov part respectively. In this notation, applying $\mathcal{T}(\Delta t)$ on the distribution f_α will advance it by time step Δt. Thus, the splitting will apply the two operators $\mathcal{T}_\mathrm{C}$ and $\mathcal{T}_\mathrm{V}$ consecutively on the distribution function. The collisional and collisionless time evolution are split, and the time step Δt has to be chosen such that both operators are individually stable. As an effect, the stricter time step criterion will apply to the total time evolution. In two consecutive applications of the total time evolution operator, the collisional steps can be combined

$$\begin{aligned} \mathcal{T}^2(\Delta t) f_\alpha &= \left(\mathcal{T}_\mathrm{C}\left(\frac{\Delta t}{2}\right) \circ \mathcal{T}_\mathrm{V}\left(\Delta t\right) \circ \mathcal{T}_\mathrm{C}\left(\frac{\Delta t}{2}\right) \circ \mathcal{T}_\mathrm{C}\left(\frac{\Delta t}{2}\right) \circ \mathcal{T}_\mathrm{V}\left(\Delta t\right) \circ \mathcal{T}_\mathrm{C}\left(\frac{\Delta t}{2}\right) \right) f_\alpha, \\ &= \left(\mathcal{T}_\mathrm{C}\left(\frac{\Delta t}{2}\right) \circ \mathcal{T}_\mathrm{V}\left(\Delta t\right) \circ \mathcal{T}_\mathrm{C}\left(\Delta t\right) \circ \mathcal{T}_\mathrm{V}\left(\Delta t\right) \circ \mathcal{T}_\mathrm{C}\left(\frac{\Delta t}{2}\right) \right) f_\alpha. \end{aligned} \tag{4.220}$$

Although this seems computationally beneficial, there are two drawbacks. First, algorithmic changes would be required for the first and last and for all the time steps where diagnostics are written to file. Second, while in the not-combined case, the collisions need to be stable concerning time step $\Delta t/2$, in the combined case, the requirement is stability for Δt. Despite splitting the collisional and collisionless parts, a reduction in Δt due to the stability of the collision operator will also reduce the time step of the collisionless part. Since the LBD collision operator is relatively cheap computationally, keeping the separate evaluations with the time step $\Delta t/2$ is beneficial.

The current default time stepping scheme in `GENE-X` using LBD collisions is Strang splitting with RK4 for both the Vlasov and the collisional part. In principle, both operators can use

*The simple picture shown here is only strictly valid if the Vlasov part is independent of $v_{||}$.

different time integrators. In practice, RK4 is chosen for the collisional step due to the large extent of the stability region on the imaginary axis. As shown in the previous sections, this allows for simulations in both advective and diffusive regimes of the collision operator.

RKC Schemes

A possible alternative time integrator for the collisional part of the gyrokinetic equation could be provided by the family of Runge-Kutta-Chebyshev (RKC) schemes[160]. Here, the stability region is determined by Chebyshev polynomials of first kind T_s (see Ref. [135] §3.11(ii)). The stability region is given by[160]

$$S_s^{\mathrm{RKC}}(z) = T_s(1 + z/s^2), \tag{4.221}$$

where s is the order of the scheme and $z \in \mathbb{C}$. These polynomials have the issue that for $s > 0$ "knots" along the negative real axis exist, where the extent of the stability region on the imaginary axis is zero (see Fig. 4.15 grey dashed line). For perfectly diffusive problems described by normal operators, this would be sufficient. However, any small imaginary eigenvalue will lead to instability. Thus, a modified version exists[160]

$$S_{s,\eta}^{\mathrm{RKC}}(z) = \frac{T_s(1 + \eta + wz)}{T_s(1 + \eta)}, \qquad w = \frac{T_s(1 + \eta)}{T_s'(1 + \eta)}, \tag{4.222}$$

where $T_s'(z) \equiv \partial T_s(z)/\partial z$ and η is a damping parameter*. The effect of this damping is an enlarged imaginary stability region close to the knots of the undamped region of stability for the price of a reduction in the extent along the negative real axis (compare the grey dashed against the dotted line in Fig. 4.15). The choice of η will also depend on the non-normality of the collision matrix since, for diffusion-dominated problems, the pseudo-eigenvalues may have substantial imaginary parts (see previous section, in particular, Fig. 4.14).

The combination of Strang splitting with RKC time integrators for the collision operator was investigated in Ref. [179] for a similar problem. There, a computational benefit was found due to the diffusive nature of the collision operator used. The same observation is made in a diffusive regime for the LBD collision operator, as shown in Fig. 4.15 (right). Here, a second-order RKC scheme could improve the possible time step by ≈ 2.86 (compared to Fig. 4.9). However, for an advection-dominated case, as in Fig. 4.15 (left), the maximal time step is restricted due to the smaller extent of the RKC2 stability region along the imaginary axis. Thus, advanced schemes must be considered for the application in real space domains where both cases happen simultaneously (such as the edge and SOL region of fusion devices). Possibilities include advanced RKC methods[180] or implicit-explicit (IMEX) (or IMEX-RK) schemes[160,181,182] using Jacobian-free Newton-Krylov methods[183] to solve the implicit part of

*The definition in Ref. [160] is slightly different, there the choice $\omega_0 = 1 + \epsilon/s^2$ corresponds to $1 + \eta$ in this work.

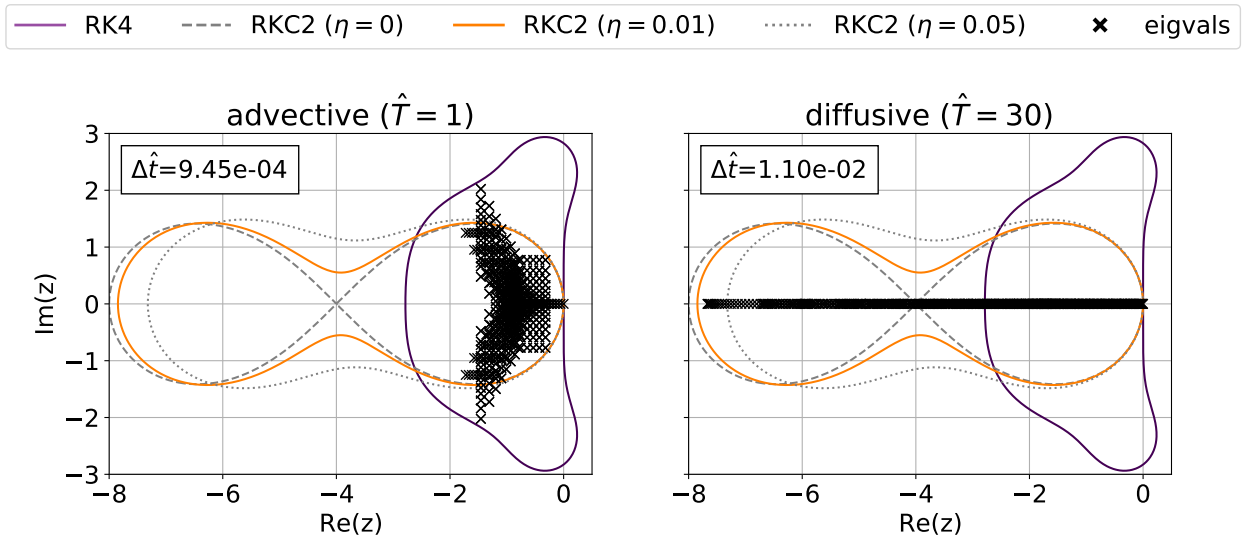

Figure 4.15. Eigenvalues of the discretized finite volume LBD collision operator for the advective ($\hat{T} = 1$) and diffusive ($\hat{T} = 30$) cases with all other parameters given in the caption of Fig. 4.6. The time step is maximal within the RKC2 (s=2) stability region with damping $\eta = 0.01$ (orange line). For comparison, the RK4 stability region and RKC2 with two different damping parameters are given.

the time evolution (such as used in Ref. [165]). For the applications in this work, using the RK4 scheme for the collisional part is sufficient.

4.6 Performance Analysis

The parallelization in the high-performance code `GENE-X` is based on a hybrid `OpenMP`[184] (open multi-processing) / `MPI`[185] (message passing interface) approach[62]. The φ, $v_{||}$, μ and α (species) dimensions of the computation are parallelized across multiple compute nodes with `MPI`, while the remaining RZ dimension is parallelized across multiple cores (processors) with `OpenMP`. The implementation is very flexible, allowing any distribution of `MPI` processes along the four dimensions just mentioned, also using multiple `MPI` processes per compute node (e.g., one per socket) if desired.

Since typical simulations with `GENE-X` consume computing resources in the range of millions of core-hours[59,112], implementing the newly developed collision operators must be highly efficient. The following section presents a performance analysis, considering only the finite volume version of the LBD collision operator.

4.6.1 Node-Level Performance

First, the performance on the level of a single compute node is analyzed. The results can be used to detect possible inefficiencies that may lead to an overall slowdown of the code. The analysis is performed with the use of the roofline model[186] (additional details are given in Ref. [62]). To summarize, the performance in terms of floating point operations per second (FLOPS) and the memory bandwidth in GB/s are measured. The performance is plotted against the arithmetic intensity in FLOP/B (often also denoted as FLOP/Byte). The memory bandwidth limits applications with low arithmetic intensity, whereas applications with high arithmetic intensity are limited by the possible amount of floating point (FP) operations. These two limits together form the shape of the roofline.

For this purpose, a benchmark program will apply the parts of the code to be analyzed over 20 times on a distribution function $f_\alpha = 1$. The code is compiled with the Intel Fortran compiler version 19.1.1, and the benchmark program is executed with the Intel Advisor 2022.3 toolkit that analyzes the execution and provides the data of interest. The benchmark is run on a single node of the Cobra supercomputer at the Max-Planck Computing and Data Facility (MPCDF), featuring two Intel Xeon Gold 6148F processors (SkyLake architecture) with 20 cores of 2.4 GHz clock rate and 27.5 MB L3 cache each. The number of `OpenMP` threads used is 40, the same as the number of cores per node available.

The chosen problem is of dimension $(RZ \times \varphi \times v_{||} \times \mu \times \alpha) = (131126 \times 4 \times 20 \times 2 \times 2)$, representing the typical load of a single compute node in a production run distributed among 320 nodes. The total amount of grid points is approximately 42 million, resulting in arrays of size 335 MB without ghosts. With four ghost points in φ and $v_{||}$ and 2 in μ, the total number of points is 201 million, with array sizes of 1611 MB. Thus the distribution function does not fit into the L3 cache, and the performance is expected to be either limited by the bandwidth of the DRAM (the memory entity next in size) or by the number of FLOPS that can be performed.

The benchmark includes the BGK and LBD collision operators as well as the velocity space moments (MOM) and, for reference, the linear combination (LC) ($y = ax_1 + bx_2$) and AXPY ($y = ax + y$) operators. All computations have been performed with double precision. Fig. 4.16 shows the result of the benchmark program in the form of the roofline model. First, the two reference operators, LC and AXPY, reproduce results from Ref. [62]. As expected, they are clearly bound by the DRAM memory bandwidth of approximately 210 GB/s due to the low arithmetic intensity of the operators. While the BGK and the MOM operators have approximately the same arithmetic intensity, the former has a memory bandwidth of approximately 846 MB/s and 150 GFLOPS against 584 MB/s and 105 GFLOPS*. The

*The memory bandwidth reported in Intel Advisor is the memory transferred between the CPU and the L1 memory subsystem.

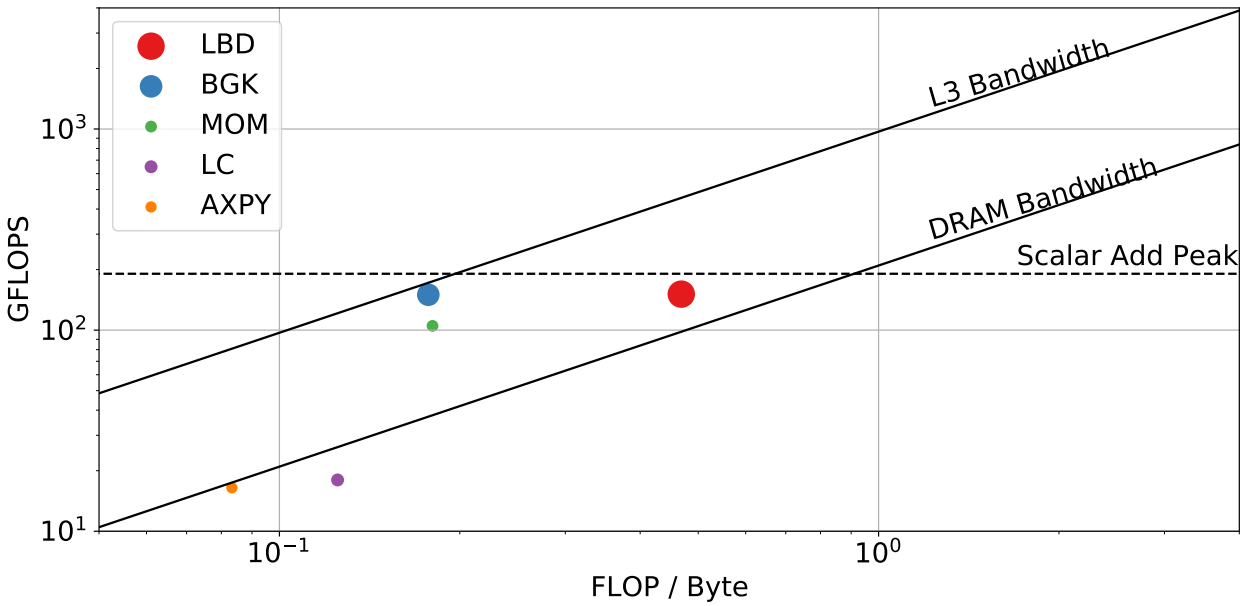

Figure 4.16. Roofline model of the performed benchmark described in the main text. The lines show the performance bounds given by the L3 bandwidth (970 GB/s), DRAM bandwidth (209 GB/s), and scalar add peak (190 GFLOPS). Other hardware limits that extend beyond the plot limits are not shown. The points represent the results for the BGK, MOM, and LBD operators and reference results for the linear combination (LC) and AXPY operators. The size of the points is scaled by the elapsed time spent in the operators.

memory traffic is close to the L3 memory bandwidth of approximately 970 GB/s, indicating that the operators most likely benefit from cache re-usage. The LBD operator has a higher arithmetic intensity due to stencil operations. Its memory bandwidth is 322 GB/s with 151 GFLOPS. The BGK and MOM operators do not use ghost points compared to the LBD operator. The execution of the BGK, LBD, and MOM operators is vectorized with an approximate vectorization efficiency (estimated gain per vector length, vector length is four here) of 100%, 88%, and 99%, respectively.

4.6.2 Parallel Efficiency

The second part of the performance analysis considers the scaling of the code with an increasing number of compute nodes. An application is parallelized by splitting the computational domain into sub-domains distributed over several compute nodes. The application considered here uses stencil operations to calculate derivatives, meaning that part of the data required to calculate the derivative at a sub-domain boundary is located at a different compute node. These points are communicated via ghost exchange. The library used to implement this approach is `MPI`. Since the ghost exchange is already required in the collisionless code, its contribution is factored out from the following analysis. Nonetheless, there is additional communication between compute nodes that are required. Calculating integrals over veloc-

ity space requires splitting sums into partial sums that are performed on each compute node. At the end of summation, the individual results must be collected across different compute nodes. This operation is called reduction. Such operations are performed when calculating the velocity space moments and the velocity space boundary sums in the conservative corrections of the finite volume LBD operator. These operations will be analyzed.

In the following, a strong scaling is performed, which means that the problem size is kept fixed while the number of nodes is increased, resulting in an expected decrease of runtime[187]. Since the φ and α dimensions are orthogonal in the computation of collisions, these will not be considered in the scaling. Further, the BGK operator does not contain stencil operations and is not dependent on ghost exchange. Hence ideal strong scaling is assumed, and no analysis is performed. For the LBD and MOM operators, a domain size of $(RZ \times \varphi \times v_{||} \times \mu \times \alpha) = (261121 \times 1 \times 64 \times 32 \times 2)$ is chosen, resulting in approximately one billion points and arrays of size 8.5 GB. With ghosts, the array size increases to 48 GB. Since multiple instances need to be stored due to the RK4 time integration, the Cobra supercomputer's fat partition must be used for the run on a single node. All other runs used the standard partitions with the same CPUs as in the node-level performance analysis. The Cobra supercomputer features an OmniPath network connecting the compute nodes with memory bandwidths of 100 GB/s.

First, a scaling only in the $v_{||}$ dimension is performed, and the contributions to the runtime by computations and reduction operations are analyzed. Figure 4.17 shows that for a small number of compute nodes, the communication part is negligible, and the scaling of the total (computation plus communication) time per time step is nearly ideal. With a more notable amount of compute nodes, the total scaling deviates from the ideal expectation due to increased required communication since the pure computation time still scales almost ideally. The communication in the MOM operator starts to dominate the overall computational cost when more than four compute nodes are used. Because the LBD operator has a higher computational intensity, the effect of communication is not as strong. The scaling performed here exhausted all available dimensions of the problem. As a result, the ratio of ghost to grid points is 4:1.

Next, the parallel efficiency of the implementation is of interest. Keeping the problem size fixed, doubling the number of processes should ideally result in half the computational time required. Due to Amdahl's law[188] the ideal speedup will be diminished due to serial parts in the program. The speedup used here is defined as[187],

$$sp(n) = \frac{t_1}{t_n}, \tag{4.223}$$

where t_1 is the execution time on one process and t_n on n processes. The parallel efficiency[187] $\eta(n) = sp(n)/n$ is a measurement of how efficiently the program is parallelized. This quantity

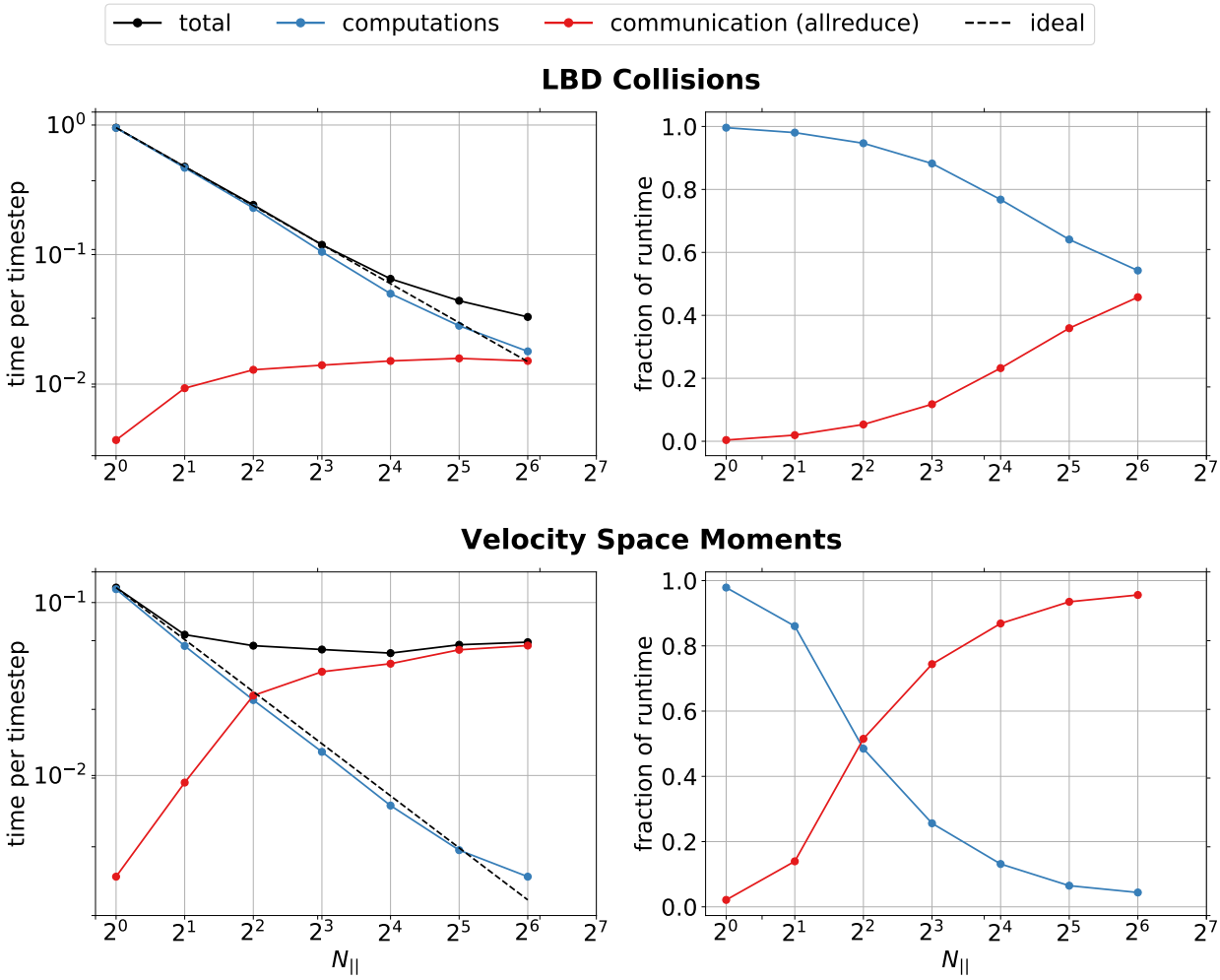

Figure 4.17. Time per time step for the strong scaling of the LBD and MOM (velocity space moments) operators in the $v_{||}$ dimension. The contributions due to computation and communication are shown separately. The black dotted line indicates the ideal scaling. The fraction of runtime (per time step) for computation and communication is shown on the right.

will be different for each test case due to runtime fluctuations. Thus an average efficiency is of greater interest. This number is obtained by fitting a function,

$$sp(N_{||}, N_\mu) = c_1 N_{||}^{\eta_{||}} N_\mu^{\eta_\mu}, \tag{4.224}$$

to the results obtained from a 2D strong scaling in the two velocity space directions. Here $\eta_{||}$ and η_μ denote the efficiency when parallelizing along the $v_{||}$ or μ dimension and c_1 is an irrelevant constant. This function is a natural choice since doubling the number of processes in one dimension would ideally result in double the speedup.

The scaling tests have been performed on the same hardware as before, scanning the 2D parameter space selectively with up to 512 compute nodes. Figs. 4.18 and 4.19 show the results of a 2D strong scaling for the computation only and the total (computation plus communication) part, together with efficiency fits. The fits have been performed with the nonlinear least squares method and the Levenberg-Marquard algorithm[189]. The results confirm the previous observations from the $v_{||}$ scaling. The computational part scales nearly ideal (≈94-96%), whereas the communication lowers the overall efficiency to ≈65-74%. For currently performed production runs, the runtime spent in communication is tolerable, since typically the number of $v_{||}$ and μ processes is around 2 and 10, respectively*. For future production runs with more than 1000 nodes, more processes in the velocity space dimensions must be used (due to the exhaustion of the φ and α dimensions), and further performance optimization may be required.

*Using a total of 320 compute nodes with 16 and 2 processes in φ and α respectively, with one process per socket.

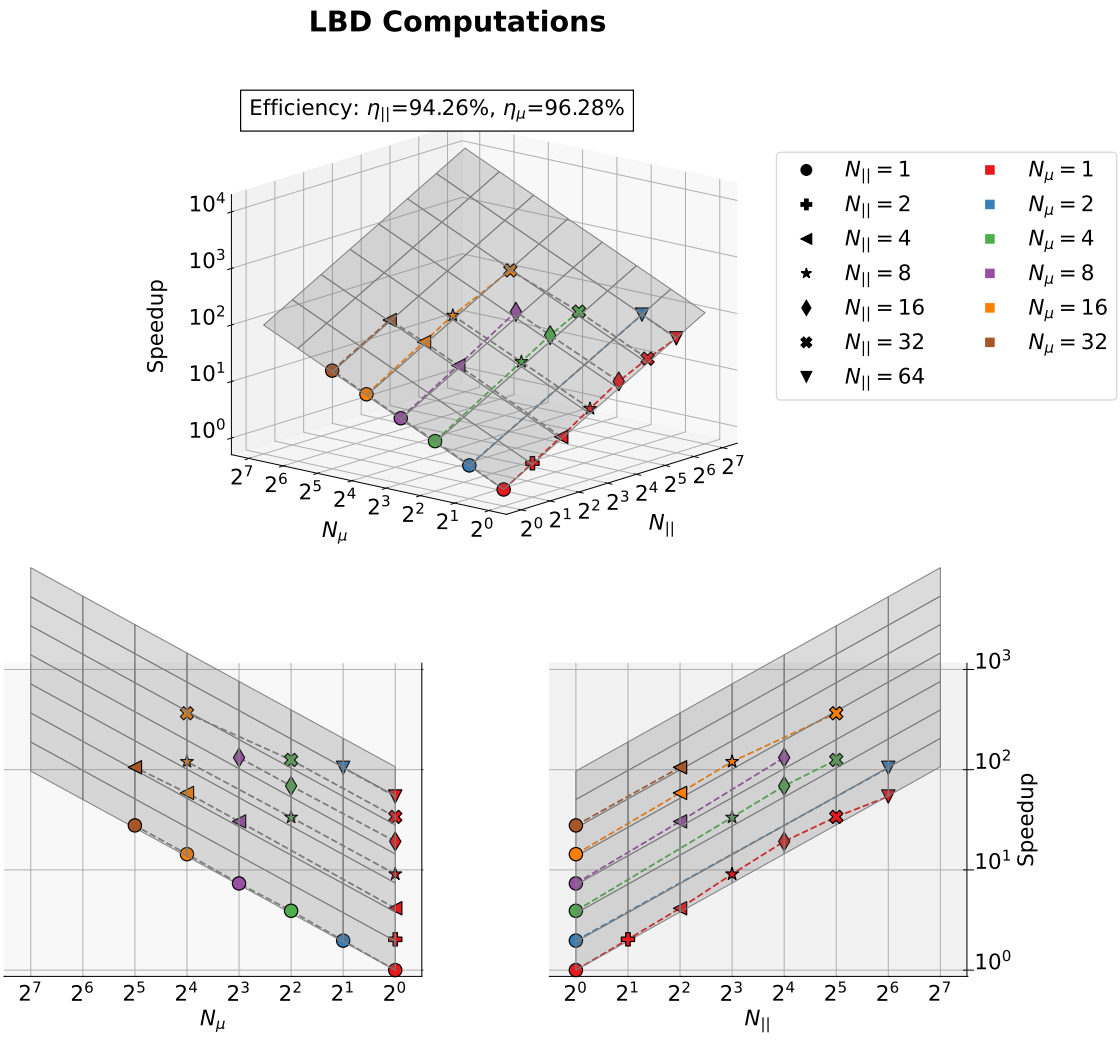

Figure 4.18. 2D strong scaling of the computational part of the LBD operator. The points show the measured results and have the same color along constant N_{μ} and the same symbols along constant $N_{||}$. The orange plane shows the fitted function (4.224) with parameters given in the box. The bottom shows two different projections of the 3D plot, where the individual $v_{||}$ or μ scalings can be analyzed.

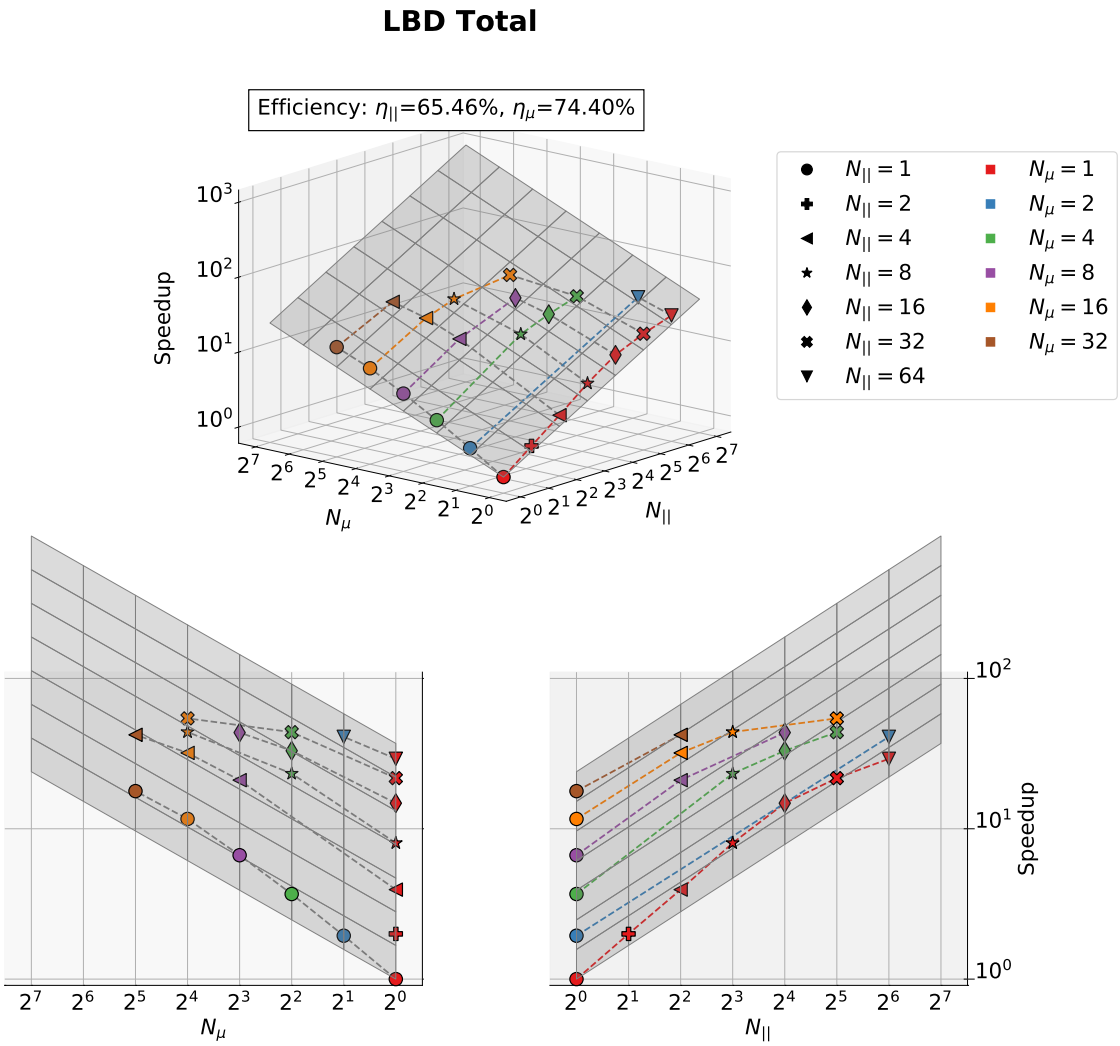

Figure 4.19. Same as Fig. 4.18 but for the total (computation plus communication) LBD operator.

4.7 Chapter Summary

In this chapter, the technical part of this thesis has been covered. First, the quadrature schemes have been improved, resulting in a better evaluation of the velocity space moments of the distribution function. Second, a basic finite difference (FD) discretization and an advanced conservative finite volume (FV) of the LBD operator were developed. A unique scheme to achieve the conservation of momentum and energy up to machine precision has been developed. Third, both discretizations have been verified, and the advantages of the FV version have been analyzed. Due to the enhanced conservation properties, the FV version can be used with much smaller grids while still being stable in contrast to the basic FD version. Fourth, the stability of the discretizations has been investigated, providing approximate criteria on the maximal time steps possible. Further, an advanced time-stepping scheme (Strang splitting) has been implemented and shown to be advantageous in the simulation of collisional kinetic equations. Fifth, the discretization presented has been implemented in a high-performance code. The node level performance and a strong scaling of the MPI parallelization have been provided.

The conservative finite volume discretization and the two verification studies have been published in Ref. [58].

Chapter 5

Collisional Gyrokinetic Simulations of the TCV Tokamak

In this chapter, the previously presented collision models will be used in the `GENE-X` code to perform gyrokinetic simulations of edge and scrape-off layer (SOL) turbulence of the "Tokamak à configuration variable" (TCV)[190]. The results of a validation study are presented, where the collisionless, BGK, and LBD models were used in three individual simulations. The validation considers the plasma profiles, power balance, and scrape-off layer fall-off length. The turbulence observed is analyzed and characterized using Fourier and trapped particle diagnostics. At the end of this chapter, an alternative, optimized implementation of the LBD operator using a formulation based on the perpendicular velocity is used to compare a simulation with lower resolution against the reference from the TCV validation. The validation and turbulence characterization results have been published in Ref. [59].

5.1 Validation against TCV-X21

The difference between verification and validation can be summarized as follows. Verification checks if a computer code (or simulation) implemented the equations given by a model correctly, whereas validation checks if the implemented model describes the physical reality (i.e., experiments) correctly[191]. For example, section 4.4 presented a verification of the implementation of the collision models by checking against known properties of collisions, such as conservation and relaxation. By passing such a check, it is inherently unclear if the collision model under consideration is sufficient to describe processes observed in the experiment, such as, for example, neoclassical physics. Thus, the way of addressing the degree to which the collision model describes the experiment in a particular application case is validation[191]. In

the following, the collisionless, BGK, and LBD collision models are used for the simulation of micro-turbulence and validation against the experiment.

The collisionless part of the GENE-X code has passed several verifications[34,62] as well as a first validation, together with simulations including BGK collisions, in the ASDEX-Upgrade (AUG) tokamak[112]. The AUG validation has shown that including collisions improves the agreement with the experiment. Besides that, two GRILLIX simulations without[192] and with[193] neutral gas physics provide strong indications that neutral gas dynamics heavily influence the chosen experimental case. These findings suggest that the current model in GENE-X should be extended to include neutral gas dynamics in future model improvements. Nonetheless, it is interesting to see if the current model in GENE-X can describe plasma micro-turbulence in experimental cases with little influence by neutral gas. Further, the question arises as to which degree collisions are required in such simulations, focusing on the edge and SOL region.

In the following, the experimental case called "TCV-X21"[194] will be used for validation. It was developed as an edge turbulence reference case, minimizing the effect of neutral gas dynamics and making simulations cheaper using a smaller magnetic field (since the real space resolution depends on the Larmor radius, which is larger for smaller magnetic fields). The original validation study has been performed in Ref. [194] and compared simulations by three different fluid turbulence codes, GRILLIX[115,192,195,196], GBS[197,198] and TOKAM3X[199,200]. The original study's results are publicly available in Ref. [201]. Additional details can be found in Ref. [202].

5.1.1 Simulation Setup

The setup of all three simulations is described in detail in Ref. [59]. This section provides a summary of the most important points. Due to the shared approach of GRILLIX and GENE-X of treating the complicated X-point geometry, the same magnetic equilibrium as in the GRILLIX simulations[194] can be used (Fig. 5.1). The grid in RZ is built with $\Delta R = \Delta Z \approx 1.23$ mm, resulting in 200657 points. In the toroidal direction, 32 planes are used, and the velocity space is discretized with $(n_{v_{||}} \times n_\mu) = (80 \times 20)$ points for the collisionless and BGK simulation and 60 μ points for the LBD simulation. The total number of grid points is thus ≈20 billion for the collisionless and BGK and ≈60 billion for the LBD simulation (without ghost points). The real space domain is chosen to cover the region from poloidal flux surface label $\rho_{\text{pol}} \in [0.74, 1.1]$. The velocity space bounds are $\hat{v}_{||,\text{max}} = 8$ and $\hat{\mu}_{\text{max}} = 64$, with a symmetric grid in parallel velocity and magnetic moment grid starting at 0. Quadrature schemes are used as mentioned in section 4.1, Simpson in $v_{||}$ and Gauss-Laguerre in μ for the collisionless and BGK simulation and midpoint in both dimensions for the LBD simulation. The reference parameters used for the normalization are $L_{\text{ref}} = 0.906$ m, $B_{\text{ref}} = 0.929$ T,

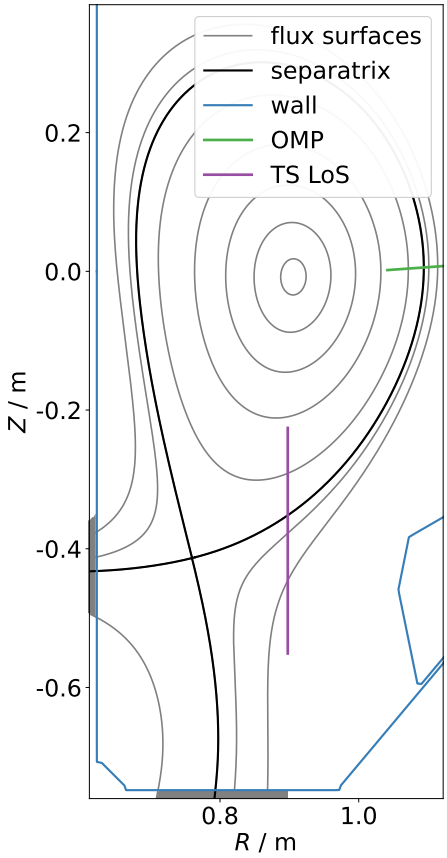

Figure 5.1. Geometry of the simulations given by flux surfaces, the separatrix, and the device wall. The simulation uses the outboard midplane (OMP) for profile comparisons. The Thomson scattering (TS) line of sight (LoS) shows the location of the experimental measurements[194]. Taken from Ref. [59].

$T_{\mathrm{ref}} = 0.02$ keV and $n_{\mathrm{ref}} = 10^{19}$ m^{-3}. The derived reference parameters read $c_{\mathrm{ref}} \approx 43769$ m/s, $\rho_{\mathrm{ref}} \approx 4.9 \times 10^{-4}$ m, $\beta_{\mathrm{ref}} \approx 9.33 \times 10^{-5}$ and `coll_ref` ≈ 0.628. For the collision operators, a floor value of 0.25 in normalized density and temperature is used because the numerical scheme in `GENE-X` is not positivity preserving, and spurious negative values of the distribution function may occur, resulting in unphysical (negative or imaginary) collision frequencies. The plasma species simulated are electrons and deuterium ions, with masses of $\hat{m}_{\mathrm{e}} \approx 1/1830$ and $\hat{m}_{\mathrm{i}} = 2$ respectively.

The simulation is initialized with a canonical Maxwellian[105,112,203,204] distribution, with profiles given by Fig. 5.2. For time integration, RK4 is used with time step $\Delta\hat{t} = 4 \times 10^{-4}$ for the collisionless and BGK simulation, chosen by trial and error starting from an estimation with the CFL criterion given in Ref. [62]. For the LBD simulation, Strang splitting (with RK4 for the Vlasov and collisional part, see section 4.5.4) is used with a decreased time step of $\Delta\hat{t} = 2 \times 10^{-4}$. Due to the splitting, the collisional step is effectively performed with $\Delta\hat{t}/2 = 10^{-4}$, being close to the stability limit of the RK4 integrator for the case where the

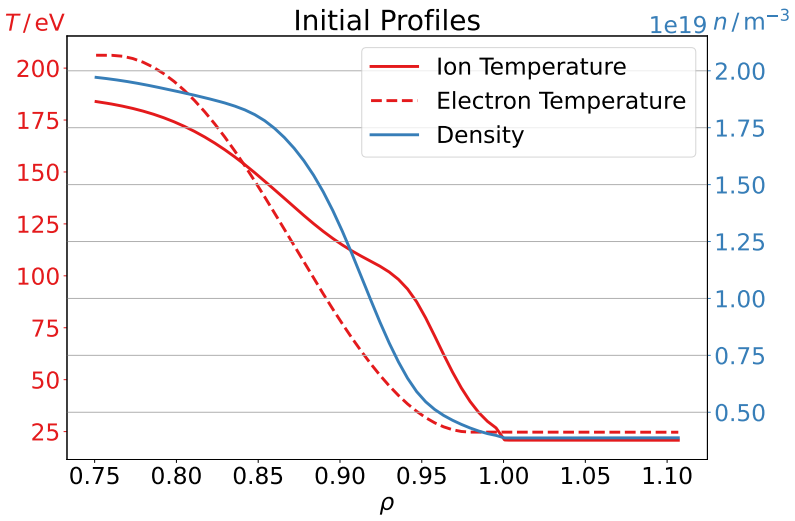

Figure 5.2. Initial profiles of the simulations. Taken from Ref. [59].

perpendicular diffusion is most unstable in the simulation domain*. The advective part of the LBD operator imposed no further restrictions since the lower limit of the temperature was chosen around 25 eV to stabilize the initial condition (see Appendix A in Ref. [59]). The simulations are performed until the turbulence reaches a quasi-stationary state (Fig. 5.3), which is approximately achieved after 85k, 53k, and 110k time steps for the collisionless, BGK, and LBD simulation. Both collisional simulations saturate faster than the collisionless simulation[59].

5.1.2 Profile Validation

After the simulations have reached a quasi-stationary state, the statistical properties of the turbulence are assumed not to change, and the time-averaged plasma profiles are validated. The results of validating the plasma profiles were presented in Ref. [59] and can be seen in Figs. 5.4-5.6. The profiles agree well within the confined region $\rho_{\text{pol}} < 1$ and deviate in the SOL. The deviation is due to the Dirichlet boundary conditions that keep the distribution function fixed at the domain boundaries of the simulation, effectively working as a heat and particle bath. The boundary conditions compensate for local positive profile gradients that arise due to lower density or temperatures than the boundary value. In principle, one can think that the profiles, while fixed at the left and right boundary, are free to evolve to any shape in between the boundaries. As discussed in Appendix A of Ref. [59], the choice of the SOL density and temperature values is due to the stability of the initialized equilibrium of

*This point is chosen where the real space dependent factor in eq. (4.169), $\hat{B}/(\nu_{\alpha\beta}T_{\alpha\beta}) \sim \hat{B}\sqrt{\hat{T}}/\hat{n}$ has a minimum. Approximate values at this point are $\hat{n} = 1.59$, $\hat{T}_e = 5.23$ and $\hat{B} = 0.86$. Using these parameters, an eigenvalue stability analysis (section 4.5.2) is performed, with the smallest negative real eigenvalue of -2.305 (83% of RK4 stability boundary).

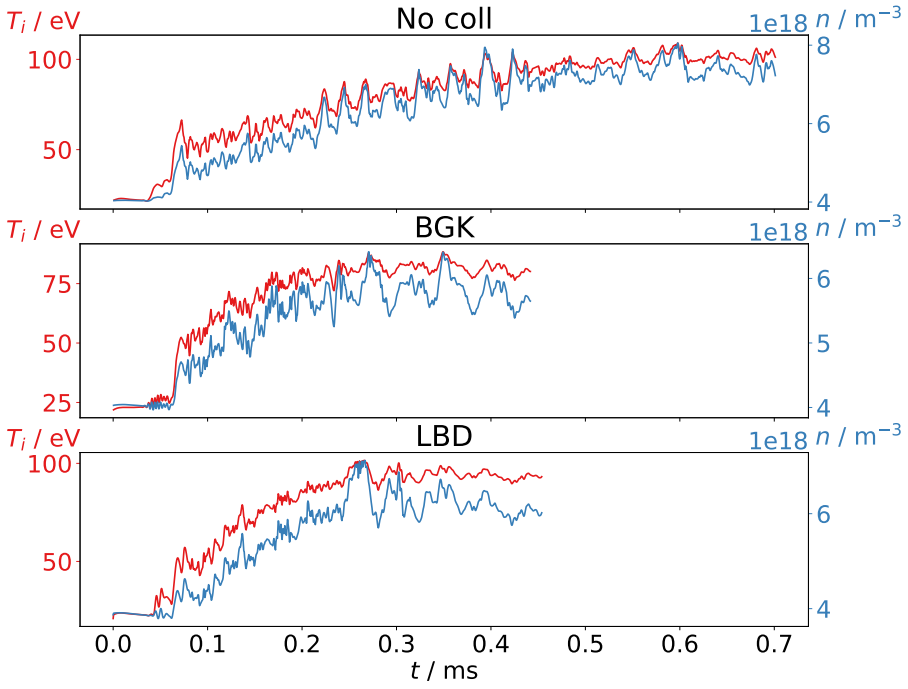

Figure 5.3. Time traces of the OMP density and ion temperature at a point close to the separatrix ($\rho_{\text{pol}} = 0.9996$). Taken from Ref. [59].

the simulation. Lower values did not lead to a stable initial state, and other equilibrating dynamics happen before the onset of turbulence[205]. For the future, an improved initial state resulting from neoclassical simulations would be beneficial to simulate in realistic SOL conditions. Such a procedure is described in, e.g., Ref. [32]. The additional diffusion applied in the buffer zone will dominate the dynamics at the domain boundaries. Results in these regions are thus not considered physical and not considered in the validation.

One of the main results is given by the validation of the electron temperature (Fig. 5.5), where the most advanced collision model, the LBD operator, reproduces the profile observed in the experiment within the error bars. The profiles can be imagined to be fixed only at the boundaries, leaving the shape free to evolve from the initial state given in Fig. 5.2. Further, only a minimal set of input parameters is used in the simulation (the values set at the boundaries in addition to the magnetic equilibrium) in contrast to δf simulations where the experimental background profiles have to be prescribed[98]. Another result concerns the electron temperature profile, which is too high in the edge and SOL, consistent with previous simulations in AUG[112]. This behavior is because trapped electrons cannot undergo collisional cooling in the collisionless simulation[59]. In other words, the collisional interaction with passing electrons that can take the excess energy to the divertor plates in the open field line region is missing. Thus the trapped electrons drift radially outward to the wall, keeping their energy, resulting in the observed temperature profile being too high. Finally,

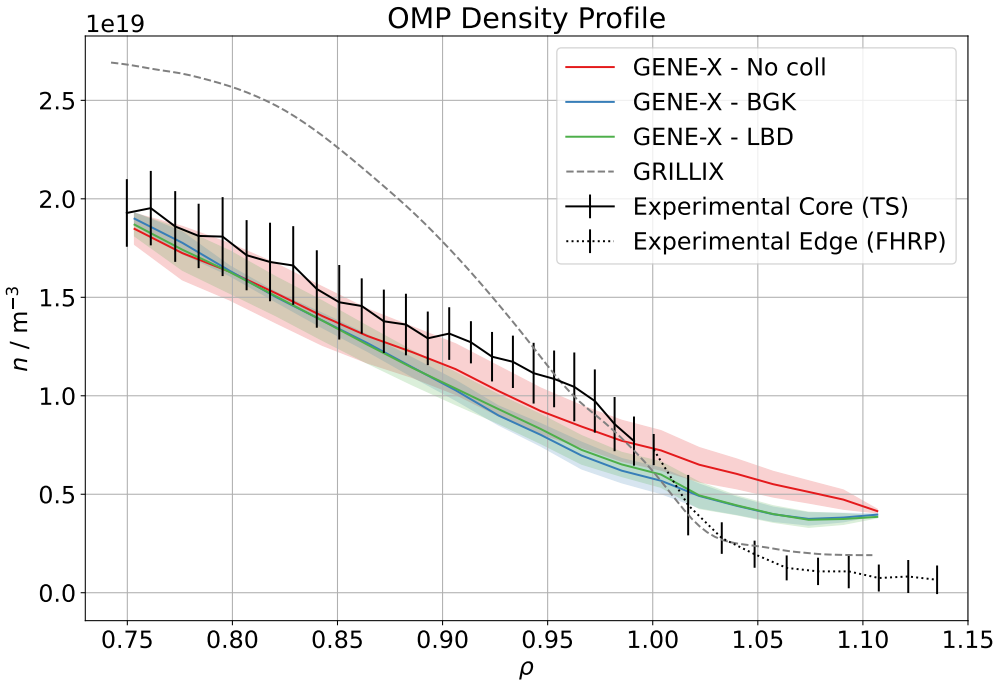

Figure 5.4. Density profiles along the OMP from the three `GENE-X` simulations using different collision models. The profiles have been averaged toroidally and temporally over 100 μs, and the shaded area shows the standard deviation. Experimental references are given by core measurements from the Thomson scattering diagnostics and SOL measurements from the fast reciprocating probe (FHRP)[194]. The result of the `GRILLIX` simulation[194] is given for comparison. Taken from Ref. [59].

a comparison with the `GRILLIX` simulations shows that, while `GRILLIX` performs very well in the SOL, the confined region is much better described with `GENE-X`. The former is due to the advanced boundary conditions in `GRILLIX`. The latter is because trapped electron modes (TEMs) were found to dominate the turbulence in the `GENE-X` simulations[59], physics which are currently not included in the `GRILLIX` model.

Additionally to the results published in Ref. [59], the density and electron temperature at the Thomson scattering (TS) line of sight as well as the OMP radial electric field are shown (Figs. 5.7-5.9). First, the qualitative difference between the OMP and TS profiles in the simulations is small, except for the collisionless electron temperature, which is higher than in the experiment but not as much as in Fig. 5.5. The reason is that the TS line of sight is located much closer to the X-point (Fig. 5.1) and, therefore, closer to the mirror point of trapped electrons in the confined region and near the mirror point in the SOL. The density of trapped particles is reduced at these radial locations and thus their contribution to the temperature (in agreement to measurements of the trapped particle density along a flux surface[59]). Second, the fluctuation amplitudes at the TS line of sight are reduced, consistent with the expected ballooning character of the turbulence. The radial electric field shown in Fig. 5.9 has a similar shape in all three simulations. The profiles contain alternating local

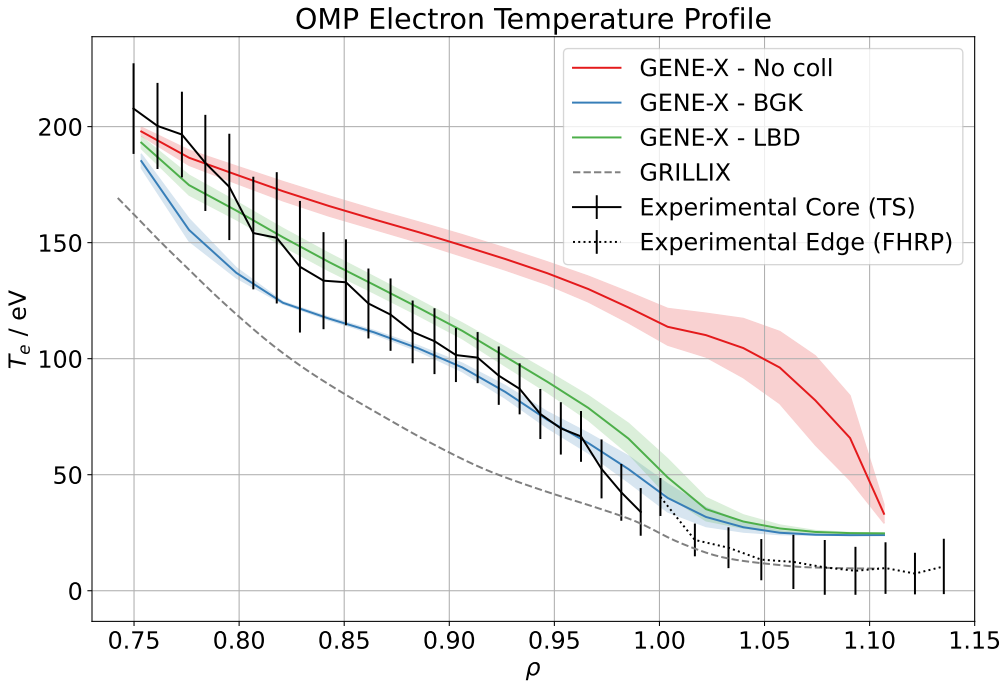

Figure 5.5. Same as Fig. 5.4 for electron temperature. Taken from Ref. [59].

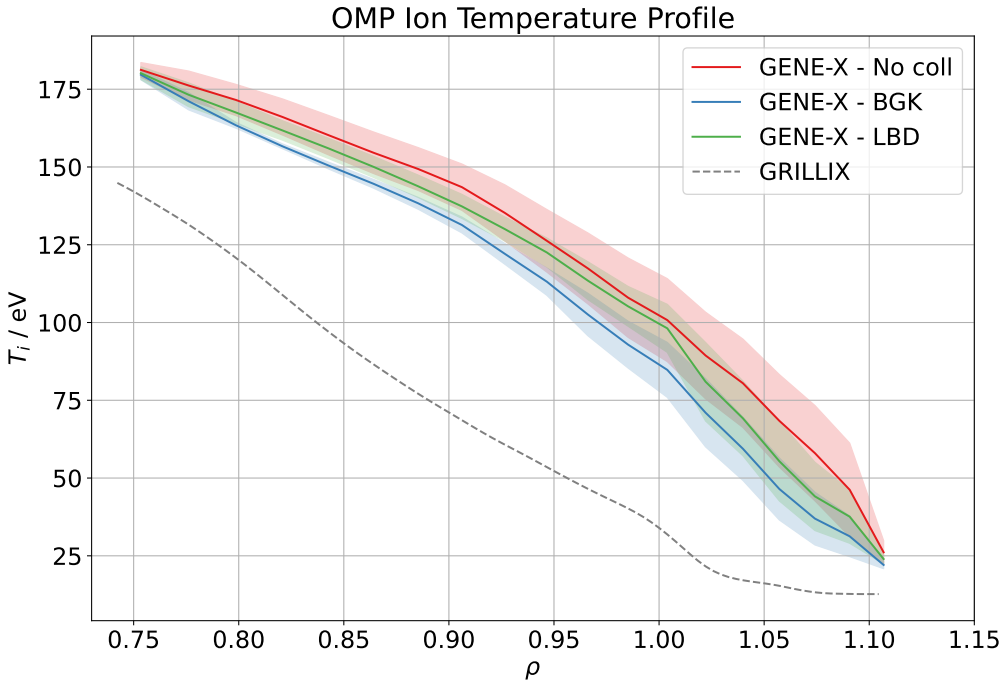

Figure 5.6. Same as Fig. 5.4 for ion temperature. Taken from Ref. [59].

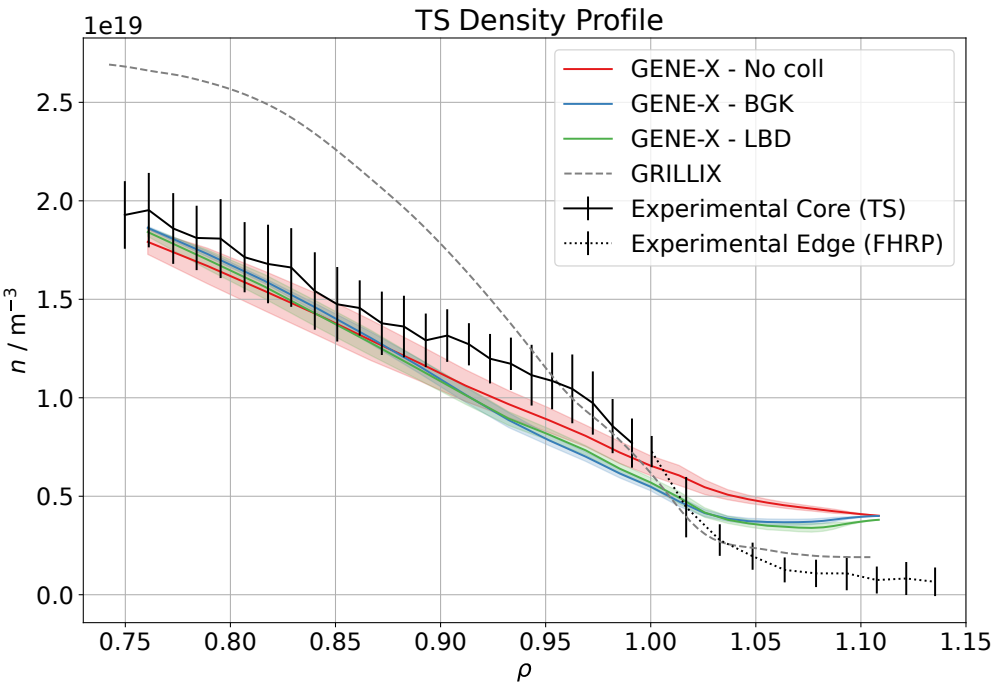

Figure 5.7. Same as Fig. 5.4 but at the location of the Thomson scattering (TS) diagnostics (Fig. 5.1).

extrema indicating the presence of zonal flows[192], which can be confirmed by investigating the video in the supplementary materials of Ref. [59]. The `GRILLIX` simulation agrees well with `GENE-X` in the open field line region, while differences are observed in the closed field line region.

5.1.3 Power Balance and Heat Exhaust Validation

The second part of the validation considers the simulation's power balance and heat exhaust. The results in this section have been published in Ref. [59]. The parallel heat flux is given by the third moment of the distribution function

$$q_{||,\alpha} = \int f_\alpha v_{||} \left(\frac{m_\alpha v_{||}^2}{2} + \mu B \right) \mathrm{d}V. \tag{5.1}$$

and the radial $\mathbf{E} \times \mathbf{B}$ heat flux is approximated as[62]

$$q_{E,\alpha} \approx -\frac{c}{B} \left\{ \nabla_\perp \phi_1 \times \mathbf{b} \right\}_r W_\alpha, \tag{5.2}$$

where W_α is the total energy (sum of parallel and perpendicular parts in section 3.2.5).

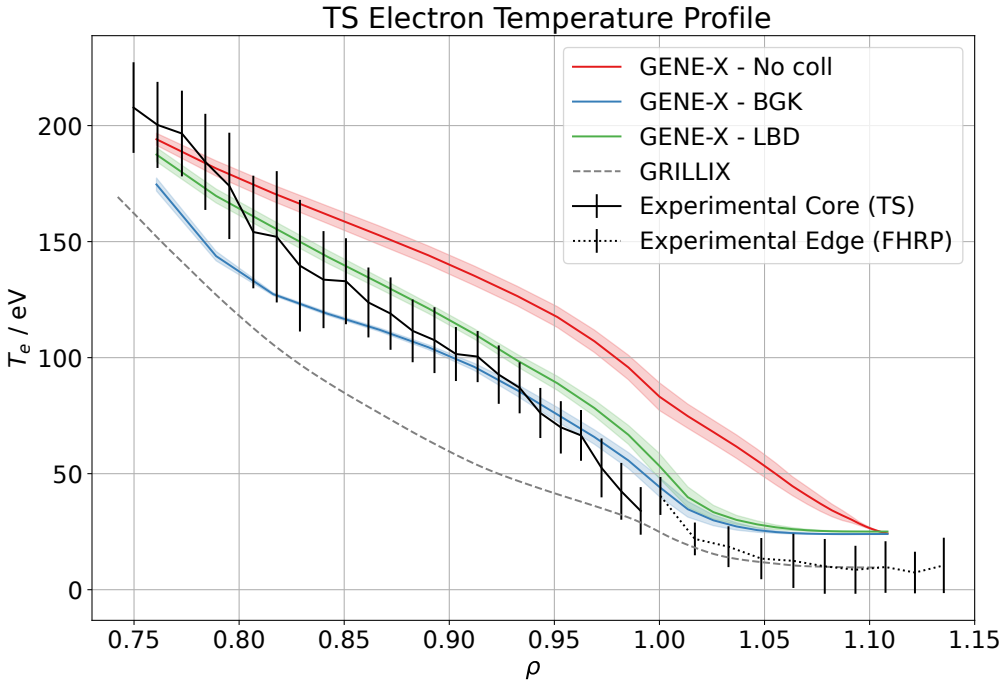

Figure 5.8. Same as Fig. 5.5 but at the location of the Thomson scattering (TS) diagnostics (Fig. 5.1).

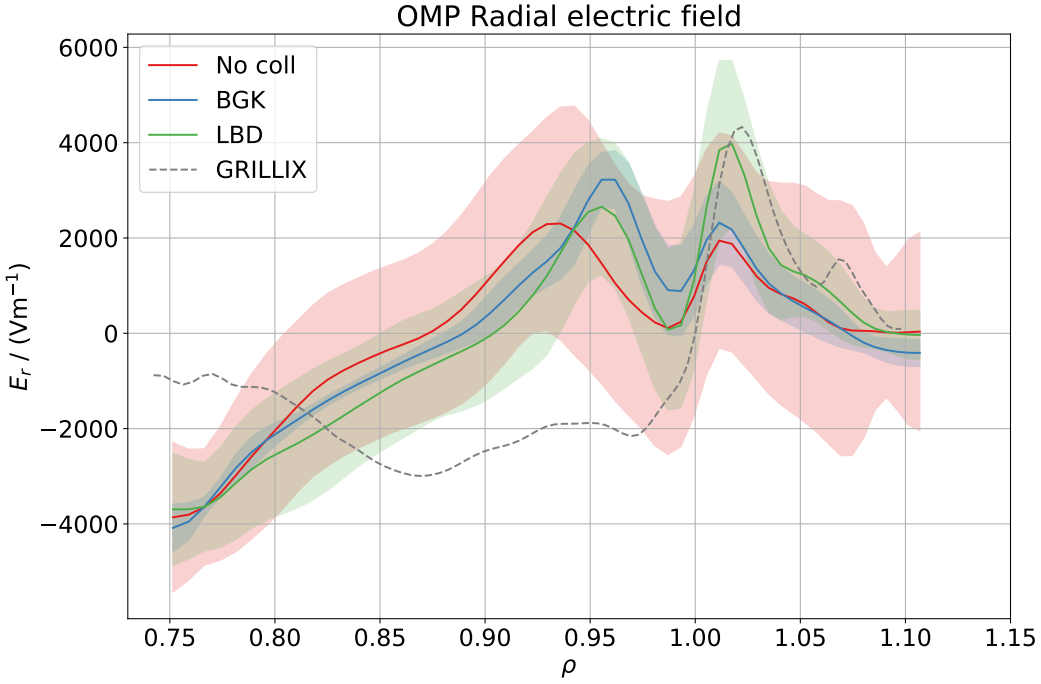

Figure 5.9. Same as Fig. 5.4 but for the radial electric field.

Table 5.1. Results of the validation of the power balance. The index "sep" indicates the total heat flux crossing the separatrix and "div" the total heat flux hitting the divertor plates. The simulation values were averaged over 100 μs. The experimental values (TCV) are from Ref. [194]. The other values have been published in Ref. [59].

	TCV	**No Coll**	**BGK**	**LBD**
Q_r^{sep} / kW	120	393.8	51.7	132.3
$Q_{\parallel}^{\mathrm{div}}$ / kW	-	134.4	92.5	145.0
$Q_{\parallel}^{\mathrm{right-div}}$ / kW	38.1	102.2	54.3	78.7
$Q_{\parallel}^{\mathrm{left-div}}$ / kW	-	32.2	38.5	66.3

The total heat fluxes are,

$$Q_{\parallel}^{\mathrm{div}} = 2\pi \sum_{\alpha} \int_{\mathrm{div}} \left\langle q_{\parallel,\alpha}(l) \right\rangle_{\varphi,t} R(l) \sin\left(\alpha_I(l)\right) \mathrm{d}l, \tag{5.3}$$

$$Q_r^{\mathrm{sep}} = 2\pi \sum_{\alpha} \oint_{\mathrm{sep}} \left\langle q_{E,\alpha}(l) \right\rangle_{\varphi,t} R(l)\, \mathrm{d}l. \tag{5.4}$$

Here, the magnetic field line incidence angle α_I (see Fig. 5.11) is accounted for the parallel heat flux on the divertor. Both expressions use the toroidal and temporal (100 μs) averaged heat fluxes, where the average operation is denoted as $\langle\cdot\rangle$. The integrals go over a line with length l of the corresponding domains shown in Fig. 5.10. The results of the power balance validation can be seen in Table 5.1. Using collisions improves the power balance significantly, in agreement with the theory of hot trapped electrons leaving the simulation at the radial domain boundary in the collisionless simulation (which was not measured here). The LBD simulation agrees with the experiment within 10% and, as the only simulation, shows a consistent power balance. The mismatch of the divertor power to the experiment is most likely due to the missing neutral gas model in `GENE-X`, as neutrals would contribute to the power balance by radiation[193]. Only contributions from $\mathbf{E}\times\mathbf{B}$ fluxes were considered for the separatrix power here.

Not only the total amount of power deposited on the divertor plates is of interest, but also the shape of the heat flux against the distance along the plates. Power spreading over a larger distance reduces the overall power density on the divertor plates. The profile is typically peaked close to the point where the separatrix hits the plates and falls off along the plate, described by the empirically established Eich function[48]

$$q_{\mathrm{div}}(r) = \frac{q_0}{2} \exp\left(\left(\frac{S}{2\lambda_q}\right)^2 - \frac{r-r_0}{\lambda_q}\right) \mathrm{erfc}\left(\frac{S}{2\lambda_q} - \frac{r-r_0}{S}\right) + q_{\mathrm{BG}}\,. \tag{5.5}$$

The parameters of this function are the SOL fall-off length λ_q, the power spreading factor S, the peak heat flux q_0, the background heat flux q_{BG} and a radial shift r_0[48]. The procedure

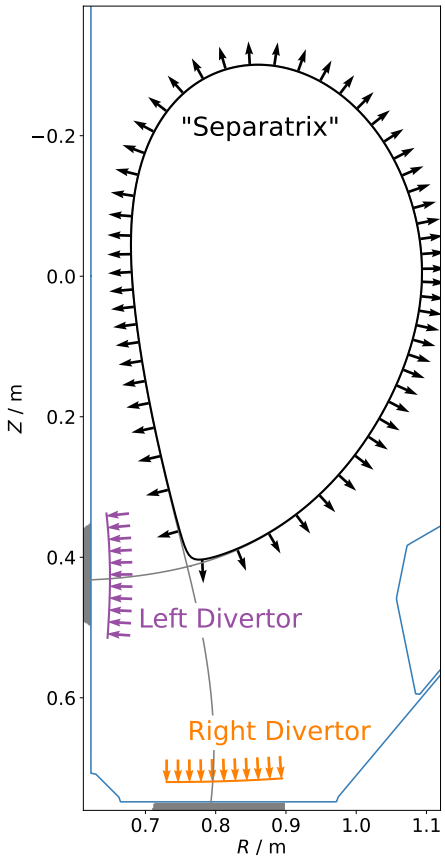

Figure 5.10. Surfaces used for the separatrix power and the divertor heat flux measurements performed in the validation. A closed flux surface approximates the separatrix with $\rho_{\mathrm{pol}} = 0.999$.

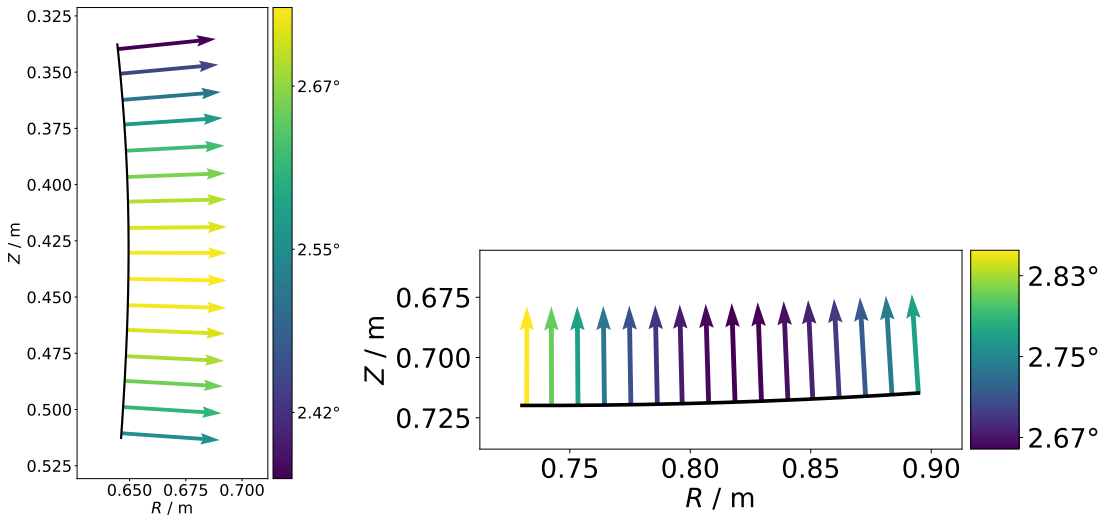

Figure 5.11. Magnetic field line incidence angles on the divertor plates given by Fig. 5.10 in the TCV geometry (Fig. 5.1).

Table 5.2. Results validating the SOL fall-off length (right divertor) by fitting the 100 μs averaged simulation values with the Eich function. The first block (upper sub-table) is taken from Ref. [194]. The second block (lower sub-table) was published in Ref. [59].

Right divertor:

	TCV	GRILLIX	GBS	TOKAM3X
λ_q / mm	5.5	1.1	11.6	0.1

		GENE-X		
		No Coll	BGK	LBD
λ_q / mm		1.34	4.68	3.75

Table 5.3. Same as Table 5.2 but for the fit of the `GENE-X` simulations on the left divertor.

Left divertor:

	GENE-X		
	No Coll	BGK	LBD
λ_q / mm	1.88	4.98	3.50

of how this quantity is measured for the `GENE-X` simulations is described in Refs. [59, 112]. The divertor lineouts in Fig. 5.10 and the magnetic field line incidence angles in Fig. 5.11 are used. Fig. 5.12 shows the fits for all simulations for both divertor plates. The Eich function describes the heat flux profiles well, and the overall fit improves by adding collisions to the simulation. The corresponding result of the fits for the quantity of interest, the SOL fall-off length λ_q are given in Table 5.2 for the right and Table 5.3 for the left divertor. The collisional gyrokinetic simulations produce the best agreement with the experiment. A collisional broadening can be observed, consistent with previous simulations in AUG[112]. However, an improved match with the LBD collision model is not achieved. This finding indicates that other physics are missing, e.g., neutral gas dynamics or improved boundary conditions.

5.2 Turbulence Characterization of TCV-X21

This section analyzes the simulations previously presented in section 5.1. The goal is to discover more about the underlying turbulence and compare the differences observed between the three simulations using different collision models. The results of this study have been published in Ref. [59]. Here a summary containing additional details is presented.

First, fluctuations of density, as well as electron and ion temperature, are considered. The fluctuations are defined by subtracting the average over a given temporal period,

$$\delta g = \frac{g - \langle g \rangle_t}{\langle g \rangle_t}, \tag{5.6}$$

where g can be any fluctuating quantity of interest. Fluctuations for the density, electron, and ion temperature are shown in Figs. 5.13, 5.14 and 5.15. All three quantities show that

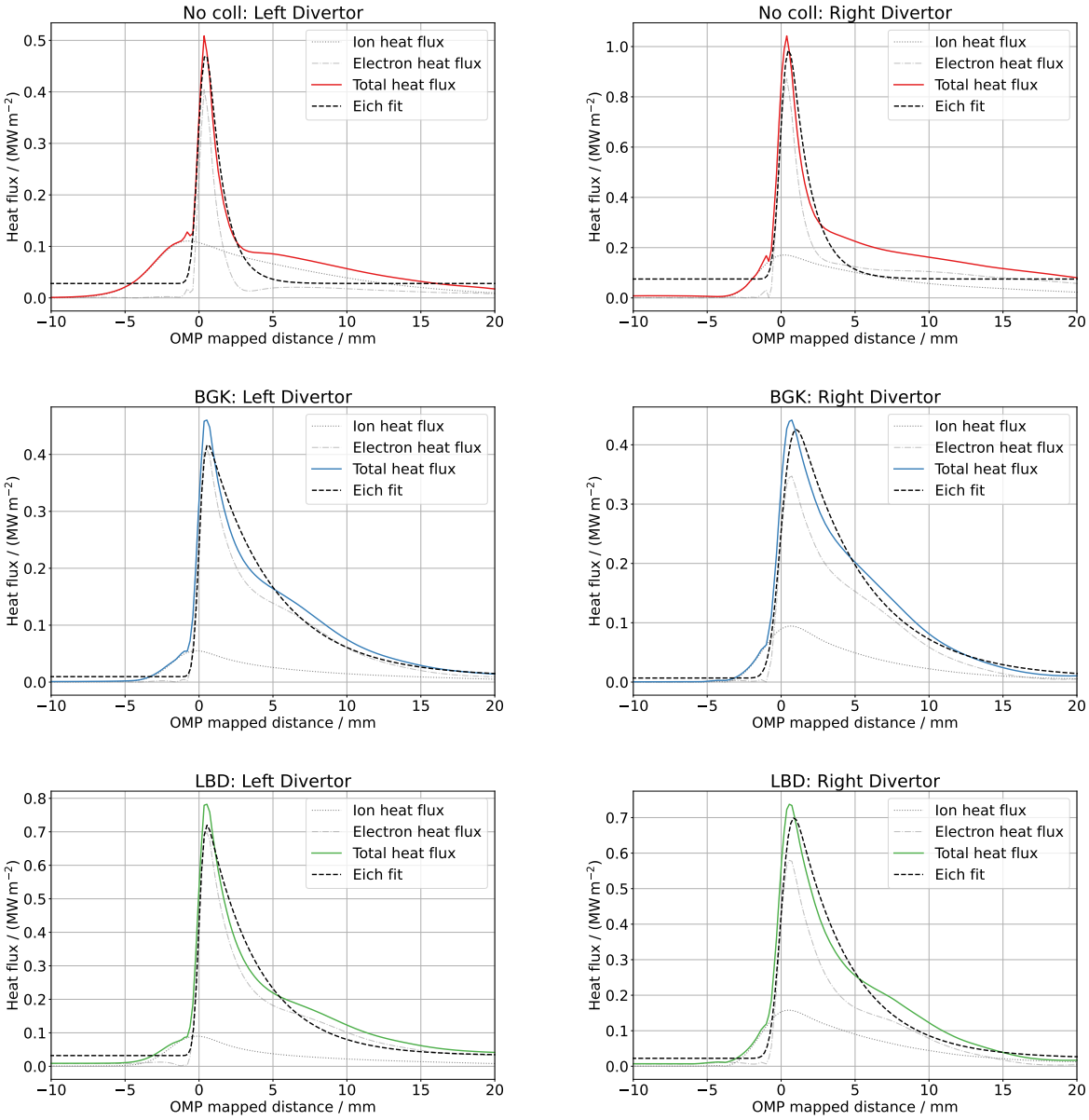

Figure 5.12. Parallel heat fluxes on the left and right divertor plates for the three simulations performed. The individual contributions of ions and electrons are separately shown, and the total heat flux is fitted with the Eich function. The lowermost right figure (LBD: Right Divertor) is taken from Ref. [59].

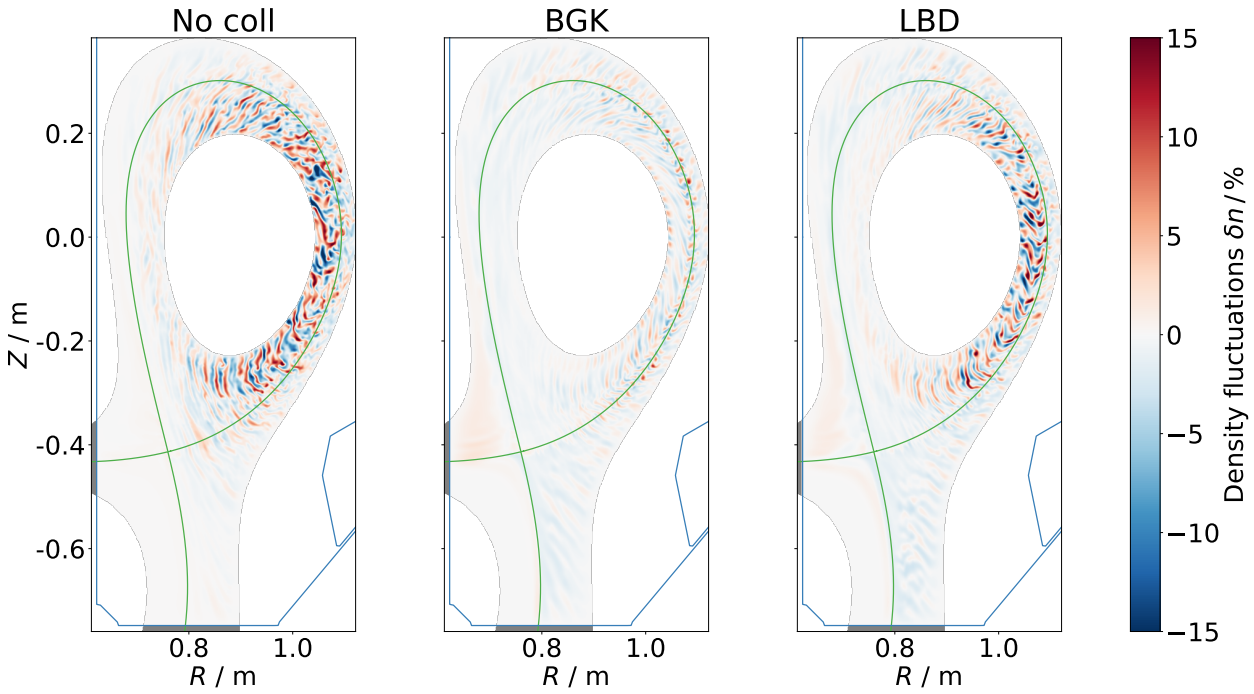

Figure 5.13. Density fluctuations relative to the temporal average over the last 100 μs at a single poloidal plane. Taken from Ref. [59].

the fluctuation amplitudes are highest in the collisionless and lowest in the BGK simulation, with LBD in between the other two. Further, the fluctuations in the SOL are similar for both collisional simulations. While the density fluctuations are not that strong in the collisionless case, the temperature fluctuations are significant and, in fact, larger than in the confined region. The larger temperature fluctuations are found for the electron temperature, which is significantly too hot in the SOL, and the ion temperature.

Second, the radial profiles of turbulence parameters are of interest. Here, the gradient lengths $L_{T,\alpha} = 1/\nabla \ln(T_\alpha)$ and $L_{n,\alpha} = 1/\nabla \ln(n_\alpha)$ can be compared to the flux surface line averaged major radius $\langle R \rangle_y$. This yields the normalized gradients $\langle R \rangle_y / L_{T,\alpha}$ and $\langle R \rangle_y / L_{n,\alpha}$. If electromagnetic effects are considered weak (as in L-mode discharges), the most dominant micro-instabilities in the confined region are the ITG and TEM[206]. The former is destabilized by ion temperature gradients[207] while stabilized by density gradients[208]. The latter is destabilized by both electron temperature and density gradients[207]. The ratios $\eta_\alpha = L_{n,\alpha}/L_{T,\alpha}$ are parameters of interest. Further, TEMs are stabilized by collisional de-trapping of trapped particles[209], thus the collisionality[64] $\nu^* = (\nu_\mathrm{e}/\epsilon)/\omega_b$ should be considered. Here, $\epsilon \approx r/\langle R \rangle_y$ denotes the inverse aspect ratio, approximated by an effective radius $r \approx r_\mathrm{eff} = L/(2\pi)$, where L is the total flux surface arc length. The electron collision rate is[16] $\nu_\mathrm{e} = 4\sqrt{2\pi} e^4 \ln \Lambda_\mathrm{ee} n_\mathrm{e} / (3\sqrt{m_\mathrm{e}} T_\mathrm{e}^{3/2})$ and $\omega_b = \sqrt{\epsilon} v_\mathrm{th,e} / (q \langle R \rangle_y)$ the electron bounce frequency[64], with safety factor q obtained by constructing a symmetry flux coordinate system (see section 5.2.1).

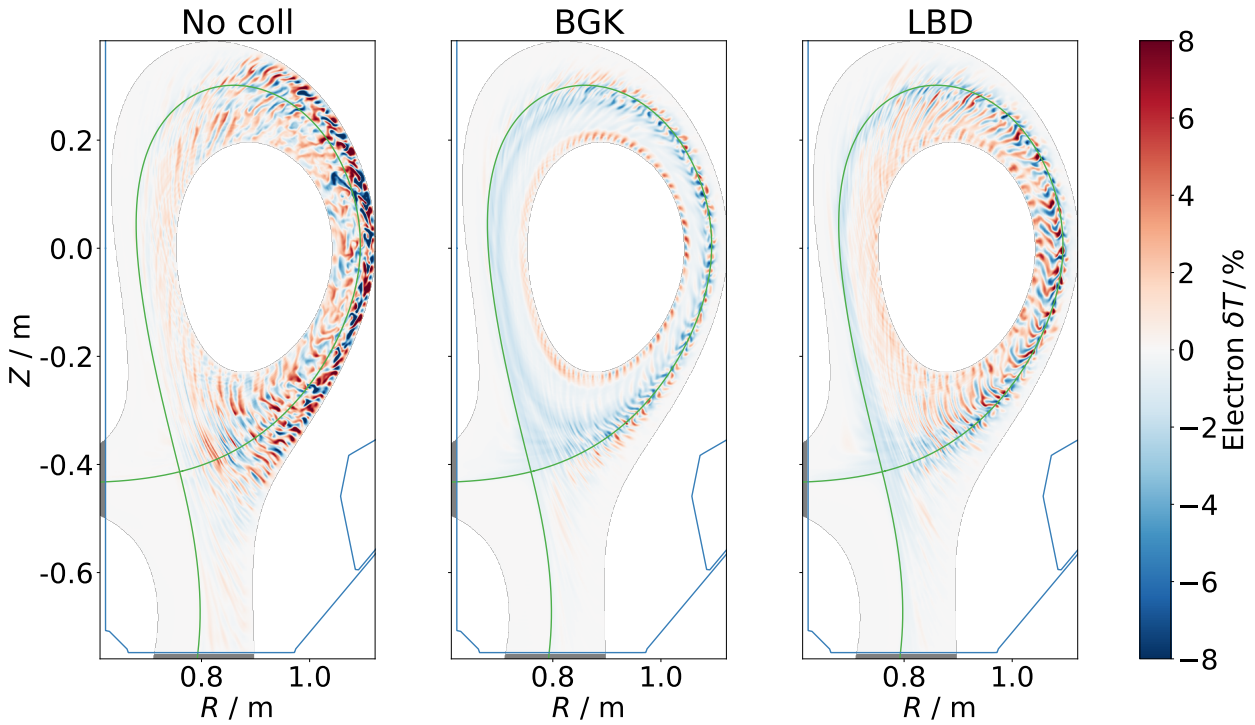

Figure 5.14. Same as Fig. 5.13 but for electron temperature.

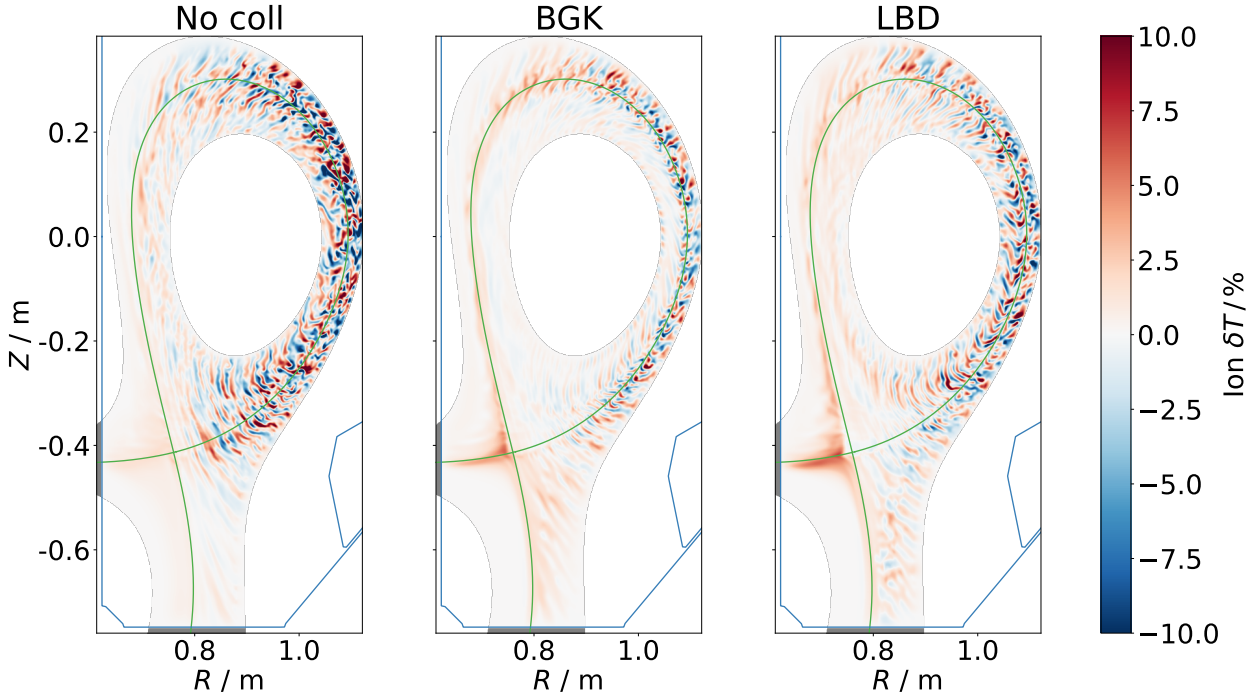

Figure 5.15. Same as Fig. 5.13 but for ion temperature.

Fig 5.16 shows radial profiles of the turbulence parameters. Since $\eta_\mathrm{i} \lesssim 1.1$, ITG modes are considered stable in the simulations[208]. On the other hand, the normalized electron temperature and density gradients are high, conditions that drive TEMs. Towards the last closed flux surface, the collisionality increases, indicating an increased stabilization of TEMs. This fact is consistent with the current understanding of edge turbulence, wherein the edge drift waves and, in the SOL, resistive ballooning modes become important[206].

5.2.1 Theory of Flux Surface Fourier Diagnostics

In the closed field line region, decomposing fluctuating quantities in Fourier modes along a flux surface is interesting. This decomposition allows the identification of contributions from large and small-scale modes. Cross-spectra and cross-phase (or phase shift) analyses can also be performed. Using a temporal Fourier analysis, the propagation direction of a Fourier mode can be identified. The combined information makes it possible to identify the main linear micro-instability driving the observed turbulence.

This section summarizes the theoretical part of the flux surface Fourier diagnostics developed in Ref. [59]. The expressions are slightly different since a modified Fourier representation is used.

Flux Surface Fourier Spectra

The coordinate system chosen here is a field-aligned symmetry flux coordinate system $(\psi, \theta_s, \varphi)$, constructed such that magnetic field lines are straight[210]. The radial component $\psi \sim \rho_\mathrm{pol} \sim r$ is given by a flux surface label, φ is the geometric toroidal angle, and θ_s is the so-called poloidal symmetry angle. The arc length along the flux surface can be represented by a bi-normal coordinate $y = r\theta_s$, where $r = L/(2\pi)$ is an effective radius obtained from the total flux surface arc length L. For a single flux surface under consideration, this is a constant.

The Fourier representation is based on Ref. [211] and defined in terms of the bi-normal coordinate y,

$$g(y) = \frac{1}{2\pi} \sum_{m=-M}^{M} \hat{g}(k_y) \mathrm{e}^{\mathrm{i}k_y y}, \tag{5.7}$$

$$\hat{g}(k_y) = \frac{1}{r} \oint_0^L g(y) \mathrm{e}^{-\mathrm{i}k_y y} \mathrm{d}y, \tag{5.8}$$

where $\hat{g}(k_y)$ is the Fourier amplitude of a single Fourier mode with poloidal mode number m and poloidal wavenumber* $k_y = m/r$, and M is the number of modes under consideration.

*The location of the factor 2π is different than in Ref. [211]. Further, the fundamental wavenumber used therein is given by $k_0 = 1/r$ in this work.

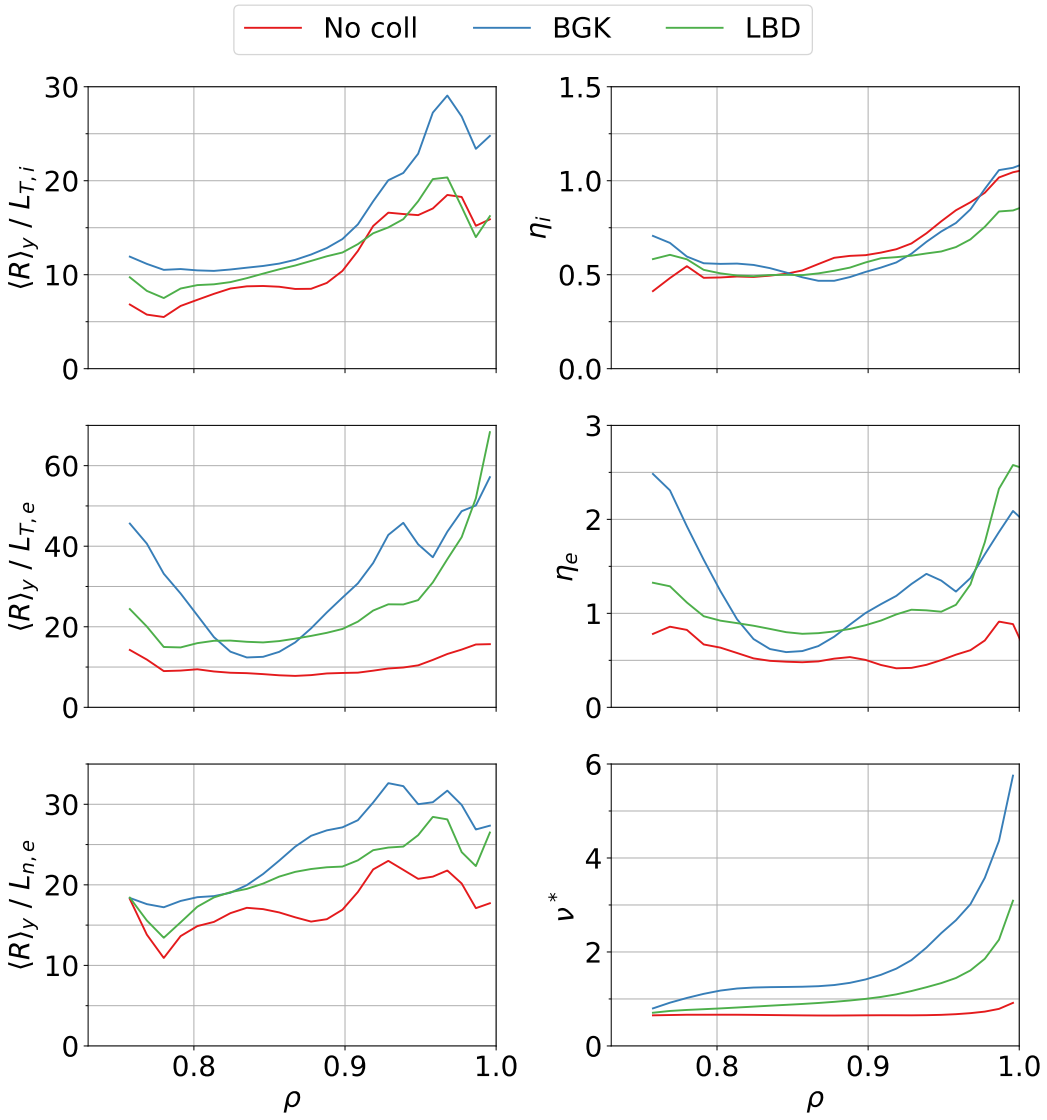

Figure 5.16. Profiles of normalized gradients $\langle R \rangle_y / L_{q,\alpha}$ (q either n or T), ratios $\eta_\alpha = L_{n,\alpha}/L_{T,\alpha}$ and the collisionality ν^* in the confined region. Taken from Ref. [59].

Any quantity given along a flux surface can be used instead of $g(y)$ in this expression. Eq. (5.7) accounts for the fact that, in reality, the simulation domain is discretized, and only a finite number of Fourier modes exist.

Since the signals to be analyzed are real-valued quantities, the Fourier modes must satisfy[211]

$$\hat{g}(-k_y) = \hat{g}^*(k_y), \tag{5.9}$$

where $\hat{g}^*$ denotes the complex conjugate. This condition makes sure that applying eq. (5.7) transforms the complex Fourier amplitudes back to a real-valued signal.

Equation (5.8) presents a standard computation that is performed with a fast Fourier transform (FFT) algorithm[163]. These algorithms typically have a specific way of performing the Fourier transform. Thus the equation needs to be discretized first. As a first step, eq. (5.8) is written with respect to a normalized variable $\xi \in [0, 1]$,

$$\hat{g}(k_y) = 2\pi \oint_0^1 g(y) \mathrm{e}^{-\mathrm{i}2\pi\xi m} \mathrm{d}\xi. \tag{5.10}$$

In a second step, this is discretized using $\xi \to \Delta\xi n = n/N$, where N denotes the number of ξ points. Then,

$$\hat{g}(k_y) \approx \frac{2\pi}{N} \sum_{n=0}^{N} g(y) \mathrm{e}^{-\mathrm{i}nm\frac{2\pi}{N}}. \tag{5.11}$$

Using a common FFT algorithm such as provided by the `scipy` package[212,213], will perform the sum and, if specified, the normalization by $1/N$. Thus, to get the correct Fourier amplitudes, the following pseudo-code has to be used

$$\hat{g}(k_y) = 2\pi\, \texttt{FFT}(g(y), \texttt{norm=forward}). \tag{5.12}$$

Temporal Fourier Spectra

Given the real-valued signals analyzed so far, the flux surface Fourier analysis produces a spectrum where the negative k-frequency Fourier amplitudes are complex conjugates of the positive ones. This information is redundant and thus usually discarded in the analysis[211]. Applying a second Fourier transform, from time to ω-frequency space, produces non-trivial negative ω-frequency Fourier amplitudes since this signal, the output of the first Fourier transform, is complex-valued. As a result, the negative and positive ω-frequency Fourier modes will distinguish modes that propagate counter- or clockwise in the specified direction of the flux surface. This information is interesting, as the different main micro-instabilities have characteristic propagation directions. While turbulence dominated by ITG or TEMs

happens on similar length scales, the modes can be distinguished due to the propagation direction, the ion diamagnetic direction for the ITG, and the electron counterpart for the TEM[206].

A summary of the temporal Fourier diagnostics developed and used in Ref. [59] is given in the following. The formulation is slightly adjusted to use similar expressions as the previously defined flux surface Fourier transform. For simplicity, the combined flux surface and temporal Fourier transform will be called the temporal Fourier transform. The definition used expands on eqs. (5.7) and (5.8),

$$h(y,t) = \frac{1}{(2\pi)^2} \sum_{m=-M}^{M} \sum_{n=-N}^{N} \hat{H}(k_y,\omega) \mathrm{e}^{\mathrm{i}(k_y y - \omega t)}, \tag{5.13}$$

$$\hat{H}(k_y,\omega) = \frac{1}{rT} \oint_0^L \mathrm{d}y \oint_0^T \mathrm{d}t\, h(y,t) \mathrm{e}^{-\mathrm{i}(k_y y - \omega t)}, \tag{5.14}$$

where $\omega = 2\pi n/T$ is the signed frequency for temporal mode number n, and T is the time period length. Since the symmetry flux angle θ_s is defined counter-clockwise, using the above definition of the Fourier transform will result in positive ω describing propagation in the counter-clockwise direction. The propagation direction is compared against the direction of the diamagnetic velocity (diamagnetic direction in the following),

$$\mathbf{v}_{D,\alpha} = q_\alpha \mathbf{b} \times \nabla_\perp (n_\alpha T_\alpha). \tag{5.15}$$

Since the profiles are monotonically decreasing, the gradient will always be radially inward. Thus, the diamagnetic direction depends on the magnetic field direction and the charge. For the TCV case considered here[194], the magnetic field points outwards of Fig. 5.1, thus the ion diamagnetic direction will be clockwise since $q_\mathrm{i} > 0$. For electrons, the diamagnetic direction is counter-clockwise.

Performing the temporal Fourier transform is more involved since the time traces for the flux surface Fourier amplitudes are not time-periodic. Additionally, residual growth from the onset of turbulence may still be present. Applying a direct temporal Fourier transform on the flux surface Fourier amplitudes will yield the propagation direction in the laboratory frame. Since the plasma can have a mean background rotation due to the electric field, the propagation of any micro-instability is superimposed on that background rotation[214]. Thus, this background rotation must be removed to get the propagation direction in the moving frame.

These points are considered using the following procedure. First, a growth function $f(k_y,t) = A(k_y)\exp(-\gamma(k_y)\,t) + B(k_y)$ is fitted for each flux surface Fourier mode*. Ideally, the growth

*The same fit procedure as described in section 4.6 was used.

rate $\gamma(k_y)$ is very small since the measurements should be performed in a steady state. The fitted growth function is then removed from the initial signal by subtraction, $\hat{g}'(k_y,t) = \hat{g}(k_y,t) - f(k_y,t)$. A Kaiser[215] window function is applied $\hat{h}'(k_y,t) = K(\hat{g}'(k_y,t),\beta)$. The window forces the signal at the time domain boundaries to zero, making it periodic. In practice, care has to be taken to not introduce too much spectral leakage with the applied window function[216]. These properties are adjusted by choosing different parameters or window functions. Here, $\beta = 8$ is used. In the final procedure, the average poloidal background rotation is approximated by,

$$v_E = -\frac{c}{B}\left\langle \{\nabla_\perp \phi_1 \times \mathbf{b}\}_y \right\rangle_{t,\varphi,y}, \tag{5.16}$$

and removed from the signal by applying a Doppler shift[214],

$$\hat{h}(k_y,t) = \hat{h}'(k_y,t)\mathrm{e}^{\mathrm{i}v_E k_y t}, \tag{5.17}$$

where $\omega_D = v_E k_y$ corresponds to the Doppler shift frequency. This function is used in the temporal Fourier transform,

$$\hat{H}(k_y,\omega) = \frac{1}{T}\oint_0^T \hat{h}(k_y,t)\mathrm{e}^{\mathrm{i}\omega t}\mathrm{d}t. \tag{5.18}$$

The discretized version of the temporal Fourier transform is obtained using $t \to \Delta t\, m = (T/M)m$, with M being the number of temporal points. This results in

$$\hat{H}(k_y,\omega) \approx \frac{1}{M}\sum_{m=0}^{M} \hat{h}(k_y,t)\mathrm{e}^{\mathrm{i}mn\frac{2\pi}{M}}. \tag{5.19}$$

An important technical detail must be considered in the analysis. It should only be applied for a single toroidal angle φ and not on a toroidal average. Within the FCI approach, because structures are mostly field-aligned, the same structures appear on nearby poloidal planes but shift slightly due to the helical twist of the magnetic field lines. Averaging such a rotating mode will have a mode structure itself[217]. The resulting spectra have bands around mode numbers $m \sim lqn_\varphi$, where $l = 0, 1, 2, \ldots$ are positive integer numbers. In the cases considered in section 5.2.2, this leads to bands around $m = 0, 84, 168, \ldots$ consistent with $n_\varphi = 32$ and $q \approx 2.6$ on the $\rho_{\mathrm{pol}} = 0.92$ flux surface. The spectrum of interest is hidden behind such a band structure. Considering only a single toroidal angle φ avoids this problem entirely.

Spectral Fluxes and Cross Phases

Part of the development of the spectral flux and cross-phase diagnostics have been performed during the master's thesis of J. Pfennig* and used in Refs. [218] and [59]. In the following, a derivation based on the Fourier decomposition in eqs. (5.7) and (5.8) is given.

The total integral radial particle flux, which in the following is called particle flux, is given by[219]

$$\Gamma_\alpha := \oint_0^{2\pi}\oint_0^{2\pi} \langle n_\alpha v_{E,r}\rangle_y \, rR\mathrm{d}\varphi\mathrm{d}\theta_s = \oint_0^{2\pi}\oint_0^{2\pi} \langle \delta n_\alpha \delta v_{E,r}\rangle_y \, rR\mathrm{d}\varphi\mathrm{d}\theta_s, \tag{5.20}$$

where splitting of fluctuating parts is performed given by $g = g_0 + \delta g$ for any function g. Only the fluctuating part of the density and $\mathbf{E}\times\mathbf{B}$ velocity contribute to the particle flux due to the assumption that the equilibrium radial $\mathbf{E}\times\mathbf{B}$ velocity is zero, $v_{0,E,r} = 0$. The average of a fluctuating quantity vanishes, $\langle \delta v_{E,r}\rangle = 0$.

In the chosen symmetry flux coordinate system, the gradient of the electrostatic potential is

$$\nabla\delta\phi_1 = \frac{1}{\sqrt{g_{\psi\psi}}}\frac{\partial\delta\phi_1}{\partial\psi}\,\mathbf{e}_\psi + \frac{1}{R}\frac{\partial\delta\phi_1}{\partial\varphi}\,\mathbf{e}_\varphi + \frac{1}{r}\frac{\partial\delta\phi_1}{\partial\theta_s}\,\mathbf{e}_{\theta_s}, \tag{5.21}$$

where $g_{\psi\psi}$ denotes the $\psi\psi$-component of the metric tensor and $\mathbf{e}$ are unit vectors. It will contribute to the particle flux via $\delta\mathbf{v}_E = (c/B)\mathbf{b}\times\nabla\delta\phi_1$. Assuming a toroidally dominant magnetic field $\mathbf{b}\sim\mathbf{e}_\varphi$, only one component of the electrostatic potential gradient will contribute to the particle flux,

$$\Gamma_\alpha \approx -\oint_0^{2\pi}\oint_0^{2\pi}\left\langle \frac{c}{B}\delta n_\alpha \frac{\partial\delta\phi_1}{\partial\theta_s}\right\rangle_y Rd\varphi\mathrm{d}\theta_s. \tag{5.22}$$

Using the Fourier representation (5.7) for both, potential and density and approximating $R\approx\langle R\rangle_y$ and $B\approx\langle B\rangle_y$ yields

$$\Gamma_\alpha \approx -\frac{c\langle R\rangle_y r}{\langle B\rangle_y}\frac{1}{(2\pi)^2}\mathrm{Re}\left(\oint_0^{2\pi}\oint_0^{2\pi}\left\langle \sum_{m,m''} \mathrm{i}k_y''\hat{n}_\alpha(k_y)\hat{\phi}_1(k_y'')\mathrm{e}^{\mathrm{i}(k_y+k_y'')y}\right\rangle_y \mathrm{d}\varphi\mathrm{d}\theta_s\right). \tag{5.23}$$

Here, $\partial\delta\phi_1/\partial\theta_s = r\partial\delta\phi_1/\partial y$ was used, which allows performing the differentiation on the exponential in the Fourier representation. Taking the real part of the right-hand side ensures the physical requirement that the particle flux is a real quantity. For simplicity in the notation, the bounds of the sums are not denoted, but it should be noted that these are

*J. Pfennig, *Turbulence Characterization for Simulations of Magnetic Confinement Fusion Devices*, unpublished master's thesis (Technische Universität München, 2022)

finite. Thus the sums and the flux surface line average operations can be interchanged. Further performing a change of variables $k_y'' = -k_y'$ while using eq. (5.9), results in

$$\Gamma_\alpha \approx \frac{c\,\langle R\rangle_y\, r}{\langle B\rangle_y}\frac{1}{(2\pi)^2}\mathrm{Re}\left(\oint_0^{2\pi}\oint_0^{2\pi}\sum_{m,m'}\mathrm{i}k_y'\hat{n}_\alpha(k_y)\hat{\phi}_1^*(k_y')\left\langle \mathrm{e}^{\mathrm{i}(k_y-k_y')y}\right\rangle_y \mathrm{d}\varphi\mathrm{d}\theta_s\right). \tag{5.24}$$

The flux surface line average of the exponential can be written in terms of an average over the symmetry flux angle θ_s,

$$\left\langle \mathrm{e}^{\mathrm{i}(k_y-k_y')y}\right\rangle_y = \frac{1}{L}\oint_0^L \mathrm{e}^{\mathrm{i}(k_y-k_y')y}\mathrm{d}y = \frac{1}{2\pi}\oint_0^{2\pi}\mathrm{e}^{\mathrm{i}(m-m')\theta_s}\mathrm{d}\theta_s. \tag{5.25}$$

This expression coincides with the contour integral representation of the Kronecker delta[220]

$$\delta_{m,m'} = \frac{1}{2\pi\mathrm{i}}\oint_{|z|=1} z^{m-m'-1}\mathrm{d}z = \frac{1}{2\pi}\int_0^{2\pi}\mathrm{e}^{\mathrm{i}(m-m')\theta}\mathrm{d}\theta, \tag{5.26}$$

where $z \in \mathbb{C}$. The first expression holds, since if $m = m'$ then z^{-1} has an isolated singularity of order one at $z = 0$ and the residue is $2\pi\mathrm{i}$. Otherwise, the expression evaluates to zero. The second equality is trivially obtained by substituting $z = \exp(\mathrm{i}\theta)$. The complex contour integral in eq. (5.26) differs from the closed integral in eq. (5.25) which is denoted by the same symbol. In the latter, the ring only indicates that the domain closes on itself and can be omitted, like in the second integral in eq. (5.26).

Substituting the Kronecker delta (5.26) for the flux surface average[219], reduces the double sum to a single sum, resulting in

$$\Gamma_\alpha = \frac{c\,\langle R\rangle_y}{2\pi}\int\sum_m \hat{\Gamma}(k_y)\mathrm{d}\varphi, \tag{5.27}$$

$$\hat{\Gamma}(k_y) = \frac{r}{\langle B\rangle_y}\mathrm{Re}\left(\mathrm{i}k_y\hat{n}_\alpha(k_y)\hat{\phi}_1^*(k_y)\right). \tag{5.28}$$

The remaining θ_s integral was trivial, leading to the cancellation of a factor of $1/(2\pi)$. This expression is equivalent to the ones in Refs. [59, 218], but based on a slightly different Fourier representation. Eq. (5.28) defines the spectral particle flux, describing the contributions from each Fourier mode k_y on the flux surface. An alternative expression is obtained by considering the relation

$$\hat{n}_\alpha(k_y) = a(k_y)\hat{\phi}_1(k_y)\mathrm{e}^{-\mathrm{i}\alpha\left(\hat{n}_\alpha,\hat{\phi}_1\right)}, \tag{5.29}$$

where $a(k_y)$ and $\alpha\left(\hat{n}_\alpha, \hat{\phi}_1\right)$ denote amplitude factor and phase shift (or cross-phase) between the two Fourier modes, respectively. It follows that $|\hat{n}(k_y)| = a(k_y)|\hat{\phi}_1(k_y)|$ and further[59,218]

$$\begin{aligned}\hat{\Gamma}(k_y) &= \frac{1}{\langle B\rangle_y}\mathrm{Re}\left(\mathrm{i}k_y|\hat{n}_\alpha(k_y)||\hat{\phi}_1(k_y)|\mathrm{e}^{-\mathrm{i}\alpha\left(\hat{n}_\alpha,\hat{\phi}_1\right)}\right),\\ &= \frac{1}{\langle B\rangle_y}k_y|\hat{n}_\alpha(k_y)|\,|\hat{\phi}_1(k_y)|\,\sin\left(\alpha\left(\hat{n}_\alpha,\hat{\phi}_1\right)\right).\end{aligned} \tag{5.30}$$

The phase shift can alternatively be defined as[211]

$$\alpha\left(\hat{n}_\alpha,\hat{\phi}_1\right) = \mathrm{Im}\left(\log(\hat{n}_\alpha^*\hat{\phi}_1)\right). \tag{5.31}$$

This expression is a more precise definition since the sign of the phase shift depends on the order of arguments applied and different notations exist*.

For the total integral heat flux[219] a similar procedure can be performed,

$$Q_\alpha := \oint_0^{2\pi}\oint_0^{2\pi}\left\langle\frac{3}{2}n_\alpha T_\alpha v_{E,r}\right\rangle_y rR\mathrm{d}\varphi\mathrm{d}\theta_s, \tag{5.32}$$

$$\approx \oint_0^{2\pi}\oint_0^{2\pi}\mathrm{d}\varphi\frac{3rR}{2}\left(\langle T_\alpha\rangle_y\langle\delta n_\alpha\delta v_{E,r}\rangle_y + \langle n_\alpha\rangle_y\langle\delta T_\alpha\delta v_{E,r}\rangle_y\right)\mathrm{d}\theta_s, \tag{5.33}$$

where the same assumptions as in eq. (5.20) have been applied and additionally triple correlations of order $\mathcal{O}(\delta^3)$ have been neglected. In the following, this quantity is called the heat flux. The first term is the same as the particle flux up to a factor of $3\langle T_\alpha\rangle_y/2$. Due to this proportionality, it is also called the convective heat flux[218]. The second term can be treated the same way as the particle flux, replacing the density with the temperature. This contribution is called the conductive heat flux[218].

In terms of flux surface Fourier modes, the heat flux is[59]

$$Q_\alpha = \frac{c\langle R\rangle_y}{2\pi}\oint_0^{2\pi}\sum_m\left(\hat{Q}_\alpha^{\mathrm{conv}}(k_y) + \hat{Q}_\alpha^{\mathrm{cond}}(k_y)\right)\mathrm{d}\varphi, \tag{5.34}$$

*Here, the same convention as in Ref. [211] is used. Comparing to Ref. [218], with notation $\alpha\left(\hat{n}_\alpha,\hat{\phi}_1\right) \to \alpha_{\hat{\phi}_1,\hat{n}_\alpha}$, substituting $\alpha_{\hat{\phi}_1,\hat{n}_\alpha} = \mathrm{Im}\left(\log(\hat{n}_\alpha^*\hat{\phi}_1)\right)$ yields the same expression as used here. Further this is the same as $\alpha(\hat{n}_\alpha\times\hat{\phi}_1) = \arctan\left(\mathrm{Im}(A/B)/\mathrm{Re}(A/B)\right)$ used in Ref. [221].

with convective

$$\begin{aligned}\hat{Q}_\alpha^{\mathrm{conv}}(k_y) &:= \frac{3r\,\langle T_\alpha\rangle_y}{2\,\langle B\rangle_y}\,\mathrm{Re}\left(\mathrm{i}k_y\hat{n}_\alpha(k_y)\hat{\phi}_1^*(k_y)\right),\\ &= \frac{3r\,\langle T_\alpha\rangle_y}{2\,\langle B\rangle_y}k_y|\hat{n}_\alpha(k_y)|\,|\hat{\phi}_1(k_y)|\,\sin\left(\alpha\left(\hat{n}_\alpha,\hat{\phi}_1\right)\right),\end{aligned} \tag{5.35}$$

and conductive part[218]

$$\begin{aligned}\hat{Q}_\alpha^{\mathrm{cond}}(k_y) &:= \frac{3r\,\langle n_\alpha\rangle_y}{2\,\langle B\rangle_y}\,\mathrm{Re}\left(\mathrm{i}k_y\hat{T}_\alpha(k_y)\hat{\phi}_1^*(k_y)\right),\\ &= \frac{3r\,\langle n_\alpha\rangle_y}{2\,\langle B\rangle_y}k_y|\hat{T}_\alpha(k_y)|\,|\hat{\phi}_1(k_y)|\,\sin\left(\alpha\left(\hat{T}_\alpha,\hat{\phi}_1\right)\right).\end{aligned} \tag{5.36}$$

The significance of these expressions lies in the fact that in this approximation, transport can only happen if density or temperature fluctuations lie out of phase with electrostatic potential fluctuations. Results from linear theory suggest that plasma micro-instabilities can be associated with cross phases (phase shifts)[207]. Typically modes are then characterized as drift-wave ($\alpha \approx 0$) or interchange ($\alpha \approx \pm\pi/2$) like[206].

Trapped Particle Contributions

Analyzing turbulent contributions by certain velocity space parts of the distribution function may be interesting. For example, TEMs are expected to be driven by the part of the distribution function, representing electrons trapped on a flux surface. Conversely, evidence that trapped electrons have a more prominent role than passing electrons would point to TEMs driving the observed turbulence. This section summarizes the developed trapped particle diagnostics from Ref. [59]. The decomposition into contributions from trapped and passing particles can be used in conjunction with the Fourier analysis presented before.

The criterion for particles to be trapped on the low field side of a flux surface is[64],

$$\text{trapped if:} \qquad v_\perp > v_\perp^{\mathrm{trap}} = \left|v_{||}\right| \Big/ \sqrt{\frac{\max_y(B)}{B} - 1}. \tag{5.37}$$

Here the maximum magnetic field on the flux surface given by $\max_y(B)$ defines the spatial point where particles are reflected. The trapped and passing parts of the distribution function are defined as

$$\begin{aligned} f_\alpha^{\mathrm{trap}} &= f_\alpha\left(\mathbf{x}, v_{||}, v_\perp > v_\perp^{\mathrm{trap}}\right),\\ f_\alpha^{\mathrm{pass}} &= f_\alpha - f_\alpha^{\mathrm{trap}}.\end{aligned} \tag{5.38}$$

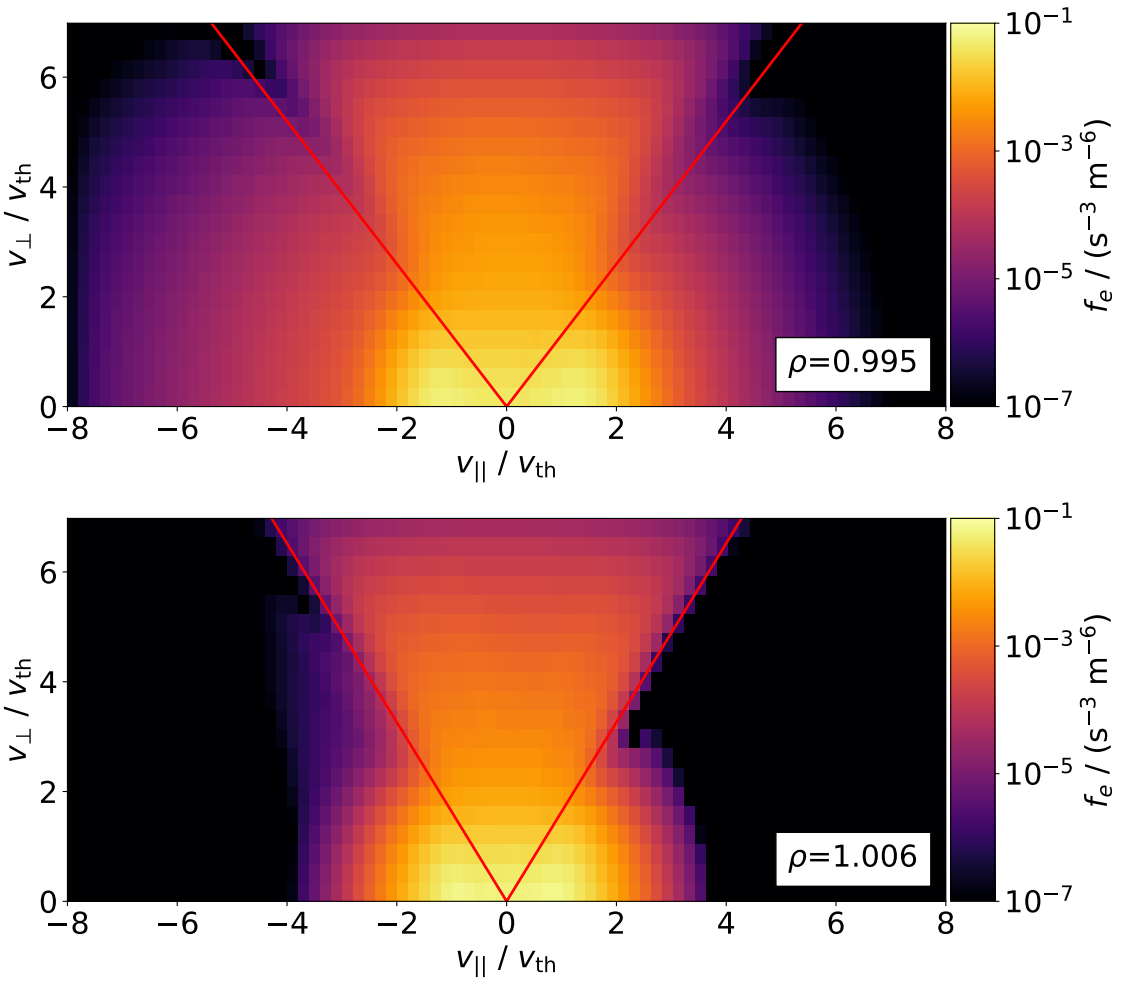

Figure 5.17. Velocity space dependence of the electron distribution function of the collisionless simulation at a single poloidal plane at the final time. A single point at the outboard midplane in the confined region / SOL, close to the separatrix, has been chosen within the poloidal plane. The red line indicates the loss cone. In the SOL, particles are trapped in a magnetic well between the bottom of the device (close to the X-point) and the top of the device.

Velocity space moments can be calculated for trapped and passing distributions, respectively. However, temperatures are ill-defined since, at some spatial locations, the density of trapped particles may be zero due to the reflection of all particles. A more robust definition of trapped and passing temperatures is given concerning the total density,

$$T_\alpha^{\mathrm{trap/pass}} = T_\alpha\Big(n_\alpha, W_\alpha^{\mathrm{trap/pass}}\Big). \tag{5.39}$$

Equation (5.37) specifies a region in velocity space $v_\perp < v_\perp^{\mathrm{trap}}$ which is typically called the loss cone (see Fig. 5.17). Particles within the loss cone have enough parallel energy to pass the reflection point given by the maximal magnetic field. Calculating the fraction of trapped particles requires the integration of the distribution function over the correct region in velocity

space[222]. Changing the velocity space coordinates to pitch-angle space, (v, θ, ζ) described by the velocity magnitude, gyroangle, and pitch-angle, respectively, allows to conveniently calculate the density of particles in the loss cone as

$$n_\alpha^{\text{loss}} = \int_0^\infty \mathrm{d}v \int_0^{2\pi} \mathrm{d}\theta \int_0^{\zeta_{\text{trap}}} \mathrm{d}\zeta v^2 \sin\zeta f_\alpha(v, \zeta), \tag{5.40}$$

where $\zeta_{\text{trap}} = \arctan(v_\perp^{\text{trap}}/v_{||})$ denotes the pitch angle of the loss cone and $v^2 \sin\zeta$ is the Jacobian. The gyroangle integral is trivial, and assuming a velocity space isotropic distribution function $f(v, \zeta) \approx f(v)$, the pitch-angle integral yields $1 - \cos(\zeta_{\text{trap}})$. The total density is obtained using the same formula, with upper bound $\zeta_{\text{max}} = \pi$ instead, resulting in a factor of 2 due to the pitch-angle integral. Fig. 5.18 shows a sketch of the loss cone in velocity space, visualizing the above integration. Because there are two loss cones, the density of passing particles is twice that of a single loss cone. This fact is used in calculating the fraction of trapped particles,

$$F_\alpha^{\text{trap}} = 1 - \frac{2n_\alpha^{\text{loss}}}{n_\alpha} = 1 - \frac{4\pi\big(1 - \cos(\zeta_{\text{trap}})\big)\int_0^\infty \mathrm{d}v v^2 f_\alpha(v)}{4\pi \int_0^\infty \mathrm{d}v v^2 f_\alpha(v)} = \cos(\zeta_{\text{trap}}). \tag{5.41}$$

Using the identity[223] $\cos(\arctan(x)) = 1/\sqrt{1+x^2}$ and the definitions for ζ_{trap} and $v_\perp^{\text{trap}}$ yields[222]

$$F_\alpha^{\text{trap}} = \sqrt{1 - \frac{B}{\max_y(B)}}. \tag{5.42}$$

5.2.2 Flux Surface Fourier Analysis

In this section, the theoretical tools presented in section 5.2.1 are applied to the simulations of TCV-X21 (section 5.1). The collisionless and BGK simulation results are shown here to allow qualitative comparisons of the turbulence characteristics between simulations with different collision models*. The results for the LBD simulation have been published in Ref. [59]. The data in the plots for all simulations were made publicly available in Ref. [224].

The signals analyzed are the electrostatic potential, the density, parallel, perpendicular, and total temperature. These are given as 2D quantities on a poloidal plane and interpolated to flux surfaces specified by a poloidal flux surface label ρ_{pol}. Fig. 5.19 shows an example of the electrostatic potential. The turbulence shows a ballooning character, meaning the

*The results here use the continuous Fourier formulation from Ref. [59]. This formulation allows a better comparison between the already published results and the additional results from the BGK and collisionless simulation. The qualitative analysis does not depend on the formulation since the Fourier amplitudes differ by constant factors only.

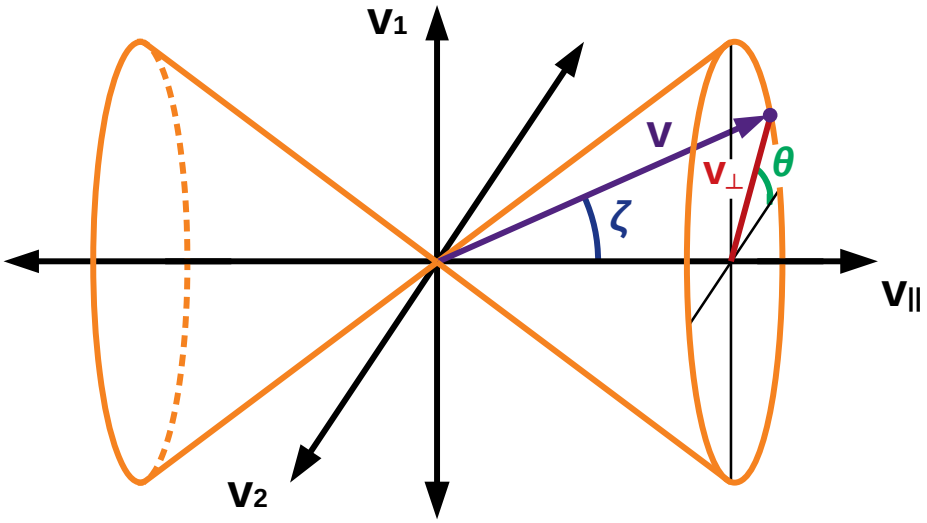

Figure 5.18. Sketch of the loss cone (orange) in the 3D velocity space coordinate system $(v_1, v_2, v_{||})$. The perpendicular velocity space here is given by $v_1 = v_\perp \cos(\theta)$ and $v_2 = v_\perp \sin(\theta)$. Two loss cones are present, facing in positive and negative $v_{||}$ direction.

fluctuations are localized at the low field side. In comparing the different collision models, the BGK simulation shows decreased fluctuation amplitudes, consistent with observations of density and temperature fluctuations in Figs. 5.13, 5.14 and 5.15. The flux surface spectra of these signals are shown in Fig. 5.20. The axis is given in dimensionless wavenumbers scaled by the local sound Larmor radius $\rho_s = c\sqrt{\langle T_\mathrm{e}\rangle_y m_\mathrm{i}} \Big/ \left(e \langle B\rangle_y\right)$. In the spectra, the broadband character of the turbulence can be observed. Collisions generally dampen the spectra, an effect that is much stronger in the BGK simulation than for LBD. Especially in the innermost flux surface considered, the BGK spectrum is significantly lower than for the other simulations. As noted in Ref. [59], the non-averaged spectra contain clear visible effects of the fourth hyperdiffusion applied, which manifests at $k_y \rho_s > 1$ by a linear decay of slope four in the double logarithmic plot.

Since six diagnostics for three cases, in total, 18 figures are considered, the figures can be found in Appendix D, where a direct comparison between the cases is made more conveniently.

The temporal flux surface Fourier spectra are shown in Figs. D.1, D.2 and D.3. The frequency is given in physical and dimensionless units, where the latter are obtained by multiplying the local sound speed $c_s = (\langle T_\mathrm{e}\rangle_y / m_\mathrm{i})^{1/2}$. In addition to the spectra, the linear frequency of the TEM[225], $\omega = \omega_D(1 + x_\mathrm{trap} - x_\mathrm{trap} \langle R\rangle_y / L_{n,\mathrm{e}})/2$ with $\omega_D = c \langle T_\mathrm{e}\rangle_y k_y/(eB_0 \langle R\rangle_y)$ and $x_\mathrm{trap} = F_\mathrm{trap}/(1 - F_\mathrm{trap})$, is given. The trapped fraction is approximated with eq. (5.42). Considering a measure for the mean frequency in the spectrum, the agreement with the linear TEM frequency is good for all cases. In the collisionless and LBD case, the mean

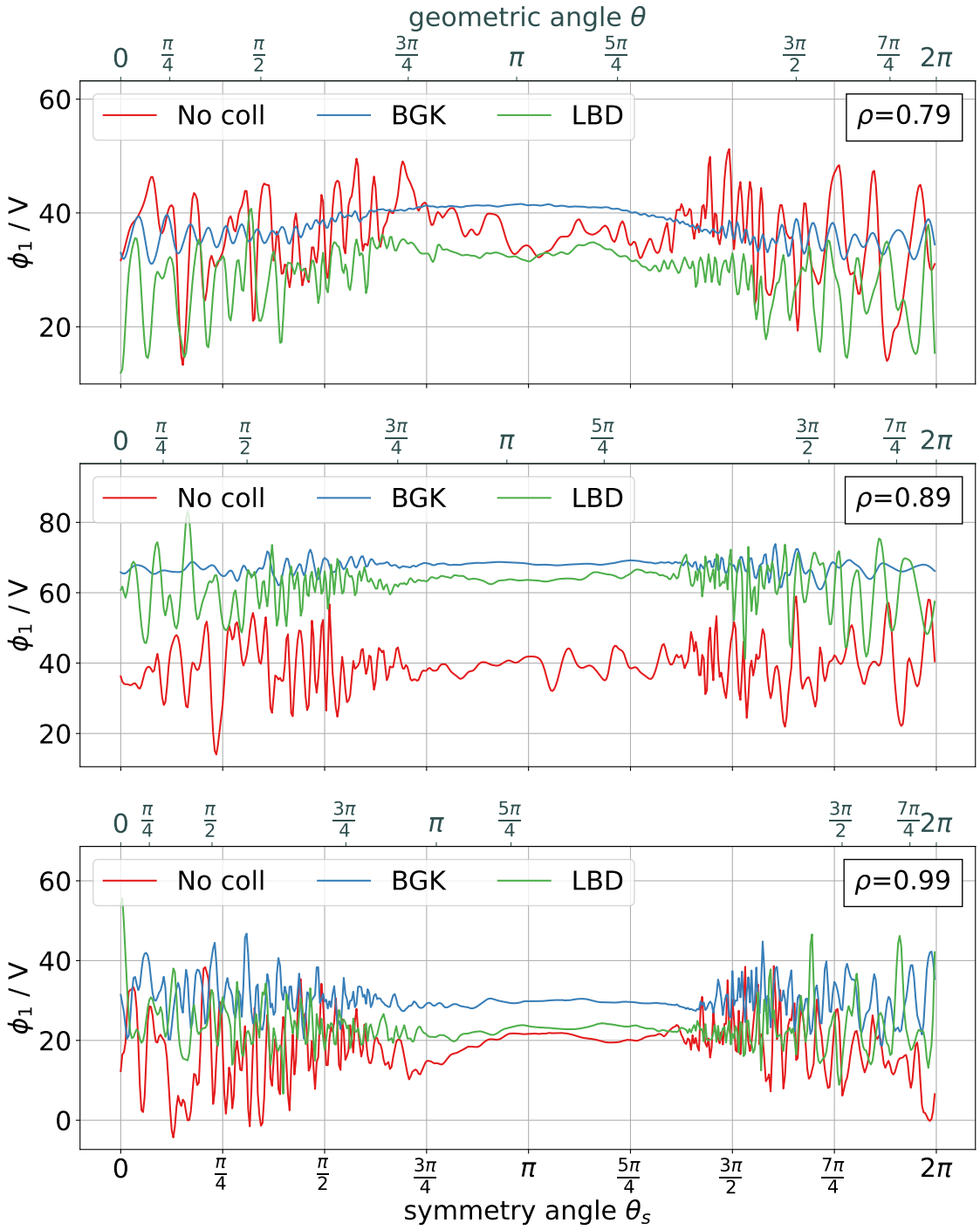

Figure 5.19. Electrostatic potential fluctuations on flux surfaces at different radial locations at the final time of the collisionless, BGK, and LBD simulations. On the bottom and top, the corresponding symmetry flux angle θ_s and geometrical angle θ are given for each flux surface, measured counter-clockwise. The outboard midplane is located close to $\theta_s = 0$ (low field side), and the inboard midplane at around $\theta_s = \pi$ (high field side). Taken from Ref. [59].

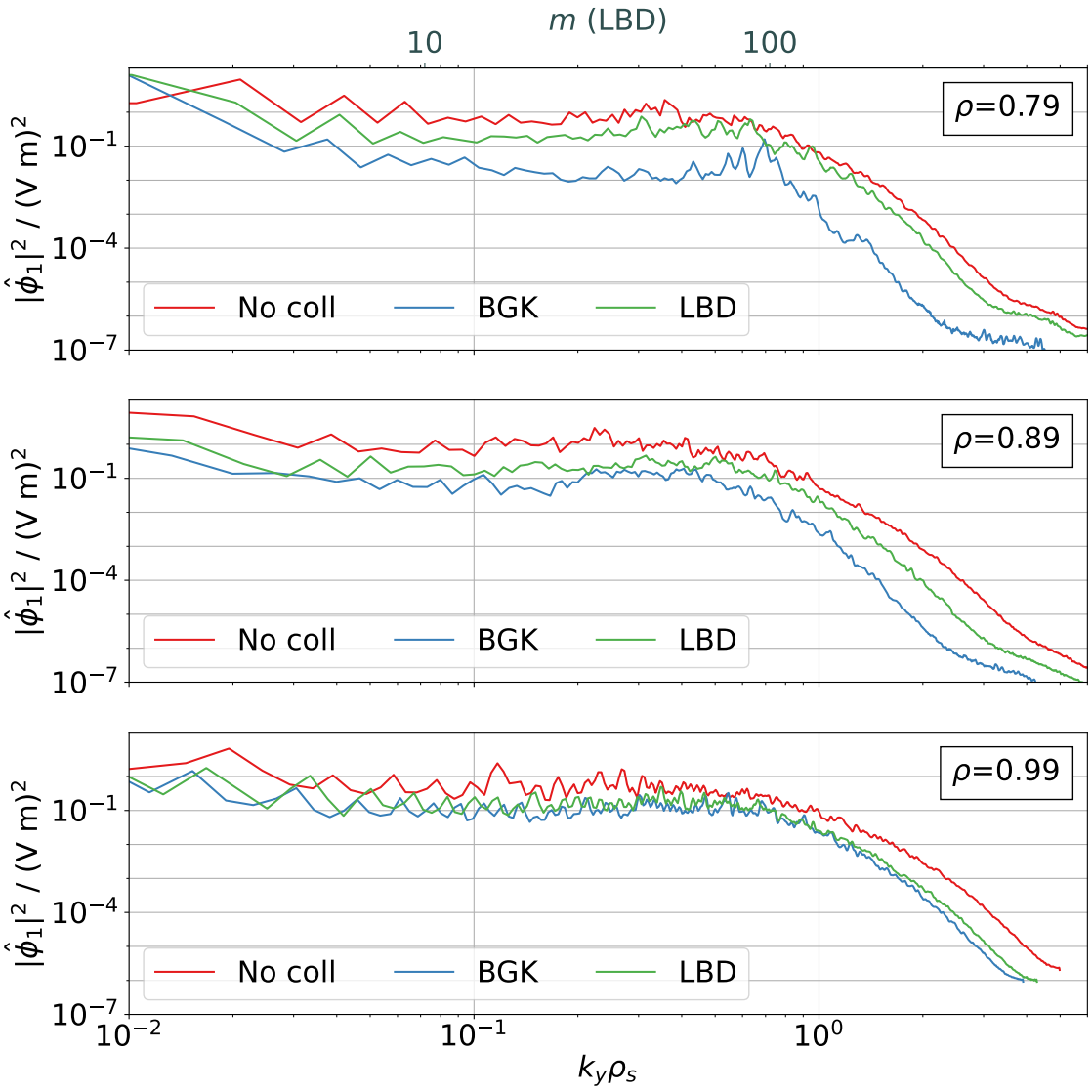

Figure 5.20. Flux surface Fourier spectra of the electrostatic potential of the collisionless, BGK, and LBD simulation averaged toroidally and temporally over 100 μs. On the top, the mode number of the LBD simulation is shown for reference. For the collisionless and BGK simulation, m is similar but not the same for the given $k_y\rho_s$ since the latter quantity is calculated based on the local electron temperature. Taken from Ref. [59].

growth rate is smaller than linear, consistent with the nonlinear saturation of TEMs[226]. The BGK simulation shows larger frequencies at small wavenumbers with the largest deviations at around $k_y\rho_s \sim 0.5$. The apparent width of the spectra depends on the color scale, which was chosen the same for all cases. Thus, with reduced fluctuation amplitudes, the collisional simulations appear to have a narrower spectrum in ω than the collisionless ones.

Figs. D.4, D.5 and D.6 shows the spectral particle and heat fluxes. The electron and ion contribution to the particle flux is the same in all simulations, while the electrons tend to dominate the heat flux. The collisional spectra peak at approximately $k_y\rho_s \approx 0.7$, which is the region where transport is expected to peak[227]. The collisionless spectral fluxes are broader and peak at around $k_y\rho_s \approx 0.5$. The region of interest is where the fluxes are non-zero, approximately between $0.2 < k_y\rho_s < 1.8$. Here, the phase shifts shown in Figs. D.7, D.8 and D.9 should additionally be considered. In all cases, all phase shifts involving ion quantities are close to $\alpha \sim 0$. The density phase shift for the electrons is $\alpha \sim 0$, whereas the temperature phase shift is $\pi/4 \lesssim \alpha \lesssim \pi/2$ in the region of interest. This phase shift indicates an interchange character of the electrons, i.e., TEMs dominate[207,228,229]. This fact is strengthened by the observation that these phase shifts are the same as for the perpendicular temperature. The parallel temperature phase shift is around $\alpha \sim \pi/4$ for both collisional cases, while in the collisionless simulation, it is around $\alpha \sim 0$. These findings are consistent with the previously made observation, where passing electrons carry most of the parallel energy. In the collisionless case, there is no interaction with trapped electrons. Thus passing electrons can be strongly adiabatic. On the other hand, trapped electrons have an interchange-like character.

Similar to the last paragraph, a decomposition of spectral fluxes and phase shifts to contributions from all (total), trapped, and passing electrons is shown in Figs. D.10, D.11, D.12 and Figs. D.13, D.14, D.15 respectively. In all cases, the trapped electrons dominate the spectral particle and heat flux. The phase shifts confirm the TEM hypothesis, previously made by analyzing the parallel and perpendicular temperature contributions. Passing electrons are mostly adiabatic, while trapped electrons have larger phase shifts between the temperature and electrostatic potential. Differences between the three collision models are not observed in the phase shifts, while the spectral fluxes differ similarly, as seen in Figs. D.4, D.5 and D.6. While the BGK flux is much smaller, the collisionless and LBD flux have similar amplitudes. The broader structure in the collisionless case results in a larger total heat flux, consistent with the total power measured, given in Table 5.1.

The characterization of the trapped and passing electrons is shown in Figs. D.16, D.17 and D.18. First, in all cases, the trapped fraction agrees well with the analytical estimate given by eq. (5.42). The densities of trapped particles are highest at the low field sides, approaching zero past the reflection point. The parallel energy is carried mostly by passing particles,

while trapped particles carry most of the perpendicular energy at the low field side. Both collisional simulations do not differ significantly, whereas the collisionless simulation shows different behavior of perpendicular energy. At the low field side, the trapped particles have substantially more perpendicular energy than the other cases, resulting in higher perpendicular temperatures. This finding is consistent with the observed too-hot electron temperature in the collisionless simulation (Fig. 5.5).

5.3 Effect of Perpendicular Velocity Space Resolution

The study of the effect of collision models on edge and SOL turbulence has shown that the LBD collision operator is a minimum requirement for realistic simulations[59]. A drawback in that study was the increased computational time required because of a large magnetic moment grid. Since the finite volume discretization of the LBD operator requires a uniform magnetic moment grid, the grid resolution was increased by a conservative factor of three[59]. It is of great interest to reduce this factor again, ideally without drawbacks in the accuracy of the simulation. A uniform magnetic moment grid is poorly suited to resolve distribution functions that fall off exponentially in that dimension. Thus, the discretization of the LBD operator is adapted to use a uniform perpendicular velocity space grid, resulting in a quadratic magnetic moment grid and improving the resolution of distribution functions close to $\mu = 0$. The explanation can be found in greater detail in Appendix C, where the new conservative discretization of the LBD operator is presented. In the remainder of this section, the initial LBD simulation from Ref. [59] is compared against the newly implemented version with reduced grid size.

The simulation with reduced grid size uses a perpendicular velocity space resolution of $N_\mu = 24$ points. Computational resources are saved by increasing the real space spacing to $\Delta R = \Delta Z \approx 1.78$ mm, resulting in $\approx 10^5$ points per poloidal plane. The time step could be increased to $\Delta t = 4 \times 10^{-4} t_{\text{ref}}$. All other parameters are kept the same as in the original LBD simulation[59]. The simulation is performed beyond a quasi-stationary state to a total time of around 950 μs. This value corresponds to approximately 114×10^3 time steps on 256 nodes (around 12k computational cores) of the Marconi supercomputer at Cineca. In total, 4.3×10^6 core-hours were spent with an average time per timestep of 11 s. The reference simulation was run for a shorter physical time. The total time from the reference simulation, 450 μs, corresponds to around 2×10^6 core-hours with lower resolution. Due to the use of different machines, the total times cannot be easily compared. The computational cost was reduced by approximately five due to the reduced velocity space, while a factor of two is due to the reduced real space grid.

Figs. 5.21, 5.22 and 5.23 show a comparison between the profiles of the original LBD simulation (labeled LBD) and the simulation with reduced resolution (labeled LBD2). These

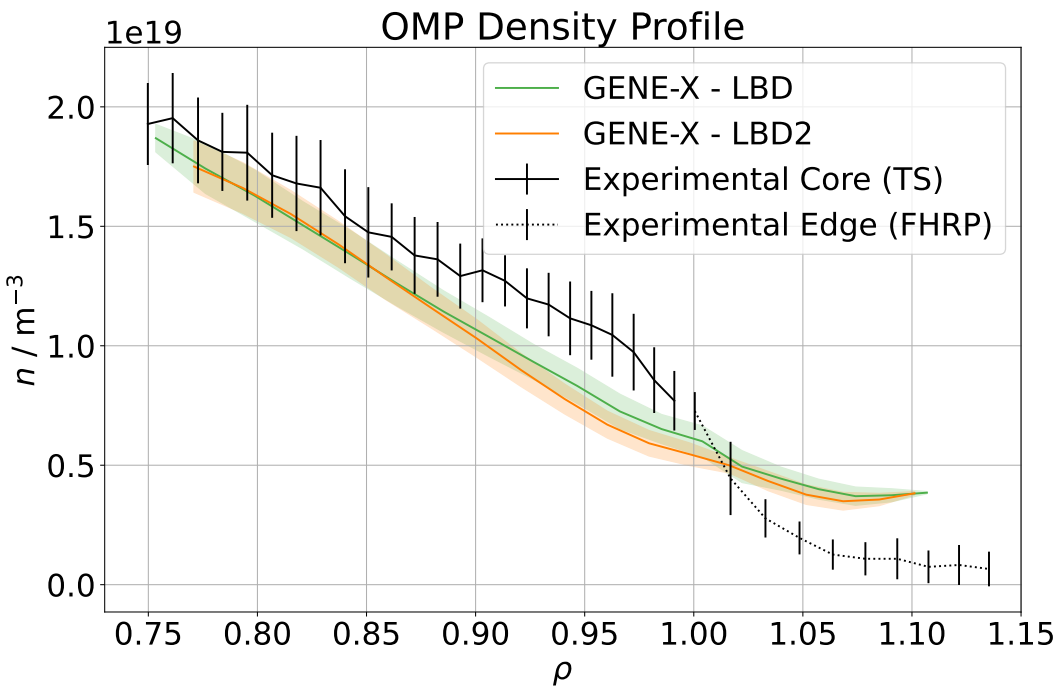

Figure 5.21. Comparison of time-averaged outboard midplane density profiles from the original LBD simulation[59] (data given in Ref. [224]) and the simulation with reduced resolution (LBD2).

Table 5.4. Comparison of the radial ion and electron heat flux crossing the separatrix, averaged over 100 μs. The symbol δ denotes the standard deviation of the temporal average. LBD denotes the reference simulation, where the electron and ion heat flux adds to the values published in Ref. [59]. LBD2 denotes the simulation with reduced resolution.

	LBD	**LBD2**
$Q_r^{\mathrm{sep,i}}$ / kW	46.2	36.9
$\delta Q_r^{\mathrm{sep,i}}$ / kW	10.2	14.9
$Q_r^{\mathrm{sep,e}}$ / kW	79.0	74.3
$\delta Q_r^{\mathrm{sep,e}}$ / kW	12.9	24.3

are given for the final times of both simulations and time-averaged over 100 μs. Assuming a quasi-stationary state in both simulations, comparing averaged profiles at different times is justified. Overall, there is an agreement observed between the two simulations.

Further, radial heat fluxes crossing the separatrix are compared. As before, the values at the final simulation time for both simulations are considered and temporally averaged over 100 μs. The results are given in Table 5.4. The values agree well for both simulations, considering the standard deviation from the temporal fluctuations of the heat fluxes.

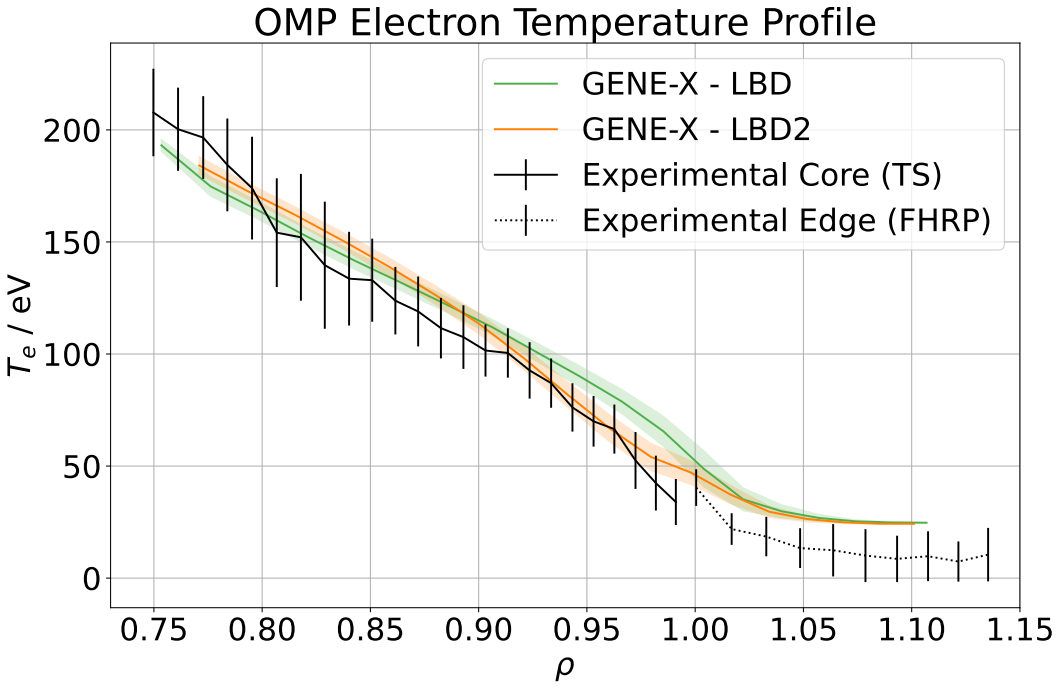

Figure 5.22. Same as Fig. 5.21 but for the electron temperature.

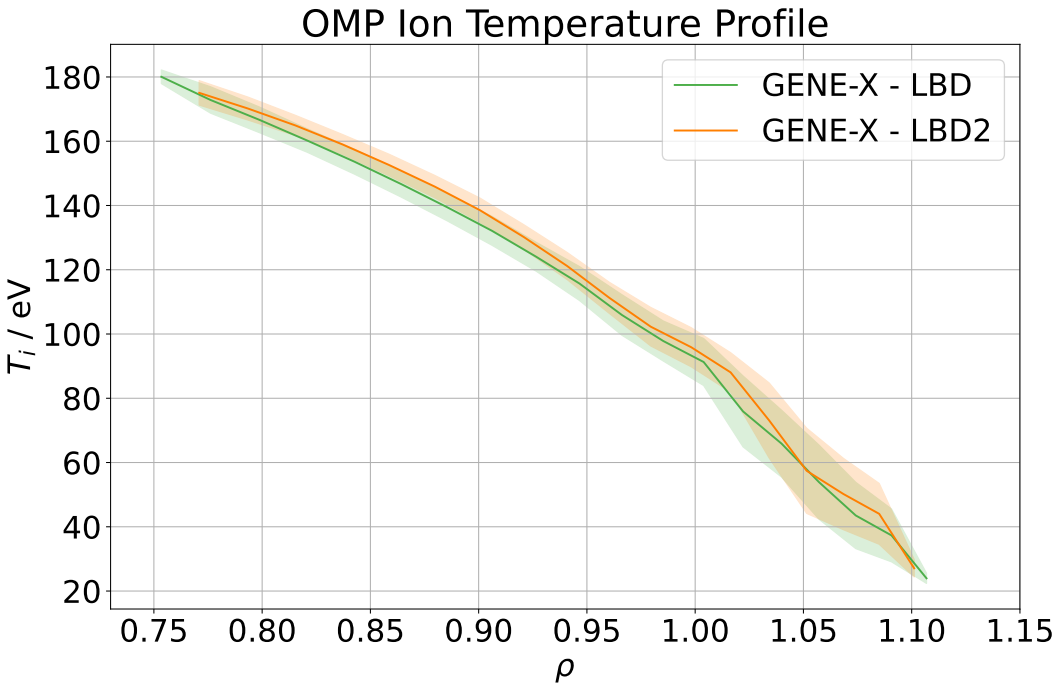

Figure 5.23. Same as Fig. 5.21 but for the ion temperature.

5.4 Chapter Summary

This chapter presented the application of the developed collision operators in this thesis. In a validation study against the TCV-X21[194] case, simulations of gyrokinetic turbulence with the `GENE-X` code have been compared against experimental measurements of physical quantities of interest, such as density and temperature profiles, as well as total power and divertor power fall-off measurements. It was shown that the newly developed LBD collision operator significantly improved the match with the experiment. A turbulence characterization was performed to unravel that the observed turbulence is dominated by the trapped electron mode (TEM), explaining the differences observed across simulations with different collision models. Finally, the finite volume discretization of the LBD operator was further improved to use a perpendicular velocity formulation that allows saving a substantial amount of computational resources, as was shown in a comparison between differently resolved simulations.

The validation and turbulence characterization has been published in Ref. [59]. The data for the additionally characterized BGK and collisionless simulation was made publicly available (along with the results from Ref. [59]) in Ref. [224].

Chapter 6

Summary and Outlook

The qualitative and quantitative understanding of turbulent transport in the plasma edge and scrape-off layer (SOL) is most important for realizing fusion energy. Due to the complex geometry and nonlinear physics present in the system, numerical modeling using gyrokinetic codes belongs to the main tools used to explore the nature of edge and SOL turbulence. Only a few computational tools exist that combine these features, one of which is the `GENE-X` code.

This thesis presents a physics extension of the `GENE-X` code by including the effect of collisions in the gyrokinetic model. Collisional gyrokinetic simulations were enabled by developing a conservative numerical discretization of the LBD collision operator. The main result is that collisions significantly impact edge and SOL turbulence. The code extension allows for realistic turbulence simulations in cold and collisional edge plasmas. The newly developed LBD collision model reproduces vital aspects of the experiment in the confined plasma region in a first-of-its-kind code validation against TCV-X21. The LBD collision model balances accuracy and computational performance, especially with optimizations implemented in the perpendicular velocity space. The developments in this thesis pave the path toward realistic simulations of plasma turbulence in future fusion devices.

6.1 Summary

A specialized numerical scheme was developed based on a finite volume discretization, augmented by correcting discretization errors. This scheme achieved the conservation of particle densities, total momentum, and energy up to machine precision. These properties allow for long-term stable simulations with moderate grid sizes, reducing the computational complexity of the simulations. Studies comparing the electron-deuterium system's physical relaxation rates have verified the newly developed discretization. The verification reproduces analytical intra- and inter-species temperature and momentum relaxation rates in good approximation.

The stability of the time-stepping schemes was analyzed in detail, providing an understanding of the numerical restrictions on the simulation speed. The resulting time-step criteria facilitate the choice of an optimal time-step to save upon the computational cost. Implementing a second-order splitting scheme allows treating collisionless and collisional terms independently, decoupling the individual dynamics and resulting in increased possible time steps. The result is a gain of a factor of two in the application cases considered. The intra- and inter-node performance of the implementation was quantified, resulting in a 95% computational efficiency of the computational part and insights into the diminishing effects of the communication. The numerical scheme was further improved, changing the perpendicular velocity space representation of the collision model, enabling the use of a better-suited quadratic magnetic moment grid in velocity space. A verification study showed that simulations using the improved perpendicular velocity space formulation could achieve the same results with reduced velocity space grid size. The reduced velocity space grid also allowed for doubling the time step in the simulation.

A code validation against the TCV-X21 experimental case tested the developed collision models. Comparing simulations without collisions against the simple BGK or advanced LBD collision operator allowed the assessment of the influence of collisions on edge turbulence. The result shows that the LBD collision operator's fidelity is required to achieve a realistic simulation that reproduces essential aspects of the experiment. The collisionless simulation resulted in electron temperature profiles that were significantly too high, an inconsistent power balance, and unrealistic fluctuation amplitudes in the SOL, which were higher than in the confined region. A systematic analysis found that collisionless trapped particles in the SOL are the reason for this observation. Collisional interactions with passing particles allow for a collisional cooling of trapped particles, resulting in electron temperature profiles closer to the experiment. The BGK collision model suppressed turbulence, especially in the confined region, resulting in electron temperature deviations and less transport. The LBD simulation shows an excellent agreement of plasma profiles in the confined plasma region, a consistent power balance, and the SOL fall-off length.

The observed turbulence in the TCV-X21 simulations was analyzed using newly developed Fourier and trapped particle diagnostics. The observed transport peaks around normalized poloidal wavenumber $k_y\rho_s \approx 0.7$, showing the same particle flux for electrons and ions, while electrons dominate the heat flux through conduction. Analyzing the trapped particle contributions revealed turbulence driven by trapped electron modes (TEMs). The temporal Fourier analysis showed a dispersion similar to the one of the linear TEM. The observations showed the expected nonlinear deviations at high mode numbers $k_y\rho_s \geq 0.5$. Additionally, performed cross-phase analyses support these findings.

In summary, the additions to the `GENE-X` code in this work have improved the realism of simulations and extended the applicability of the code.

6.2 Outlook

The presented developments of the `GENE-X` code have proven to be a crucial step towards being a predictive tool for the simulation of edge and SOL turbulence. There are various model and code extensions possible. The following provides a selection.

First, the scrape-off layer physics in the presented simulations is still to be improved. Effects of the plasma sheath[108], neutral gas dynamics[193], as well as impurities[230], need to be included in future simulations. The LBD collision model could not significantly improve the heat flux fall-off length in the TCV-X21 validation. Thus the remaining mismatch is anticipated to result from missing non-collisional physics.

Second, the current gyrokinetic model employs the long-wavelength approximation. Relaxing this approximation is necessary for simulations of the plasma core, full device simulations, and future benchmarks against traditional field-aligned gyrokinetic codes such as `GENE`. Thus, adding gyroaverages and higher-order finite Larmor radius effects is vital when considering such applications.

Third, the LBD collision model, while advancing the fidelity and realism of the simulations, yet contains some deficiencies. Due to the approximation of anisotropic diffusion and simplified velocity-constant collision rates, the accurate reproduction of neoclassical physics cannot be expected[231]. Considering the application in pedestal-like narrow real space and high gradient regions, the collision operator's details can significantly impact the turbulence evolving in the simulation[57,155].

Fourth, the performance of the `GENE-X` code, while being excellent for modest cases considered here, requires significant improvements in the view of large-scale simulations of huge devices such as ITER, full device simulations of current medium-sized tokamaks or simulations in

the three-dimensional geometry of stellarators. Achieving these goals could be accomplished with multiple improvements. The main one is porting the code to graphical processing units (GPUs), allowing for significant speedups. Additionally, algorithmic changes, such as block-structured velocity space grids[232], or pseudo-spectral methods[25,233], are promising optimizations.

Many of the points mentioned above are already under active development. For example, alongside the main developments in this work, the full nonlinear Fokker-Planck-Landau collision operator has been implemented[152]. The current stage of development focuses on computational improvements. This collision operator requires storing multiple eight-dimensional arrays, exceeding the memory capabilities of current supercomputers, rendering it inapplicable to use in realistic device simulations. The optimization of this operator, or the development of a highly efficient nonlinear Fokker-Planck operator based on Rosenbluth potentials, is the next step in developing advanced collision models.

The current version of `GENE-X` allows investigating many interesting applications already because it is one of the few available codes which combines a high fidelity collisional, electromagnetic, gyrokinetic model with the capability of simulating in highly complex realistic tokamak geometries. So far, only L-mode discharges have been considered in `GENE-X` simulations, leaving gyrokinetic edge and SOL turbulence simulations of H-modes unexplored. The transition of L- to H-mode is yet to be fully understood, and any progress along these lines would help to improve the current models and theories about the cause of the LH transition[234–237]. In H-mode discharges, periodic large-scale magnetohydrodynamic instabilities, so-called edge localized modes (ELMs) occur, linked to turbulence during a density build-up in the inter-ELM phases[238]. Improved confinement regimes and turbulence are fundamentally connected[237], making the former highly interesting for future code applications. Examples are the I-mode[239], QH-mode[240] and strongly shaped negative triangularity scenarios[241].

In conclusion, this thesis has achieved the overall aim: the collisional physics added to the `GENE-X` code has proven necessary to understand edge turbulence better. These improvements provide a considerable step towards unraveling the nature of edge and SOL turbulence. Future extensions, expanding the physics, numerics, or performance of the code will enable truly realistic simulations and provide predictive capabilities for simulating turbulent transport in future fusion devices.

Appendix A

Quadrature Schemes

The quadrature schemes used in collisionless and BGK simulations in the `GENE-X` code are derived and summarized in this appendix.

A.1 Simpson Quadrature

This section presents the derivation of the Simpson quadrature weights given in Ref. [62]. The standard Simpson's rule as well as Simpson's 3/8 rule are[163]

$$\int_{x_1}^{x_3} f dx \approx \Delta x \left[\frac{1}{3}f(1) + \frac{4}{3}f(2) + \frac{1}{3}f(3)\right], \tag{A.1}$$

$$\int_{x_1}^{x_4} f dx \approx \Delta x \left[\frac{3}{8}f(1) + \frac{9}{8}f(2) + \frac{9}{8}f(3) + \frac{3}{8}f(4)\right], \tag{A.2}$$

where the grid spacing $\Delta x = x_2 - x_1$ is assumed uniform and $f(i)$ denotes the function on a grid point i. These will approximate the integral between grid points x_1 and x_3, and x_1 and x_4, respectively. An extended (or composite[164]) scheme is obtained by applying the rules on each grid point and summing over the result. The extended Simpson scheme is[163]

$$\int_{x_1}^{x_N} f dx \approx \Delta x \Bigg[\frac{1}{3}f(1) + \frac{4}{3}f(2) + \frac{2}{3}f(3) + \frac{4}{3}f(4) + \dots + \frac{2}{3}f(N-2) + \frac{4}{3}f(N-1) + \frac{1}{3}f(N)\Bigg], \tag{A.3}$$

where the factors 2/3 and 4/3 alternate and N denotes the number of grid points. This scheme will give an approximation of the integral over the whole domain. Alternative extended

schemes are obtained by a combination of other (extended) schemes (see Ref. [163]). The alternative scheme used here can be found in Ref. [242]. The extended Simpson scheme (A.3) and a modified version where Simpson's 3/8 rule (A.2) is instead used at the domain boundaries are written as

$$\begin{aligned}
\mathcal{I}_1 &= h\Bigg[\frac{1}{3}f(1)+\frac{4}{3}f(2)+\frac{2}{3}f(3)+\frac{4}{3}f(4)+\dots \\
&\qquad +\frac{2}{3}f(N-2)+\frac{4}{3}f(N-1)+\frac{1}{3}f(N)\Bigg], \\
\mathcal{I}_2 &= h\left[\frac{1}{3}f(2)+\frac{4}{3}f(3)+\frac{2}{3}f(4)+\frac{4}{3}f(5)+\dots+\frac{2}{3}f(N-3)+\frac{4}{3}f(N-2)+\frac{1}{3}f(N-1)\right] \\
&\quad + h\Bigg[\frac{3}{8}f(1)+\frac{9}{8}f(2)+\frac{9}{8}f(3)+\frac{3}{8}f(4) \\
&\qquad +\frac{3}{8}f(N-3)+\frac{9}{8}f(N-2)+\frac{9}{8}f(N-1)+\frac{3}{8}f(N)\Bigg], \\
&= h\Bigg[\frac{3}{8}f(1)+\frac{9}{8}f(2)+\frac{9}{8}f(3)+\frac{17}{24}f(4)+\frac{4}{3}f(5)+\frac{2}{3}f(6)+\dots \\
&\quad +\frac{4}{3}f(N-4)+\frac{17}{24}f(N-3)+\frac{9}{8}f(N-2)+\frac{9}{8}f(N-1)+\frac{3}{8}f(N)\Bigg].
\end{aligned}$$

The average of these results is the "alternative" Simpson scheme[62,242]

$$\begin{aligned}
\int_{x_1}^{x_N} f dx \approx \frac{\mathcal{I}_1+\mathcal{I}_2}{2} = \Delta x\Bigg[&\frac{17}{48}f(1)+\frac{59}{48}f(2)+\frac{43}{48}f(3)+\frac{49}{48}f(4)+f(5)+\dots \\
&+f(N-4)+\frac{49}{48}f(N-3)+\frac{43}{48}f(N-2) \\
&+\frac{59}{48}f(N-1)+\frac{17}{48}f(N)\Bigg].
\end{aligned} \tag{A.4}$$

This scheme has the advantage that the weights are very simple since all except eight weights are one. Further, it has no special requirements on the number of grid points, unlike the extended Simpson scheme that requires pairs of intervals, i.e., an odd number of grid points[163]. The scheme converges with fourth -order in grid spacing (same order as the original schemes used in the construction).

A.2 Gauss-Laguerre Quadrature

Gauss-Quadrature is a standard technique for numerical integration. This section presents a summary based on Ref. [163]. The definition is

$$\int_a^b W(x)f(x)\mathrm{d}x \approx \sum_{i=1}^{N} w(i)f(x(i)), \tag{A.5}$$

where $W(x)$ is a weight function, w_i are integration weights and $x(i)$ are the abscissas. Gauss quadrature methods are designed to integrate a polynomial $P(x)$ times the weight function $W(x)$ exactly. Alternatively, one may write eq. (A.5) as

$$\int_a^b f(x)\mathrm{d}x \approx \sum_{i=1}^{N} \frac{w(i)}{W(x(i))} f(x(i)) \equiv \sum_{i=1}^{N} \widetilde{w}(i)f(x(i)). \tag{A.6}$$

Given a weight function $W(x)$, the abscissas of the N-point Gauss quadrature are defined as the roots of the Nth polynomial p_N, orthogonal under the scalar product defined as $\int_a^b W(x)p_N(x)p_j(x) \sim \delta_{Nj}$, where $1 < j < N$ and δ_{ij} is the Kronecker delta. Consequently, grid points cannot be chosen arbitrarily but must coincide with the roots of Nth degree polynomials.

To calculate the velocity space moments of the distribution function (3.100)-(3.103), one in principle may use Gauss-Laguerre quadrature in μ and Gauss-Hermite quadrature in $v_{||}$. These methods have weight functions that coincide with the functional form of the Maxwellian (3.76), $f_\alpha \sim \exp(-\mu)$ and $f_\alpha \sim \exp(-v_{||}^2)$, respectively[163]. However, as mentioned above, the velocity space grid points must then coincide with the roots of Laguerre and Hermite polynomials, respectively. This restriction is non-ideal for calculating velocity space derivatives based on central finite differences on a regular grid. Since the gyrokinetic equation contains $v_{||}$ derivatives, Simpson quadrature (see last section) is used instead for the parallel velocity space. Gauss-Laguerre quadrature is used for the perpendicular velocity space because the magnetic moment is a parameter for collisionless systems or using BGK collisions.

Gauss-Laguerre quadrature uses the weight function $W(x) = \exp(-x)$ on the interval $[0, \infty)$ with abscissas defined by $L_N(x(i)) = 0$, where L_N is the Nth Laguerre polynomial (see Ref. [135] §18) and $i = 1..N$. The weights are given by[62]

$$\widetilde{w}(i) = \frac{x(i)\mathrm{e}^{-x(i)}}{(N+1)^2[L_{N+1}(x(i))]^2}, \tag{A.7}$$

where the formulation given by eq. (A.6) is used. The roots of the Nth Laguerre polynomial are calculated with an algorithm given in Ref. [163].

Further, since the use of Gauss-Laguerre quadrature defines the grid points that are used, a re-scaling is applied to map the grid back to a chosen interval $\mu \in [0, L_\mu]$. First, a "typical" length is evaluated by calculating the integral of the simplest polynomial $P(x) = 1$ in eq. (A.6)*,

$$b - a = \sum_{i=1}^{N} \widetilde{w}(i). \tag{A.8}$$

Then, the points and weights are re-scaled according to

$$\text{fac} = \frac{L_\mu}{\sum_{i=1}^{N} \widetilde{w}(i)}, \qquad x(i) = x(i) \times \text{fac} \qquad w(i) = w(i) \times \text{fac}. \tag{A.9}$$

The re-scaling makes sure that the last grid point generated by the Gauss-Laguerre quadrature algorithm lies within the specified simulation domain $[0, L_\mu]$.

*This length coincides with the interval length of most Gauss methods (e.g., Gauss-Legendre[163]). For Gauss-Laguerre quadrature, the left-hand side is ill-defined if the correct bounds $[0, \infty)$ are used, which is the case since version (A.6) instead of (A.5) has been used. However, one can treat the bounds as unknowns that determine the typical length by summation over the integration weights.

Appendix B

Finite Difference Stencils

The method to obtain finite difference coefficients presented in the following uses Lagrange interpolation[168]. The derivative of a function q will be approximated on grid points x_k close to a point x. The function is interpolated through all these points using a Lagrange polynomial (see Ref. [135] §3.3(i)),

$$P(x) = \sum_{k=0}^{n} q_k l_k(x), \tag{B.1}$$

$$l_k(x) = \prod_{\substack{j=0 \\ j\neq k}}^{n} \frac{x - x_j}{x_k - x_j}, \tag{B.2}$$

$$l_k(x_j) = \delta_{kj}, \tag{B.3}$$

where n is the order of the polynomial or scheme, l_k are the Lagrange basis functions and the set (x_k, q_k) contains the grid points and values of q at these points that are used in the interpolation. The symbol δ_{kj} denotes the Kronecker delta, and $q_k \equiv q(k) \equiv q(x_k)$. The derivative of q at x is approximated by differentiating the Lagrange polynomial and evaluating the result at x. A different set of interpolation points will lead to a different order and different type of stencil.

Higher-order derivatives of q are obtained by calculating higher derivatives of the Lagrange polynomial, requiring a minimum amount of grid points. The strength of this method is that it can be easily implemented in any computer algebra tool, automating the creation of finite difference stencils and allowing one to obtain custom stencils.

Example

The previously shown method is explained based on the example of the first derivative at a grid point x_i. In choosing a symmetric 3-point stencil, the two neighbors x_{i-1} and x_{i+1} are considered. Thus, a second-order polynomial $n = 2$ needs to be chosen.

The basis functions are (B.2),

$$\begin{aligned} l_{i-1}(x) &= \frac{x - x_i}{x_{i-1} - x_i} \frac{x - x_{i+1}}{x_{i-1} - x_{i+1}} = \frac{x^2 - x(x_i + x_{i+1}) + x_i x_{i+1}}{(x_{i-1} - x_i)(x_{i-1} - x_{i+1})}, \\ l_i(x) &= \frac{x - x_{i-1}}{x_i - x_{i-1}} \frac{x - x_{i+1}}{x_i - x_{i+1}} = \frac{x^2 - x(x_{i-1} + x_{i+1}) + x_{i-1} x_{i+1}}{(x_i - x_{i-1})(x_i - x_{i+1})}, \\ l_{i+1}(x) &= \frac{x - x_{i-1}}{x_{i+1} - x_{i-1}} \frac{x - x_i}{x_{i+1} - x_i} = \frac{x^2 - x(x_{i-1} + x_i) + x_{i-1} x_i}{(x_{i+1} - x_{i-1})(x_{i+1} - x_i)}, \end{aligned}$$

and their derivatives,

$$\begin{aligned} l'_{i-1}(x) &= \frac{2x - (x_i + x_{i+1})}{(x_{i-1} - x_i)(x_{i-1} - x_{i+1})}, \\ l'_i(x) &= \frac{2x - (x_{i-1} + x_{i+1})}{(x_i - x_{i-1})(x_i - x_{i+1})}, \\ l'_{i+1}(x) &= \frac{2x - (x_{i-1} + x_i)}{(x_{i+1} - x_{i-1})(x_{i+1} - x_i)}. \end{aligned}$$

Constructing the polynomials (B.1) and evaluating it at x_i yields the general centered difference scheme for arbitrary grid spacing,

$$\begin{aligned} q'_i \approx P'(x_i) = &\frac{x_i - x_{i+1}}{(x_{i-1} - x_i)(x_{i-1} - x_{i+1})} q_{i-1} \\ &+ \frac{2x_i - (x_{i-1} + x_{i+1})}{(x_i - x_{i-1})(x_i - x_{i+1})} q_i \\ &+ \frac{x_i - x_{i-1}}{(x_{i+1} - x_{i-1})(x_{i+1} - x_i)} q_{i+1}. \end{aligned} \tag{B.4}$$

For constant grid spacing $x_{i+1} - x_i = \Delta x$, the common second order centered difference formula is obtained,

$$q'_i \approx \frac{1}{\Delta x} \left(-\frac{1}{2} q_{i-1} + \frac{1}{2} q_{i+1} \right). \tag{B.5}$$

Appendix C

Perpendicular Velocity Formulation of the LBD Operator

The finite volume formulation constructed in section 4.3 relies on an equidistant grid in velocity space. This restriction from the collision operator also affects other parts of the code, especially the calculation of velocity space moments. Typically distribution functions are Maxwellian-like, and especially in the magnetic moment direction, a uniform grid is poorly suited to resolve such functions (see Fig. C.1). Construction of a finite volume discretization utilizing non-equidistant grids is non-trivial. Nonetheless, improvements can be made by using a uniform grid in perpendicular velocity for the collision operator. Since $\mu \sim v_\perp^2$ this would result in a quadratic μ grid for the non-collisional part of the code that is much better suited to resolve Maxwellian-like functions (Fig. C.1)*. This appendix gives a finite volume discretization of the LBD operator based on the perpendicular velocity coordinate.

The relation between magnetic moment and perpendicular velocity is given by,

$$\mu = \frac{m_\alpha v_\perp^2}{2B}, \qquad \mathrm{d}\mu = \frac{m_\alpha}{B} v_\perp \mathrm{d}v_\perp, \tag{C.1}$$

$$v_\perp = \sqrt{\frac{2B\mu}{m_\alpha}}, \qquad \frac{\partial f}{\partial \mu} = \frac{v_\perp}{2\mu}\frac{\partial f}{\partial v_\perp}. \tag{C.2}$$

The velocity space element in this formulation depends on the cell element under consideration. Instead of ΔW, the symbol ΔV will be chosen for the velocity space cell size to

*Such a quadratic magnetic moment grid was used previously but with a trapezoidal quadrature for collisionless and BGK simulations only[62].

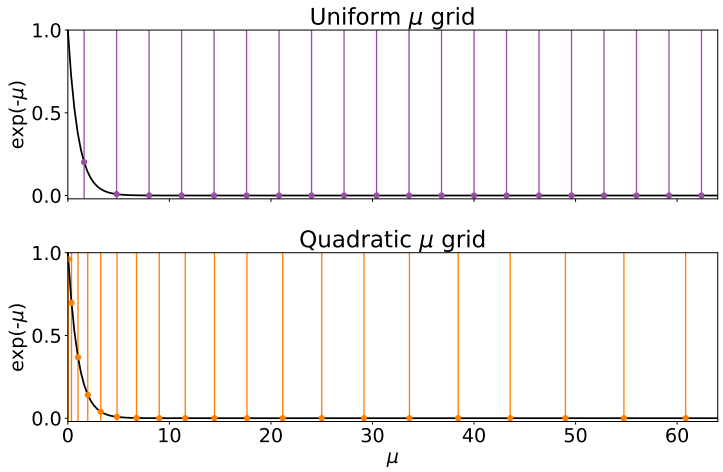

Figure C.1. Schematic comparison of a uniform and quadratic μ grid used to resolve a function $\exp(-\mu)$.

distinguish between the magnetic moment and perpendicular velocity formulation. Both are given by,

$$\Delta W(j) = \Delta W = 2\pi \Delta v_{||} \Delta \mu, \tag{C.3}$$

$$\Delta V(j) = \Delta V v_{\perp}(j) = 2\pi \Delta v_{||} \Delta v_{\perp} v_{\perp}(j). \tag{C.4}$$

The cell size is chosen not to depend on the magnetic field and species mass.

C.1 Velocity Space Moments

The velocity space moments in the perpendicular velocity formulation are given by,

$$M_{0,\alpha} = \Delta V \sum_{i=1}^{N} \sum_{j=1}^{M} v_{\perp}(j) f_{\alpha}(i,j) \frac{B_{||}^{*}(i)}{B}, \tag{C.5}$$

$$M_{1,\alpha} = \Delta V \sum_{i=1}^{N} \sum_{j=1}^{M} v_{\perp}(j) v_{||}(i) f(i,j) \frac{B_{||}^{*}(i)}{B}, \tag{C.6}$$

$$M_{2,\perp,\alpha} = \frac{1}{2} m_{\alpha} \Delta V \sum_{i=1}^{N} \sum_{j=1}^{M} v_{\perp}^{3}(j) f(i,j) \frac{B_{||}^{*}(i)}{B}, \tag{C.7}$$

$$M_{2,||,\alpha} = \frac{1}{2} m_{\alpha} \Delta V \sum_{i=1}^{N} \sum_{j=1}^{M} v_{\perp}(j) v_{||}^{2}(i) f(i,j) \frac{B_{||}^{*}(i)}{B}, \tag{C.8}$$

$$M_{2} = M_{2,\perp} + M_{2,||}. \tag{C.9}$$

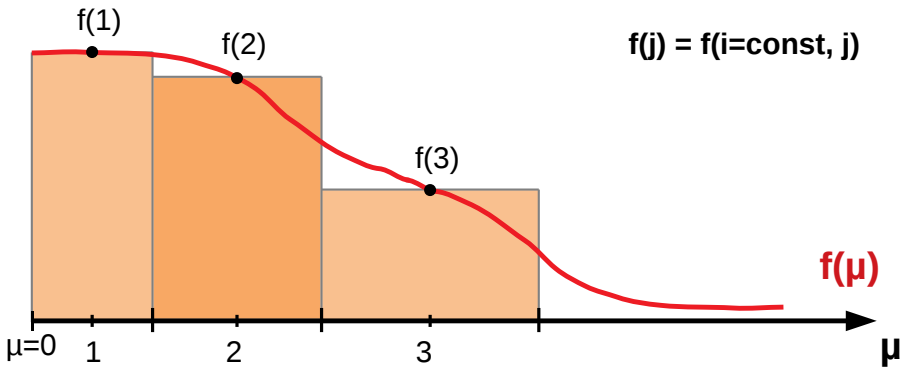

Figure C.2. Midpoint boxes for a quadratic μ grid. The box width is chosen such that the symmetric half-width is given by the distance of a grid point to the closest previous box boundary.

These are discretized with the midpoint method (see section 4.1). The midpoint boxes are chosen such that at each grid point, the distance to the closest previous box boundary is used as a symmetric half-width of the box. Fig. C.2 provides a visualization.

C.2 Finite Volume Discretization

The construction of the finite volume scheme is similar to the one in section 4.3. A second-order midpoint scheme approximates the volume integral of the collision operator,

$$\int_{V(i,j)} B_{||}^{*} C_{\alpha\beta} f_\alpha \mathrm{d}V \approx B_{||}^{*}(i)(C_{\alpha\beta} f_\alpha)(i,j)\Delta V(j). \tag{C.10}$$

The surface integral is split into four edges,

$$\begin{aligned}\oint_{\partial V(i,j)} \mathbf{J}\cdot\mathbf{n}\,\mathrm{d}\partial V = 2\pi\Bigg[&- \int_{v_{||}(i-\frac{1}{2})}^{v_{||}(i+\frac{1}{2})} \mathrm{d}v_{||} v_\perp J_\perp(v_{||}, v_\perp)\Big|_{j-\frac{1}{2}} + \int_{v_\perp(j-\frac{1}{2})}^{v_\perp(j+\frac{1}{2})} \mathrm{d}v_\perp v_\perp J_{||}(v_{||}, v_\perp)\Big|_{i+\frac{1}{2}} \\ &+ \int_{v_{||}(i+\frac{1}{2})}^{v_{||}(i-\frac{1}{2})} \mathrm{d}v_{||} v_\perp J_\perp(v_{||}, v_\perp)\Big|_{j+\frac{1}{2}} - \int_{v_\perp(j+\frac{1}{2})}^{v_\perp(j-\frac{1}{2})} \mathrm{d}v_\perp v_\perp J_{||}(v_{||}, v_\perp)\Big|_{i-\frac{1}{2}}\Bigg],\end{aligned} \tag{C.11}$$

and approximated with the second-order midpoint rule

$$\begin{aligned}\oint_{\partial V(i,j)} \mathbf{J}\cdot\mathbf{n}\,\mathrm{d}\partial V \approx 2\pi\Big[&- \Delta v_{||} v_\perp(j-\frac{1}{2}) J_\perp(i, j-\frac{1}{2}) + \Delta v_\perp v_\perp(j) J_{||}(i+\frac{1}{2}, j) \\ &+ \Delta v_{||} v_\perp(j+\frac{1}{2}) J_\perp(i, j+\frac{1}{2}) - \Delta v_\perp v_\perp(j) J_{||}(i-\frac{1}{2}, j)\Big].\end{aligned} \tag{C.12}$$

The resulting expression for the collision operator is

$$(C_{\alpha\beta}f_\alpha)(i,j) = \frac{1}{B^*_{||}(i)}\Bigg[\ \frac{1}{\Delta v_{||}}\left(J_{||}(i+\frac{1}{2},j) - J_{||}(i-\frac{1}{2},j)\right) + \frac{1}{\Delta v_\perp v_\perp(j)}\left(v_\perp(j+\frac{1}{2})J_\perp(i,j+\frac{1}{2}) - v_\perp(j-\frac{1}{2})J_\perp(i,j-\frac{1}{2})\right)\Bigg]. \tag{C.13}$$

Defining,

$$\widetilde{J}_\perp(j\pm\frac{1}{2}) = \frac{v_\perp(j\pm\frac{1}{2})}{v_\perp(j)}J_\perp(j\pm\frac{1}{2}), \tag{C.14}$$

leads to a more symmetric form,

$$(C_{\alpha\beta}f_\alpha)(i,j) = \frac{1}{B^*_{||}(i)}\left[\frac{1}{\Delta v_{||}}\left(J_{||}(i+\frac{1}{2},j) - J_{||}(i-\frac{1}{2},j)\right) + \frac{1}{\Delta v_\perp}\left(\widetilde{J}_\perp(i,j+\frac{1}{2}) - \widetilde{J}_\perp(i,j-\frac{1}{2})\right)\right]. \tag{C.15}$$

Equations (3.72) and (3.70) give the fluxes,

$$J_{||} = \nu_{\alpha\beta}\left[\left(v_{||}-u_{||,\alpha\beta}\right)f_\alpha B^*_{||} + \frac{T_{\alpha\beta}}{m_\alpha}\frac{\partial f_\alpha B^*_{||}}{\partial v_{||}}\right] \equiv \nu_{\alpha\beta}\left(J^c_{||}+J^d_{||}\right), \tag{C.16}$$

$$J_\perp = \nu_{\alpha\beta}\left[v_\perp f_\alpha B^*_{||} + \frac{T_{\alpha\beta}}{m_\alpha}\frac{\partial f_\alpha B^*_{||}}{\partial v_\perp}\right] \equiv \nu_{\alpha\beta}\left(J^c_\perp+J^d_\perp\right). \tag{C.17}$$

In second-order midpoint discretization, the parallel flux is

$$J^c_{||}(i\pm\frac{1}{2},j) = \left(v_{||}(i\pm\frac{1}{2})-u_{||,\alpha\beta}\right)f_\alpha(i\pm\frac{1}{2},j)\,B^*_{||}(i\pm\frac{1}{2}), \tag{C.18}$$

$$J^d_{||}(i\pm\frac{1}{2},j) = \left.\frac{T_{\alpha\beta}}{m_\alpha}\frac{\partial f_\alpha B^*_{||}}{\partial v_{||}}\right|_{i\pm\frac{1}{2},j}. \tag{C.19}$$

with

$$f_\alpha(i\pm\frac{1}{2},j) = \frac{1}{2}\Big(f_\alpha(i,j)+f_\alpha(i\pm1,j)\Big), \tag{C.20}$$

$$\left.\frac{\partial f_\alpha B^*_{||}}{\partial v_{||}}\right|_{i\pm\frac{1}{2},j} = \frac{1}{\Delta v_{||}}\Big(\pm f_\alpha(i\pm1,j)B^*_{||}(i\pm1) \mp f_\alpha(i,j)B^*_{||}(i)\Big). \tag{C.21}$$

The perpendicular flux in second-order midpoint discretization is

$$J^c_\perp(i,j\pm\frac{1}{2}) = v_\perp(j\pm\frac{1}{2}) f_\alpha(i,j\pm\frac{1}{2})\, B^*_{||}(i), \tag{C.22}$$

$$J^d_\perp(i,j\pm\frac{1}{2}) = \frac{T_{\alpha\beta}}{m_\alpha}\frac{\partial f_\alpha B^*_{||}}{\partial v_\perp}\bigg|_{i,j\pm\frac{1}{2}}, \tag{C.23}$$

with

$$f_\alpha(i,j\pm\frac{1}{2}) = \frac{1}{2}\Big(f_\alpha(i,j) + f_\alpha(i,j\pm 1)\Big), \tag{C.24}$$

$$\frac{\partial f_\alpha}{\partial v_\perp}\bigg|_{i,j\pm\frac{1}{2}} = \frac{1}{\Delta v_\perp}\Big(\pm f_\alpha(i,j\pm 1) \mp f_\alpha(i,j)\Big). \tag{C.25}$$

C.3 Conservation Properties

Eq. (C.15) has the same form as used in the conservation equation in the magnetic moment formulation (4.58). The result that the partial integration is conserved (4.63) also holds for the perpendicular velocity formulation. The only change is in the velocity space element, which now depends on j,

$$\sum_{i=1}^{N}\sum_{j=1}^{M}\Delta V(j)\phi(i,j)(\nabla\cdot\mathbf{J})(i,j) = \sum_{i=1}^{N}\sum_{j=1}^{M}\Delta V(j)\phi(i,j)\Bigg[\frac{1}{\Delta v_\perp}\Big(\widetilde{J}_\perp(i,j+\frac{1}{2}) - \widetilde{J}_\perp(i,j-\frac{1}{2})\Big) + \frac{1}{\Delta v_{||}}\Big(J_{||}(i+\frac{1}{2},j) - J_{||}(i-\frac{1}{2},j)\Big)\Bigg]. \tag{C.26}$$

The calculations that follow are the same as starting from eq. (4.59). One difference considers the expression for the perpendicular flux, which upon re-indexing $j \to j+1$ becomes

$$\frac{v_\perp(j-\frac{1}{2})}{v_\perp(j)} J_\perp(i,j-\frac{1}{2}) \to \frac{v_\perp(j+\frac{1}{2})}{v_\perp(j+1)} J_\perp(i,j+\frac{1}{2}). \tag{C.27}$$

This right-hand side of this expression is not the same as $\widetilde{J}_\perp(i,j+\frac{1}{2})$. The equation corre-

sponding to eq. (4.62) is,

$$\Delta V\Bigg\{\sum_{i=1}^{N}\sum_{j=1}^{M-1} J_{\perp}(i,j+\frac{1}{2})v_{\perp}(j+\frac{1}{2})\frac{\phi(i,j)-\phi(i,j+1)}{\Delta v_{\perp}} + \sum_{i=1}^{N-1}\sum_{j=1}^{M} J_{||}(i+\frac{1}{2},j)v_{\perp}(j)\frac{\phi(i,j)-\phi(i+1,j)}{\Delta v_{||}}\Bigg\}. \tag{C.28}$$

The result of the calculation is,

$$\sum_{i=1}^{N}\sum_{j=1}^{M}\Delta V(j)\phi(i,j)\{\nabla\cdot\mathbf{J}\}(i,j) = -\Delta V\Bigg\{\sum_{i=1}^{N}\sum_{j=1}^{M-1} J_{\perp}(i,j+\frac{1}{2})v_{\perp}(j+\frac{1}{2})\frac{\partial\phi}{\partial v_{\perp}}\Bigg|_{i,j+\frac{1}{2}} + \sum_{i=1}^{N-1}\sum_{j=1}^{M} J_{||}(i+\frac{1}{2},j)v_{\perp}(j)\frac{\partial\phi}{\partial v_{||}}\Bigg|_{i+\frac{1}{2},j}\Bigg\}, \tag{C.29}$$

$$= -\Delta V\Bigg\{\sum_{i=1}^{N}\sum_{j=1}^{M-1} \widetilde{J}_{\perp}(i,j+\frac{1}{2})v_{\perp}(j)\frac{\partial\phi}{\partial v_{\perp}}\Bigg|_{i,j+\frac{1}{2}} + \sum_{i=1}^{N-1}\sum_{j=1}^{M} J_{||}(i+\frac{1}{2},j)v_{\perp}(j)\frac{\partial\phi}{\partial v_{||}}\Bigg|_{i+\frac{1}{2},j}\Bigg\}. \tag{C.30}$$

C.3.1 Momentum Conservation

Using $\phi_{\alpha} = m_{\alpha}v_{||}$, the momentum is

$$P_{\alpha} = -\Delta V m_{\alpha}\sum_{i=1}^{N-1}\sum_{j=1}^{M} J_{||}(i+\frac{1}{2},j)v_{\perp}(j). \tag{C.31}$$

With the explicit form of the parallel flux,

$$\widetilde{P}_{\alpha} = -\Delta V\sum_{i=1}^{N-1}\sum_{j=1}^{M} v_{\perp}(j)\left[\left(v_{||}(i+\frac{1}{2}) - u_{\alpha\beta}\right)f_{\alpha}(i+\frac{1}{2},j)B^{*}_{||}(i+\frac{1}{2}) + \frac{T_{\alpha\beta}}{m_{\alpha}}\frac{\partial f_{\alpha}B^{*}_{||}}{\partial v_{||}}\Bigg|_{i+\frac{1}{2},j}\right], \tag{C.32}$$

where prefactors are put into $\widetilde{P}_{\alpha} = P/(m_{\alpha}\nu_{\alpha\beta})$. Repeating the same calculations as in section 4.3 gives the total momentum

$$\frac{P_{\alpha}}{m_{\alpha}\nu_{\alpha\beta}B} = -\left(M_{1,\alpha} - u_{\alpha\beta}M_{0,\alpha} - P_{\mathrm{BC},\alpha\beta}\right), \tag{C.33}$$

where a factor of $1/B$ has been added on both sides. The boundary correction term is

$$P_{\mathrm{BC},\alpha\beta} = \frac{\Delta V}{2B}\sum_{j=1}^{M} v_\perp(j)\Bigg[\left(v_{||}(\frac{1}{2}) - u_{\alpha\beta} + \frac{2T_{\alpha\beta}}{m_\alpha \Delta v_{||}}\right) f_\alpha(1,j)B^*_{||}(1) \\ + \left(v_{||}(N+\frac{1}{2}) - u_{\alpha\beta} - \frac{2T_{\alpha\beta}}{m_\alpha \Delta v_{||}}\right) f_\alpha(N,j)B^*_{||}(N)\Bigg]. \tag{C.34}$$

C.3.2 Energy Conservation

Using $\phi_\alpha = m_\alpha(v_{||}^2 + v_\perp^2)/2$, the energy is

$$E_\alpha = \underbrace{-m_\alpha \Delta V \sum_{i=1}^{N}\sum_{j=1}^{M-1} v_\perp(j) v_\perp(j+\frac{1}{2})\tilde{J}_\perp(i,j+\frac{1}{2})}_{E_{\perp,\alpha}} \underbrace{-m_\alpha \Delta V \sum_{i=1}^{N-1}\sum_{j=1}^{M} v_\perp(j) v_{||}(i+\frac{1}{2}) J_{||}(i+\frac{1}{2},j)}_{E_{||,\alpha}}, \tag{C.35}$$

the energy contribution is split into parallel and perpendicular parts. The calculation for the parallel energy is the same as in section 4.3 and results in

$$\frac{E_{||,\alpha}}{\nu_{\alpha\beta}B} = -2\left(M_{2,||,\alpha} + \frac{(\Delta v_{||})^2}{8} m_\alpha M_{0,\alpha} - \frac{u_{\alpha\beta}}{2} m_\alpha M_{1,\alpha} - \frac{T_{\alpha\beta}}{2} M_{0,\alpha} - m_\alpha E_{\mathrm{BC},||,\alpha\beta}\right), \tag{C.36}$$

with

$$E_{\mathrm{BC},||,\alpha\beta} = \frac{\Delta V}{2B}\Bigg\{\sum_{j=1}^{M}\frac{1}{2}v_\perp(j)\left[v_{||}^2(\frac{1}{2}) - \left(u_{\alpha\beta} - \frac{2T_{\alpha\beta}}{m_\alpha \Delta v_{||}}\right) v_{||}(\frac{1}{2})\right] f_\alpha(1,j)B^*_{||}(1) \\ + \sum_{j=1}^{M}\frac{1}{2}v_\perp(j)\left[v_{||}^2(N+\frac{1}{2}) - \left(u_{\alpha\beta} + \frac{2T_{\alpha\beta}}{m_\alpha \Delta v_{||}}\right) v_{||}(N+\frac{1}{2})\right] f_\alpha(N,j)B^*_{||}(N)\Bigg\}. \tag{C.37}$$

Perpendicular Energy

The calculation of the perpendicular energy is different than in section 4.3 and is detailed in the following. The energy contribution is written explicitly as

$$\widetilde{E}_{\alpha,\perp} = -m_\alpha \Delta V \sum_{i=1}^{N}\sum_{j=1}^{M-1} v_\perp^2(j+\frac{1}{2})\left[v_\perp(j+\frac{1}{2}) f_\alpha(i,j+\frac{1}{2})B^*_{||}(i) + \frac{T_{\alpha\beta}}{m_\alpha}\frac{\partial f_\alpha B^*_{||}}{\partial v_\perp}\bigg|_{i,j+\frac{1}{2}}\right], \tag{C.38}$$

using $\widetilde{E}_{\alpha,\perp} = E_{\alpha,\perp}/\nu_{\alpha\beta}$. Applying eqs. (C.24) and (C.25),

$$\widetilde{E}_{\alpha,\perp} = -m_\alpha \Delta V \sum_{i=1}^{N}\sum_{j=1}^{M-1} B_{||}^*(i)\Bigg\{ f_\alpha(j)\left[\frac{1}{2}v_\perp^3(j+\frac{1}{2}) - \frac{T_{\alpha\beta}}{m_\alpha \Delta v_\perp} v_\perp^2(j+\frac{1}{2})\right] + f_\alpha(j+1)\left[\frac{1}{2}v_\perp^3(j+\frac{1}{2}) + \frac{T_{\alpha\beta}}{m_\alpha \Delta v_\perp} v_\perp^2(j+\frac{1}{2})\right]\Bigg\}, \tag{C.39}$$

or with re-indexing $j \to j+1$ in the second sum,

$$\widetilde{E}_{\alpha,\perp} = -m_\alpha \Delta V \Bigg\{ \sum_{i=1}^{N}\sum_{j=1}^{M-1} B_{||}^*(i) f_\alpha(j)\left[\frac{1}{2}v_\perp^3(j+\frac{1}{2}) - \frac{T_{\alpha\beta}}{m_\alpha \Delta v_\perp} v_\perp^2(j+\frac{1}{2})\right] \sum_{i=1}^{N}\sum_{j=2}^{M} B_{||}^*(i) f_\alpha(j)\left[\frac{1}{2}v_\perp^3(j-\frac{1}{2}) + \frac{T_{\alpha\beta}}{m_\alpha \Delta v_\perp} v_\perp^2(j-\frac{1}{2})\right]\Bigg\}. \tag{C.40}$$

Splitting off the boundary correction terms,

$$\widetilde{E}_{\alpha,\perp} = -m_\alpha \Delta V \sum_{i=1}^{N}\sum_{j=1}^{M} B_{||}^*(i) f_\alpha(j)\frac{1}{2}\Bigg[v_\perp^3(j+\frac{1}{2}) - \frac{2T_{\alpha\beta}}{m_\alpha \Delta v_\perp} v_\perp^2(j+\frac{1}{2}) + v_\perp^3(j-\frac{1}{2}) + \frac{2T_{\alpha\beta}}{m_\alpha \Delta v_\perp} v_\perp^2(j-\frac{1}{2})\Bigg] + 2m_\alpha E_{\mathrm{BC},\perp,\alpha\beta}, \tag{C.41}$$

where

$$E_{\mathrm{BC},\perp,\alpha\beta} = \frac{\Delta V}{2B}\Bigg\{ \sum_{i=1}^{N}\frac{1}{2}\left(v_\perp^3(\frac{1}{2}) + \frac{2T_{\alpha\beta}}{m_\alpha \Delta v_\perp} v_\perp^2(\frac{1}{2})\right) f_\alpha(i,1) B_{||}^*(i) + \sum_{i=1}^{N}\frac{1}{2}\left(v_\perp^3(M+\frac{1}{2}) - \frac{2T_{\alpha\beta}}{m_\alpha \Delta v_\perp} v_\perp^2(M+\frac{1}{2})\right) f_\alpha(i,M) B_{||}^*(i)\Bigg\}. \tag{C.42}$$

The squares and cubes are expanded as,

$$v_\perp^2(j+\frac{1}{2}) = v_\perp^2(j) + \Delta v_\perp v_\perp(j) + \frac{(\Delta v_\perp)^2}{4}, \tag{C.43}$$

$$v_\perp^2(j-\frac{1}{2}) = v_\perp^2(j) - \Delta v_\perp v_\perp(j) + \frac{(\Delta v_\perp)^2}{4}, \tag{C.44}$$

$$v_\perp^3(j+\frac{1}{2}) = v_\perp^3(j) + 3v_\perp^2(j)\frac{\Delta v_\perp}{2} + \frac{3(\Delta v_\perp)^2}{4} v_\perp(j) + \frac{(\Delta v_\perp)^3}{6}, \tag{C.45}$$

$$v_\perp^2(j-\frac{1}{2}) = v_\perp^3(j) - 3v_\perp^2(j)\frac{\Delta v_\perp}{2} + \frac{3(\Delta v_\perp)^2}{4} v_\perp(j) - \frac{(\Delta v_\perp)^3}{6}, \tag{C.46}$$

resulting in a cancellation of terms with same signs for the squares and a cancellation of terms with opposite signs for the cubes. This yields,

$$\widetilde{E}_{\alpha,\perp} = -m_\alpha \Delta V \sum_{i=1}^{N}\sum_{j=1}^{M} B_{||}^*(i) f_\alpha(j) v_\perp(j) \left[v_\perp^2(j) + \frac{3(\Delta v_\perp)^2}{4} - \frac{2T_{\alpha\beta}}{m_\alpha} \right] + 2m_\alpha E_{\mathrm{BC},\perp,\alpha\beta} \quad \text{(C.47)}$$

Using the definition of the velocity space moments results in

$$\frac{E_{\alpha,\perp}}{\nu_{\alpha\beta} B} = -2 \left(M_{2,\perp,\alpha} + \frac{3(\Delta v_\perp)^2}{8} m_\alpha M_{0,\alpha} - T_{\alpha\beta} M_{0,\alpha} - m_\alpha E_{\mathrm{BC},\perp,\alpha\beta} \right). \quad \text{(C.48)}$$

Total Energy

The final result for the total energy conservation equation is,

$$\frac{E_\alpha}{2\nu_{\alpha\beta} B} = -\left(M_{2,\alpha} - \frac{1}{2} u_{\alpha\beta} m_\alpha M_{1,\alpha} + \frac{(\Delta v_{||})^2 + 3(\Delta v_\perp)^2}{8} m_\alpha M_{0,\alpha} - \frac{3}{2} T_{\alpha\beta} M_{0,\alpha} - m_\alpha E_{\mathrm{BC},\alpha\beta} \right), \quad \text{(C.49)}$$

with boundary corrections,

$$\begin{aligned} E_{\mathrm{BC},\alpha\beta} = {} & \frac{\Delta V}{2B} \Bigg\{ \sum_{j=1}^{M} \frac{1}{2} v_\perp(j) \left[v_{||}^2(\tfrac{1}{2}) - \left(u_{\alpha\beta} - \frac{2T_{\alpha\beta}}{m_\alpha \Delta v_{||}} \right) v_{||}(\tfrac{1}{2}) \right] f_\alpha(1,j) B_{||}^*(1) \\ & + \sum_{j=1}^{M} \frac{1}{2} v_\perp(j) \left[v_{||}^2(N+\tfrac{1}{2}) - \left(u_{\alpha\beta} + \frac{2T_{\alpha\beta}}{m_\alpha \Delta v_{||}} \right) v_{||}(N+\tfrac{1}{2}) \right] f_\alpha(N,j) B_{||}^*(N) \Bigg\} \\ & + \frac{\Delta V}{2B} \Bigg\{ \sum_{i=1}^{N} \frac{1}{2} \left(v_\perp^3(\tfrac{1}{2}) + \frac{2T_{\alpha\beta}}{m_\alpha \Delta v_\perp} v_\perp^2(\tfrac{1}{2}) \right) f_\alpha(i,1) B_{||}^*(i) \\ & + \sum_{i=1}^{N} \frac{1}{2} \left(v_\perp^3(M+\tfrac{1}{2}) - \frac{2T_{\alpha\beta}}{m_\alpha \Delta v_\perp} v_\perp^2(M+\tfrac{1}{2}) \right) f_\alpha(i,M) B_{||}^*(i) \Bigg\}. \end{aligned} \quad \text{(C.50)}$$

In addition to the $(\Delta v_{||})^2$ term which is also present in the magnetic moment formulation (4.81), the perpendicular velocity formulation has a $(\Delta v_\perp)^2$ contribution.

C.3.3 Conservative Corrections

Defining the boundary sums,

$$S_{1,\alpha} = \frac{\Delta V}{4}\sum_{j=1}^{M} v_{\perp}(j) f_{\alpha}(1,j)\frac{B_{||}^{*}(1)}{B}, \qquad S_{3,\alpha} = \frac{\Delta V}{4}\sum_{i=1}^{N} f_{\alpha}(i,1)\frac{B_{||}^{*}(i)}{B}, \tag{C.51}$$

$$S_{2,\alpha} = \frac{\Delta V}{4}\sum_{j=1}^{M} v_{\perp}(j) f_{\alpha}(N,j)\frac{B_{||}^{*}(N)}{B}, \qquad S_{4,\alpha} = \frac{\Delta V}{4}\sum_{i=1}^{N} f_{\alpha}(i,M)\frac{B_{||}^{*}(i)}{B}, \tag{C.52}$$

the boundary corrections can be written as

$$P_{\mathrm{BC},\alpha\beta} = 2S_{1,\alpha}\left(v_{||}(\frac{1}{2}) - u_{\alpha\beta} + \frac{2T_{\alpha\beta}}{m_{\alpha}\Delta v_{||}}\right) + 2S_{2,\alpha}\left(v_{||}(N+\frac{1}{2}) - u_{\alpha\beta} - \frac{2T_{\alpha\beta}}{m_{\alpha}\Delta v_{||}}\right), \tag{C.53}$$

$$\begin{aligned} E_{\mathrm{BC},\alpha\beta} = {} & S_{1,\alpha}\left(v_{||}^{2}(\frac{1}{2}) - \left(u_{\alpha\beta} - \frac{2T_{\alpha\beta}}{m_{\alpha}\Delta v_{||}}\right)v_{||}(\frac{1}{2})\right) \\ & + S_{2,\alpha}\left(v_{||}^{2}(N+\frac{1}{2}) - \left(u_{\alpha\beta} + \frac{2T_{\alpha\beta}}{m_{\alpha}\Delta v_{||}}\right)v_{||}(N+\frac{1}{2})\right) \\ & + S_{3,\alpha}\left(v_{\perp}^{3}(\frac{1}{2}) + \frac{2T_{\alpha\beta}}{m_{\alpha}\Delta v_{\perp}}v_{\perp}^{2}(\frac{1}{2})\right) + S_{4,\alpha}\left(v_{\perp}^{3}(M+\frac{1}{2}) - \frac{2T_{\alpha\beta}}{m_{\alpha}\Delta v_{\perp}}v_{\perp}^{2}(M+\frac{1}{2})\right). \end{aligned} \tag{C.54}$$

This can be cast into the following form,

$$P_{\mathrm{BC},\alpha\beta} = u_{\alpha\beta}p_{1,\alpha} + T_{\alpha\beta}p_{2,\alpha} + p_{3,\alpha}, \tag{C.55}$$

$$E_{\mathrm{BC},\alpha\beta} = u_{\alpha\beta}p_{4,\alpha} + T_{\alpha\beta}p_{5,\alpha} + p_{6,\alpha}. \tag{C.56}$$

using

$$p_{1,\alpha} = -2\left(S_{1,\alpha} + S_{2,\alpha}\right), \tag{C.57}$$

$$p_{2,\alpha} = \frac{4}{m_{\alpha}\Delta v_{||}}\left(S_{1,\alpha} - S_{2,\alpha}\right), \tag{C.58}$$

$$p_{3,\alpha} = 2\left(v_{||}(\frac{1}{2})S_{1,\alpha} + v_{||}(N+\frac{1}{2})S_{2,\alpha}\right), \tag{C.59}$$

$$p_{4,\alpha} = -\left(v_{||}(\frac{1}{2})S_{1,\alpha} + v_{||}(N+\frac{1}{2})S_{2,\alpha}\right) = -\frac{1}{2}p_{3,\alpha}, \tag{C.60}$$

$$\begin{aligned} p_{5,\alpha} = {} & \frac{2}{m_{\alpha}\Delta v_{||}}\left(v_{||}(\frac{1}{2})S_{1,\alpha} - v_{||}(N+\frac{1}{2})S_{2,\alpha}\right) \\ & + \frac{2}{m_{\alpha}\Delta v_{\perp}}\left(v_{\perp}^{2}(\frac{1}{2})S_{3,\alpha} - v_{\perp}^{2}(M+\frac{1}{2})S_{4,\alpha}\right), \end{aligned} \tag{C.61}$$

$$p_{6,\alpha} = \left(v_{||}^{2}(\frac{1}{2})S_{1,\alpha} + v_{||}^{2}(N+\frac{1}{2})S_{2,\alpha}\right) + \left(v_{\perp}^{3}(\frac{1}{2})S_{3,\alpha} + v_{\perp}^{3}(M+\frac{1}{2})S_{4,\alpha}\right). \tag{C.62}$$

The condition to achieve momentum and energy conservation is

$$0 = m_\alpha \nu_{\alpha\beta} \left(M_{1,\alpha} - u_{\alpha\beta} M_{0,\alpha} - P_{\mathrm{BC},\alpha\beta} \right) + m_\beta \nu_{\beta\alpha} \left(M_{1,\beta} - u_{\beta\alpha} M_{0,\beta} - P_{\mathrm{BC},\beta\alpha} \right), \tag{C.63}$$

$$\begin{aligned} 0 = {} & \nu_{\alpha\beta} \left(M_{2,\alpha} - \frac{1}{2} u_{\alpha\beta} m_\alpha M_{1,\alpha} - \frac{3}{2} T_{\alpha\beta} M_{0,\alpha} + \frac{(\Delta v_{||})^2 + 3(\Delta v_\perp)^2}{8} m_\alpha M_{0,\alpha} - m_\alpha E_{\mathrm{BC},\alpha\beta} \right) \\ & + \nu_{\beta\alpha} \left(M_{2,\beta} - \frac{1}{2} u_{\beta\alpha} m_\beta M_{1,\beta} - \frac{3}{2} T_{\beta\alpha} M_{0,\beta} + \frac{(\Delta v_{||})^2 + 3(\Delta v_\perp)^2}{8} m_\beta M_{0,\beta} - m_\beta E_{\mathrm{BC},\beta\alpha} \right). \end{aligned} \tag{C.64}$$

For the collision frequency, the combined form of eqs. (3.135) and (3.140) for EM and ET can be used,

$$\nu_{\beta\alpha} = \nu_{\alpha\beta} \frac{M_{0,\alpha}}{M_{0,\beta}} \kappa_{\alpha\beta}, \tag{C.65}$$

$$\kappa_{\alpha\beta} = \begin{cases} \frac{m_\alpha}{m_\beta}, & \text{EM}, \\ 1, & \text{ET}. \end{cases} \tag{C.66}$$

The parallel flow is written the same as in the magnetic moment version,

$$u_{\beta\alpha} = u_{\alpha\beta} \eta, \tag{C.67}$$

$$\eta \equiv \begin{cases} 1, & \text{physical units}, \\ \eta_{\mathrm{ref}}, & \text{normalized units}. \end{cases} \tag{C.68}$$

Inserting these relations yields

$$0 = m_\alpha \left(\frac{M_{1,\alpha}}{M_{0,\alpha}} - u_{\alpha\beta} - \frac{P_{\mathrm{BC},\alpha\beta}}{M_{0,\alpha}} \right) + m_\beta \kappa_{\alpha\beta} \left(\frac{M_{1,\beta}}{M_{0,\beta}} - u_{\alpha\beta} \eta - \frac{P_{\mathrm{BC},\beta\alpha}}{M_{0,\beta}} \right), \tag{C.69}$$

$$\begin{aligned} 0 = {} & \left(\frac{M_{2,\alpha}}{M_{0,\alpha}} - \frac{1}{2} u_{\alpha\beta} m_\alpha \frac{M_{1,\alpha}}{M_{0,\alpha}} - \frac{3}{2} T_{\alpha\beta} + m_\alpha \frac{(\Delta v_{||})^2 + 3(\Delta v_\perp)^2}{8} - m_\alpha \frac{E_{\mathrm{BC},\alpha\beta}}{M_{0,\alpha}} \right) \\ & + \kappa_{\alpha\beta} \left(\frac{M_{2,\beta}}{M_{0,\beta}} - \frac{1}{2} u_{\alpha\beta} \eta m_\beta \frac{M_{1,\beta}}{M_{0,\beta}} - \frac{3}{2} T_{\alpha\beta} + m_\beta \frac{(\Delta v_{||})^2 + 3(\Delta v_\perp)^2}{8} - m_\beta \frac{E_{\mathrm{BC},\beta\alpha}}{M_{0,\beta}} \right). \end{aligned} \tag{C.70}$$

Using the formulation with "s-factors",

$$\begin{aligned} s_{1,\alpha\beta} u_{\alpha\beta} + s_{2,\alpha\beta} T_{\alpha\beta} &= s_{3,\alpha\beta}, \\ s_{4,\alpha\beta} u_{\alpha\beta} + s_{5,\alpha\beta} T_{\alpha\beta} &= s_{6,\alpha\beta}. \end{aligned} \tag{C.71}$$

with the coefficients

$$s_{1,\alpha\beta} = \left(m_\alpha + m_\beta \kappa_{\alpha\beta}\eta + \frac{p_{1,\alpha} m_\alpha}{M_{0,\alpha}} + \frac{p_{1,\beta} m_\beta \kappa_{\alpha\beta}\eta}{M_{0,\beta}} \right), \tag{C.72}$$

$$s_{2,\alpha\beta} = \left(\frac{p_{2,\alpha} m_\alpha}{M_{0,\alpha}} + \frac{p_{2,\beta} m_\beta \kappa_{\alpha\beta}}{M_{0,\beta}} \right), \tag{C.73}$$

$$s_{3,\alpha\beta} = \left(\frac{M_{1,\alpha} m_\alpha}{M_{0,\alpha}} + \frac{M_{1,\beta} m_\beta \kappa_{\alpha\beta}}{M_{0,\beta}} - \frac{p_{3,\alpha} m_\alpha}{M_{0,\alpha}} - \frac{p_{3,\beta} m_\beta \kappa_{\alpha\beta}}{M_{0,\beta}} \right), \tag{C.74}$$

$$s_{4,\alpha\beta} = \left(\frac{1}{2}\frac{M_{1,\alpha} m_\alpha}{M_{0,\alpha}} + \frac{1}{2}\frac{M_{1,\beta} m_\beta \kappa_{\alpha\beta}\eta}{M_{0,\beta}} + \frac{p_{4,\alpha} m_\alpha}{M_{0,\alpha}} + \frac{p_{4,\beta} m_\beta \kappa_{\alpha\beta}\eta}{M_{0,\beta}} \right), \tag{C.75}$$

$$s_{5,\alpha\beta} = \left(\frac{3}{2}(1+\kappa_{\alpha\beta}) + \frac{p_{5,\alpha} m_\alpha}{M_{0,\alpha}} + \frac{p_{5,\beta} m_\beta \kappa_{\alpha\beta}}{M_{0,\beta}} \right), \tag{C.76}$$

$$s_{6,\alpha\beta} = \left(\frac{M_{2,\alpha}}{M_{0,\alpha}} + \frac{M_{2,\beta}\kappa_{\alpha\beta}}{M_{0,\beta}} + \frac{(\Delta v_{||})^2 + 3(\Delta v_\perp)^2}{8}(m_\alpha + m_\beta\kappa_{\alpha\beta}) - \frac{p_{6,\alpha} m_\alpha}{M_{0,\alpha}} - \frac{p_{6,\beta} m_\beta \kappa_{\alpha\beta}}{M_{0,\beta}} \right). \tag{C.77}$$

The system of equations is solved by (4.113) and (4.114).

C.4 Normalized Version

The normalized perpendicular velocity and cell sizes are,

$$\hat{v}_\perp = \sqrt{\hat{\mu}\hat{B}}, \tag{C.78}$$

$$\hat{\mu} = \frac{\hat{v}_\perp^2}{\hat{B}}, \tag{C.79}$$

$$\Delta\hat{\mu} = \frac{2\hat{v}_\perp \Delta\hat{v}_\perp}{\hat{B}}, \tag{C.80}$$

$$\Delta\hat{v}_\perp(j) = \hat{v}_\perp \Delta\hat{v}_\perp = \frac{1}{2}\hat{B}\sqrt{\hat{\mu}\Delta\hat{\mu}}. \tag{C.81}$$

C.4.1 Normalized Velocity Space Moments

The velocity space moments are normalized as,

$$\hat{M}_{0,\alpha} = \Delta\hat{V} \sum_{i=1}^{N}\sum_{j=1}^{M} \hat{v}_{\perp}(j)\hat{f}_{\alpha}(i,j)\frac{\hat{B}^{*}_{||}(i)}{\hat{B}}, \tag{C.82}$$

$$\hat{M}_{1,\alpha} = \Delta\hat{V} \sum_{i=1}^{N}\sum_{j=1}^{M} \hat{v}_{\perp}(j)\hat{v}_{||}(i)\hat{f}(i,j)\frac{\hat{B}^{*}_{||}(i)}{\hat{B}}, \tag{C.83}$$

$$\hat{M}_{2,\perp,\alpha} = \Delta\hat{V} \sum_{i=1}^{N}\sum_{j=1}^{M} \hat{v}^{3}_{\perp}(j)\hat{f}(i,j)\frac{\hat{B}^{*}_{||}(i)}{\hat{B}}, \tag{C.84}$$

$$\hat{M}_{2,||,\alpha} = \Delta\hat{V} \sum_{i=1}^{N}\sum_{j=1}^{M} v_{\perp}(j)\hat{v}^{2}_{||}(i)\hat{f}(i,j)\frac{\hat{B}^{*}_{||}(i)}{\hat{B}}, \tag{C.85}$$

$$\hat{M}_{2} = \hat{M}_{2,\perp} + \hat{M}_{2,||}, \tag{C.86}$$

with $\Delta\hat{V} = 2\pi\Delta\hat{v}_{||}\Delta\hat{v}_{\perp}$. The reference quantities used are

$$M_{0,\mathrm{ref},\alpha} = n_{\mathrm{ref}}, \tag{C.87}$$

$$M_{1,\mathrm{ref},\alpha} = v_{\mathrm{th},\alpha} n_{\mathrm{ref}}, \tag{C.88}$$

$$M_{2,\mathrm{ref},\alpha} = T_{\mathrm{ref}} n_{\mathrm{ref}}. \tag{C.89}$$

Using eq. (C.81) allows to write,

$$\hat{M}_{0,\alpha} = \pi\Delta\hat{v}_{||}\sqrt{\Delta\hat{\mu}} \sum_{i=1}^{N}\sum_{j=1}^{M} \sqrt{\hat{\mu}(j)}\hat{f}_{\alpha}(i,j)\hat{B}^{*}_{||}(i), \tag{C.90}$$

$$\hat{M}_{1,\alpha} = \pi\Delta\hat{v}_{||}\sqrt{\Delta\hat{\mu}} \sum_{i=1}^{N}\sum_{j=1}^{M} \sqrt{\hat{\mu}(j)}\hat{v}_{||}(i)\hat{f}(i,j)\hat{B}^{*}_{||}(i), \tag{C.91}$$

$$\hat{M}_{2,\perp,\alpha} = \pi\Delta\hat{v}_{||}\sqrt{\Delta\hat{\mu}} \sum_{i=1}^{N}\sum_{j=1}^{M} \sqrt{\hat{\mu}(j)}\hat{\mu}\hat{B}\hat{f}(i,j)\hat{B}^{*}_{||}(i), \tag{C.92}$$

$$\hat{M}_{2,||,\alpha} = \pi\Delta\hat{v}_{||}\sqrt{\Delta\hat{\mu}} \sum_{i=1}^{N}\sum_{j=1}^{M} \sqrt{\hat{\mu}(j)}\hat{v}^{2}_{||}(i)\hat{f}(i,j)\hat{B}^{*}_{||}(i). \tag{C.93}$$

The above formulation is convenient because the integrand is the same as in the magnetic moment formulation, apart from the integration weights ($\sqrt{\hat{\mu}(j)}$ that can be moved to new, grid-dependent integration weights).

C.4.2 Normalized Finite Volume Discretization

Normalizing eq. (C.15),

$$(\hat{C}_{\alpha\beta}\hat{f}_\alpha)(i,j) = \frac{t_{\text{ref}}J_{\text{ref}}}{f_{\text{ref}}B_{\text{ref}}v_{\text{th},\alpha}}\frac{1}{\hat{B}^*_{||}(i)}\left[\frac{1}{\Delta\hat{v}_{||}}\left(\hat{J}_{||}(i+\frac{1}{2},j)-\hat{J}_{||}(i-\frac{1}{2},j)\right)\right.$$
$$\left.+\frac{1}{\Delta\hat{v}_\perp}\left(\hat{\tilde{J}}_\perp(i,j+\frac{1}{2})-\hat{\tilde{J}}_\perp(i,j-\frac{1}{2})\right)\right], \tag{C.94}$$

yields the required reference for the collisional flux,

$$J_{\text{ref}} = \frac{f_{\text{ref}}B_{\text{ref}}v_{\text{th},\alpha}}{t_{\text{ref}}}, \tag{C.95}$$

which components are given as

$$\hat{J}_{||} = \hat{\nu}_{\alpha\beta}\left[(\hat{v}_{||}-\hat{u}_{\alpha\beta})\hat{f}_\alpha\hat{B}^*_{||}+\frac{1}{2}\hat{T}_{\alpha\beta}\frac{\partial\hat{f}_\alpha\hat{B}^*_{||}}{\partial\hat{v}_{||}}\right], \tag{C.96}$$

$$\hat{J}_\perp = \hat{\nu}_{\alpha\beta}\left[\hat{v}_\perp\hat{f}_\alpha\hat{B}^*_{||}+\frac{1}{2}\hat{T}_{\alpha\beta}\frac{\partial\hat{f}_\alpha\hat{B}^*_{||}}{\partial\hat{v}_\perp}\right]. \tag{C.97}$$

We normalize the boundary sums,

$$\hat{S}_{1,\alpha} = \frac{\Delta\hat{V}}{4}\sum_{j=1}^{M}\hat{v}_\perp(j)\hat{f}_\alpha(1,j)\frac{\hat{B}^*_{||}(1)}{\hat{B}}, \qquad \hat{S}_{3,\alpha} = \frac{\Delta\hat{V}}{4}\sum_{i=1}^{N}\hat{f}_\alpha(i,1)\frac{\hat{B}^*_{||}(i)}{\hat{B}}, \tag{C.98}$$

$$\hat{S}_{2,\alpha} = \frac{\Delta\hat{V}}{4}\sum_{j=1}^{M}\hat{v}_\perp(j)\hat{f}_\alpha(N,j)\frac{\hat{B}^*_{||}(N)}{\hat{B}}, \qquad \hat{S}_{4,\alpha} = \frac{\Delta\hat{V}}{4}\sum_{i=1}^{N}\hat{f}_\alpha(i,M)\frac{\hat{B}^*_{||}(i)}{\hat{B}}, \tag{C.99}$$

with

$$S_{1,\text{ref}} = S_{2,\text{ref}} = n_{\text{ref}}, \qquad S_{3,\text{ref}} = S_{4,\text{ref}} = \frac{n_{\text{ref}}}{v_{\text{th},\alpha}}. \tag{C.100}$$

The normalized boundary corrections are

$$\hat{P}_{\mathrm{BC},\alpha\beta} = 2\hat{S}_{1,\alpha}\left(\hat{v}_{||}(\frac{1}{2}) - \hat{u}_{\alpha\beta} + \frac{\hat{T}_{\alpha\beta}}{\Delta\hat{v}_{||}}\right) + 2\hat{S}_{2,\alpha}\left(\hat{v}_{||}(\frac{1}{2})(N+\frac{1}{2}) - \hat{u}_{\alpha\beta} - \frac{\hat{T}_{\alpha\beta}}{\Delta\hat{v}_{||}(\frac{1}{2})}\right), \quad \text{(C.101)}$$

$$\begin{aligned}\hat{E}_{\mathrm{BC},\alpha\beta} = {} & \hat{S}_{1,\alpha}\left(\hat{v}_{||}^2(\frac{1}{2}) - \left(\hat{u}_{\alpha\beta} - \frac{\hat{T}_{\alpha\beta}}{\Delta\hat{v}_{||}}\right)\hat{v}_{||}(\frac{1}{2})\right) \\ & + \hat{S}_{2,\alpha}\left(\hat{v}_{||}^2(N+\frac{1}{2}) - \left(\hat{u}_{\alpha\beta} + \frac{\hat{T}_{\alpha\beta}}{\Delta\hat{v}_{||}^2}\right)\hat{v}_{||}^2(N+\frac{1}{2})\right) \\ & + \hat{S}_{3,\alpha}\left(\hat{v}_{\perp}^3(\frac{1}{2}) + \frac{\hat{T}_{\alpha\beta}}{\Delta\hat{v}_{\perp}}\hat{v}_{\perp}^2(\frac{1}{2})\right) + \hat{S}_{4,\alpha}\left(\hat{v}_{\perp}^3(M+\frac{1}{2}) - \frac{\hat{T}_{\alpha\beta}}{\Delta\hat{v}_{\perp}}\hat{v}_{\perp}^2(M+\frac{1}{2})\right). \quad \text{(C.102)}\end{aligned}$$

with

$$P_{\mathrm{BC,ref}} = n_{\mathrm{ref}} v_{\mathrm{th},\alpha}, \qquad E_{\mathrm{BC,ref}} = n_{\mathrm{ref}} v_{\mathrm{th},\alpha}^2. \quad \text{(C.103)}$$

The normalization of the alternative form

$$\hat{P}_{\mathrm{BC},\alpha\beta} = \hat{u}_{\alpha\beta}\hat{p}_{1,\alpha} + \hat{T}_{\alpha\beta}\hat{p}_{2,\alpha} + \hat{p}_{3,\alpha}, \quad \text{(C.104)}$$

$$\hat{E}_{\mathrm{BC},\alpha\beta} = \hat{u}_{\alpha\beta}\hat{p}_{4,\alpha} + \hat{T}_{\alpha\beta}\hat{p}_{5,\alpha} + \hat{p}_{6,\alpha}, \quad \text{(C.105)}$$

yields expressions for the normalized "p-factors",

$$\hat{p}_{1,\alpha} = -2\left(\hat{S}_{1,\alpha} + \hat{S}_{2,\alpha}\right), \quad \text{(C.106)}$$

$$\hat{p}_{2,\alpha} = \frac{2}{\Delta\hat{v}_{||}}\left(\hat{S}_{1,\alpha} - \hat{S}_{2,\alpha}\right), \quad \text{(C.107)}$$

$$\hat{p}_{3,\alpha} = 2\left(\hat{v}_{||}(\frac{1}{2})\hat{S}_{1,\alpha} + \hat{v}_{||}(N+\frac{1}{2})\hat{S}_{2,\alpha}\right), \quad \text{(C.108)}$$

$$\hat{p}_{4,\alpha} = -\left(\hat{v}_{||}(\frac{1}{2})\hat{S}_{1,\alpha} + \hat{v}_{||}(N+\frac{1}{2})\hat{S}_{2,\alpha}\right) = -\frac{1}{2}\hat{p}_{3,\alpha}, \quad \text{(C.109)}$$

$$\hat{p}_{5,\alpha} = \frac{1}{\Delta\hat{v}_{||}}\left(\hat{v}_{||}(\frac{1}{2})\hat{S}_{1,\alpha} - \hat{v}_{||}(N+\frac{1}{2})\hat{S}_{2,\alpha}\right) + \frac{1}{\Delta\hat{v}_{\perp}}\left(\hat{v}_{\perp}^2(\frac{1}{2})\hat{S}_{3,\alpha} - \hat{v}_{\perp}^2(M+\frac{1}{2})\hat{S}_{4,\alpha}\right), \quad \text{(C.110)}$$

$$\hat{p}_{6,\alpha} = \left(\hat{v}_{||}^2(\frac{1}{2})\hat{S}_{1,\alpha} + \hat{v}_{||}^2(N+\frac{1}{2})\hat{S}_{2,\alpha}\right) + \left(\hat{v}_{\perp}^3(\frac{1}{2})\hat{S}_{3,\alpha} + \hat{v}_{\perp}^3(M+\frac{1}{2})\hat{S}_{4,\alpha}\right). \quad \text{(C.111)}$$

The normalized conservation equations are

$$0 = \hat{\epsilon}_\alpha \sqrt{\hat{m}_\alpha} \left(\frac{\hat{M}_{1,\alpha}}{\hat{M}_{0,\alpha}} - \hat{u}_{\alpha\beta} - \frac{\hat{P}_{\mathrm{BC},\alpha\beta}}{\hat{M}_{0,\alpha}} \right) + \hat{\epsilon}_\beta \sqrt{\hat{m}_\beta} \left(\frac{\hat{M}_{1,\beta}}{\hat{M}_{0,\beta}} - \hat{u}_{\alpha\beta} \sqrt{\frac{\hat{m}_\beta}{\hat{m}_\alpha}} - \frac{\hat{P}_{\mathrm{BC},\beta\alpha}}{\hat{M}_{0,\beta}} \right), \tag{C.112}$$

$$\begin{aligned} 0 = {} & \hat{\epsilon}_\alpha \left(\frac{\hat{M}_{2,\alpha}}{\hat{M}_{0,\alpha}} - \hat{u}_{\alpha\beta} \frac{\hat{M}_{1,\alpha}}{\hat{M}_{0,\alpha}} - \frac{3}{2} \hat{T}_{\alpha\beta} + \frac{(\Delta\hat{v}_{||})^2 + 3(\Delta\hat{v}_\perp)^2}{4} - \frac{2\hat{E}_{\mathrm{BC},\alpha\beta}}{\hat{M}_{0,\alpha}} \right) \\ & + \hat{\epsilon}_\beta \left(\frac{\hat{M}_{2,\beta}}{\hat{M}_{0,\beta}} - \hat{u}_{\alpha\beta} \sqrt{\frac{\hat{m}_\beta}{\hat{m}_\alpha}} \frac{\hat{M}_{1,\beta}}{\hat{M}_{0,\beta}} - \frac{3}{2} \hat{T}_{\alpha\beta} + \frac{(\Delta\hat{v}_{||})^2 + 3(\Delta\hat{v}_\perp)^2}{4} - \frac{2\hat{E}_{\mathrm{BC},\beta\alpha}}{\hat{M}_{0,\beta}} \right), \end{aligned} \tag{C.113}$$

with

$$\hat{\epsilon}_\alpha = \begin{cases} \frac{1}{\hat{m}_\alpha}, & \text{EM}, \\ 1, & \text{ET}. \end{cases} \tag{C.114}$$

Writing the normalized system of equations,

$$\hat{u}_{\alpha\beta} \hat{s}_{1,\alpha} + \hat{T}_{\alpha\beta} \hat{s}_{2,\alpha} = \hat{s}_{3,\alpha}, \tag{C.115}$$

$$\hat{u}_{\alpha\beta} \hat{s}_{4,\alpha} + \hat{T}_{\alpha\beta} \hat{s}_{5,\alpha} = \hat{s}_{6,\alpha}. \tag{C.116}$$

gives the normalized "s-factors",

$$\hat{s}_{1,\alpha\beta} = \hat{\gamma}_\alpha + \hat{\gamma}_\beta \delta_{\alpha\beta} + \hat{\gamma}_\alpha \frac{\hat{p}_{1,\alpha}}{\hat{M}_{0,\alpha}} + \hat{\gamma}_\beta \delta_{\alpha\beta} \frac{\hat{p}_{1,\beta}}{\hat{M}_{0,\beta}}, \tag{C.117}$$

$$\hat{s}_{2,\alpha\beta} = \hat{\gamma}_\alpha \frac{\hat{p}_{2,\alpha}}{\hat{M}_{0,\alpha}} + \hat{\gamma}_\beta \frac{\hat{p}_{2,\beta}}{\hat{M}_{0,\beta}}, \tag{C.118}$$

$$\hat{s}_{3,\alpha\beta} = \hat{\gamma}_\alpha \frac{\hat{M}_{1,\alpha}}{\hat{M}_{0,\alpha}} + \hat{\gamma}_\beta \frac{\hat{M}_{1,\beta}}{\hat{M}_{0,\beta}} - \hat{\gamma}_\alpha \frac{\hat{p}_{3,\alpha}}{\hat{M}_{0,\alpha}} - \hat{\gamma}_\beta \frac{\hat{p}_{3,\beta}}{\hat{M}_{0,\beta}}, \tag{C.119}$$

$$\hat{s}_{4,\alpha\beta} = \hat{\epsilon}_\alpha \frac{\hat{M}_{1,\alpha}}{\hat{M}_{0,\alpha}} + \hat{\epsilon}_\beta \delta_{\alpha\beta} \frac{\hat{M}_{1,\beta}}{\hat{M}_{0,\beta}} + \hat{\epsilon}_\alpha \frac{2\hat{p}_{4,\alpha}}{\hat{M}_{0,\alpha}} + \hat{\epsilon}_\beta \delta_{\alpha\beta} \frac{2\hat{p}_{4,\beta}}{\hat{M}_{0,\beta}}, \tag{C.120}$$

$$\hat{s}_{5,\alpha\beta} = \frac{3}{2}(\hat{\epsilon}_\alpha + \hat{\epsilon}_\beta) + \hat{\epsilon}_\alpha \frac{2\hat{p}_{5,\alpha}}{\hat{M}_{0,\alpha}} + \hat{\epsilon}_\beta \frac{2\hat{p}_{5,\beta}}{\hat{M}_{0,\beta}}, \tag{C.121}$$

$$\hat{s}_{6,\alpha\beta} = \hat{\epsilon}_\alpha \frac{\hat{M}_{2,\alpha}}{\hat{M}_{0,\alpha}} + \hat{\epsilon}_\beta \frac{\hat{M}_{2,\beta}}{\hat{M}_{0,\beta}} + \frac{1}{4} \left(\left(\Delta\hat{v}_{||} \right)^2 + 3 \left(\Delta\hat{v}_\perp \right)^2 \right) (\hat{\epsilon}_\alpha + \hat{\epsilon}_\beta) - \hat{\epsilon}_\alpha \frac{2\hat{p}_{6,\alpha}}{\hat{M}_{0,\alpha}} - \hat{\epsilon}_\beta \frac{2\hat{p}_{6,\beta}}{\hat{M}_{0,\beta}}, \tag{C.122}$$

with

$$\hat{\gamma}_\alpha = \sqrt{\hat{m}_\alpha}\hat{\epsilon}_\alpha = \begin{cases} \frac{1}{\sqrt{\hat{m}_\alpha}}, & \text{EM}, \\ \sqrt{\hat{m}_\alpha}, & \text{ET}, \end{cases} \tag{C.123}$$

$$\delta_{\alpha\beta} = \sqrt{\frac{\hat{m}_\beta}{\hat{m}_\alpha}}. \tag{C.124}$$

Appendix D

Turbulence Characterization Figures

This appendix contains a collection of figures of the turbulence characterization from section 5.2.2.

D.1 Temporal Fourier Spectra

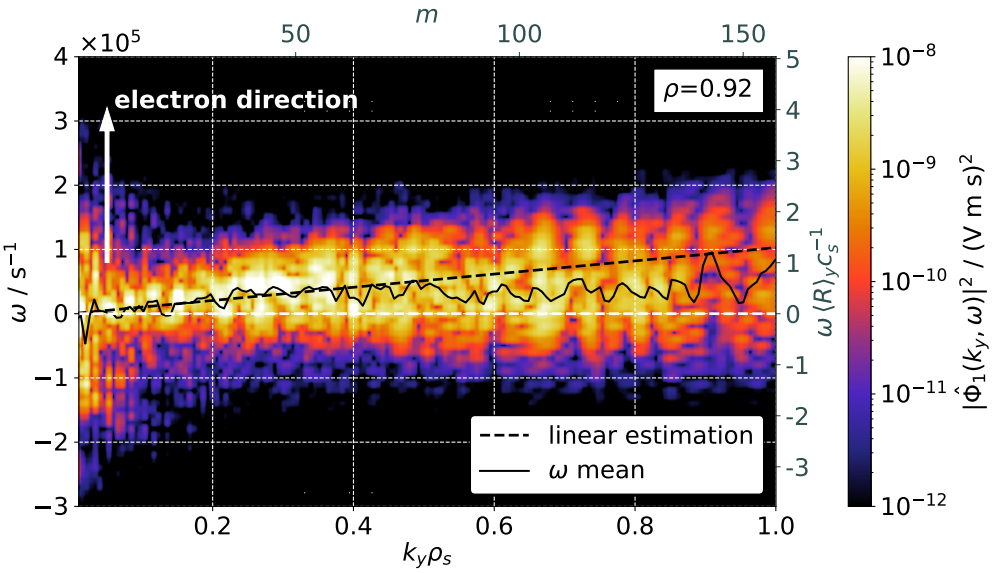

Figure D.1. Temporal flux surface Fourier transform of the electrostatic potential over the last 100 μs of the LBD simulation. The solid line shows a measure for the mean value of ω, whereas the dotted line shows a linear estimation for the frequency of the TEM. Taken from Ref. [59].

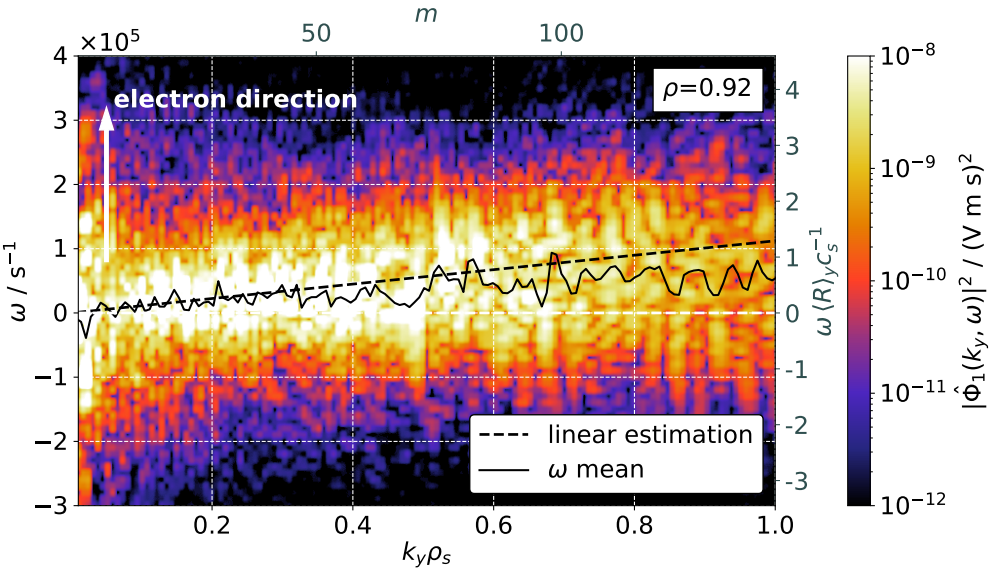

Figure D.2. Same as Fig. D.1 but for the collisionless simulation. Based on data available at Ref. [224].

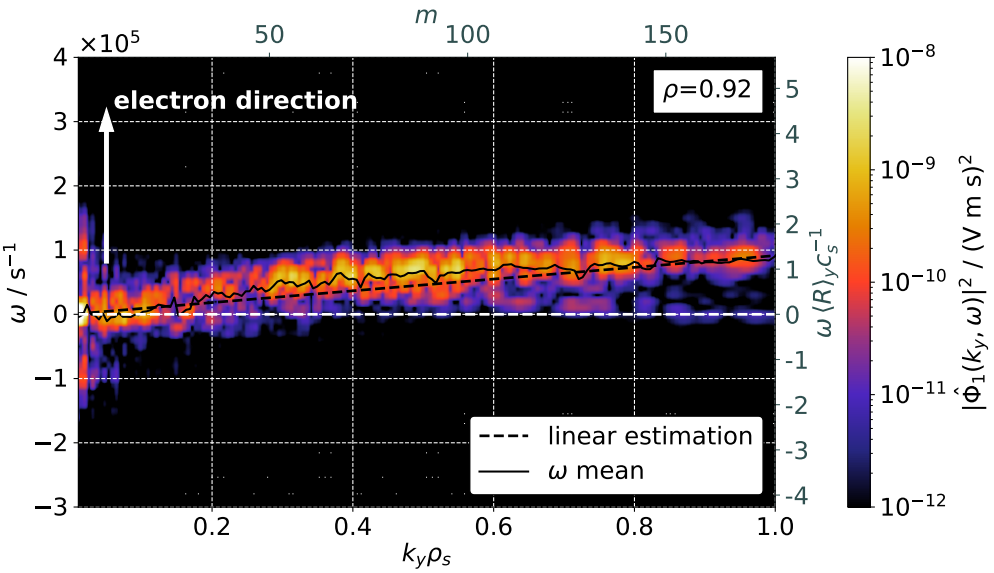

Figure D.3. Same as Fig. D.1 but for the BGK simulation. Based on data available at Ref. [224].

D.2 Spectral Fluxes

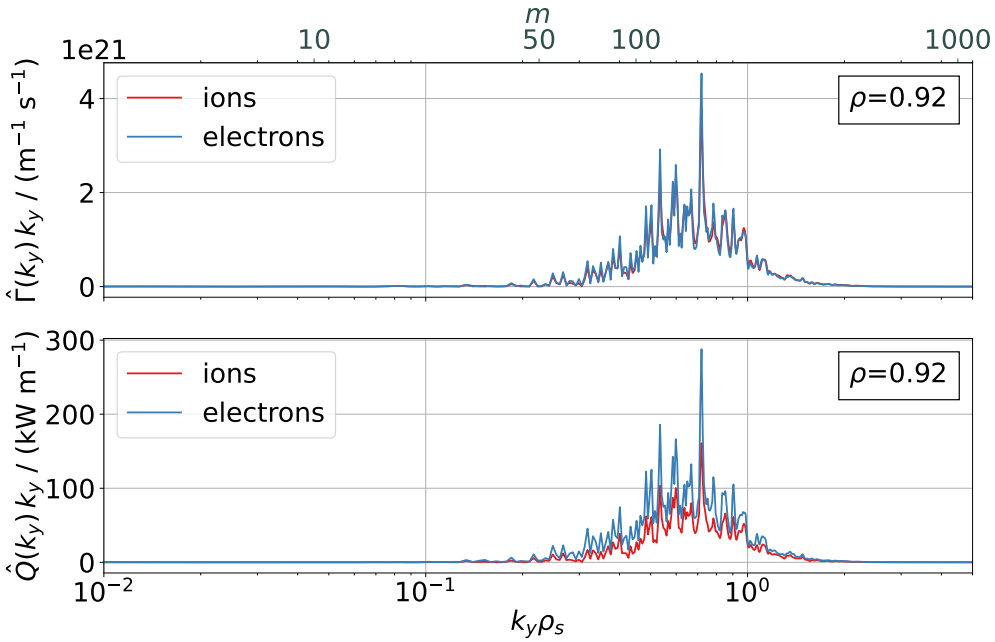

Figure D.4. Spectral particle and heat flux for electrons and ions from the LBD simulation, averaged toroidally and temporally over 100 μs. The fluxes are weighted by k_y to account for the logarithmic scale of the abscissa. Taken from Ref. [59].

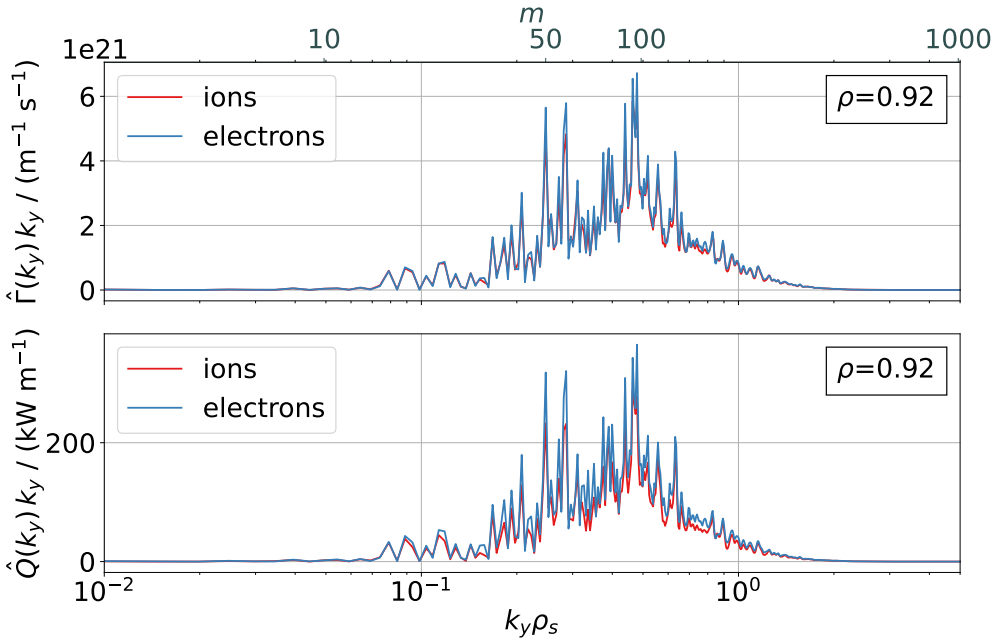

Figure D.5. Same as Fig. D.4 but for the collisionless simulation. Based on data available at Ref. [224].

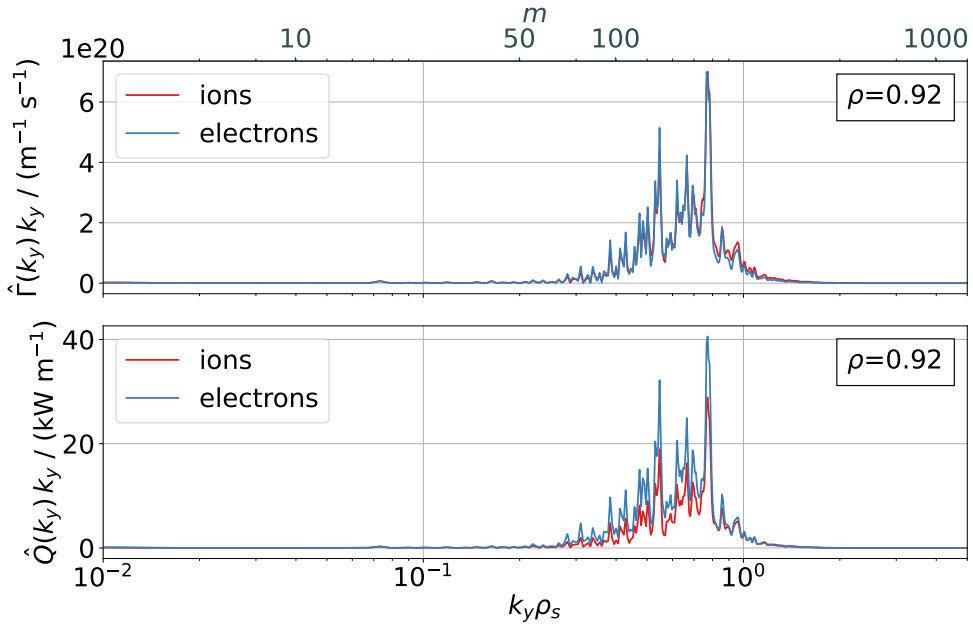

Figure D.6. Same as Fig. D.4 but for the BGK simulation. Based on data available at Ref. [224].

D.3 Phase Shifts

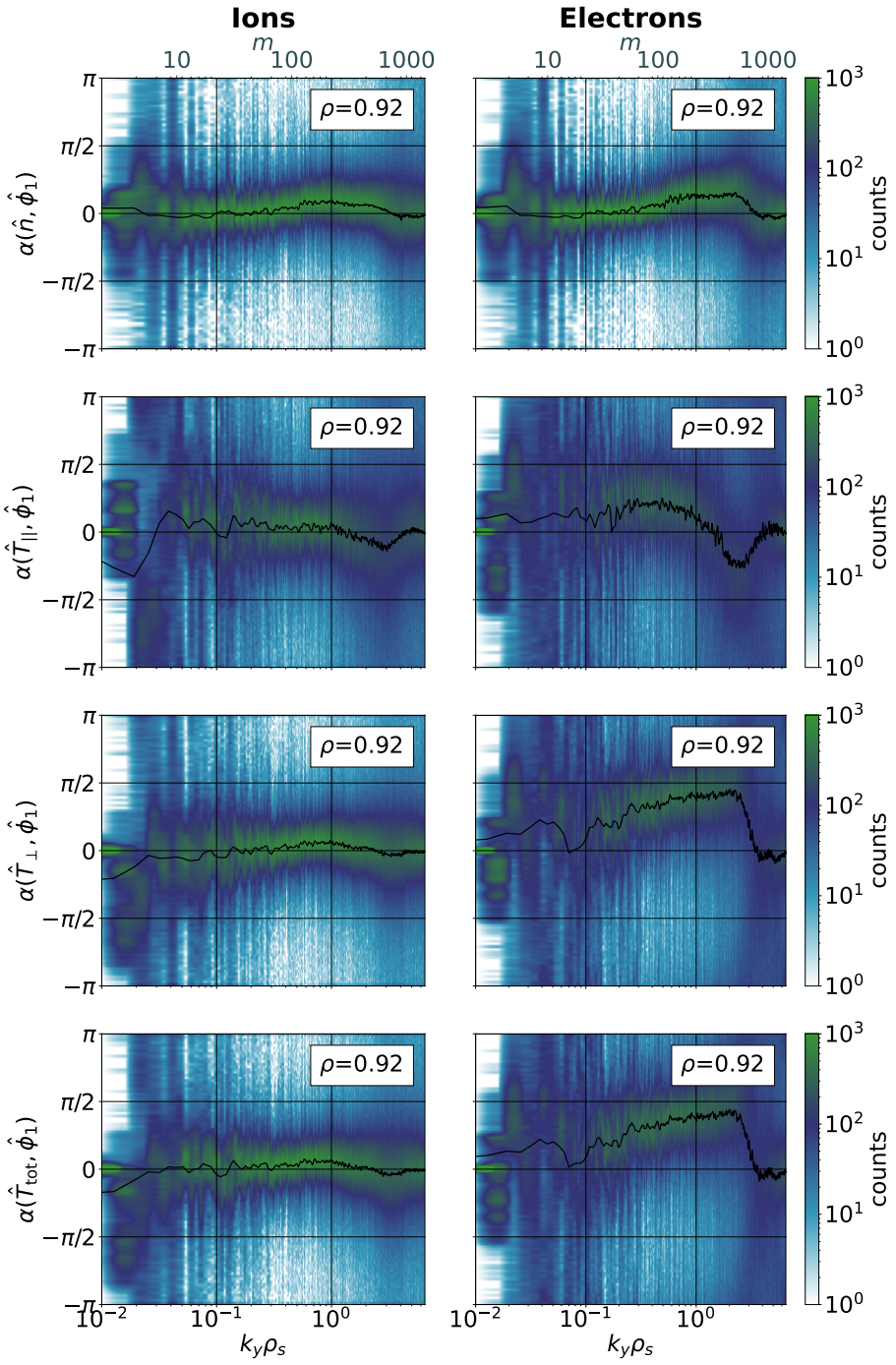

Figure D.7. Histogram count of phase shifts (cross-phases) between the density, the parallel, perpendicular, and total temperature of electrons and ions, and the electrostatic potential for the LBD simulation. The histogram counts are collected over 100 μs, and the black line shows a measure for the mean value by taking a rolling average over the last three mean values on the phase shift dimension. Taken from Ref. [59].

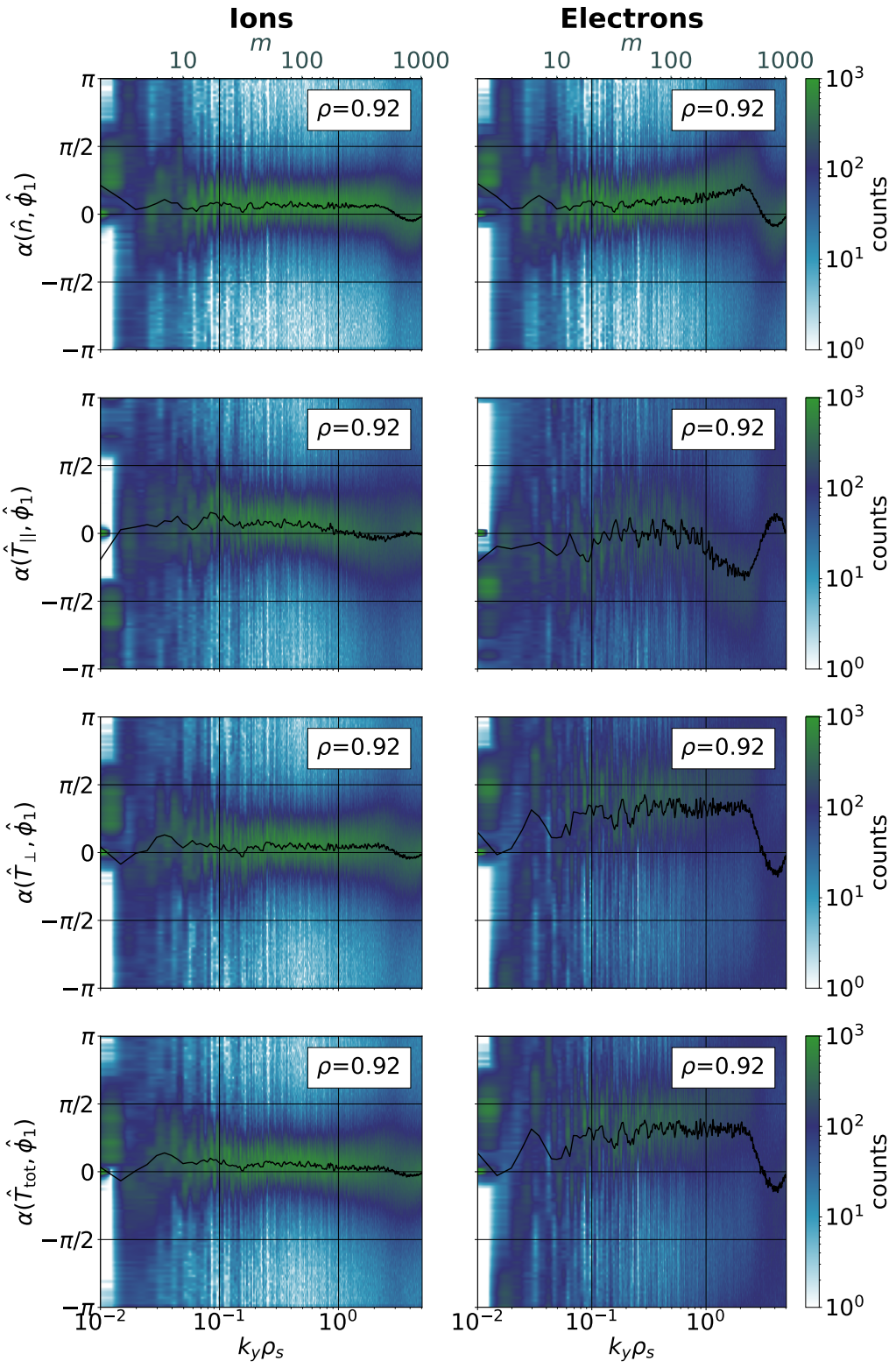

Figure D.8. Same as Fig. D.7 but for the collisionless simulation. Based on data available at Ref. [224].

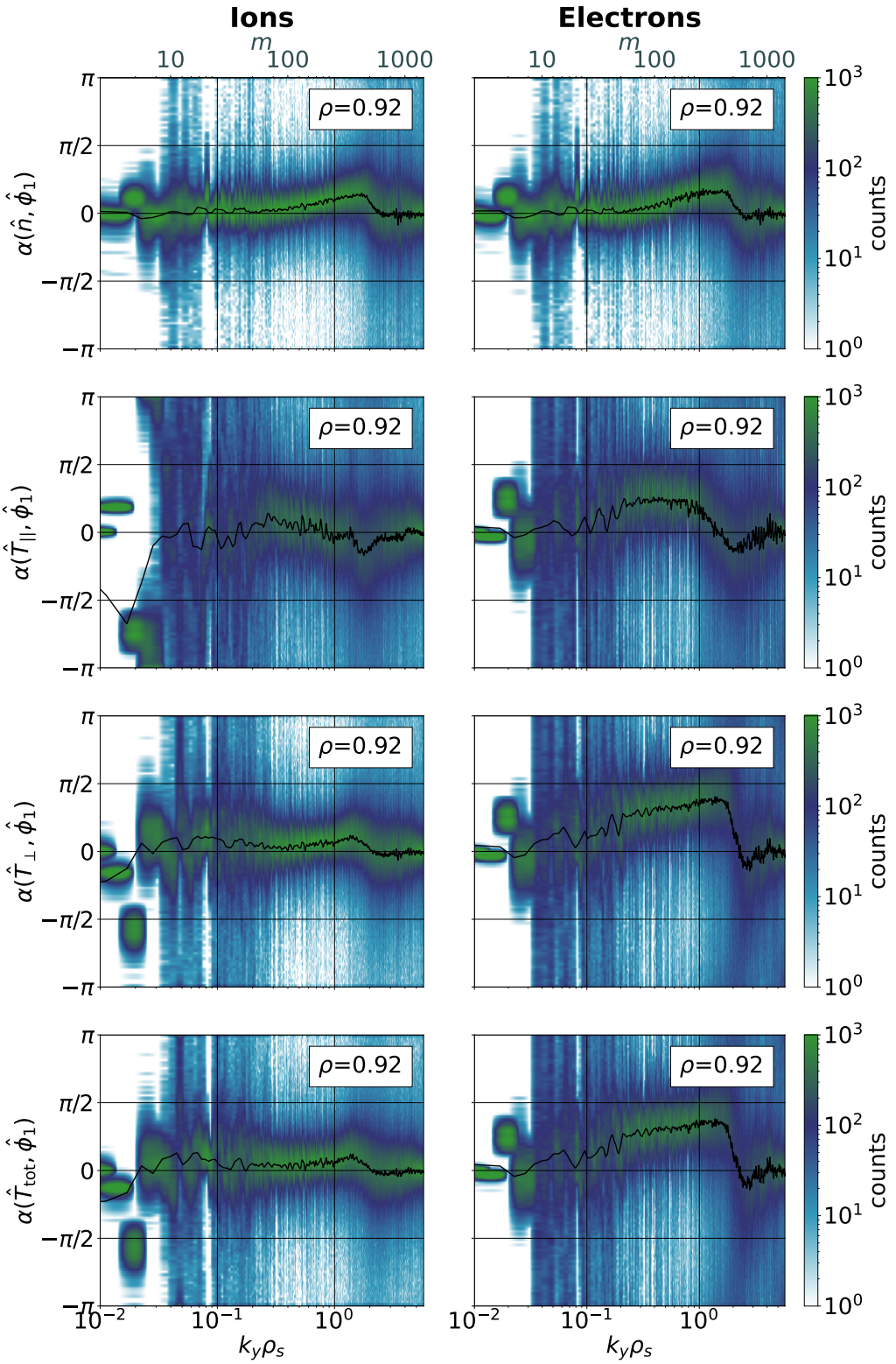

Figure D.9. Same as Fig. D.7 but for the BGK simulation. Based on data available at Ref. [224].

D.4 Trapped Particle Fluxes

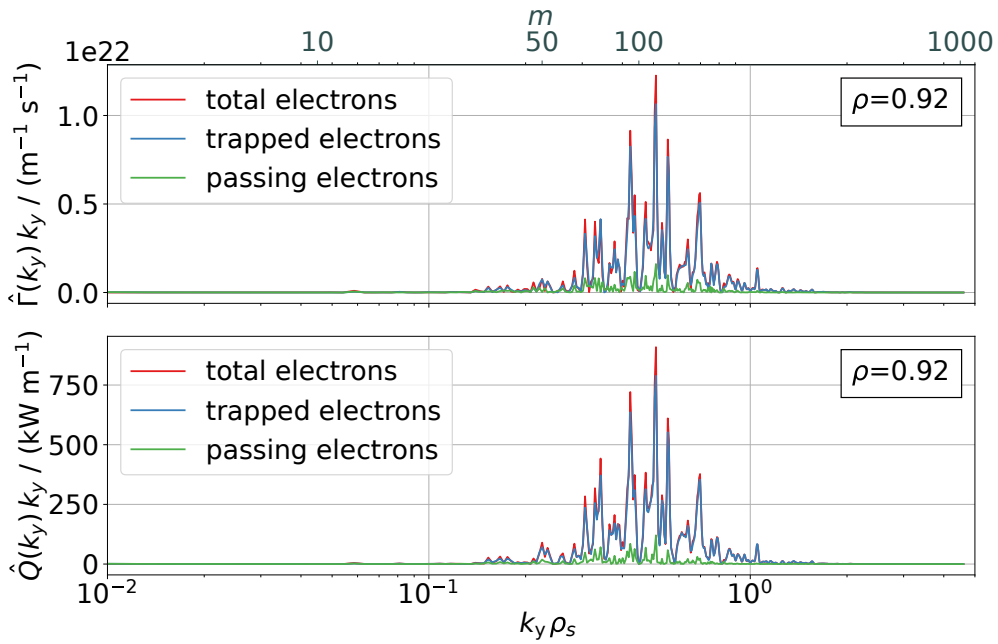

Figure D.10. Spectral total, trapped and passing electron particle and heat flux at the final time of the LBD simulation. Taken from Ref. [59].

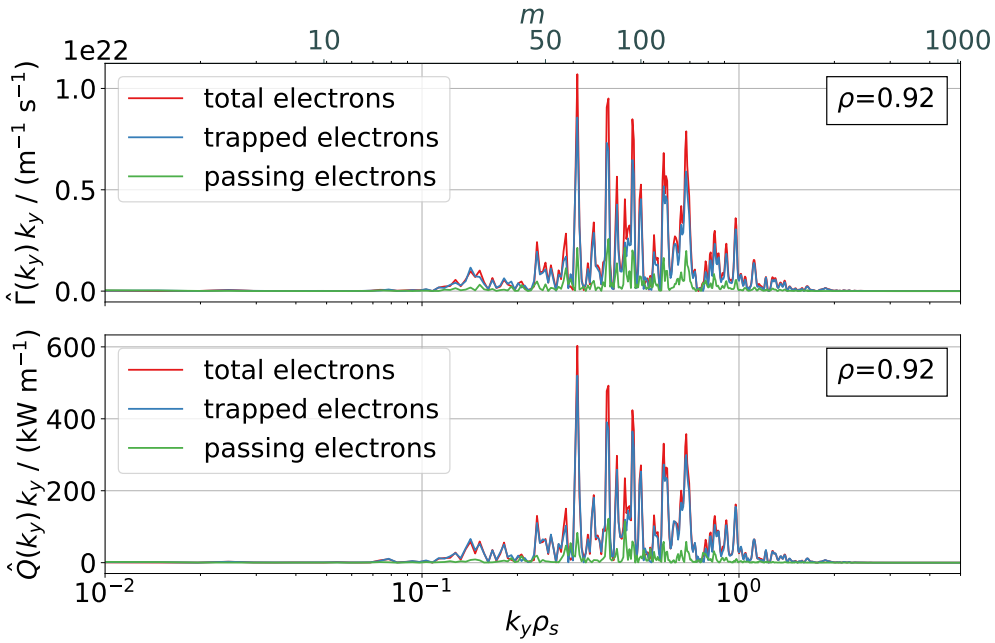

Figure D.11. Same as Fig. D.10 but for the collisionless simulation. Based on data available at Ref. [224].

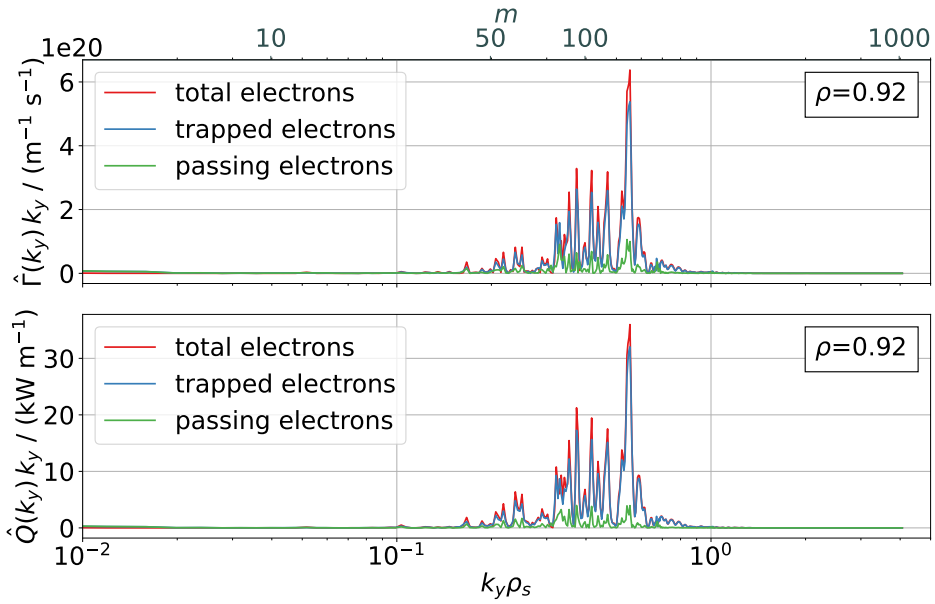

Figure D.12. Same as Fig. D.10 but for the BGK simulation. Based on data available at Ref. [224].

D.5 Trapped Particle Phase Shifts

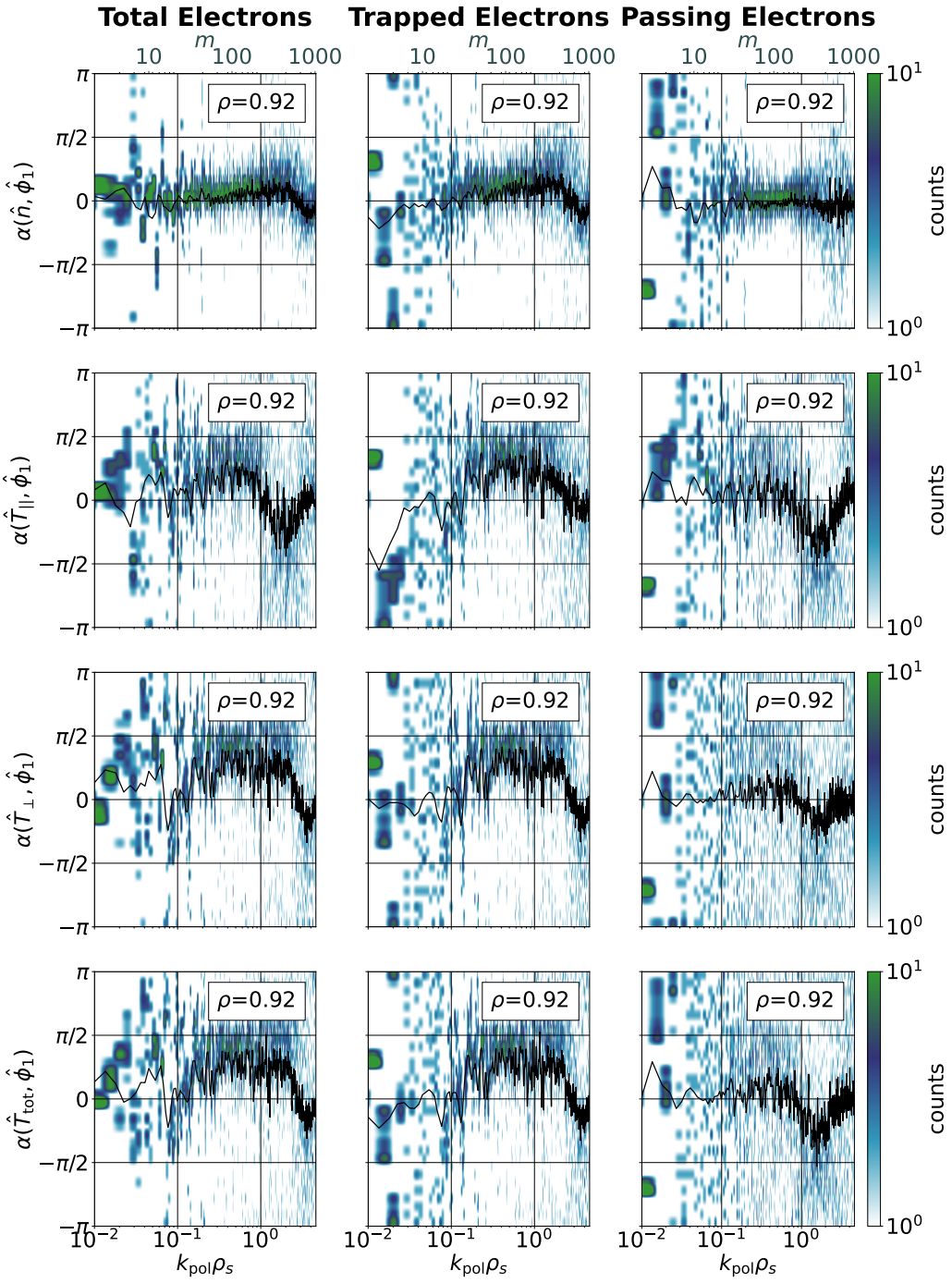

Figure D.13. Histogram count of phase shifts (cross-phases) between total, trapped, and passing electron density, parallel, perpendicular, and total temperature, and the electrostatic potential for the LBD simulation. The histogram counts were collected toroidally at the final time of the simulation. The black line shows a measure for the mean value by taking a rolling average over the last three mean values on the phase shift dimension. Taken from Ref. [59].

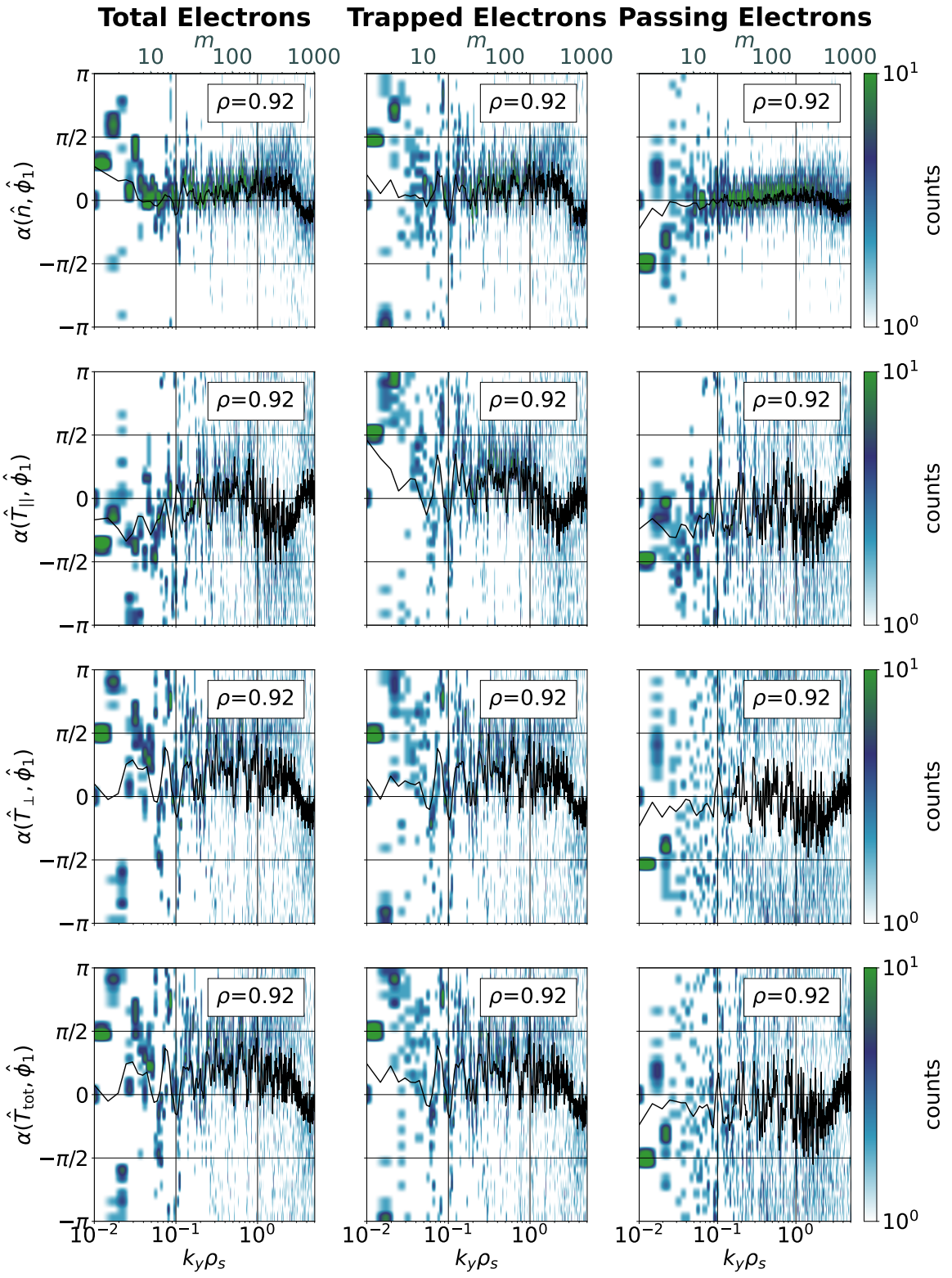

Figure D.14. Same as Fig. D.13 but for the collisionless simulation. Based on data available at Ref. [224].

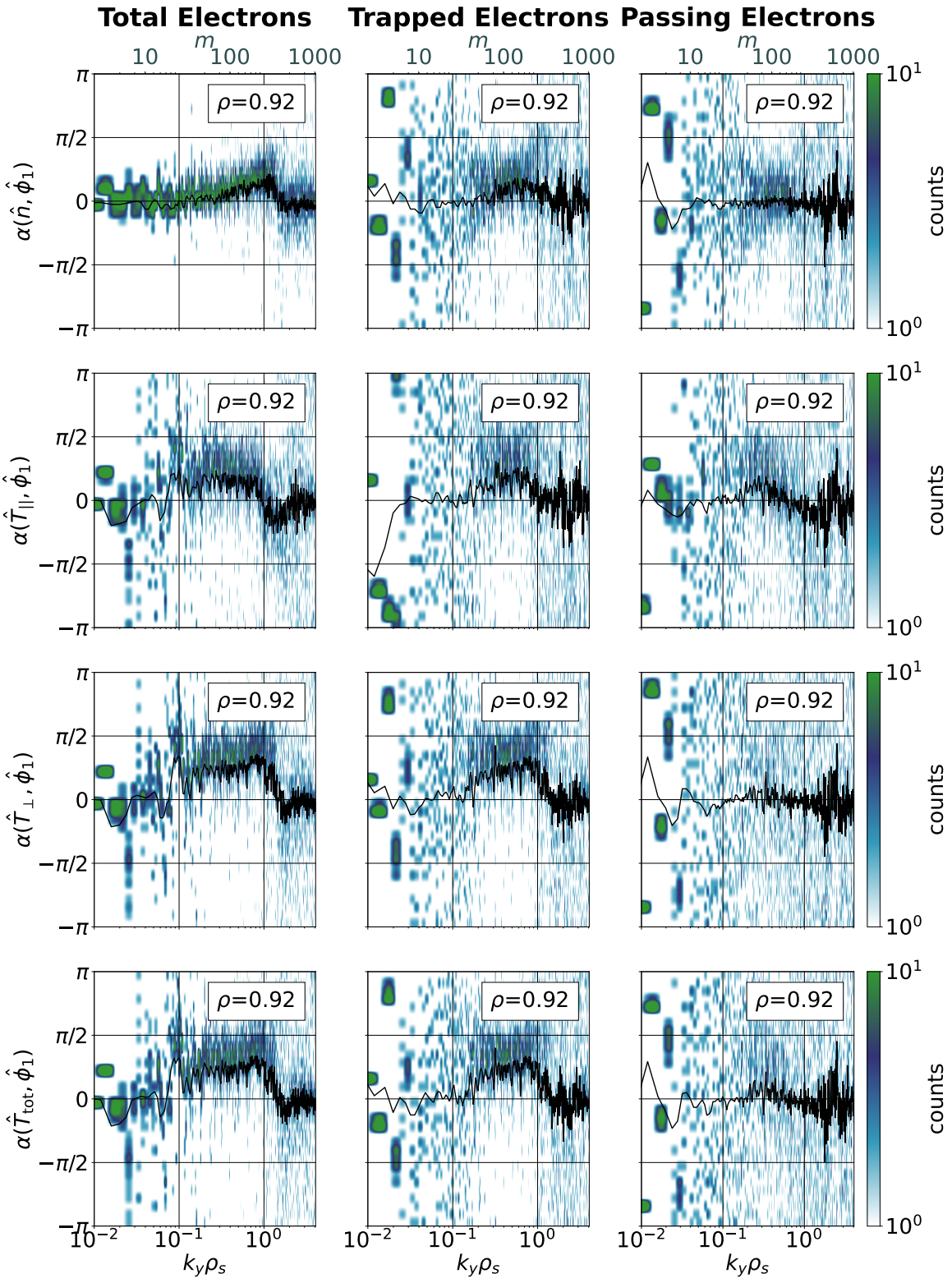

Figure D.15. Same as Fig. D.13 but for the BGK simulation. Based on data available at Ref. [224].

D.6 Trapped Particle Characterization

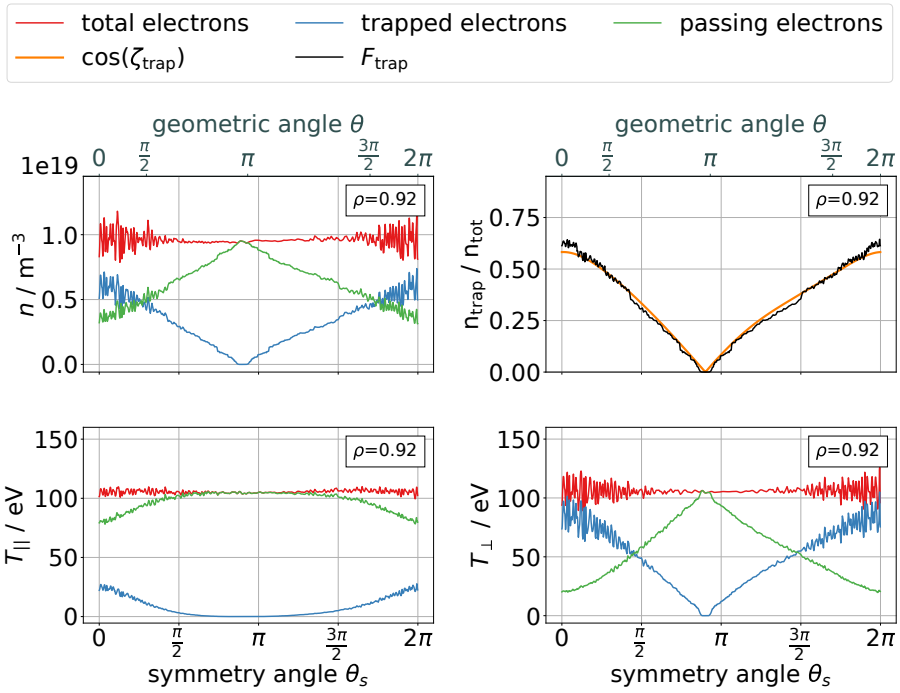

Figure D.16. Density, parallel and perpendicular temperature for total, trapped, and passing electrons as well as the trapped fraction at the final time of the LBD simulation. The orange line shows the analytical estimation for the trapped particle fraction. Taken from Ref. [59].

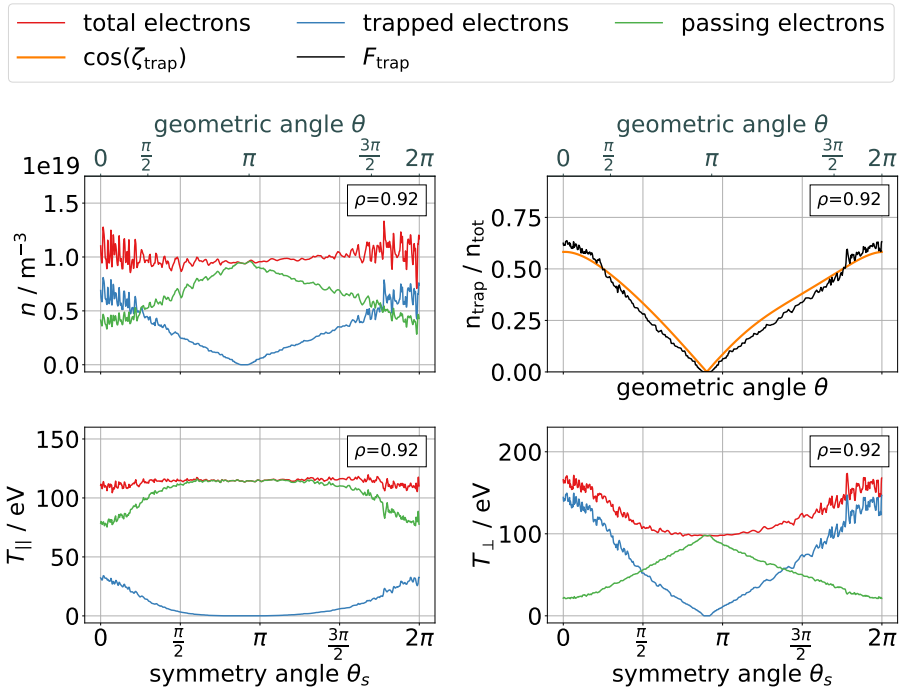

Figure D.17. Same as Fig. D.16 but for the collisionless simulation. Based on data available at Ref. [224].

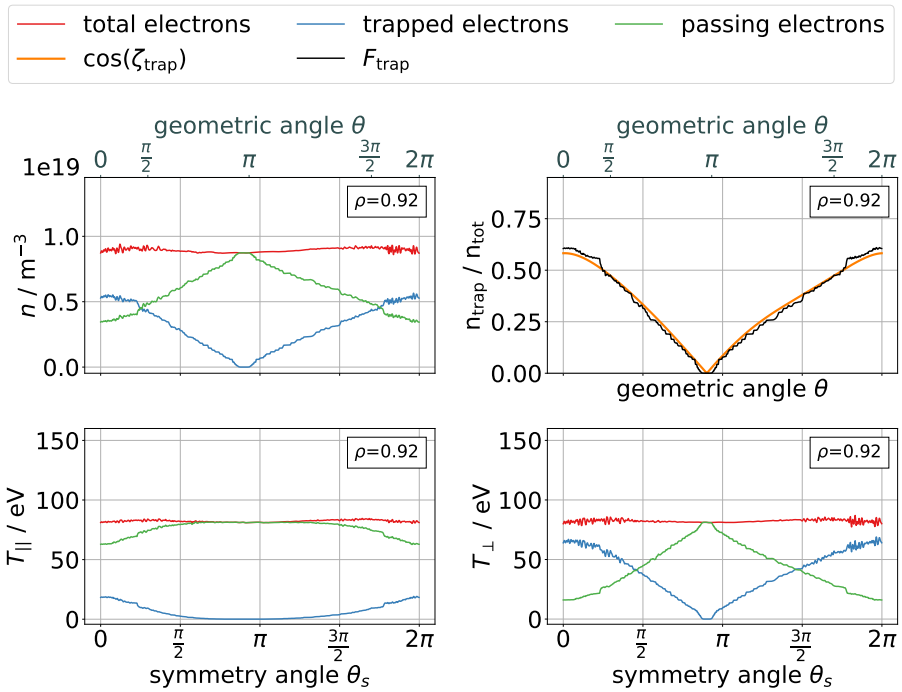

Figure D.18. Same as Fig. D.16 but for the BGK simulation. Based on data available at Ref. [224].

Bibliography

[1] J. Ongena, R. Koch, R. Wolf, H. Zohm, *Nat. Phys.* **12**, 398, DOI: 10.1038/NPHYS3745 (2016).

[2] EUROfusion Consortium Research Institutions, *European Research Roadmap to the Realisation of Fusion Energy*, https://euro-fusion.org/eurofusion/roadmap/ on 2023-06-15, 2023.

[3] S. C. Cowley, *Nat. Phys.* **12**, 384, DOI: 10.1038/nphys3719 (2016).

[4] H. J. G. L. M. Lamers, E. M. Levesque, *Understanding Stellar Evolution* (IOP Publishing, 2017), ISBN: 978-0-7503-1278-3, DOI: 10.1088/978-0-7503-1278-3.

[5] D. Prialnik, *An Introduction to the Theory of Stellar Structure and Evolution (second edition)* (Cambridge University Press, 2010), ISBN: 978-0-521-86604-0.

[6] J. Wesson, *Tokamaks (4th edition)* (Oxford University Press, 2011), ISBN: 9780199592234.

[7] M. Stix, *The Sun: An Introduction* (Springer-Verlag Berlin Heidelberg, 2002), ISBN: 978-3-642-56042-2, DOI: 10.1007/978-3-642-56042-2.

[8] IEA (International Energy Agency), *World Energy Balances: Overview*, IEA (2021), Paris https://www.iea.org/reports/world-energy-balances-overview/world on 2023-06-09.

[9] S. Atzeni, J. Meyer-ter-Vehn, *The Physics of Inertial Fusion: BeamPlasma Interaction, Hydrodynamics, Hot Dense Matter* (Oxford University Press, 2004), ISBN: 0-19-856264-0, DOI: 10.1093/acprof:oso/9780198562641.001.0001.

[10] P. Atkins, J. de Paula, *Physical Chemistry, Eighth Edition* (W. H. Freeman and Company, 2006), ISBN: 0-7167-8759-8.

[11] H. Zohm, *Magnetohydrodynamic Stability of Tokamaks* (WILEY-VCH Verlag GmbH & Co. KGaA, 2015), ISBN: 978-3-527-67736-8.

[12] J. P. Freidberg, *Ideal MHD* (Cambridge University Press, 2014), ISBN: 978-1-107-00625-6.

[13] *Fusion Physics* (INTERNATIONAL ATOMIC ENERGY AGENCY, 2012), ISBN: 978-92-0-130410-0.

[14] J. D. Lawson, *Proc. Phys. Soc.* **B 70**, 6, DOI: 10.1088/0370-1301/70/1/303 (1957).

[15] M. Greenwald, *Plasma Phys. Control. Fusion* **44**, R27, DOI: 10.1088/0741-3335/44/8/201 (2002).
[16] F. L. Hinton, R. D. Hazeltine, *Rev. Mod. Phys.* **48**, 239, DOI: 10.1103/RevModPhys.48.239 (1976).
[17] R. Balescu, *Aspects of anomalous transport in plasmas* (IOP Publishing Ltd, 2005), ISBN: 0-7503-1030-8.
[18] P. L. Similon, R. N. Sudan, *Annu. Rev. Fluid Mech.* **22**, 317–347, DOI: 10.1146/annurev.fl.22.010190.001533 (119).
[19] T. Yamada *et al.*, *Nat. Phys.* **4**, 721, DOI: 10.1038/nphys1029 (2008).
[20] I. Organization, *ITER - the way to new energy*, `https://www.iter.org/`, 2023.
[21] A. Hasegawa, K. Mima, *Phys. Fluids* **21**, 87–92, DOI: 10.1063/1.862083 (1978).
[22] A. Hasegawa, M. Wakatani, *Phys. Rev. Lett.* **50**, 682, DOI: 10.1103/PhysRevLett.50.682 (1983).
[23] A. Zeiler, J. F. Drake, B. Rogers, *Phys. Plasmas* **4**, 2134–2138, DOI: 10.1063/1.872368 (1997).
[24] M. A. Beer, G. W. Hammett, *Phys. Plasmas* **3**, 4046–4064, DOI: 10.1063/1.871538 (1996).
[25] B. J. Frei, R. Jorge, P. Ricci, *J. Plasma Phys.* **86**, 905860205, DOI: 10.1017/S0022377820000100 (2020).
[26] M. N. Rosenbluth, F. L. Hinton, *Phys. Rev. Lett.* **80**, 724, DOI: 10.1103/PhysRevLett.80.724 (1998).
[27] F. Jenko, B. D. Scott, *Phys. Rev. Lett.* **80**, 4883, DOI: 10.1103/PhysRevLett.80.4883 (1998).
[28] J. A. Krommes, *Annu. Rev. Fluid Mech.* **44**, 175–201, DOI: 10.1146/annurev-fluid-120710-101223 (2012).
[29] X. Garbet, Y. Idomura, L. Villard, T. H. Watanabe, *Nucl. Fusion* **50**, 043002, DOI: 10.1088/0029-5515/50/4/043002 (2010).
[30] N. Walkden *et al.*, *Commun. Phys.* **2**, 139, DOI: 10.1038/s42005-022-00906-2 (2022).
[31] S. Ku, C. S. Chang, P. H. Diamond, *Nucl. Fusion* **49**, 115021, DOI: 10.1088/0029-5515/49/11/115021 (2009).
[32] R. Hager *et al.*, *Phys. Plasmas* **29**, 112308, DOI: 10.1063/5.0097855 (2022).
[33] M. Dorf, M. Dorr, *Phys. Plasmas* **28**, 032508, DOI: 10.1063/5.0039169 (2021).
[34] D. Michels, A. Stegmeir, P. Ulbl, D. Jarema, F. Jenko, *Comput. Phys. Commun.* **264**, 107986, DOI: 10.1016/j.cpc.2021.107986 (2021).
[35] M. R. Wade, J. A. Leuer, *Fusion Sci. Technol.* **77**, 119–143, DOI: 10.1080/15361055.2020.1858670 (2021).
[36] F. Wagner *et al.*, *Phys. Rev. Lett.* **49**, 1408, DOI: 10.1103/PhysRevLett.49.1408 (1982).
[37] F. Wagner, *Plasma Phys. Control. Fusion* **49**, B1–B33, DOI: 10.1088/0741-3335/49/12B/S01 (2007).

[38] U. Plank *et al.*, *Plasma Phys. Control. Fusion* **65**, 014001, DOI: 10.1088/1361-6587/aca35b (2023).
[39] U. Plank *et al.*, *Phys. Plasmas* **30**, 042513, DOI: 10.1063/5.0102763 (2023).
[40] E. R. Solano *et al.*, *Nucl. Fusion* **62**, 076026, DOI: 10.1088/1741-4326/ac4ed8 (2022).
[41] L. Schmitz *et al.*, *Nucl. Fusion* **62**, 126050, DOI: 10.1088/1741-4326/ac94e1 (2022).
[42] L. Howlett, I. Cziegler, S. Freethy, H. Meyer, the MAST team, *Nucl. Fusion* **63**, 052001, DOI: 10.1088/1741-4326/acc2cf (2023).
[43] C. Bourdelle, *Nucl. Fusion* **60**, 102002, DOI: 10.1088/1741-4326/ab9e15 (2020).
[44] C. Angioni *et al.*, *Nucl. Fusion* **63**, 056005, DOI: 10.1088/1741-4326/acc193 (2023).
[45] T. Eich, P. Manz, the ASDEX Upgrade team, *Nucl. Fusion* **61**, 086017, DOI: 10.1088/1741-4326/ac0412 (2021).
[46] C. S. Chang *et al.*, *Nucl. Fusion* **57**, 116023, DOI: 10.1088/1741-4326/aa7efb (2017).
[47] A. Loarte, R. Neu, *Fusion Eng.* **122**, 256–273, DOI: 10.1016/j.fusengdes.2017.06.024 (2017).
[48] T. Eich *et al.*, *Nucl. Fusion* **53**, 093031, DOI: 10.1088/0029-5515/53/9/093031 (2013).
[49] Z.-Y. Li, X. Q. Xu, N.-M. Li, V. S. Chan, X.-G. Wang, *Nucl. Fusion* **59**, 046014, DOI: 10.1088/1741-4326/ab0184 (2019).
[50] R. M. Churchill *et al.*, *Nucl. Fusion* **59**, 096002, DOI: 10.1088/1741-4326/ab2af9 (2019).
[51] C. S. Chang *et al.*, *Phys. Plasmas* **28**, 022501, DOI: 10.1063/5.0027637 (2021).
[52] R. A. Pitts *et al.*, *Nucl. Mater. Energy* **20**, 100696, DOI: 10.1016/j.nme.2019.100696 (2019).
[53] G. Dif-Pradalier *et al.*, *Commun. Phys.* **2**, 229, DOI: 10.1038/s42005-022-01004-z (2022).
[54] P. H. Diamond, S.-I. Itoh, K. Itoh, T. S. Hahm, *Plasma Phys. Control. Fusion* **47**, R35–R161, DOI: 10.1088/0741-3335/47/5/R01 (2005).
[55] F. L. Hinton, M. N. Rosenbluth, *Plasma Phys. Control. Fusion* **41**, A653–A662, DOI: 10.1088/0741-3335/41/3A/059 (1999).
[56] P. Manas, Y. Camenen, S. Benkadda, W. A. Hornsby, A. G. Peeters, *Phys. Plasmas* **22**, L051202, DOI: 10.1063/1.4922754 (2015).
[57] Q. Pan, D. R. Ernst, D. R. Hatch, *Phys. Rev. E* **103**, L051202, DOI: 10.1103/PhysRevE.103.L051202 (2021).
[58] P. Ulbl, D. Michels, F. Jenko, *Contrib. Plasma Phys.* **62**, e202100180, DOI: 10.1002/ctpp.202100180 (2021).
[59] P. Ulbl *et al.*, *Phys. Plasmas* **30**, 052507, DOI: 10.1063/5.0144688 (2023).
[60] E. A. Frieman, L. Chen, *Phys. Fluids* **25**, 502, DOI: 10.1063/1.863762 (1982).
[61] A. J. Brizard, T. S. Hahm, *Rev. Mod. Phys* **79**, 421, DOI: 10.1103/RevModPhys.79.421 (2007).

[62] D. Michels, *Development of a high-performance gyrokinetic turbulence code for the edge and scrape-off layer of magnetic confinement fusion devices*, doctoral dissertation (Technische Universität München, 2022).
[63] R. D. Hazeltine, J. D. Meiss, *Plasma Confinement* (Addison-Wesley Publishing Company, 1991), ISBN: 0-201-50394-8.
[64] P. Helander, D. J. Sigmar, *Collisional Transport in Magnetized Plasmas* (Cambridge University Press, 2004), ISBN: 978-0-521-02098-5, DOI: 10.1017/S0022377804233086.
[65] D. R. Nicholson, *Introduction to Plasma Theory* (John Wiley & Sons, 1983), ISBN: 0-471-09045-X.
[66] J. D. Huba, *NRL Plasma Formulary* (Naval Research Laboratory, 2016).
[67] J. D. Jackson, *Classical Electrodynamics (2nd ed.)* (John Wiley & Sons, Inc., 1975), ISBN: 0-471-43132-X.
[68] R. J. Goldston, P. H. Rutherford, *Introduction to Plasma Physics* (Institute of Physics Publishing Bristol and Philadelphia, 1995), ISBN: 0-7503-0325-5.
[69] S. I. Braginskii, *Reviews of Plasma Physics* **1**, 205–311 (1965).
[70] T. G. Northrop, *Rev. Geophys.* **1**, 283, DOI: 10.1029/RG001i003p00283 (1963).
[71] R. G. Littlejohn, *The Physics of Fluids* **24**, 1730, DOI: 10.1063/1.863594 (1981).
[72] R. G. Littlejohn, *J. Plasma Phys.* **29**, 111–125, DOI: 10.1017/S002237780000060X (1983).
[73] A. I. Morozov, L. S. Solov'ev, *Reviews of Plasma Physics* **2**, 201 (1966).
[74] J. R. Cary, A. J. Brizard, *Rev. Mod. Phys* **81**, 693, DOI: 10.1103/RevModPhys.81.693 (2009).
[75] J. R. Cary, A. J. Brizard, *Phys. Plasmas* **20**, 092309, DOI: 10.1063/1.4823716 (2013).
[76] A. J. Brizard, C. Tronci, *Phys. Plasmas* **23**, 062107, DOI: 10.1063/1.4953431 (2016).
[77] J. R. Cary, *Phys. Rept.* **79**, 131–159, DOI: 10.1016/0370-1573(81)90175-7 (1981).
[78] J. R. Cary, R. G. Littlejohn, *Ann. Phys.* **51**, 1–34, DOI: 10.1016/0003-4916(83)90313-5 (1983).
[79] T. S. Hahm, W. W. Lee, A. Brizard, *Phys. Fluids* **31**, 1940, DOI: 10.1063/1.866641 (1988).
[80] A. J. Brizard, *J. Plasma Phys.* **41**, 541–559, DOI: 10.1017/S0022377800014070 (1989).
[81] H. Sugama, *Phys. Plasmas* **7**, 466, DOI: 10.1063/1.873832 (2000).
[82] A. J. Brizard, *Phys. Rev. Lett.* **84**, 5768, DOI: 10.1103/PhysRevLett.84.5768 (2000).
[83] A. J. Brizard, *Phys. Plasmas* **7**, 4816, DOI: 10.1063/1.1322063 (2000).
[84] N. Tronko, C. Chandre, *J. Plasma Phys.* **84**, 925840301, DOI: 10.1017/S0022377818000430 (2018).
[85] N. Miyato, B. D. Scott, M. Yagi, *Plasma Phys. Control. Fusion* **55**, 074011, DOI: 10.1088/0741-3335/55/7/074011 (2013).
[86] A. Bottino, E. Sonnendrücker, *J. Plasma Phys.* **81**, 435810501, DOI: 10.1017/S0022377815000574 (2015).

[87] J. A. Krommes, *Phys. Scr.* **T142**, 014035, DOI: 10.1088/0031-8949/2010/T142/014035 (2010).
[88] B. Scott, J. Smirnov, *Phys. Plasmas* **17**, 112302, DOI: 10.1063/1.3507920 (2010).
[89] W. W. Lee, *Phys. Fluids* **26**, 556, DOI: 10.1063/1.864140 (1983).
[90] C. K. Birdsall, A. B. Langdon, *Plasma Physics via Computer Simulation* (Taylor & Francis Group, 2004), ISBN: 978-1-4822-6306-0, DOI: 10.1201/9781315275048.
[91] E. Sonnendruecker, J. Roche, P. Bertrand, A. Ghizzo, *J. Comp. Phys.* **149**, 201–220, DOI: 10.1006/jcph.1998.6148 (1999).
[92] M. Kotschenreuther, G. Rewoldt, W. M. Tang, *Comp. Phys. Commun.* **88**, 128–140, DOI: 10.1016/0010-4655(95)00035-E (1995).
[93] B. Wang *et al.*, presented at the, pp. 1–12, ISBN: 9781450323789, DOI: 10.1145/2503210.2503258.
[94] S. Jolliet *et al.*, *Comput. Phys. Comm.* **177**, 409, DOI: 10.1016/j.cpc.2007.04.006 (2007).
[95] W. X. Wang *et al.*, *Phys. Plasmas* **13**, 092505, DOI: 10.1063/1.2338775 (2006).
[96] Y. Chen, J. Chowdhury, N. Maksimovic, S. E. Parker, W. Wan, *Phys. Plasmas* **23**, 056101, DOI: 10.1063/1.4943105 (2016).
[97] F. Jenko, W. Dorland, M. Kotschenreuther, B. Rogers, *Phys. Plasmas* **7**, 1904, DOI: 10.1063/1.874014 (2000).
[98] T. Görler *et al.*, *J. Comput. Phys.* **230**, 7053–7071, DOI: 10.1016/j.jcp.2011.05.034 (2011).
[99] W. Dorland, F. Jenko, M. Kotschenreuther, B. N. Rogers, *Phys. Rev. Lett.* **85**, 5579, DOI: 10.1103/PhysRevLett.85.5579 (2000).
[100] M. Barnes *et al.*, *GS2 v8.1.2*, Zenodo, `https://doi.org/10.5281/zenodo.6882296`, 2022, DOI: 10.5281/zenodo.6882296.
[101] J. Candy, R. E. Waltz, *Phys. Rev. Lett.* **91**, 045001, DOI: 10.1103/PhysRevLett.91.045001 (2003).
[102] J. Candy, E. Belli, R. Bravenec, *J. Comput. Phys.* **324**, 73, DOI: 10.1016/j.jcp.2016.07.039 (2016).
[103] A. G. Peeters *et al.*, *Comput. Phys. Comm.* **180**, 2650, DOI: 10.1016/j.cpc.2009.07.001 (2009).
[104] T.-H. Watanabe, H. Sugama, *Nucl. Fusion* **46**, 24, DOI: 10.1088/0029-5515/46/1/003 (2006).
[105] Y. Idomura, M. Ida, T. Kano, N. Aiba, S. Tokuda, *Comput. Phys. Comm.* **179**, 391–403, DOI: 10.1016/j.cpc.2008.04.005 (2008).
[106] V. Grandgirard *et al.*, *Comput. Phys. Comm.* **207**, 35, DOI: 10.1016/j.cpc.2016.05.007 (2017).
[107] M. Boesl *et al.*, *Phys. Plasmas* **26**, 122302, DOI: 10.1063/1.5121262 (2019).

[108] E. L. Shi, G. W. Hammett, T. Stoltzfus-Dueck, A. Hakim, *J. Plasma Phys.* **83**, 905830304, DOI: 10.1017/S002237781700037X (2017).
[109] A. Hakim, M. Francisquez, J. Juno, G. W. Hammett, *J. Plasma Phys.* **86**, 905860403, DOI: 10.1017/S0022377820000586 (2020).
[110] F. Hariri, M. Ottaviani, *Comput. Phys. Comm.* **184**, 2419–2429, DOI: 10.1016/j.cpc.2013.06.005 (2013).
[111] A. Stegmeir, D. Coster, O. Maj, K. Hallatschek, K. Lackner, *Comput. Phys. Comm.* **198**, 139–153, DOI: 10.1016/j.cpc.2015.09.016 (2016).
[112] D. Michels *et al.*, *Phys. Plasma* **29**, 032307, DOI: 10.1063/5.0082413 (2022).
[113] N. R. Mandell, A. Hakim, G. W. Hammett, M. Francisquez, *J. Plasma Phys.* **86**, 905860109, DOI: 10.1017/S0022377820000070 (2020).
[114] A. Arakawa, *J. Comput. Phys.* **1**, 119–143, DOI: 10.1016/0021-9991(66)90015-5 (1966).
[115] A. Stegmeir *et al.*, *Phys. Plasmas* **26**, 052517, DOI: 10.1063/1.5089864 (2019).
[116] W. Hackbusch, *Multi-Grid Methods and Applications* (Springer-Verlag Berlin Heidelberg, 1985), ISBN: 978-3-662-02427-0, DOI: 10.1007/978-3-662-02427-0.
[117] Y. Saad, M. H. Schultz, *SIAM J. Sci. Stat. Comput.* **7**, 856, DOI: 10.1137/0907058 (1986).
[118] M. J. Pueschel, T. Dannert, F. Jenko, *Comput. Phys. Comm.* **181**, 1428–1437, DOI: 10.1016/j.cpc.2010.04.010 (2010).
[119] M. Badino, *Eur. Phys. J. H* **36**, 353, DOI: 10.1140/epjh/e2011-10048-5 (2011).
[120] H. Goldstein, *Classical Mechanics* (Pearson Education Inc., 2002), ISBN: 0321-18897 7.
[121] D. C. Montgomery, D. A. Tidman, *Plasma Kinetic Theory* (McGraw-Hill, 1964).
[122] L. Landau, *Phys. Z. Sowjet.* **10**, 154 (1936).
[123] M. N. Rosenbluth, W. M. Macdonald, D. L. Judd, *Phys. Review* **107**, 1, DOI: 10.1103/PhysRev.107.1 (1957).
[124] S. Chandrasekhar, *Rev. Mod. Phys.* **15**, 1, DOI: 10.1103/RevModPhys.15.1 (1943).
[125] B. A. Trubnikov, *J. Exptl. Theoret. Phys. (U.S.S.R.)* **7**, 926 (1958).
[126] Y. N. Dnestrovskii, D. P. Kostomarov, *Numerical Simulation of Plasmas* (Springer Verlage Berlin Heidelberg New York Tokyo, 1986), ISBN: 3-540-15835-9.
[127] J. L. Spitzer, *Physics of Fully Ionized Gases* (John Wiley & Sons, Inc., 1962), ISBN: 0-470-81723-2.
[128] D. V. Sivukhin, *Reviews of Plasma Physics* **4**, 93 (1966).
[129] D. O. Gericke, M. S. Murillo, M. Schlanges, *Phys. Rev. E* **65**, 036418, DOI: 10.1103/PhysRevE.65.036418 (2001).
[130] S. P. Hirshman, D. J. Sigmar, *Phys. Fluids* **19**, 1532, DOI: 10.1063/1.861356 (1976).
[131] A. Lenard, I. B. Bernstein, *Phys. Review* **112**, 1456, DOI: 10.1103/PhysRev.112.1456 (1958).
[132] J. P. Dougherty, *Phys. Fluids* **7**, 1788, DOI: 10.1063/1.2746779 (1964).

[133] M. Francisquez, T. N. Bernard, N. R. Mandell, G. W. Hammett, A. Hakim, *Nucl. Fusion* **60**, 096021, DOI: 10.1088/1741-4326/aba0c9 (2020).
[134] M. N. Rosenbluth, R. D. Hazeltine, *Phys. Fluids* **15**, 116, DOI: 10.1063/1.1693728 (1972).
[135] F. W. J. Olver *et al.*, *NIST Digital Library of Mathematical Functions*, `https://dlmf.nist.gov/`, Release 1.1.8 of 2022-12-15, 2016.
[136] E. Hirvijoki, J. W. Burby, A. J. Brizard, *Phys. Plasmas* **29**, 060701, DOI: 10.1063/5.0091727 (2022).
[137] A. J. Brizard, *Physics of Plasmas* **11**, 4429, DOI: 10.1063/1.1780532 (2004).
[138] I. G. Abel, M. Barnes, S. C. Cowley, W. Dorland, A. A. Schekochihin, *Phys. Plasmas* **15**, 122509, DOI: 10.1063/1.3046067 (2008).
[139] H. Sugama, T.-H. Watanabe, M. Nunami, *Phys. Plasmas* **16**, 112503, DOI: 10.1063/1.3257907 (2009).
[140] E. Hirvijoki, A. Brizard, A. Snicker, T. Kurki-Suonio, *Phys. Plasmas* **20**, 092505, DOI: 10.1063/1.4820951 (2013).
[141] J. R. Haack, C. D. Hauck, M. S. Murillo, *Journal of Statistical Physics* **168**, 826, DOI: 10.1007/s10955-017-1824-9 (2017).
[142] P. L. Bhatnagar, E. P. Gross, M. Krook, *Phys. Review* **94**, 511, DOI: 10.1103/PhysRev.94.511 (1954).
[143] T. F. Morse, *Phys. Fluids* **6**, 1420, DOI: 10.1063/1.1710963 (1963).
[144] J. M. Greene, *Phys. Fluids* **16**, 2022, DOI: 10.1063/1.1694254 (1973).
[145] M. Francisquez, J. Juno, A. Hakim, G. W. Hammett, D. R. Ernst, *J. Plasma Phys.* **88**, 905880303, DOI: 10.1017/S0022377822000289 (2022).
[146] T. Görler, F. Jenko, *Phys. Rev. Lett.* **100**, 185002, DOI: 10.1103/PhysRevLett.100.185002 (2008).
[147] P. Crandall, *Collisional and Electromagnetic Physics in Gyrokinetic Models*, doctoral dissertation (University of California, Los Angeles, 2019).
[148] X. Garbet *et al.*, *Phys. Plasmas* **16**, 062503, DOI: 10.1063/1.3153328 (2009).
[149] J. Angus, *On Anomalous Plasma Transport in The Edge of Magnetic Confinement Devices*, doctoral dissertation (University of California, San Diego, 2012).
[150] M. Boesl *et al.*, *Contrib. Plasma Phys.* **60**, e201900117, DOI: 10.1002/ctpp.201900117 (2019).
[151] M. A. Dorf, R. H. Cohen, M. Dorr, J. Hittinger, T. D. Rognlien, *Contrib. Plasma Phys.* **54**, 517, DOI: 10.1002/ctpp.201410023 (2014).
[152] R. Hager *et al.*, *Journal of Computational Physics* **315**, 644, DOI: 10.1016/j.jcp.2016.03.064 (2016).
[153] H. Sugama, S. Matsuoka, S. Satake, M. Nunami, T.-H. Watanabe, *Phys. Plasmas* **26**, 102108, DOI: 10.1063/1.5115440 (2019).

[154] P. Donnel *et al.*, *Comput. Phys. Comm.* **234**, 1–13, DOI: 10.1016/j.cpc.2018.08.008 (2019).

[155] Q. Pan, D. R. Ernst, P. Crandall, *Phys. Plasmas* **27**, 042307, DOI: 10.1063/1.5143374 (2020).

[156] B. J. Frei *et al.*, *J. Plasma Phys.* **87**, 905870501, DOI: 10.1017/S0022377821000830 (2021).

[157] E. A. Belli, J. Candy, *Plasma Phys. Control. Fusion* **59**, 045005, DOI: 10.1088/1361-6587/aa5c94 (2017).

[158] P. Crandall *et al.*, *Comput. Phys. Comm.* **255**, 107360, DOI: 10.1016/j.cpc.2020.107360 (2020).

[159] B. J. Frei, A. C. D. Hoffmann, P. Ricci, *J. Plasma Phys.* **88**, 905880304, DOI: 10.1017/S0022377822000344 (2022).

[160] W. Hundsdorfer, J. Verwer, *Numerical Solution of Time-Dependent Advection-Diffusion-Reaction Equations* (Springer-Verlag Berlin Heidelberg, 2003), ISBN: 978-3-642-05707-6, DOI: 10.1007/978-3-662-09017-6.

[161] E. Hairer, S. P. Norsett, G. Wanner, *Solving Ordinary Differential Equations I (2nd Edition)* (Springer-Verlag Berlin Heidelberg, 1993), ISBN: 3-540-56670-8, DOI: 10.1007/978-3-540-78862-1.

[162] J. H. Ferziger, M. Peric, *Computational Methods for Fluid Dynamics (3rd rev. ed.)* (Springer-Verlag Berlin Heidelberg New York, 2002), ISBN: 978-3-540-42074-3, DOI: 10.1007/978-3-642-56026-2.

[163] W. H. Press, S. A. Teukolsky, W. T. Vetterling, B. P. Flannery, *Numerical Recipes in FORTRAN (2nd Edition)* (Cambridge University Press, 1992), ISBN: 0-521-43064-X.

[164] R. L. Burden, J. D. Faires, *Numerical Analysis (9th ed.)* (Brooks/Cole, Cengage Learning, 2010), ISBN: 978-0-538-73351-9.

[165] D. Ghosh, M. A. Dorf, M. R. Dorr, J. A. F. Hittinger, *J. Sci. Comput.* **193**, 819–849, DOI: 10.1007/s10915-018-0726-6 (2018).

[166] E. Hairer, G. Wanner, *Solving Ordinary Differential Equations II (2nd Revised Edition)* (Springer-Verlag Berlin Heidelberg, 1993), ISBN: 978-3-642-05220-0, DOI: 10.1007/978-3-642-05221-7.

[167] R. Courant, K. Friedrichs, H. Lewy, *Mathematische Annalen* **100**, 32, DOI: 10.1007/BF01448839 (1928).

[168] R. J. LeVeque, *Finite Difference Methods for Ordinary and Partial Differential Equations* (Society for Industrial and Applied Mathematics, 2007), ISBN: 978-0-89871-629-0, DOI: 10.1137/1.9780898717839.

[169] R. J. LeVeque, *Finite Volume Methods for Hyperbolic Problems* (Cambridge University Press, 2002), ISBN: 0-511-04219-1, DOI: 10.1017/CBO9780511791253.

[170] E. W. Weisstein, *Kronecker Sum*, From MathWorld–A Wolfram Web Resource, `https://mathworld.wolfram.com/KroneckerSum.html` on 2023-05-05.

[171] R. Grone, C. R. Johnson, E. M. Sa, H. Wolkowicz, *Linear Algebra Appl.* **87**, 213–225, DOI: 10.1016/0024-3795(87)90168-6 (1987).

[172] S. C. Reddy, L. N. Trefethen, *SIAM J. Appl. Math.* **54**, 1634–1649, DOI: 10.1137/S0036139993246982 (1994).

[173] L. N. Trefethen, M. Embree, *Spectra and Pseudospectra* (Princeton University Press, 2005), ISBN: 9780691119465, DOI: 10.1515/9780691213101.

[174] L. Elsner, M. H. C. Paardekooper, *Linear Algebra Appl.* **92**, 107–123, DOI: 10.1016/0024-3795(87)90253-9 (1987).

[175] S. C. Reddy, L. N. Trefethen, *Numer. Math.* **62**, 235–267, DOI: 10.1007/BF01396228 (1992).

[176] P. D. Lax, R. D. Richtmyer, *Commun. Pure Appl. Math.* **IX**, 267–293, DOI: 10.1002/cpa.3160090206 (1956).

[177] A. Gaul, *PseudoPy v1.2.5*, Github, `https://github.com/andrenarchy/pseudopy` on 2023-05-17.

[178] G. Strang, *SIAM J. Numer. Anal.* **5**, 506, DOI: 10.1137/0705041 (1968).

[179] H. Doerk, F. Jenko, *Comput. Phys. Commun.* **185**, 1938, DOI: 10.1016/j.cpc.2014.03.024 (2014).

[180] I. Almuslimani, *Bit Numer. Math.* **63**, 3, DOI: 10.1007/s10543-023-00945-3 (2023).

[181] U. M. Ascher, S. J. Ruuth, B. T. R. Wetton, *SIAM J. Numer. Anal.* **32**, 797–823, DOI: 10.1137/0732037 (1995).

[182] U. M. Ascher, S. J. Ruuth, R. J. Spiteri, *Appl. Numer. Math.* **25**, 151–167, DOI: 10.1016/S0168-9274(97)00056-1 (1997).

[183] D. A. Knoll, D. E. Keyes, *J. Comput. Phys.* **193**, 357–397, DOI: 10.1016/j.jcp.2003.08.010 (2004).

[184] OpenMP Architecture Review Board, *OpenMP Application Program Interface Version 4.5*, `https://www.openmp.org/wp-content/uploads/openmp-4.5.pdf` on 2023-05-24, 2015.

[185] Message Passing Interface Forum, *MPI: A Message-Passing Interface Standard Version 3.1*, `https://www.mpi-forum.org/docs/mpi-3.1/mpi31-report.pdf` on 2023-05-24, 2015.

[186] S. Williams, A. Waterman, D. Patterson, *Commun. ACM* **52**, 65–76, DOI: 10.1145/1498765.1498785 (2009).

[187] G. Hager, G. Wellein, *Introduction to High Performance Computing for Scientists and Engineers* (CRC Press, 2011), ISBN: 978-1-4398-1192-4, DOI: 10.1201/EBK1439811924.

[188] G. M. Amdahl, *Validity of the single processor approach to achieving large scale computing capabilities*, Proceedings of the April 18-20, 1967, Spring Joint Computer Conference, Association for Computing Machinery, 1967, DOI: 10.1145/1465482.1465560.

[189] C. T. Kelley, *Iterative Methods for Optimization* (Society for Industrial and Applied Mathematics, 1999), ISBN: 978-0-89871-433-3, DOI: 10.1137/1.9781611970920.
[190] S. Coda *et al.*, *Nucl. Fusion* **58**, 102011, DOI: 10.1088/1741-4326/aa6412 (2017).
[191] M. Greenwald, *Phys. Plasmas* **17**, 058101, DOI: 10.1063/1.3298884 (2010).
[192] W. Zholobenko *et al.*, *Plasma Phys. Control. Fusion* **63**, 034001, DOI: 10.1088/1361-6587/abd97e (2021).
[193] W. Zholobenko *et al.*, *Nucl. Fusion* **61**, 116015, DOI: 10.1088/1741-4326/ac1e61 (2021).
[194] D. S. Oliveira *et al.*, *Nucl. Fusion* **62**, 096001, DOI: 10.1088/1741-4326/ac4cde (2022).
[195] A. Stegmeir *et al.*, *Plasma Phys. Control. Fusion* **60**, 035005, DOI: 10.1088/1361-6587/aaa373 (2018).
[196] W. Zholobenko *et al.*, *Contrib. Plasma Phys.* **60**, e201900131, DOI: 10.1002/ctpp.201900131 (2019).
[197] P. Ricci *et al.*, *Plasma Phys. Control. Fusion* **54**, 124047, DOI: 10.1088/0741-3335/54/12/124047 (2012).
[198] F. D. Halpern *et al.*, *J. Comput. Phys.* **315**, 388–408, DOI: 10.1016/j.jcp.2016.03.040 (2016).
[199] P. Tamain *et al.*, *J. Comput. Phys.* **321**, 606–623, DOI: 10.1016/j.jcp.2016.05.038 (2016).
[200] F. Nespoli *et al.*, *Nucl. Fusion* **59**, 096006, DOI: 10.1088/1741-4326/ab2813 (2019).
[201] D. S. de Oliveira, T. Body, D. Galassi, C. Theiler, *TCV-X21: a FAIR dataset of TCV experimental results for validating edge/divertor turbulence models*, Zenodo, `https://doi.org/10.5281/zenodo.5776286`, 2021, DOI: 10.5281/zenodo.5776286.
[202] T. Body, *Development of Turbulence Simulations for the Edge & Divertor and Validation against Experiment*, doctoral dissertation (Technische Universität München, 2022).
[203] P. Angelino *et al.*, *Phys. Plasmas* **13**, 052304, DOI: 10.1063/1.2193947 (2006).
[204] G. Dif-Pradalier *et al.*, *Phys. Plasmas* **15**, 042315, DOI: 10.1063/1.2904901 (2008).
[205] G. Dif-Pradalier, V. Grandgirard, Y. Sarazin, X. Garbet, P. Ghendrih, *Commun. Nonlinear Sci.* **13**, 65, DOI: 10.1016/j.cnsns.2007.05.004 (2008).
[206] P. Manz, *The Microscopic Picture of Plasma Edge Turbulence*, habilitation (Technische Universität München, 2018).
[207] P. Manz *et al.*, *Plasma Phys. Control. Fusion* **56**, 035010, DOI: 10.1088/0741-3335/56/3/035010 (2014).
[208] A. Zeiler, *Tokamak Edge Turbulence*, habilitation (Universität Ulm, 1999).
[209] B. B. Kadomtsev, O. P. Pogutse, *Nucl. Fusion* **11**, 67, DOI: 10.1088/0029-5515/11/1/010 (1971).
[210] T. T. Ribeiro, B. D. Scott, *IEEE Transactions on Plasma Science* **38**, 2159–2168, DOI: 10.1109/TPS.2010.2056935 (2010).

[211] B. Scott, *Turbulence and Instabilities in Magnetised Plasmas, Volume 1* (IOP Publishing Ltd, 2021), ISBN: 978-0-7503-2504-2, DOI: 10.1088/978-0-7503-2504-2.
[212] P. Virtanen *et al.*, *Nat. Methods* **17**, 261–272, DOI: 10.1038/s41592-019-0686-2 (2020).
[213] The SciPy community, *Fourier Transforms*, https://docs.scipy.org/doc/scipy/tutorial/fft.html on 2023-06-01, 2023.
[214] G. D. Conway *et al.*, *Plasma Phys. Control. Fusion* **46**, 951, DOI: 10.1088/0741-3335/46/6/003 (2004).
[215] J. F. Kaiser, *Digital Filters* (John Wiley and Sons, New York, 1966), pp. 218–285.
[216] D. A. Lyon, *J. Object Technol.* **8**, 23–34, DOI: 10.5381/jot.2009.8.7.c2 (2009).
[217] A. Ross, *Extension of GRILLIX: Towards a global fluid turbulence code for realistic magnetic geometries*, doctoral dissertation (Technische Universität München, 2018).
[218] W. Zholobenko *et al.*, *Nucl. Mater. Energy* **34**, 101351, DOI: 10.1016/j.nme.2022.101351 (2023).
[219] F. Jenko, B. D. Scott, *Phys. Plasmas* **6**, 2418–2424, DOI: 10.1063/1.873513 (1999).
[220] E. W. Weisstein, *Kronecker Delta*, From MathWorld–A Wolfram Web Resource, https://mathworld.wolfram.com/KroneckerDelta.html on 2023-06-01.
[221] T. Görler *et al.*, *Phys. Plasmas* **21**, 122307, DOI: 10.1063/1.4904301 (2014).
[222] B. Scott, *Turbulence and Instabilities in Magnetised Plasmas, Volume 2* (IOP Publishing Ltd, 2021), ISBN: 978-0-7503-3855-4, DOI: 10.1088/978-0-7503-3855-4.
[223] M. Abramowitz, I. A. Stegun, *Handbook of Mathematical Functions with Formulas, Graphs, and Mathematical Tables (9th edition)* (New York: Dover Publications, 1972), ISBN: 978-0-486-61272-0.
[224] P. Ulbl *et al.*, *TCV-X21-GENEX: influence of collisions on the validation of global gyrokinetic simulations*, Zenodo, https://doi.org/10.5281/zenodo.7894731, 2023, DOI: 10.5281/zenodo.7894731.
[225] T. Dannert, *Gyrokinetische Simulation von Plasmaturbulenz mit gefangenen Teilchen und elektromagnetischen Effekten*, doctoral dissertation (Technische Universität München, 2004).
[226] F. Merz, F. Jenko, *Phys. Rev. Lett.* **100**, 035005, DOI: 10.1103/PhysRevLett.100.035005 (2008).
[227] B. Scott, *New J. Phys.* **7**, 92, DOI: 10.1088/1367-2630/7/1/092 (2005).
[228] T. Dannert, F. Jenko, *Phys. Plasmas* **12**, 072309, DOI: 10.1063/1.1947447 (2005).
[229] D. Told *et al.*, *Phys. Plasmas* **20**, 122312, DOI: 10.1063/1.4858899 (2013).
[230] D. Estève *et al.*, *Nucl. Fusion* **58**, 036013, DOI: 10.1088/1741-4326/aa6ebb (2018).
[231] G. Dif-Pradalier *et al.*, *Phys. Plasmas* **18**, 062309, DOI: 10.1063/1.3592652 (2011).
[232] D. Jarema *et al.*, *Comput. Phys. Commun.* **215**, 49–62, DOI: 10.1016/j.cpc.2017.02.005 (2017).
[233] M. Landreman, D. R. Ernst, *J. Comput. Phys.* **243**, 130–150, DOI: 10.1016/j.jcp.2013.02.041 (2013).

[234] E. Kim, P. H. Diamond, *Phys. Rev. Lett.* **90**, 185006, DOI: 10.1103/PhysRevLett.90.185006 (2003).
[235] P. Manz *et al.*, *Phys. Plasmas* **19**, 072311, DOI: 10.1063/1.4737612 (2012).
[236] S. Ku *et al.*, *Phys. Plasmas* **25**, 056107, DOI: 10.1063/1.5020792 (2018).
[237] F. Wagner, *Eur. Phys. J. H* **43**, 523–549, DOI: 10.1140/epjh/e2016-70064-9 (2018).
[238] D. R. Hatch *et al.*, *Nucl. Fusion* **55**, 063028, DOI: 10.1088/0029-5515/55/6/063028 (2015).
[239] D. G. Whyte *et al.*, *Nucl. Fusion* **50**, 105005, DOI: 10.1088/0029-5515/50/10/105005 (2010).
[240] K. H. Burrell *et al.*, *Plasma Phys. Control. Fusion* **44**, A253, DOI: 10.1088/0741-3335/44/5A/325 (2002).
[241] Y. Camenen *et al.*, *Nucl. Fusion* **47**, 510, DOI: 10.1088/0029-5515/47/7/002 (2007).
[242] E. W. Weisstein, *Newton-Cotes Formulas*, From MathWorld–A Wolfram Web Resource, `https://mathworld.wolfram.com/Newton-CotesFormulas.html` on 2023-05-02.